On the configuration of arrays of floating wave energy converters

Benjamin F. M. Child

A thesis submitted for the degree of Doctor of Philosophy

The University of Edinburgh

2011

Abstract

In this thesis, certain issues relating to a number of wave energy absorbers operating in the same vicinity are investigated. Specifically, arrangements of the devices within such an array are sought, such that beneficial hydrodynamic interference between members is exploited and unwanted effects mitigated.

Arrays of 'point absorber' devices as well as converters with multiple closely spaced floats are modelled and a frequency domain hydrodynamic solution derived. This is implemented as efficient computer code, capable of producing the full linear wave theory solution to any desired degree of accuracy. Furthermore, the results are verified against output from the boundary element code WAMIT.

Initially, detailed analysis of an isolated absorber is conducted, with motion responses, forces, power output and velocity potentials at the free surface computed for a range of different device specifications. Elementary examples of arrays are then used to demonstrate the influence of factors such as device separation, wave heading angle, number of devices and array configuration upon collective performance.

Subsequently, the power output from an array of five devices is optimised with respect to its layout, using two different routines. The first is a new heuristic approach, named the Parabolic Intersection (PI) method, that efficiently creates array configurations using only basic computations. The second is a Genetic Algorithm (GA) with a novel 'crossover' operator. Each method is applied to maximise the output at a given regular wave frequency and direction under two different power take-off regimes and also to minimise power in a third, cautionary example. The resulting arrays are then analysed and the optimisation procedures themselves evaluated.

Finally, the effects of irregular seas on array interactions are investigated. The configurations that were optimised for regular wave climates are assessed in a range of irregular sea-states. The GA is then used once more to create optimal array layouts for each of these seas. The characteristics of the arrays are subsequently examined and the influence of certain spectral parameters on the optimal solutions considered.

The optimisation procedures were both found to be effective, with the GA marginally outperforming the PI method in all cases. Significant positive and negative modifications to the power output were observed in the arrays optimised in regular waves, although the effects weakened when the same arrays were subjected to irregular sea-states. However, arrays optimised specifically in irregular seas exhibited differences in net power output equivalent to over half that produced from the same number of devices in isolation.

Declaration

I hereby declare that this thesis has been composed by myself and that except where stated, the work contained is my own.

I also declare that the work contained in this thesis has not been submitted for any other degree or professional qualification except as specified.

Benjamin F. M. Child

Acknowledgements

The first lot of thanks must go to my supervisors, Vengatesan Venugopal and David Ingram, who have nurtured my academic development and been wholeheartedly supportive of my chosen direction of research throughout. I am also indebted to Grég Payne for the time he volunteered to provide me with help and to Chris Dent, Richard Crozier and Ally Price for engaging in some enlightening discussions with me.

This research was made possible by the financial support of the SuperGen Marine Consortium and I am particularly grateful to Robin Wallace for approving several rewarding trips abroad on conferences throughout my study. The contribution of the school IT team to the success of this project must also be acknowledged. To my former and current superiors Richard Porter and João Cruz, I owe thanks for respectively igniting my interest in wave energy and supporting me in the final stages of this project. I would also like to thank David and Michele Jones for being, amongst other things, first-rate landlords.

I have found my time at the Institute for Energy Systems to be both enjoyable and stimulating and would therefore like to thank all the people there for making it so. In particular, I am thankful to my 'mentors' Scott Couch and Henry Jeffrey for teaching me how to be an academic and a businessman. I am also grateful to David Forehand and Helen Bailey for their invaluable help, encouragement and friendship. Away from home, my time was invariably enlivened by the wider 'inorean' community of young researchers in offshore renewables, for which I thank them. I will also never forget the good times I have spent with my friends outside of work, relaxing, recharging and experiencing the best (and sometimes the worst) of what Edinburgh has to offer.

I would like to express my enormous gratitude to my mum, my dad and the rest of my family whose continuing love and encouragement, not to mention helpful advice, pre-dates any desire of mine to become the second doctor amongst us. Finally, and most importantly, I would like to thank Alice for helping me in too many ways to even begin to describe here. Her support, for which I only hope I can one day repay, has in no small part made this thesis what you see before you.

For the surge is sown with barley
The cattle graze on the covered foam

Dylan Thomas
Ballad of the Long-Legged Bait

Contents

List of figures

List of tables

Nomenclature

$\mathbb{C}$	Set of complex numbers
$\mathbb{N}$	Set of natural numbers $0, 1, 2, \ldots$
$\mathbb{R}$	Set of real numbers
$\mathbb{Z}$	Set of integers $\ldots, -2, -1, 0, 1, 2, \ldots$
$\mathbf{0}$	The zero matrix
$\mathbf{I}$	The identity matrix
$\frac{\mathrm{D}}{\mathrm{D}t}$	Lagrangian derivative
∇	Vector differential operator: del, nabla
Im{}	Imaginary part of expression
Re{}	Real part of expression
i	The imaginary number, $\sqrt{-1}$
*	Complex conjugate operator
$^\mathsf{T}$	Transpose operator: the matrix (a_{ji}) given the matrix (a_{ij})
$H_n(x)$	Hankel function of the first kind of order n
$I_n(x)$	Modified Bessel function of the first kind of order n
$J_n(x)$	Bessel function of the first kind of order n
$K_n(x)$	Modified Bessel function of the second kind of order n
$Y_n(x)$	Bessel function of the second kind of order n
Γ	Legendre Gamma function
$\mathcal{O}$	Landau symbol: "of order"
$O_j r_j \theta_j z$	Global cylindrical polar coordinate system with O_j at the intersection of the centre line of Cylinder j and the seabed, the z-direction pointing vertically upwards

$Or\theta z$	Local cylindrical polar coordinate system with O on seabed and the z-direction pointing vertically upwards
$Oxyz$	Global Cartesian coordinate system with O on seabed and the z-direction pointing vertically upwards
ρ	Fluid density
d	Water depth
g	Gravitational acceleration
t	Time
H	Amplitude of ambient incident wave
T	Period of ambient incident wave
β	Wave heading angle in an anticlockwise direction from the positive x-direction
ω	Angular frequency of ambient incident wave
f	Frequency of ambient incident wave
k_0	Progressive wave number of ambient incident wave
k_m, $m \geq 1$	Evanescent wave number
$S(k_0, \beta)$	Wave energy spectrum
$S^{\mathrm{P}}(k_0, \beta)$	Power spectrum
α_{p}	Phillips constant
γ_{p}	Peak enhancement parameter
σ_{p}	Peak width parameter
c_{g}	Group velocity
s_{p}	Spreading parameter
M	Mass of device
a	Radius of device
b	Draught of device
h	Clearance beneath device
ϵ	Power take-off mass coefficient
γ	Power take-off damping coefficient
δ	Power take-off spring coefficient

N Number of cylinders in array

L_{ij} Distance between centres of Cylinders i and j

α_{ij} Angle at Cylinder i between the positive x-direction and line joining the centre of i to that of j in an anti-clockwise direction

(x_j, y_j) Global Cartesian coordinates of centre of Cylinder j

Φ, ϕ Velocity potential: time-dependent and -independent forms

$\zeta^{(t)}$, ζ Free surface elevation relative to still water level $z = d$: time-dependent and time-independent forms

$F^{(t)}$, F Force: time-dependent and -independent forms

$p^{(t)}$, p Pressure in the fluid: time-dependent and time-independent forms

$X^{(t)}$, X Heave displacement: time-dependent and -independent forms

$\dot{X}^{(t)}$, X' Heave velocity: time-dependent and -independent forms

$\ddot{X}^{(t)}$, X'' Heave acceleration: time-dependent and -independent forms

$P^{(t)}, P$ Power: time-dependent and -independent forms

P^{T} Net power in an irregular sea-state

ℓ Capture width

J Power contained in an ambient incident wave of unit width

b_{33} Heave added damping for an isolated device

m_{33} Heave added mass for an isolated device

q Optimal interaction factor

$\bar{q}$ Interaction factor

$\overline{Q}$, $(\overline{Q}_{\mathrm{X}})$ Net interaction factor (in sea-state X)

c Consistency constant

w Interaction factor peak width constant

D_{ij} Interaction distance from Device i to Device j

η_{ij} Interaction phase from Device i to Device j

L_{R} Separation repeat value

k_{R} Wave number repeat value

$i - j$ Interaction originating at Device i, experienced by Device j

R	Radiation characteristics
$\mathbf{B}$	Diffraction transfer matrix
$\mathbf{T}$	Coordinate transformation matrix
$\mathbf{\Psi}$	Vector of partial waves
ψ	Spatially-dependent basis function
$(\,)_m^n$	Element of a vector (or set) whose row index (or spatial variation) corresponds to the m^{th} z-mode and the n^{th} θ-mode
$(\,)_{qm}^{nl}$	Element of a matrix whose row index corresponds to the q^{th} z-mode and n^{th} θ-mode and whose column index corresponds to the m^{th} z-mode and the l^{th} θ-mode
$\widehat{\ }$	Non-dimensional form of variable
$\widetilde{\ }$	Concerning interior region. Equivalent symbol without a tilde concerns exterior region
$_{i,\ j,\ 0}$	Concerning device labelled i, j or isolated device respectively
$_{\mathrm{A}}$	Concerning ambient incident wave field
$_{\mathrm{D}}$	Concerning diffracted wave field
$_{\mathrm{I}}$	Concerning incident wave field
$_{\mathrm{R}}$	Concerning radiated wave field
$_{\mathrm{S}}$	Concerning scattered wave field
$_{\mathrm{B}}$	Concerning buoyancy spring
$_{\mathrm{G}}$	Concerning generator
$_{\mathrm{H}}$	Concerning hydrodynamic effects
$[p]$	p^{th} component of an irregular sea-state
M_{T}	Truncation constant for vertical mode numbers
N_{T}	Truncation constant for angular mode numbers

Chapter 1

Introduction

1.1 Research question

The central objective of the research contained in this thesis is to answer the following question:

> How can the configuration of an array of floating wave energy converters be chosen so that gains in absorbed power resulting from hydrodynamic interactions are maximised and losses minimised?

Before a more detailed description of the aims of the research is given in Section 1.4, the remainder of this introductory chapter is designed to illuminate the context of the work for specialists and non-technical readers alike.

1.2 Wave energy

1.2.1 Motivation

Around the world, there is a growing recognition that man-made climate change will have a damaging effect on the environment unless urgent action is taken. Greenhouse gases originating from the burning of fossil fuels have a major role to play in this phenomenon, with the production and use of energy alone accounting for over two-thirds of global carbon dioxide emissions. However, the problem is only set to become more acute. If current trends were to be continued, worldwide energy demand would be over 50% higher in 2030 than 2006. Consequently harmful emissions are on course to reach double pre-industrial levels by 2050, giving rise to significant economic and

environmental problems throughout the world. It is therefore imperative that clean alternative sources of power are sought (Department of Trade and Industry, 2007).

The United Kingdom has further pressing reasons to invest in new power generation, which are by no means uncommon amongst developed nations. One such issue, which is becoming increasingly important, is the security and affordability of energy supplies. Since domestic reserves of oil and gas are in decline, the UK is relying ever more on energy imports. These may not be from dependable sources and could allow the suppliers to exert undesirable political and economic influence (Winstone, Bolton, and Gore, 2007). Furthermore, alongside scheduled nuclear power plant closures in the coming years, demand for energy in the UK is projected to rise. It is therefore estimated that 30-35GW of new generation capacity will be needed in the next two decades (Department of Trade and Industry, 2007).

One possible source of unlimited, carbon-free energy involves harnessing the power of ocean waves. Although the associated industry is currently in its infancy compared with other renewable technologies, there is great potential for future exploitation. A report by the Carbon Trust (2006) estimates the practically achievable worldwide wave energy resource to be between 2000 and 4000TWh/year. More specifically, the figure for the UK alone is given as 50TWh/year, equating to roughly one-seventh of national electricity demand. The firm conclusion from this review is that, along with tidal energy, wave power technology has the potential for bulk electricity supply.

1.2.2 Current status

In order to address the need for clean power sources, the UK Government has adopted European Union targets of generating 15% of its energy from renewables by 2020. This represents a seven-fold increase in the figure relating to 2008 (Department of Energy & Climate Change, 2010a). Although more mature technologies such as wind are likely to make up the largest contribution by this date, wave energy may well have a crucial role to play in meeting medium to long-term renewable energy targets. The Energy Technologies Institute, a partnership between energy-focussed companies and the UK Government, has stated an aim that the deployment of marine renewables (that is, wave and tidal) should increase to 2GW by 2020 and towards 30GW by 2050. They have also outlined an aspiration that by these two dates, the associated generation costs will be competetive with other renewables and with conventional generation respectively

(Energy Technologies Institute, 2010a).

Various incentives have been put into place to encourage the development of wave energy technologies. The UK and Scottish governments have introduced banded Renewable Obligation Certificates (ROCs) to encourage electricity suppliers to produce a larger proportion of their output from renewable sources. Electricity generated from wave energy is financially rewarded (and at a higher rate than other renewables) whilst insufficient renewable energy generation is penalised (Department of Trade and Industry, 2007).

In addition to the promise of a good rate of return on investments, schemes have been encouraged through capital grants and prizes. In the UK, the Marine Renewables Proving/Deployment Funds (MRPF/MRDF) have been set up to help with the costs of deploying full-scale prototype and commercial devices respectively (Carbon Trust, 2010; Department of Energy & Climate Change, 2010b). Furthermore, Scotland has its own targets and incentives for the marine energy industries. An as yet unclaimed fund of £10 million (named the Saltire Prize) has been provided for the team that can demonstrate in Scottish waters, a commercially viable wave or tidal stream energy technology (The Scottish Government, 2010).

An important aspect of any commercial scheme is obtaining a suitable site for installation. The Crown Estate, which owns 55% of the foreshore and all the seabed out to the 12 nautical miles limit in the UK, has recently leased six sites around the Pentland Firth and Orkney waters to wave energy developers. These projects will deliver up to 600MW into the grid, enough to power 375,000 homes. The lease of further full-size and demonstration sites around Scotland is also planned in support of the Saltire Prize (The Crown Estate, 2010).

Ideas for wave energy extraction date back at least as far as Girard *père et fils*, who in 1799 filed a patent in France for such a device (Falcão, 2010). However, it was not until the Oil Crisis of 1973 that research began to accelerate into the utilisation of ocean waves as a means for large scale electricity production (Salter, 2008). Stephen Salter of the University of Edinburgh is generally credited with writing the first scientific publication (Salter, 1974) in the modern era of wave energy research and development. In this paper, a device known as the 'Duck' (Figure 1.1(a)) was proposed that could achieve very high efficiencies in sinusoidal seas. Although investigations with this particular converter have largely been discontinued, interest in the principle of wave energy conversion has

persisted and given rise to research at many academic establishments across the world (see Chapter 2). Moreover, a number of commercial enterprises have since come into existence bringing with them a fascinating spectrum of different device concepts.

One of the first commercial-scale devices to feed electricity into the grid was one named Limpet (Land Installed Marine Powered Energy Transformer), installed on the island of Islay off the west coast of Scotland in 2000 (Voith Hydro Wavegen Ltd., 2010). This converter (Figure 1.1(b)) consists of three equal air chambers attached to the shore, each with its lower face open to the ocean and its top connected to the surrounding atmosphere via a turbine. As the waves oscillate within the chambers, air is pushed through the turbine which consequently generates electricity. This type of device is therefore known as an oscillating water column (OWC).

Today, one of the leading technologies in the field is the Pelamis wave energy converter. This device is composed of several cylindrical tubes that are attached together at their ends by hinged joints. The whole arrangement floats horizontally at the water surface, with the action of the waves inducing relative motions in two modes at each of the four joints between the tubes, resisted by hydraulic rams. These drive high-pressure fluid through hydraulic motors attached to generators in order to produce electricity. In 2008, the company successfully installed the first ever wave farm off the coast of northern Portugal at Aguçadoura, consisting of three 'P1-A' machines (Figure 1.1(c)). The latest 180m long 750kW 'P2' version of the device is currently being commissioned at the European Marine Energy Centre (EMEC) in Orkney for evaluation and testing. Eventually this type of device will be deployed at three sites leased from the Crown Estate in 50MW farms (Pelamis Wave Power, 2010).

Another device that appears to be close to commercial deployment is the Oyster wave energy converter of Aquamarine Power (Figure 1.1(d)). The concept involves a flap that is hinged on the seabed, extending throughout the water depth to just above the surface. The back-and-forth motion of the flap drives hydraulic pistons which pump water to shore at high pressure. This is then used to drive a hydro-electric turbine and generate electricity. Full-scale tests on the Oyster 1 version of the device at EMEC were conducted in 2009, with electricity being successfully transferred to the National Grid. The 20m wide 16m deep second iteration of the design (Oyster 2) is designed to be installed along with two other machines as a 2.5MW array and is due for construction this year (2010). A joint venture between Aquamarine Power and SSE Renewables

(a) The Duck, 1979: sealed gyro-tube. Source: ETSU/The Universtiy of Edinburgh (2010).

(b) Limpet on the island of Islay. Picture courtesy of Voith Hydro Wavegen Ltd.

(c) Three Pelamis P1-A devices at the Aguçadoura wave farm, Portugal. Picture courtesy of Pelamis Wave Power Ltd.

(d) The first full-scale Oyster 1 device. Picture courtesy of Aquamarine Power Ltd.

Figure 1.1: Various wave energy devices.

has plans to develop up to 1GW of wave farms in UK and Irish waters by 2020, with 200MW to be installed in clusters between Costa Head and Neban Point off Orkney (Aquamarine Power, 2010).

The taxonomy of devices is by no means simple as a result of the variety of different concepts that have been proposed. However, devices of a similar nature to Oyster are sometimes referred to as 'oscillating wave surge converters.' Furthermore, Pelamis is termed an 'attenuator' to reflect the notion that energy and motions decay as the wave travels down the length of the machine (see Section 6.3 for a discussion concerning arrays of point absorbers, related to this choice of terminology). Another category of device is the 'overtopping' variety, where water carried upwards by waves is captured in a reservoir before being released back into the sea via a low-head turbine. Other categories and sub-categories of device may be defined in a similar way, although an inspection of the range of current technology concepts (see for example the website of The European Marine Energy Centre Ltd. (2010)) indicates how difficult a task this is.

1.3 Wave energy device arrays

1.3.1 Motivation

Many developers and researchers are now looking beyond the deployment of a single device to the installation of multiple converters in the same area. Wave farms of this nature may allow considerable savings in terms of the cost of mooring, electrical connection, maintenance and other requirements. However, care must be taken to ensure that matters specifically arising with multiple device deployments are properly addressed. Similar issues may be encountered in the case of converters that themselves consist of multiple closely spaced floats (described here as 'multiple-float' devices). Both of these situations will be considered as 'arrays' in the remainder of this thesis.

1.3.2 Current status

Although it is sensible to deploy more than one of any kind of device in a particularly advantageous location, the 'point absorber' type of converter was designed to be part of an array from the outset (Budal and Falnes, 1975). This type of floating device has a horizontal extent much smaller than one wavelength and manifests itself in many different forms. Several examples are approximately cylindrical in geometry and extract

(a) The PB40ES PowerBuoy device at Santander, Spain. Picture courtesy of Ocean Power Technologies, Inc.

(b) The Sperboy device. Picture courtesy of Embley Energy Ltd.

(c) Two test devices (foreground) and one measurement buoy (background) from Uppsala University at Lysekil, Sweden.

Figure 1.2: 'Point absorber' wave energy devices.

power from their vertical (heaving) motion.

PowerBuoy® (Ocean Power Technologies, 2010) is a point absorber that consists of two bodies; the upper float moves with the incoming waves and reacts against the relatively stationary submerged plate below (Figure 1.2(a)). The hydraulic power take-off then converts this motion to electrical energy. Ocean Power Technologies (OPT) have tested prototypes in the sea and have formed a joint venture with a number of partners to construct a wave farm of nine 150kW machines off the north coast of Spain at Santoña.

As an alternative to being fixed to the shoreline, the power conversion mechanism of an OWC may be attached to a floating structure. An example of this type of device is the Sperboy™ converter shown in Figure 1.2(b) (Embley Energy Ltd., 2010). Hydrodynamic analysis of a single tube version of this device has previously been conducted by the present author on behalf of Embley Energy (Child, 2006). The developer envisages that a full-size farm will eventually consist of a thousand 1MW units.

Another variation on the concept of a point absorber involves a single float extracting power from its motion relative to the seabed. Seabased (2010), in close collaboration with Uppsala University, Sweden are developing such a converter. Here, an axi-symmetric float is attached by a taught tether to a linear generator fixed to the seabed. The academic partners are currently undertaking a research project on a test farm situated off the coast of southern Sweden at Lysekil (Figure 1.2(c)). A small array of devices has already been tested, although plans have been made to install up to ten wave power devices at the site (Uppsala University, 2010).

The Manchester Bobber (Manchester Bobber, 2010) is an example of a multiple-float device (Figure 1.3(a)). This concept involves between twenty-five and fifty floats suspended from a common floating frame via tethers. These are in turn attached to independent generators mounted on top of the frame which are thus driven by the vertical motion of the absorbers. Experiments and numerical modelling exercises have been carried out on the converter at the University of Manchester.

Research into the FO^3 device has been conducted by a collaboration involving Ghent University and Fred Olsen Ltd (SEEWEC, 2010). In common with the Manchester Bobber, this concept involves several (12 or 21) absorbers attached to a floating platform. A one-third scale rig named the 'Buldra platform' was installed

at Jomfruland, Norway in 2005 and subsequently used for testing and monitoring purposes (Figure 1.3(b)). However, the final report on the project suggested instead pursuing a single-absorber device (Rouck and Meirschaert, 2009). This decision was principally a result of revised calculations which estimated the power capture of the multiple-float device at approximately one-third of initial assessments. The simplified single-buoy concept was also found to be more economical in terms of manufacturing cost per unit of installed capacity as well as other expenses incurred throughout the lifetime of the product.

A concept from Trident Energy (2010) involves several floats, rigidly attached to vertical poles, in close proximity to each other. These drive linear generators mounted on a fixed frame above (Figure 1.3(c)). An arrangement with four floats has been tested at the New and Renewable Energy Centre (Narec) at Blyth, Northumberland.

The Wave Star machine (Wave Star A/S, 2010) comprises a fixed central structure above the water surface with floats attached either side in rows perpendicular to the wave crests. The motion of the buoys as the wave travels along the line is transferred via arms to a common transmission system where high pressure oil drives a hydraulic motor, which in turn drives a generator. A grid connected one-tenth scale model (Figure 1.3(d)) has been operating in the sea for three years whilst a section of a full-scale twenty-float (500kW) machine was installed at Hanstholm, Denmark in 2009.

In the same way that the EMEC and Narec test facilities have accelerated the learning process of deploying single devices, a new centre named Wave Hub aims to fulfill the same function for arrays of several converters. The project, currently under construction at Hayle in Cornwall, will eventually provide an offshore grid connection for four technologies, each of which will have 2km^2 and be able to generate up to 5MW of power (Wave Hub, 2010). One developer, OPT, has already signed up to test an array of its PowerBuoy devices upon completion of the facility (Ocean Power Technologies, 2010).

UK Government-supported research schemes continue to provide valuable insight into issues associated with arrays. The SuperGen Marine Consortium, now in its second phase, has devoted one of its 'work streams' specifically to the analysis of arrays, wakes and near field effects for wave and tidal devices (SuperGen Marine Consortium, 2010). The PerAWaT project (Performance Assessment of Wave and Tidal array systems), on the other hand, is devoted solely to multiple device analysis. This four-year research

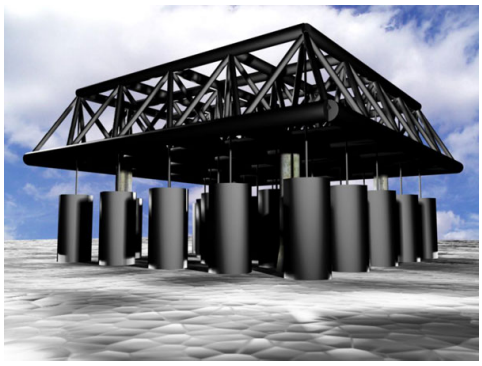

(a) Commercial vision of the Manchester Bobber. Source: Manchester Bobber (2010).

(b) The 1:3 scale version of the FO^3 platform ('Buldra'). Source: SEEWEC (2010).

(c) The Trident device. Picture courtesy of Trident Energy Ltd.

(d) The 1:10 Wave Star machine. Picture courtesy of Wave Star A/S.

Figure 1.3: 'Multiple-float' wave energy devices.

programme, financed by £8 million from the Energy Technologies Institute, is led by the renewable energy consultants GL Garrad Hassan. The aim is to establish and validate numerical models to predict the hydrodynamic performance of wave and tidal energy converters operating in arrays (Energy Technologies Institute, 2010b). These projects should help reduce uncertainty and risk for investors and thus accelerate the adoption of large-scale wave energy farms.

1.3.3 Array-related issues

The deployment of a wave energy device array presents several issues that are unique or at least accentuated in comparison with the case of an isolated device. One matter that does arise but to a lesser extent in the latter case is the environmental impact of the scheme; in a large array it is imperative that the project is assessed in terms of its effect on marine life, coastal processes and other users of the sea. Another issue in this

category is the capacity of the grid connection in the locality of the site to export all of the electricity that is generated. Installation, operation and maintenance of devices is also important since the array must be able to provide sufficient access for these functions to be carried out.

Problems that are particular to arrays on the other hand include the need to ensure that mooring lines are efficiently used, yet are not so close as to collide with each other. Conversely devices cannot be separated by too large a distance since the costs associated with the site mean that the available area must be utilised efficiently. Also, due to the expense of electrical cabling and connection equipment, the exact arrangements between one device and another as well as the route from the whole array to the shore need to be carefully planned. One problem that may be easier to solve with arrays of devices, however, is the smoothing of electrical power output from the scheme.

Some of the aforementioned issues may only be resolved with growing practical experience of deploying single devices and small arrays. Others are being actively researched in academic and commercial organisations. These matters will not be covered in detail within the scope of the present work, although more information may be obtained from some of the references in Chapter 2.

1.4 Research objectives

One area involved in the study of wave energy device arrays that has been known about for some time, yet is still not adequately understood, relates to the associated hydrodynamic interactions. In addition to the incoming wave field, devices in an array will be subject to waves that have been reflected or radiated from other converters. The modification to the force felt by each device due to these interactions may result in an increase or decrease in its power output compared to if it were in isolation. Hence, the total power from the array cannot simply be assumed proportional to the number of devices.

There are many factors that can influence the nature of this interference, including the shape of the device, what forces the generator exerts on the converter and the layout of the elements within the array. This last factor deserves serious consideration since its impact is expected to be significant and it is perhaps the most easily modified once the design of single absorber has been determined. Therefore, it is the central objective of this thesis to provide insight into how the configuration of devices within an array

affects the total power output.

More specifically, the aims of this project are:

- To model the hydrodynamic interactions in arrays of wave energy absorbers, including wave farms of 'point absorber' devices and 'multiple-float' devices in isolation
- To implement an accurate and efficient computer code for calculating the hydrodynamic interactions
- To understand the behaviour of an isolated absorber and how it can affect the interaction processes within an array
- To understand the interactions that occur in a wave energy device array and explain their effects in terms of fundamental properties of the arrangement
- To effectively and efficiently optimise the power output from an array with respect to the configuration of devices under regular wave incidence
- To be able to understand and interpret the behaviour of optimised arrays in regular waves
- To be able to analyse arrays in irregular waves and optimise their configuration in different irregular sea-states

A review of the available literature relevant to these objectives is provided first (Chapter 2). This is followed in Chapter 3 with a description of the generic model to be used as a representation of the converters and array. A detailed account is also given of the new combination of techniques used to calculate the consequent hydrodynamic interactions. Chapter 4 contains a report of how the associated numerical code was created, including verification of the results. Isolated device analysis is given in Chapter 5 with details of how each parameter affects behaviour. Consideration is then given to elementary array formations in Chapter 6 and how the associated additional parameters influence performance. Two methods for optimising the configuration of arrays in regular waves are presented in Chapter 7; one of which is completely new and the other involves a new component devised for this research. The results and methods are then evaluated in Chapter 8 in relation to regular waves. In Chapter 9 the previously created arrays are analysed in irregular waves. The same wave climates are

used to perform, for the first time, a full optimisation of the array configuration using the exact linear wave theory solution. Finally, some concluding remarks are given in Chapter 10.

1.5 Publications

In the course of this research, the author has published the following academic papers:

1. B. F. M. Child and V. Venugopal. Interaction of waves with an array of floating wave energy devices. In *Proceedings of the 7th European Wave and Tidal Energy Conference, Porto, Portugal*, September 2007

2. B. F. M. Child and V. Venugopal. Non-optimal tuning of wave energy device arrays. In *2nd International Conference on Ocean Energy, Brest, France*, October 2008

3. B. F. M. Child and V. Venugopal. Modification of power characteristics in an array of floating wave energy devices. In *Proceedings of the 8th European Wave and Tidal Energy Conference, Uppsala, Sweden*, September 2009

4. B. F. M. Child and V. Venugopal. Optimal configurations of wave energy device arrays. *Ocean Engineering*, 37(16):1402–1417, 2010

These works in their entirety represent the original research of the present author, under the supervision of the second named contributor. Paper 1 summarises the work contained in Chapter 3, whilst Paper 2 forms the basis for Chapter 6. A preliminary methodology and associated results relating to Chapters 7 and 8 is documented in Paper 3. Finally Paper 4 contains the definitive methodologies and results relating to the preceding works.

Chapter 2

Literature Review

2.1 Introduction

In this chapter, a review of the published literature relevant to the topics explored in this thesis is presented. To reflect the focus of the present work, we shall be concentrating our attention on the computation and optimisation of hydrodynamic interactions in arrays of wave energy devices. However, research concerning other structures in water waves, and indeed waves in other media, will also prove enlightening.

The account given here begins in Section 2.2 with a brief review of significant works in the field of wave energy and the interaction of waves with a single structure. We then proceed in Section 2.3 to summarise the existing body of knowledge relating to arrays of both wave energy devices and structures of other types. Investigations employing similar methodologies will be grouped together for this purpose. Finally, Section 2.4 gives an account of the existing research into optimising the configuration of an array of floating bodies.

2.2 Isolated structures

The first concept to be proposed in the modern era of wave energy research was a horizontal cylinder of cam-shaped cross-section known as the Duck (Salter, 1974). The device was to lie on the surface of the ocean with its long surface perpendicular to the oncoming waves, absorbing energy from pitching movements. Successful experiments were conducted in sinusoidal (regular) waves, where over 80% of the power incident upon the converter was able to be extracted. This type of device, that features a uniform

vertical cross-section along its length, is sometimes referred to as a two-dimensional absorber.

Shortly after results from experiments on the Duck had been reported, a completely different principle for absorbing wave power was advocated in an article by Budal and Falnes (1975). This type of converter floats on the surface of the water and utilises its wave-induced heave motion to harness power. It is referred to as a three-dimensional or 'point' absorber since its horizontal extent is much smaller than one wavelength.

Many of the attempts since these initial investigations have used linear wave theory in the frequency domain to explain the behaviour observed in experiments. This assumes that the fluid is incompressible and inviscid, the flow irrotational and also that wave and body motion amplitudes are small. Optimal conditions for power absorption may then be derived in terms of the forces applied to the device by the generator. Budal and Falnes (1975) were the first to suggest that the inertia of the system should be such that its resonant frequency corresponds to the characteristic frequency of the waves and that the applied damping force should equal the hydrodynamic (added) damping of the body at the same frequency. Mei (1976) and Evans (1976) both then derived precise mathematical expressions for these conditions. The motions of the body needed to achieve this optimal state were provided by Newman (1976) for two- and three-dimensional absorbers.

An important principle of wave energy conversion was subsequently asserted by Falnes and Budal (1978); a good absorber of waves must also be a good generator of waves. If the motion of the system can be controlled in such a way that the radiated waves cancel out the transmitted and reflected waves, then all the incident wave power is absorbed. Therefore, 100% efficiency can in principle be acheived through effective radiation.

The maximum efficiency of two-dimensional absorbers that are symmetric with respect to their axis of oscillation was found to be 50% for one mode of motion and 100% for two modes (Evans, 1976; Newman, 1976). In contrast, three-dimensional absorbers may absorb more power than is contained in a wave of equal frontage to the width of the device (Budal and Falnes, 1975). Evans (1976) and Newman (1976) independently discovered that the maximum power available from an axi-symmetric buoy moving in heave, surge or sway is related only to incident wavelength and not the body dimensions. It should be noted, however, that these efficiencies are only possible with optimal power

absorption, which requires some knowledge of the future state of the system when the waves are not simply sinusoidal (Price, Forehand, and Wallace, 2009).

Since the aforementioned investigations, there have been many works on the topic of wave energy conversion which are too numerous to cover comprehensively here. Not only have new theoretical results been derived but also many innovative device concepts imagined. For more information on the subject, the reader is directed to the popular textbook by Falnes (2002) and to the more recent collection of expert discourse edited by Cruz (2008). Review articles by Falnes (2007) and Falcão (2010) on the state of the art in theory and technology respectively may also be of interest.

Alongside developments in the area of wave energy conversion, research has been undertaken into the interaction of waves with structures in a number of other contexts. Garrett (1971) analysed the exciting forces on a vertical cylindrical 'dock' fixed in its position at the surface of fluid of finite constant depth. A solution to the problem had previously been attempted by Miles and Gilbert (1968), although this had contained errors. Garrett (1971) separately expanded the velocity potential in the volume of fluid directly underneath the body and in the remaining domain using infinite series of 'eigenfunctions.' These were multiplied by a set of unknown complex coefficients which were subsequently determined by imposing the conditions of pressure and velocity continuity across the boundary between fluid regions.

Yeung (1981) used the same type of solution as Garrett (1971) on a truncated vertical cylinder, in order to calculate the hydrodynamic coefficients (added mass and damping) associated with motion in the three non-equivalent modes (heave, sway and roll). Both the diffraction and heave radiation problems were combined by Bhatta and Rahman (1995) who also calculated the resulting forces for a number of examples. Bhatta and Rahman (2003) later incorporated the other radiation problems to form the complete solution. Expressions contained in the latter work have subsequently been used by Eriksson, Isberg, and Leijon (2005) with an application to a heaving wave energy device.

2.3 Arrays

2.3.1 The Point Absorber method

Research into arrays of wave energy converters was initiated by Budal (1977) who studied a collection of point absorber devices. In this work, an assertion was made that became known as the 'point absorber approximation;' that the diameter of the devices is small in comparison to the distance between them. Hence the wave field radiated by the motion of each device may be calculated without reference to the diffraction effect of other elements in the array. In the ensuing analysis, the power output from the array was partially optimised, although the amplitude of oscillation was incorrectly assumed to be the same for each device. The q-factor was introduced in this work to denote the ratio of maximum power that may be absorbed by the array of devices to that by the same number of converters when isolated from each other. This quantity therefore encapsulates the power multiplying effect of the array and, in this work, was shown to be capable of exhibiting significant modifications from unity.

Except in special cases, Evans (1979, 1980) showed the equal amplitude assumption of Budal (1977) not to be valid. Furthermore, the amended analysis used point absorber theory to provide a condition on the body velocity amplitudes that ensures optimal power absorption. This is in fact a natural extension of the equivalent single device condition and was arrived at independently by Falnes (1980). Falnes and Budal (1982) and Falnes (1984) later provided scenarios in which all the power that is incident upon the width of the array from regular waves can be absorbed.

Although the point absorber approximation is capable of determining optimal absorption characteristics without reference to the exact geometry of the devices, Thomas and Evans (1981) noted that no such result is available for their displacements. These quantities may provide important information regarding the applicability of linear wave theory and may be crucial in informing the design process. Hence for a specific device geometry, the authors numerically maximised power capture from the array, given that motion amplitudes had been limited to a fixed multiple of the incident wave amplitude. If this factor is set to a value of three then acceptable performance still may be obtained. However, if it is reduced to a value of two, there was found to be a significant degradation in the power output. A relationship was also established between the nature of hydrodynamic interference and the difference in phase that a

wave of frequency equal to the incident wave would experience when travelling from one body to the next.

Point absorber theory was recently used as the basis for an optimisation of array layout with respect to the q-factor in regular waves (Fitzgerald, 2006; Fitzgerald and Thomas, 2007). An important result derived in the course of this analysis is that the average value of q over the entire angular range is equal to unity. Hence there is no net improvement or degradation in optimum array performance over all possible wave headings, compared with a single device.

Folley and Whittaker (2009) have also used this approximation to analyse one of the arrays presented by Fitzgerald and Thomas (2007) and, separately, to optimise the position of devices in irregular waves. However, the optimum positioning was found to be constrained slightly by the minimum separation required by point absorber theory. This was remedied by choosing the position of the second device to be on the optimal wave heading in relation to the first but with the separation increased to that recommended by Mavrakos and McIver (1997).

2.3.2 The Plane Wave method

The analogy between ocean and electromagnetic waves has proved to be particularly fruitful over the years. The diffraction of the latter wave field by several cylinders was the focus of research that culminated in the invention of a direct matrix method by Zaviska (1913). This was subsequently resurrected by Spring and Monkmeyer (1974) to deal with diffraction of water waves by bottom-mounted, surface-piercing circular cylinders. The technique uses the body boundary conditions to simultaneously determine the unknown scattered wave amplitudes.

Simon (1982) adopted a direct matrix approach to analyse wave energy devices but approximated the diverging wave from one device as a plane wave upon reaching other devices in the array, ignoring evanescent waves. The resulting 'plane wave' method requires that the spacing between elements (non-dimensionalised using the incident wave number) is large. This restriction was judged to be a worthwhile sacrifice as a result of the improved efficiency of the method. The results suggested a significant modification in the forces felt by devices when scattering is included in the calculations. Therefore, the plane wave method represents a marked improvement on point absorber theory in the analysis of wave energy devices.

McIver and Evans (1984) later added a 'first correction' term to the expression of the plane wave and derived significantly improved accuracy of results for bottom-mounted, surface-piercing cylinders with little extra effort. On application to floating axi-symmetric bodies, McIver (1984) found the method (including local waves) to be accurate in comparison to a numerical solution, even when the wide spacing assumption is violated.

2.3.3 The Multiple Scattering method

Twersky (1952) discovered an alternative way of solving the multi-body diffraction problem in the field of acoustics by considering the interactions to be a series of consecutive scattering events. Intuitively, contact with each body reduces the amplitude of the resulting wave and so a solution is reached by the convergence of an iterated sequence. This 'multiple scattering' technique was applied to water waves by Ohkusu (1972, 1974) in the study of offshore mobile platforms with multiple supporting bodies.

Work on the multiple scattering method continued with Mavrakos and Koumoutsakos (1987) and Mavrakos (1991), in whose articles the scattering and radiation problems were solved respectively. In these investigations, the interaction theory was combined with an analytic solution for axi-symmetric bodies in isolation. An application of this theory to wave energy devices was made by Mavrakos and Kalofonos (1997) with several device and array geometries being assessed. Later, several absorbing floats placed in front of a reflecting breakwater were analysed using the same method (Mavrakos et al., 2004).

A comparison of the multiple scattering, plane wave and point absorber methods has been carried out by McIver, Mavrakos, and Singh (1996a,b) and Mavrakos and McIver (1997) in the context of wave power. They measured the accuracy of the latter two techniques against that of the former, 'exact' method. In general, the plane wave method was found to break down in long waves but perform well in the high frequency range, whilst for the point absorber approximation the converse was seen to be true. The multiple scattering technique has, however, itself been criticised. Linton and McIver (2001) state that the multiple scattering method 'rapidly becomes unmanageable as the number of scatterers increases.'

2.3.4 The Direct Matrix method

Kagemoto and Yue (1986) combined the physical concepts associated with the multiple scattering approach and a direct formulation to form what is often referred to as the 'direct matrix' method. This technique is in principle exact within the context of linear wave theory, subject to the truncation of an infinite summation. The scattering characteristics of each individual body under incident progressive and evanescent waves are encapsulated in the diffraction transfer matrix, which allows the unknown wave amplitudes to be solved for simultaneously. The method is widely applicable, requiring only that the vertical projections of interacting bodies onto a horizontal plane do not overlap and that a circumscribed vertical cylinder around each body centred on its imaginary origin does not contain the origin of any other body. The comparison with results from a numerical technique is excellent in all cases given in this work. The presented method also uses considerably less computer time and storage than that used to verify the output.

A considerable simplification to the direct matrix method was discovered by Linton and Evans (1990) in the special case of bottom-mounted, surface-piercing circular cylinders. This has since been used extensively in the investigation of the near trapping phenomenon in periodic arrays (Maniar and Newman, 1997; Evans and Porter, 1997). Here, near-resonant modes occur at certain wave numbers and cause unusually large wave loads. The case of arrays of elliptical cylinders was later considered by Chatjigeorgiou and Mavrakos (2010).

Following its formulation, the theory of Kagemoto and Yue (1986) has been widely applied, especially in the field of very large floating structures (VLFSs). These were the subject of a study by the same authors (Kagemoto and Yue, 1993) who incorporated the radiation problem from the motion of the bodies. Modifications have also been made in order to efficiently apply the method to a much greater number (~ 5000) of columns supporting a VLFS (Kashiwagi, 2000). Another extension of the direct matrix method is in the case of infinite water depth (Peter and Meylan, 2004), where the diffraction transfer matrix becomes a linear integral operator.

Yilmaz (1998) incorporated the single body solution of Garrett (1971) into the array interaction procedure of Kagemoto and Yue (1986), in order to analyse tension-leg platforms (TLPs). They also added the effects of radiation in the case that all bodies move in synchrony and included evanescent waves. A similar combination of techniques

was first applied in the wave energy field by the present author (Child and Venugopal, 2007). In that work and this thesis, the independent movement of converters is accounted for and the effects of energy extraction included. This method was later adopted by Siddorn and Eatock Taylor (2008) with a view to an application in the field of wave energy, although no motion or power values were calculated there. They also considered the occurrence of near-trapped modes, although these may be difficult to exploit in arrays of wave energy devices due to their extreme sensitivity to body positioning, incident wave direction and frequency.

2.3.5 Other analytic methods

Early studies that used an analytical approach not described so far include the work of Srokosz (1980). Here, the equivalence between an infinite line of equally spaced absorbers parallel to the wave crests and a single body in a channel is exploited. Kyllingstad (1984), on the other hand, presented a 'low scattering' approximation that incorporates an estimate of the diffraction effects from a single body but does not account for multiple scattering from other devices.

Wave energy systems involving fixed structures have also been studied analytically in the literature. In order to take advantage of resonance effects of harbour walls surrounding a wave power device, McIver and Evans (1988) analysed several such arrangements in the same vicinity using the method of matched asymptotic expansions. Also, Falcão (2002) presented a solution to the problem of determining interference in an array of fixed oscillating water columns.

For periodic arrays of bodies, Linton and Evans (1992, 1993) used the 'multipole' method to solve the hydrodynamic problem. This involves the superposition of singular solutions to the governing equations and choosing their coefficients so as to satisfy the body boundary conditions. The technique was applied to an infinite array of 'Bristol cylinder' wave energy devices by McIver and McIver (1995). Since then, Justino and Falcão (2002) have used the multipole expansion method on small arrays of spherical wave energy devices.

The phenomenon of Bragg resonance was studied by Li and Mei (2007) in the context of a periodic array of circular cylinders. In that work, certain approximations were made based on the assumptions that the incident wavelength is comparable to the spacing between bodies and that the cylinders themselves are much smaller than this length. The

same approach has recently been applied to an array of floating wave energy converters by Garnaud and Mei (2010).

2.3.6 Boundary Element Methods

A popular method for solving the problem of wave diffraction that can be applied with multiple bodies is the source distribution or boundary element method (BEM). Here, the boundary condition on the body is satisfied by placing a number of pulsating point sources across its surface. The velocity potential in the surrounding fluid domain is then determined using Green's functions (Lee, 1995). Several commercial codes are available to perform these calculations, including WAMIT®[1] and ANSYS AQWA.

Some investigations involving multiple bodies have utilised a BEM for calculation of the hydrodynamic properties of each element, whilst employing an alternative method to determine the interactions between them. Matsui and Tamaki (1981) used a multiple scattering approach for the latter task in the study of groups of axi-symmetric bodies. Conversely Goo and Yoshida (1990) and Chakrabarti (2000) chose the direct matrix method for this purpose.

Recently, BEMs have been more widely used as a way of computing hydrodynamic properties of both the isolated body and interactions between them. This was the approach taken by Justino and Clément (2003) who used the code AQUADYN (developed at ECN-Nantes) to analyse arrays of spherical wave energy devices. They noted that the optimal force to be applied by the power take-off to each array element depends on the motions of all of the other bodies in the array. Since implementation of this scheme could raise significant practical problems, alternatives are suggested where just the diagonal elements of appropriate matrices are used.

Constraints such as stroke and slamming restrictions were incorporated into the study of an array of twelve absorbers by De Backer et al. (2009) using WAMIT. The control parameters of the devices were subsequently optimised using three different methods, with the best performance being achieved by optimising the damping settings of each float individually. Bellew, Stallard, and Stansby (2009) also performed an optimisation on these values in order to maximise total power and to minimise variation in power across the array in regular waves. Cruz et al. (2009) went further, providing optimal power take-off characteristics for an array of four devices in irregular seas

[1] WAMIT is a registered trademark of WAMIT, Inc.

with different wave headings (or equivalently, array orientations) using an exhaustive approach.

Ricci, Saulnier, and de O. Falcão (2007) calculated the yearly average power output from two different configurations of wave energy device array at a particular site location. Their main conclusions were that directional wave spreading may be an important factor affecting long-term performance but that spacing between devices (if sufficiently large) is not. More recently, Babarit (2010) used AQUADYN to calculate hydrodynamic interactions between two bodies separated by different distances in regular and irregular waves. In the case where one body is exactly down-wave of the other, interaction effects were found to decay with the square root of distance between them. Thus in contrast to the research of Ricci et al. (2007), the overall performance of the array was found to be significantly modified even at relatively large spacings.

Taghipour and Moan (2008) and Taghipour et al. (2008) used WAMIT to efficiently analyse the motions of a floating platform with several absorbers attached. Instead of applying the BEM code before eliminating constrained degrees of freedom, they instead input the problem into the software in terms of 'generalised modes' so that no unnecessary calculation was performed. Efficiency of BEMs has also been the focus of research by Borgarino, Babarit, and Ferrant (2010). This involved the Fast Multipole Method (FMM), a particular expansion of the free surface Green's function, to reduce the computation time for N bodies from $\mathcal{O}(N^3)$ to $\mathcal{O}(N)$. The method will eventually be incorporated into the code being developed at ECN-Nantes, Aquaplus.

BEMs have also been used to compare predictions from linear wave theory with experimental and second-order results (Thomas, Weller, and Stallard, 2008; Bellew and Stallard, 2010) for arrays of floating hemispheres. It was found that agreement with experiment was good when the hydrostatic stiffness was adjusted to take account of the varying waterplane area of the body as its vertical displacement changes. Initial calculation of second-order forces showed their effect to be small compared to their linear counterparts.

2.3.7 Other numerical methods

There are a number of alternative techniques to the BEM for computing wave-structure interactions. Finite element methods (FEMs) employ a discretisation of the fluid domain itself rather than just the boundary. Alternatively, the hybrid element method (HEM)

combines an FEM, solving the flow in the immediate vicinity of the structure, with an analytical technique in the remainder of the domain. This approach was used by Kagemoto and Yue (1986) to calculate the single body diffraction characteristics in the examples given in that paper.

Several commercial codes including MIKE 21 and FUNWAVE make use of the Boussinesq equations to describe the flow. This model, formed by depth-averaging the governing equations, can be applied in the nearshore region to model nonlinear waves (Lin, 2008). Venugopal and Smith (2007a) and Venugopal, Bryden, and Wallace (2010) have successfully used MIKE 21 to analyse arrays of wave overtopping and fixed oscillating water column devices respectively.

An alternative to the Boussinesq model is the set of mild slope equations (MSEs). These too are depth-integrated but are based on linear wave theory and so require less computational time for numerical solution. The hyperbolic form of these equations is the basis for the MILDwave code developed at the University of Ghent. Beels et al. (2010b) used this model together with a numerical 'sponge layer' to model energy absorption in the region surrounding each overtopping device of an array. Five devices in a staggered formation were tested to find an acceptable spacing between the rows of two and three converters. The same approach has also been applied to analyse the wake from two different layouts of nine converters (Beels et al., 2010a).

A greater level of efficiency compared to all of the aforementioned techniques may be attained at the expense of the solution detail by using spectral wave models. These are based on the energy balance equations and neglect the phase information of the waves (Lin, 2008). Implementations include WAM, the spectral module of MIKE 21 and SWAN. The latter has been used by Alexandre, Stallard, and Stansby (2009) in order to assess how the wave spectrum is modified as a result of energy extraction from an array. This is may be important in assessing the impact of such a scheme on coastal processes.

The time-varying profile of the power produced by one or more wave energy converters may be an important issue in terms of the effect that electricity production has on the grid. The smoothing of such an output may be achieved through aggregating the power from devices in an array. Tissandier, Babarit, and Clément (2008) used the BEM code ACHIL3D with a time domain formulation to show that, in terms of this smoothness alone, it is the number of devices and not their arrangement that is

significant.

The nonlinear array interaction problem remains more complicated and computationally expensive to solve than its linear counterpart. Many of the existing investigations have focused on the second-order problem, where the velocity potential is decomposed into a perturbation expansion in some small parameter. Examples of solutions of this type have been provided by Malenica, Eatock Taylor, and Huang (1999) and Yilmaz (2007) in the case of bottom-mounted vertical circular cylinders. Second-order forces are calculated using WAMIT by Bellew and Stallard (2010) in the case of a closely spaced array, as previously described. Viscous forces that depend on the square of the body velocity may be expressed using the product of the velocity and an estimate of it. Thus some of the associated effects may be observed with a modified treatment of the linear problem (Söylemez and Yilmaz, 2003).

Computational Fluid Dynamics (CFD) may be required where it is not possible to obtain an explicit solution to the fully nonlinear problem. Yang, Löhner, and Yim (2005) and Wang and Wu (2010) used a Volume of Fluid (VOF) technique and an FEM respectively to solve the problem of extreme wave interaction with a group of bottom-mounted cylinders. An extensive search of the literature has revealed no studies on the use of CFD with an array of floating wave energy devices, presumably due to the prohibitive computational expense.

Useful reviews on hydrodynamic array interactions have been provided by McIver (2002) and Newman (2001), whilst the book by Martin (2006) contains more general information on multiple scattering in a range of media. As has been mentioned before, this subject matter is actively researched in the context of a variety of offshore applications such as in the analysis of VLFSs, TLPs, mobile offshore bases (MOBs) and ice floes. Similarities in the underlying mathematics mean that analogous problems are solved in the areas of acoustic and electromagnetic waves as well as for their own sake. The interested reader is therefore encouraged to search the literature in these areas for further information.

2.3.8 Experimental methods

There have been relatively few experimental investigations into array interactions for wave energy converters to compliment the numerical work that has been undertaken. Some results for two devices are reported by Count and Jeffereys (1980), who also

undertook more detailed experiments for the Central Electricity Generating Board (CEGB) around the same time. Unfortunately internal reports on the findings from the latter investigation appear to have been lost or destroyed (J. Taylor, private communication, 1st April 2008). Budal et al. (1980) meanwhile conducted tests on one and two floats in a narrow flume to simulate the behaviour of infinite rows of devices parallel to the wave crests. In the given situation, they found good agreement between point absorber theory and the experimental results they obtained.

More recently, work has been progressing on the Manchester Bobber using experimental techniques (Stallard, Stansby, and Williamson, 2008b; Weller, Stallard, and Stansby, 2009, 2010). These investigations with closely spaced floats have been successfully conducted in regular and irregular waves. It should be noted however that because the power take-off force is not time-harmonic, only the free response may be compared with frequency domain theory.

Work on arrays of up to five 1/20th scale floating oscillating water column devices has also been carried out in the NTNU Trondheim basin, funded by the UK SuperGen Marine Energy Research Consortium (Bryden and Linfoot, 2010). Some results have emerged from these tests (Ashton, Johanning, and Linfoot, 2009) although detailed analysis has not been published. Further experiments on the same models are now planned in alternative facilities.

2.3.9 Non-hydrodynamic considerations

One of the aims of the aforementioned SuperGen experiments was to gain an understanding of device moorings in an array setting. In those tests, the converters were arranged in an isometric grid with each device having three mooring lines and each anchor attached to lines leading to three devices (Bryden and Linfoot, 2010). Two of the participating researchers discussed some of the issues relating to moorings within an array in a subsequent paper (Vickers and Johanning, 2009). Important considerations include keeping the overall footprint of the arrangement small and the avoidance of excessive device and mooring line excursions to minimise the risk of collisions.

One economically attractive option for the mooring of multiple wave energy devices is to connect them together and attach the whole arrangement to the seabed as one. Vicente et al. (2009) used linearised mooring and hydrodynamic interaction forces to

apply a frequency domain approach in this scenario. Devices were arranged in an isometric grid with a weight attached to the lines emanating from each adjacent set of three converters. Mooring forces were found to be significant despite some important effects having been neglected. Gao and Moan (2009) considered the possibility of mooring together several platforms that themselves consist of multiple wave energy absorbers. This study did not take into account the hydrodynamic interactions between converters. Nonetheless, they concluded that large forces in the lines between the devices make this arrangement undesirable.

Grid integration issues (especially concerning the smoothness of power) may be important for the viability of a wave farm project. To these ends Molinas et al. (2007) proposed staggering the position of the wave energy converters so that the phases of the incoming wave and hence power output at each device are also staggered with respect to time. This has the effect of smoothing the output, reducing the need for energy storage. Like Tissandier et al. (2008), Thorburn and Leijon (2007) found that a larger number of devices in the array means that the total power output is smoother. In contrast to the former work, (Kiprakis et al., 2009) found power smoothing characteristics to be dependent on the configuration of devices in the array, even for irregular waves. This work is part of the development of a model described as 'wave-to-wire' (to denote the completeness of the intended treatment) by members of the SuperGen consortium.

The arrangement of electrical cabling and terminals for a given layout of devices was the subject of an investigation by Czech et al. (2009). They considered various factors in their analysis such as annual energy yield, yearly losses, price and levelised production cost. Many of the issues associated with connection are discussed in a set of protocols devised for the EquiMar project (Ricci et al., 2009).

Some economic aspects of large wave power projects have been examined by Stallard, Rothschild, and Aggidis (2008a). They presented a methodology by which wave power devices and schemes may be compared with one another in order to aid investment decisions connected with such projects.

The environmental impact of an array of wave energy devices has been considered by Langhamer (2009). In particular the effects on the marine life of the Lysekil wave power project in Sweden were examined. More research on all of the aspects mentioned in this subsection are required, however, before major schemes become viable.

2.4 Optimisation of array configuration

There are three main ways of optimising the position of elements in an array. The first and most simple is an exhaustive search of the possibilities. Folley and Whittaker (2009) used this method to identify the best location for a second device in a two-converter array. However, if the configuration is not tightly constrained, this process rapidly becomes unfeasible in terms of computation time as the number of elements increases. One way to mitigate this is to impose a formation template of some kind upon the array which is governed by a small set of parameters. In this way Beels (2009) was able to find the best down-wave and cross-wave spacings for a staggered formation (amongst others) of overtopping devices. Similarly, several authors (for example Thomas and Evans (1981) and McIver et al. (1996a)) have imposed a linear formation type on the array and examined behaviour for a range of inter-device separations.

The second strategy for configuration optimisation is to use a local minimisation algorithm. There are numerous well-known procedures of this type that are capable of improving a given solution to this problem. Kagemoto (1992) used such a routine with an analytical expression for the derivative of the objective function to minimise the forces on a multi-member floating body. The locations of the floats could be varied within certain formations and known rules for finding the locations of the minima were used to solve the problem fully.

One of the inherent difficulties with local minimisation techniques is in ensuring that all of the appropriate stationary points are able to be found. This is particularly important in applications relating to the configuration of bodies in waves since the spatial periodicity of the wave field naturally leads to a multi-peaked solution space. One way around this obstacle is to commence optimisation with several different initial solutions in the hope that all local maxima will be captured. The global maximum may then simply be selected from the set of its local counterparts. This was the approach adopted by Fitzgerald (2006) and Fitzgerald and Thomas (2007) to optimise the hydrodynamic interference amongst wave energy absorbers. A sequential quadratic programming algorithm was applied to arrays of three and five devices. In the latter case a multiplication in optimal performance of 2.777 compared to the same number of devices in isolation was achieved though the choice of array configuration. Motion constraints were also incorporated into the problem towards the end of the dissertation.

The final way to solve array configuration problems is to use the class of global

optimisation algorithms. These techniques directly search for the overall maximum or minimum of a function throughout the entire search space. Unfortunately, these types of routines are generally less numerous and less well-understood than local optimisation algorithms, meaning that their application is often challenging. One such routine that has received a lot of attention in recent years is the Genetic Algorithm (GA) due to Holland (1975). This involves a collection of solutions changing over a number of iterations in a stochastic manner until a global optimum is reached. Further details will be given in Chapter 7 or for a fuller description, the reader is referred to the book by Mitchell (1996).

GAs have been applied extensively in the field of electromagnetic antenna design with the aim of improving certain characteristics such as the 'sidelobe level.' Haupt (1995) describes such a use where the spacings between a linear array of elements are to be optimised.

Two-dimensional antenna arrays have also been formed using GAs. Fridman (2001) achieved this by perturbing the locations of elements given in an initial configuration. Here, the coordinates were represented with continuous real parameters. However a popular alternative is to start with a large but discrete set of possible locations and encode the solution as a binary string of digits. The procedure in which the grid is initially fully populated and members are removed (whilst certain properties preserved) is known as 'array thinning' (Li and Gong, 2000). Array thinning has also been applied in the design of acoustic lenses (Håkansson, Sánchez-Dehesa, and Sanchis, 2004) and photonic crystals (Sanchis et al., 2004).

Another array configuration problem where GAs have been applied is that of 'location allocation.' This involves the strategic distribution of resources in a variety of settings for maximum efficiency. Examples of this include the location of fire stations in a city (Yang, Jones, and Yang, 2007) and the placement of machines in a factory to minimise material handling costs (Mak, Wong, and Chan, 1998).

Finally the location of wireless mobile communication antennas in an urban environment has also been approached using GAs. Chopard et al. (1997) used a novel 'crossover operator' where the solutions belonging to a given iteration were designed to resemble parts of those solutions in previous generations that were well optimised.

2.5 Evaluation

This literature survey has revealed along with much good work that has been done on the subject of wave energy device arrays, there are clearly inadequacies with and omissions in these investigations. Although widely used, point absorber theory does not take into account the diffraction of waves between the elements of the array. The plane wave method on the other hand cannot model long wave interference well. The multiple scattering method is 'exact' with respect to linear wave theory but is not suitable for larger arrays. Adequate solutions may be obtained using boundary element codes but this provides little in the way of understanding about the underlying hydrodynamics and has been shown here to be slower than the method employed in the rest of the thesis. Other methods of the same or lower level of complexity may be well suited to some specific situations but not necessarily the one considered here. Conversely many of the more sophisticated techniques, such as the use of general purpose computational fluid dynamics software, are currently too computationally intensive to be used in an optimisation.

It is evident merely from the volume of published material that the research area under consideration has received a lot more attention in recent years than it once did. Despite this fact there has, at the time of writing, still been relatively few investigations into the free optimisation of layout (not constrained to a template for the arrangement) in an array of wave energy devices. Similarly analysis of arrays in irregular waves and the use of sub-optimal power take-off characteristics has been under-represented in the literature to-date. It is therefore hoped that the work in this thesis will help to remedy these omissions.

Areas that have not received a great deal of attention in the literature, but will not be explored in this thesis include the study of viscous effects on array behaviour. Thomas (2008) noted that as the dimensions of point absorber devices reduce, an increase in effects due to viscosity results. Hence in this regime, the accuracy of all inviscid flow theories described in this chapter is reduced. Also the difficulties associated with the control of devices (such as the need to limit motion amplitudes and applied forces, reduce large flows of reactive power and provide sufficient information to the device controller) only increase in complexity when considering arrays. Finally the applicability of the principle of linear superposition will not be considered here but may also be important when considering behaviour in irregular waves.

Chapter 3

Theory

3.1 Introduction

In this chapter, we present details of the theory that will be used to generate results contained in the remainder of the thesis. We wish to be able to calculate quantities such as the power, motion amplitudes and forces on devices in any given array. This will require modelling the interactions between devices, since waves will be scattered and radiated from each element towards others in the array. Such processes may be complex and numerous, so it is essential that they are accounted for efficiently and accurately. Our primary aim is therefore to construct a hydrodynamic solution to the problem of multiple interactions amongst an array of devices.

Linear wave theory underpins analysis used here and a brief summary of the key assumptions and results are given in Section 3.2. The solution is 'exact' within this context, in that any desired level of accuracy may be attained. Details of the modelling of the devices and surrounding environment are provided in Section 3.3, along with a mathematical statement of the hydrodynamic problem. In Section 3.4, the solution for an isolated device under a range of conditions is presented using an 'eigenfunction expansion' for the velocity potential. The hydrodynamic characteristics of each body are combined with equations of motion in Section 3.5 to fully account for the interactions in an array of devices. Finally, some useful quantities are derived from this solution in Section 3.6, including the *interaction factor* ($\bar{q}$) for an array. The work contained in this chapter was first presented in Child and Venugopal (2007) and Child and Venugopal (2010).

3.2 Linear wave theory

Since the analysis in this thesis will be performed entirely using linear wave theory, an overview of the standard assumptions and results is contained in this section. Further details are available in a number of standard texts (see for example Acheson (2001) or Newman (1977)). A frequency domain approach is adopted here, allowing examination of hydrodynamic systems in a steady state. Initially only regular incident waves (that is to say with a single amplitude, phase, direction and frequency) will be considered. However, once calculations have been made for a number of such waves, the principle of linear superposition will be used to construct irregular wave solutions.

Although this approach cannot take into account forces that are not time-harmonic as well as the spatial and temporal variability of the wave resource, it offers considerable efficiency savings over time-domain formulations. A more thorough examination of the design space is thus facilitated where, in later chapters, optimisation of the array configuration is considered.

In what is to follow, a Cartesian coordinate system $Oxyz$ is adopted such that the positive z-axis points vertically upwards, with the still water level occurring at $z = d$. Time will be denoted by t. The flow is assumed to be irrotational and thus the fluid velocity vector $\mathbf{u}$ may be written as the gradient of a scalar velocity potential $\Phi(x, y, z, t)$:

$$\nabla\Phi = \mathbf{u}. \tag{3.1}$$

Density is assumed to be constant throughout time and space, which leads to the following incompressibility condition:

$$\nabla \,.\, \mathbf{u} = 0 \qquad \text{throughout the fluid.} \tag{3.2}$$

The flow is then subject to the *kinematic boundary condition* which stipulates that fluid elements on a boundary must remain there. If the boundary is defined by $G(x, y, z, t) = 0$, this is equivalent to insisting that $\frac{\mathrm{D}G}{\mathrm{D}t} = 0$. Taking G to be any solid boundary yields the Neumann boundary condition:

$$\mathbf{n}.\nabla\Phi = \mathbf{n}.\mathbf{v}, \tag{3.3}$$

where $\mathbf{v}$ is the boundary velocity vector and $\mathbf{n}$ is a normal vector to the surface. Taking

$G = z - d - \zeta^{(t)}$, where $z = d + \zeta^{(t)}(x, y, t)$ describes the free surface, leads to a further kinematic boundary condition:

$$-\frac{\partial \zeta^{(t)}}{\partial t} - \frac{\partial \Phi}{\partial x}\frac{\partial \zeta^{(t)}}{\partial x} - \frac{\partial \Phi}{\partial y}\frac{\partial \zeta^{(t)}}{\partial y} + \frac{\partial \Phi}{\partial z} = 0 \qquad \text{on } z = d + \zeta^{(t)}. \tag{3.4}$$

If waves that occur on the surface are assumed to have small amplitude, compared to their wavelength and the water depth, then derivatives of Φ, $\zeta^{(t)}$ are all small and of the same order. Equation (3.4) may therefore be linearised about its undisturbed state, neglecting terms that are of quadratic order or higher in these small quantities. Linearising a Taylor expansion of the remaining quantities about $z = d$ leaves only the first term in each, so that they may in fact be evaluated at the still water level:

$$\frac{\partial \Phi}{\partial z} = \frac{\partial \zeta^{(t)}}{\partial t} \qquad \text{on } z = d. \tag{3.5}$$

Similarly, if the condition (3.3) is to be enforced on a boundary whose position oscillates with small amplitude, linearisation allows its application on the mean boundary position.

Now, for an inviscid, irrotational flow Φ_C of a fluid with constant density, conservation of momentum leads to the unsteady Bernoulli equation (Acheson, 2001, (3.19)):

$$\frac{\partial \Phi_C}{\partial t} + \frac{p^{(t)}}{\rho} + \frac{1}{2}\left|\nabla \Phi_C\right|^2 + gz = C(t) \qquad \text{throughout the fluid,} \tag{3.6}$$

where $p^{(t)}$ is the pressure in the fluid, ρ is its density, g is gravitational acceleration and $C(t)$ is an arbitrary function of time. Defining $\Phi_C = \Phi - (\frac{p_\mathrm{a}}{\rho} + gd)t - \int^{t'} C(t')\,\mathrm{d}t'$, where p_a is the constant atmospheric pressure, Φ_C results in the same flow velocity as Φ everywhere. Hence, assuming that the flow Φ is inviscid, Φ_C possesses all of the required properties to apply the Bernoulli equation. Inserting the expression for Φ_C into (3.6) and linearising then leads to:

$$\frac{\partial \Phi}{\partial t} + \frac{p^{(t)} - p_\mathrm{a}}{\rho} + g(z - d) = 0 \qquad \text{throughout the fluid.} \tag{3.7}$$

We next apply this on the free surface of the fluid. Assuming that surface tension forces are negligible, we have that $p^{(t)} = p_\mathrm{a}$. After further linearisation, the term in Φ may effectively be evaluated at $z = d$, as before. This yields the following *dynamic boundary*

condition on the free surface:

$$\frac{\partial \Phi}{\partial t} = -g\zeta^{(t)} \qquad \text{on } z = d. \tag{3.8}$$

Combining equations (3.5) and (3.8), we obtain a single *free surface condition*:

$$\frac{\partial^2 \Phi}{\partial t^2} = -g\frac{\partial \Phi}{\partial z} \qquad \text{on } z = d. \tag{3.9}$$

Any wave which is radiated or diffracted by a finite object is also subject to the *radiation condition.* This states that all such waves must propagate away from the body towards infinity. That is to say

$$\lim_{k_0 r \to \infty} r^{1/2} \left(\frac{\partial \Phi}{\partial r} - \mathrm{i}k_0 \Phi \right) = 0, \tag{3.10}$$

where Φ is the potential of a progressive wave of positive wave number k_0 and r is the distance from the body in the horizontal plane (Martin, 2006, (1.25)).

We also assume that all time-varying quantities oscillate with the same angular frequency ω. In particular,

$$\Phi(x, y, z, t) = \mathrm{Re}\{\phi(x, y, z)\mathrm{e}^{-\mathrm{i}\omega t}\}. \tag{3.11}$$

All other temporal variables (including body heave displacement, velocity and acceleration X, X', X'', free surface elevation ζ, pressure p and power P) will have *time-dependent* form $\Xi^{(t)}$ and *time-independent* form Ξ related as follows:

$$\Xi^{(t)}(x, y, z, t) = \mathrm{Re}\{\Xi(x, y, z)\mathrm{e}^{-\mathrm{i}\omega t}\}. \tag{3.12}$$

Derivatives of these quantities with respect to time therefore induce a pre-factor of $-\mathrm{i}\omega$.

By linearity of the governing equation and boundary conditions, the wave-body interaction problem may be decomposed into a number of related problems. The associated potential may thus be written as:

$$\phi = \phi^{\mathrm{I}} + \phi^{\mathrm{S}} + \phi^{\mathrm{R}}. \tag{3.13}$$

Here, the incident potential ϕ^{I} represents the disturbance that would occur at the location of the body without its presence there. The scattered potential ϕ^{S} concerns the

waves that would emanate from the body if it were to be held fixed in the incident wave field. The radiated wave field ϕ^{R} is that which results from the motion of the body in the absence of incident waves. The sum $\phi^{\mathrm{D}} = \phi^{\mathrm{I}} + \phi^{\mathrm{S}}$ may subsequently be referred to as the diffracted wave field whilst ϕ^{A} may be used to denote the ambient incident wave field in the absence of any bodies whatsoever. Note that the latter is in the general case distinct from Φ^{I} which may include the effects of bodies other than that in question. In the sequel, the incident, radiated and scattered wave fields will always be defined relative to a specific body, rather than in relation to a combination of effects at several bodies.

Several assumptions have been made thus far, which we shall now briefly examine. The constant density assumption holds well for sea water at typical temperatures and pressures. Also, surface tension forces may be justifiably neglected for typical wavelengths involved in wave energy conversion. For an inviscid flow, vorticity is conserved for each fluid element, so the validity of the irrotationality assumption depends heavily on that of inviscidity, provided that initially the flow has no vorticity. Viscosity may lead to skin friction forces and flow separation. The latter may be especially significant around bodies with sharp corners, causing nonlinear drag forces. As long as the small amplitude assumptions are obeyed, forces due to flow separation are likely to remain small. However, care must be taken when a body is excited at its resonant frequency, since small amplitude incident waves may then lead to large motion amplitudes. The most significant effect of this is that motion amplitudes will be diminished in practice compared to those predicted by linear theory. Nonlinearities may also be important where the principle of linear superposition is used in an irregular sea of two or more frequency components. High frequency harmonics and low frequency beats may result from this, causing effects not accounted for by linear wave theory. For a thorough analysis of these assumptions and their validity, see Payne (2006).

3.3 Model

Here we present the mathematical model of the array. This consists of an arrangement of N devices floating in water of finite, constant depth d. The theory will be derived for devices with different physical and mechanical properties, although results will ultimately only be presented for arrays of identical devices. In practice, economic constraints of mass producing the devices may actually dictate the latter (McIver et al.,

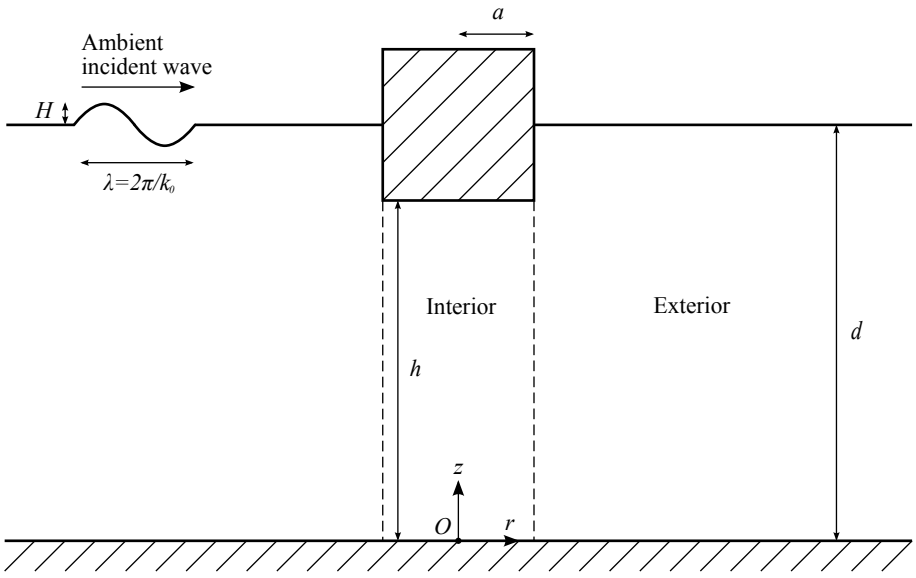

Figure 3.1: Definition sketch for a single device.

1996a). The only constraint on their arrangement is that no two devices may have overlapping horizontal projections.

The devices will be modelled by truncated circular cylinders, oriented with their axis of symmetry in the vertical direction. Although this shape may lead to undesirable flow separation at the corners in practice, it has been chosen here in order to represent a wide range of existing devices and to allow the resulting hydrodynamic problem to be solved efficiently. Cylinder j is of radius a_j, has clearance h_j beneath it to the seabed, draught $b_j = d - h_j$ and mass M_j, as illustrated in Figure 3.1.

The cylinders may move independently, constrained to the vertical direction, from their neutrally buoyant rest position. The heave mode is chosen because it is this motion from which most point absorber and multiple-float devices take off power. The main principles of wave interaction may clearly be demonstrated with just this mode, although the analysis may readily be extended to the other five degrees of freedom if necessary. It is acknowledged if motions become large, phenomena associated with the other modes may become important. These include reduction in power production from the desired mode, modification of buoyancy forces and perturbation of the array configuration.

The vertical motion of the bodies is subject to external stiffness and damping forces,

which model the power take-off (PTO). This represents, for example, the situation where each buoy is attached via a taut tether to the PTO, secured to the seabed. We assume that these forces may be written as linear functions of displacement and velocity respectively, which is valid at low velocities (Eriksson et al., 2005). The associated spring and damping constants for Cylinder j are δ_j and γ_j respectively. No other mechanical forces act on the device. Power take-off characteristics are 'sub-optimal' in the sense that they are fixed to be in some sense optimal for a single wave frequency and retained for the analysis of other wave frequencies and irregular sea-states where they may or may not be optimal.

The ambient incident wave field (Φ^{A}) consists of a sinusoidal plane wave. This has progressive wave number k_0 (angular frequency ω) and the direction of propagation makes an angle β with the positive x-axis.

An origin O is fixed in the domain and a global Cartesian coordinate system $Oxyz$ defined with the z-axis pointing vertically upwards from the seabed. A global cylindrical polar coordinate system $Or\theta z$ shares the same origin and z-axis. Local cylindrical polar coordinate systems $O_j r_j \theta_j z$ relative to each body j will be defined similarly with the origin at the intersection of the centre line of the cylinder and the seabed. The domain $0 \leq r_j \leq a_j$ will be referred to as the *interior* region and that for which $r_j \geq a_j$ as the *exterior* region to Cylinder j. In the global Cartesian system, the centres of each cylinder will have coordinates (x_j, y_j), $j = 1, \ldots, N$. The distance between centres of Cylinders i and j will be L_{ij} with α_{ij} representing the angle at Cylinder i between the positive x-direction and line joining the centre of i to that of j in an anti-clockwise direction. These quantities are illustrated in Figure 3.2.

We may now derive the specific governing equation and boundary conditions for this problem. Firstly, the incompressibility condition (3.2) implies that the time-independent velocity potential must satisfy Laplace's equation everywhere in the fluid. The Neumann boundary condition (3.3) may be applied on the seabed and the sides of the bodies where the normal fluid velocity is zero. Linearisation of this condition on the under surface of each buoy leads to its application at the mean position where the normal velocity amplitude is equal to that of the body X'. Furthermore the potential is subject to the

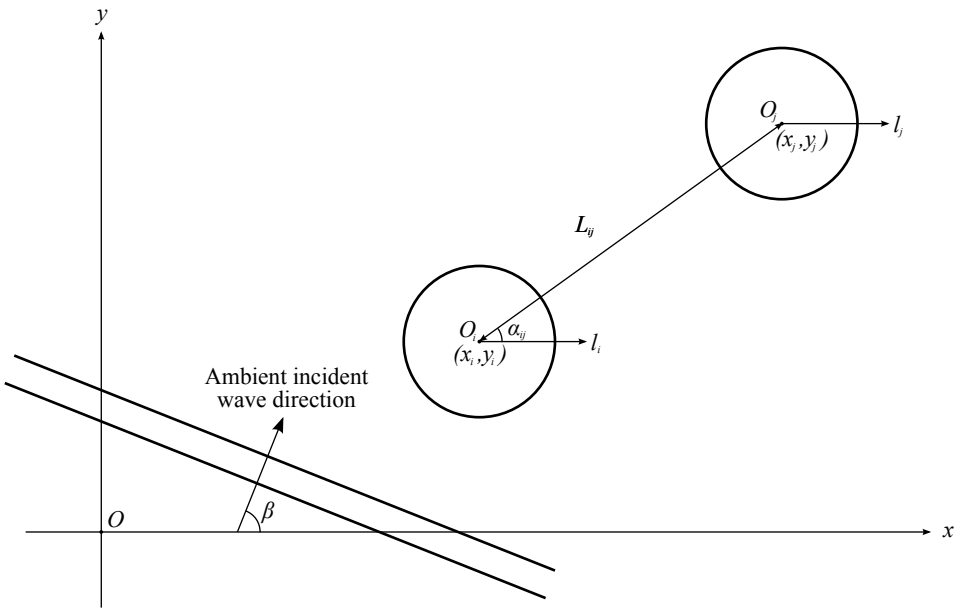

Figure 3.2: Definition sketch for an array of devices. Global Cartesian coordinates $Oxyz$. Local cylindrical polar coordinates $O_i r_i \theta_i z_i$ relative to Body i, where θ_i is taken in an anti-clockwise direction from the initial line l_i.

free surface condition (3.9). Hence

$$\nabla^2 \phi = 0 \qquad \text{throughout the fluid,} \tag{3.14}$$

$$\frac{\partial \phi}{\partial z} = 0 \qquad \text{on } z = 0, \tag{3.15}$$

$$\frac{\partial \phi}{\partial r_j} = 0 \qquad \text{on } r_j = a_j,\ h_j \le z \le d,\ j = 1, \ldots, N, \tag{3.16}$$

$$\frac{\partial \phi}{\partial z} = X_j' \qquad \text{on } z = h_j,\ 0 \le r_j \le a_j,\ j = 1, \ldots, N, \tag{3.17}$$

$$\frac{\partial \phi}{\partial z} = \frac{\omega^2}{g} \phi \qquad \text{on } z = d,\ r_j \ge a_j,\ j = 1, \ldots, N. \tag{3.18}$$

Finally, the radiation condition given below holds for scattered and radiated potentials:

$$\lim_{k_0 r_j \to \infty} \sqrt{r_j} \left(\frac{\partial \phi}{\partial r_j} - \mathrm{i} k_0 \phi \right) = 0, \qquad j = 1, \ldots, N. \tag{3.19}$$

3.4 Hydrodynamic solution for an isolated device

In preparation for studying devices within an array, we need to analyse the behaviour of an isolated device under all possible wave conditions. The scattered and radiated

wave fields will both be represented by linear combinations of a set of *basis* functions, derived in Section 3.4.1, whilst a different set will be used for the incident wave field (Section 3.4.2).

Linearity of the governing equation and boundary conditions (3.14-3.19) means that the operators that transform incident waves and body motions into scattered and radiated wave potentials must also be linear. Hence, the diffracted potential need only be computed for each incident basis function (Section 3.4.3). Similarly, it is sufficient to solve for the radiated wave potential just once in order to describe all possible motions (Section 3.4.4). The general scattering solution may then be reconstructed by linear superposition of the resulting potentials, whereas only multiplication by a scalar factor is required for the radiation solution.

Isolated device potentials must be calculated for each distinct body geometry in the array. Since only one such device will be considered at a time, subscripts relating to the body number will be omitted. The velocity potential solutions in the present work mirror those of Yilmaz (1998), although some errors and omissions in the latter will be highlighted in the course of our analysis. Thus in order to allow easy comparison, the notation used here is largely the same as employed in that work. In turn, the diffraction solution of Garrett (1971) provided the basis for that of Yilmaz (1998).

3.4.1 Scattered wave basis

Here, we seek a set of *basis* functions that may be linearly combined to form any given scattered wave potential (that is, that *spans* the solution space).

The scattered potential ϕ^{S} satisfies (3.14-3.19) with (3.17) replaced by

$$\frac{\partial \phi^{\mathrm{S}}}{\partial z} = 0 \qquad \text{on } z = h,\ 0 \leq r \leq a. \tag{3.20}$$

Writing Laplace's equation (3.14) in cylindrical polar coordinates gives

$$\frac{\partial^2 \phi^{\mathrm{S}}}{\partial r^2} + \frac{1}{r}\frac{\partial \phi^{\mathrm{S}}}{\partial r} + \frac{1}{r^2}\frac{\partial^2 \phi^{\mathrm{S}}}{\partial \theta^2} + \frac{\partial^2 \phi^{\mathrm{S}}}{\partial z^2} = 0. \tag{3.21}$$

We then assume a separable solution for the potential, of the form

$$\phi^{\mathrm{S}} = \sigma_r(r)\sigma_\theta(\theta)\sigma_z(z). \tag{3.22}$$

Substituting (3.22) into (3.21), and introducing separation constant $-\mu^2$, we obtain

$$\frac{\sigma_r''}{\sigma_r} + \frac{\sigma_r'}{\sigma_r r} + \frac{\sigma_\theta''}{r^2 \sigma_\theta} = -\frac{\sigma_z''}{\sigma_z} = -\mu^2, \qquad \mu \in \mathbb{C}, \tag{3.23}$$

where the prime $'$ denotes differentiation with respect to the functional variable. The remainder of the derivation depends upon the region in which the solution is valid.

3.4.1.1 Exterior region

Separating the z-coordinate. The middle and right-hand side expressions in (3.23) yield the following equation:

$$\sigma_z'' - \mu^2 \sigma_z = 0, \tag{3.24}$$

which has general solution

$$c_1 \cosh \mu z + c_2 \sinh \mu z, \qquad c_1, c_2 \in \mathbb{C} \tag{3.25}$$

for $\sigma_z(z)$. Application of (3.15) implies $c_2 = 0$, so that (3.18) leads to

$$\frac{\omega^2}{g} = \mu \tanh \mu d \tag{3.26}$$

for non-trivial solutions. This equation defines the *eigenvalues* μ in the vertical direction and is referred to as the *dispersion relation*. Solutions of the equation are either purely real or imaginary (Mei, 1989, (4.2,4)). Those with negative real or imaginary parts will be abandoned, since the corresponding velocity potentials do not satisfy the radiation condition (3.19). If μ is real, we then get a unique solution $\mu = k_0$, known as the *progressive wave number*. This corresponds to travelling wave solutions (see Section 3.4.2) and satisfies

$$\frac{\omega^2}{g} = k_0 \tanh k_0 d, \qquad k_0 \geq 0 \ (k_0 \in \mathbb{R}). \tag{3.27}$$

If, on the other hand, μ is purely imaginary then there exists a countably infinite set of solutions $\mu = \mathrm{i}k_q \, (q = 1, 2, \ldots)$ to (3.26). The values k_q are known as the *evanescent wave numbers* and are thus given by

$$\frac{\omega^2}{g} = -k_q \tan k_q d, \qquad k_q \geq 0 \ (k_q \in \mathbb{R}), \ q \geq 1 \ (q \in \mathbb{N}), \tag{3.28}$$

corresponding to standing wave solutions. The spatial functions associated with the eigenvalues are known as *eigenfunctions*, which take the form

$$\sigma_z^q(z) = \begin{cases} N_0^{-\frac{1}{2}} \cosh k_0 z, & q = 0, \\ N_q^{-\frac{1}{2}} \cos k_q z, & q \geq 1 \ (q \in \mathbb{N}), \end{cases} \tag{3.29}$$

where normalising factors are defined by

$$N_0 = \frac{1}{2}\left(1 + \frac{\sinh 2k_0 d}{2k_0 d}\right), \tag{3.30}$$

$$N_q = \frac{1}{2}\left(1 + \frac{\sin 2k_q d}{2k_q d}\right), \qquad q \geq 1. \tag{3.31}$$

Any solution may be written as a linear combination of eigenfunctions of the form (3.29), regardless of the pre-factors N_0, N_q chosen. However, the present choice ensures that the set $\{\sigma_z^q : q \in \mathbb{N}\}$ is orthonormal with respect to the L^2 inner product (Priestley, 1997, p.211) on the interval $[0, d]$:

$$\frac{1}{d}\int_0^d \sigma_z^q(z)\,\sigma_z^m(z)\,\mathrm{d}z = \begin{cases} 1, & q = m, \\ 0, & q \neq m. \end{cases} \tag{3.32}$$

Separating the θ-coordinate. From the outermost expressions in (3.23), a further separation constant $-\nu^2$ may be introduced to give

$$-\mu^2 r^2 - \frac{\sigma_r'' r^2}{\sigma_r} - \frac{\sigma_r' r}{\sigma_r} = \frac{\sigma_\theta''}{\sigma_\theta} = -\nu^2, \qquad \nu \in \mathbb{C}. \tag{3.33}$$

The middle and right-hand expressions of this then yield

$$\sigma_\theta'' + \nu^2 \sigma_\theta = 0. \tag{3.34}$$

If $\nu \neq 0$, equation (3.34) has the following solution for σ_θ:

$$c_1 \mathrm{e}^{\mathrm{i}\nu\theta} + c_2 \mathrm{e}^{-\mathrm{i}\nu\theta}, \qquad c_1, c_2 \in \mathbb{C}. \tag{3.35}$$

However, continuity of the potential as θ increases from 2π to 0 requires that $\nu = n$ be an integer. Hence the values that ν may take form a further set of eigenvalues. In the degenerate case where $\nu = 0$, equation (3.34) may be integrated directly to give the

solution

$$c_1\theta + c_2, \qquad c_1, c_2 \in \mathbb{C}. \tag{3.36}$$

Applying continuity of the potential again means that $c_1 = 0$, with the (constant) remainder of this solution capable of being incorporated into (3.35) as the $\nu = 0$ case. The eigenfunctions in the angular coordinate are therefore given by

$$\sigma_\theta^{n\pm}(\theta) = \mathrm{e}^{\pm \mathrm{i}n\theta}, \qquad n \in \mathbb{Z}. \tag{3.37}$$

Separating the r-coordinate. The outermost expressions of (3.33) lead to

$$-\mu^2 r^2 - \frac{\sigma_r'' r^2}{\sigma_r} - \frac{\sigma_r' r}{\sigma_r} = -\nu^2. \tag{3.38}$$

Inserting the eigenvalues μ and ν gives an equation for every pair of values. In the progressive case, the transformation $\hat{r}(r) = k_0 r$ with $\hat{\sigma}_r(\hat{r}(r)) = \sigma_r(r)$ then leads to

$$\hat{\sigma}_r''\hat{r}^2 + \hat{\sigma}_r'\hat{r} + (\hat{r}^2 - n^2)\hat{\sigma}_r = 0. \tag{3.39}$$

This is Bessel's equation in the variable $\hat{r}$, which has linearly independent solutions $J_n(\hat{r})$ and $Y_n(\hat{r})$ (Bessel functions of the first and second kind of order n). It will in fact be convenient to express the solution using the Hankel function of the first kind of order n:

$$H_n = H_n^{(1)} = J_n + \mathrm{i}Y_n. \tag{3.40}$$

The required space is still spanned if the function H_n is used instead of Y_n. Furthermore this choice of function allows the radiation condition (3.19) to be satisfied. Hence the solution for σ_r in the original variable is

$$c_1 J_n(k_0 r) + c_2 H_n(k_0 r), \qquad c_1, c_2 \in \mathbb{C}, \tag{3.41}$$

which exists for each n. The evanescent case involves substitution of the imaginary eigenvalues into (3.38). Using the transformation $\hat{r}(r) = k_q r$ with $\hat{\sigma}_r(\hat{r}(r)) = \sigma_r(r)$, this gives

$$\hat{\sigma}_r''\hat{r}^2 + \hat{\sigma}_r'\hat{r} + (-\hat{r}^2 - n^2)\hat{\sigma}_r = 0. \tag{3.42}$$

This is the modified Bessel equation in $k_q r$, so we have the following solution for σ_r:

$$c_1 I_n(k_q r) + c_2 K_n(k_q r), \qquad c_1, c_2 \in \mathbb{C},\ q \geq 1, \tag{3.43}$$

for each pair q, n. Here, I_n and K_n are the modified Bessel functions of the first and second kind of order n. Application of the radiation condition (3.19) to solutions (3.41) and (3.43) for large argument prohibits inclusion of the functions J_n and I_n. Hence the permitted solutions in the r-coordinate are

$$\sigma_r^{q,n}(r) = \begin{cases} \frac{H_n(k_0 r)}{H_n'(k_0 a)}, & q = 0,\ n \in \mathbb{Z}, \\ \frac{K_n(k_q r)}{K_n'(k_q a)}, & q \geq 1\ (q \in \mathbb{N}),\ n \in \mathbb{Z}. \end{cases} \tag{3.44}$$

Here, the spatial functions have been normalised by their derivatives at $r = a$ to simplify further analysis and to improve the scaling of relevant matrices in the numerical implementation. This theoretically allows the functions in (3.44) to become undefined if the denominators become zero. However, no such instances were encountered in the numerical implementation, whilst the improvement in accuracy obtained by normalising in this way was noticeable.

General solution. For each pair of eigenvalues (μ, ν), the separable solution for ϕ^{S} may be reconstructed as the product of spatial functions (3.29), (3.37) and (3.44) in each coordinate. After some manipulation, the solutions containing σ_θ^{n-} may be seen to differ from those containing σ_θ^{n+} by only a scalar factor and so are subsequently omitted. The general solution for ϕ^{S} in the exterior region may then be written as a linear combination of the following basis functions:

$$(\psi^{\mathrm{S}})_q^n = \begin{cases} \frac{gH}{\omega} N_0^{-\frac{1}{2}} \cosh k_0 z\, \frac{H_n(k_0 r)}{H_n'(k_0 a)}\, \mathrm{e}^{\mathrm{i}n\theta}, & q = 0,\ n \in \mathbb{Z}, \\ \frac{gH}{\omega} N_q^{-\frac{1}{2}} \cos k_q z\, \frac{K_n(k_q r)}{K_n'(k_q a)}\, \mathrm{e}^{\mathrm{i}n\theta}, & q \geq 1\ (q \in \mathbb{N}),\ n \in \mathbb{Z}, \end{cases} \tag{3.45}$$

where the factor gH/ω is included so that the associated complex coefficients will be non-dimensional. The term in such a summation that relates to eigenvalues $\mu = k_q\,(q = 0)$ or $\mu = \mathrm{i}k_q\,(q \geq 1)$ and $\nu = n\,(n \in \mathbb{Z})$ will be referred to as the solution in *z-mode* q and *θ-mode* n.

3.4.1.2 Interior region

Separating the z-coordinate. In this region, the same general solution (3.25) exists as in the exterior region. However, in addition to the seabed boundary condition (3.15), the condition on under surface of body (3.20) gives

$$\sinh \mu h = 0, \tag{3.46}$$

which leads to purely imaginary eigenvalues $\mu = \mathrm{i}\frac{s\pi}{h}$, $s \in \mathbb{Z}$. We may arbitrarily scale the solution for $s = 0$ by $1/2$ so that the eigenfunctions in this region are

$$\sigma_z^s(z) = \begin{cases} \frac{1}{2}, & s = 0, \\ \cos(s\pi z/h), & s \neq 0 \ (s \in \mathbb{Z}). \end{cases} \tag{3.47}$$

Then if we restrict our attention to non-negative mode numbers only, we have a property that will perform the same task as the orthonormality of basis functions in the exterior region (3.32):

$$\frac{2}{h}\int_0^h \sigma_z^s(z)\cos(m\pi z/h)\,\mathrm{d}z = \begin{cases} 1, & s = m \ (s, m \in \mathbf{N}), \\ 0, & s \neq m \ (s, m \in \mathbf{N}). \end{cases} \tag{3.48}$$

Separating the θ-coordinate. Exactly as in the exterior region (3.37), here the eigenfunctions in the angular coordinate are given by

$$\sigma_\theta^{n\pm}(\theta) = \mathrm{e}^{\pm \mathrm{i}n\theta}, \qquad n \in \mathbb{Z}, \tag{3.49}$$

where the eigenvalues n are the same as before.

Separating the r-coordinate. When $s \neq 0$, the eigenvalue $\mu = \mathrm{i}\frac{s\pi}{h}$ inserted into (3.38) with $\nu = n$ gives the modified Bessel equation. Hence, as in the exterior region, the solutions for σ_r are

$$c_1 I_n(s\pi r/h) + c_2 K_n(s\pi r/h), \qquad c_1, c_2 \in \mathbb{C},\ s \neq 0 \ (s \in \mathbb{Z}),\ n \in \mathbb{Z}. \tag{3.50}$$

When $s = 0$, the eigenvalue μ is zero, so the form of equation (3.38) changes. If additionally $n \neq 0$, the transformation $\hat{r}(r) = r/a$ with $\hat{\sigma}_r(\hat{r}(r)) = \sigma_r(r)$ gives Euler's

equation in the new variable:

$$\hat{\sigma}_r''\hat{r}^2 + \hat{\sigma}_r'\hat{r} - \hat{\sigma}_r n^2 = 0, \tag{3.51}$$

with solutions for σ_r in the original variable given by

$$c_1\left(\frac{r}{a}\right)^n + c_2\left(\frac{r}{a}\right)^{-n}, \qquad c_1, c_2 \in \mathbb{C},\ s = 0,\ n \neq 0\ (n \in \mathbb{Z}). \tag{3.52}$$

If both $s = 0$ and $n = 0$, (3.51) becomes

$$\hat{\sigma}_r''\hat{r}^2 + \hat{\sigma}_r'\hat{r} = 0, \tag{3.53}$$

which may be solved using an integrating factor, giving the following solutions for σ_r in the original variable:

$$c_1 \log\left(\frac{r}{a}\right) + c_2, \qquad c_1, c_2 \in \mathbb{C},\ s = 0,\ n = 0. \tag{3.54}$$

In this region, we must discount the second term of (3.50) because it becomes unbounded as $r \to 0$. The same applies for the first term of (3.52) if $n < 0$ and the second term if $n > 0$. Similarly, abandoning the first term of (3.54), the constant second term may be incorporated into the solution (3.52) as the $n = 0$ case. The permitted solutions in the r-coordinate are therefore

$$\sigma_r^{s,n}(r) = \begin{cases} \frac{I_n(s\pi r/h)}{I_n(s\pi a/h)}, & s \neq 0\ (s \in \mathbb{Z}),\ n \in \mathbb{Z}, \\ \left(\frac{r}{a}\right)^{|n|}, & s = 0,\ n \in \mathbb{Z}, \end{cases} \tag{3.55}$$

where once more the spatial functions have been normalised, this time by their value at $r = a$.

General solution. Combining solutions (3.47), (3.49) and (3.55), we once more see that the terms involving $\sigma_\theta^{n-}(\theta)$ may be neglected. Furthermore, all modes involving a negative value of s may be written in terms of a positive value with the same modulus. The general solution for ϕ^{S} in the interior region may then be written as a linear

combination of the following basis functions:

$$(\widetilde{\psi}^{\mathrm{D}})_s^n = \begin{cases} \frac{gH}{\omega} \cos(s\pi z/h) \, \frac{I_n(s\pi r/h)}{I_n(s\pi a/h)} \, \mathrm{e}^{\mathrm{i}n\theta}, & s \neq 0 \ (s \in \mathbb{N}), \ n \in \mathbb{Z}, \\ \frac{gH}{\omega} \left(\frac{1}{2}\right) \left(\frac{r}{a}\right)^{|n|} \mathrm{e}^{\mathrm{i}n\theta}, & s = 0, \ n \in \mathbb{Z}. \end{cases} \tag{3.56}$$

The superscript $^{\mathrm{D}}$ in the notation is motivated by the fact that these functions also span the space of diffracted (incident and scattered) waves in this region. The tilde $\widetilde{\ }$ from here on will refer to quantities related to the interior region.

3.4.2 Incident wave basis

We now seek basis functions that are able to generate all incident wave solutions. These velocity potentials must satisfy Laplace's equation (3.14) and the seabed (3.15) and free surface (3.18) conditions only.

Commencing with consideration of the ambient incident wave field, we assume a plane wave disturbance with a sinusoidal profile. If this has amplitude H, wave number k and is travelling in the positive x-direction, it can be represented by the free surface elevation $z = d + \zeta^{(t)}$ where

$$\zeta^{(t)}(x, y, t) = H \cos(kx - \omega t + \xi) \tag{3.57}$$

$$= \mathrm{Re}\{H\mathrm{e}^{\mathrm{i}(kx - \omega t + \xi)}\} \tag{3.58}$$

and $\xi \in \mathbb{R}$ is some phase shift. Without loss of generality we may set $\xi = \pi/2$ for convenience. This free surface may be represented as a velocity potential, separable in Cartesian coordinates x and z, since the plane waves do not vary with y:

$$\phi^{\mathrm{A}} = \sigma_x(x)\sigma_z(z). \tag{3.59}$$

Laplace's equation (3.14) in Cartesian coordinates dictates that

$$\frac{\partial^2 \phi}{\partial x^2} + \frac{\partial^2 \phi}{\partial y^2} + \frac{\partial^2 \phi}{\partial z^2} = 0 \tag{3.60}$$

and so insertion of the separated potential (3.59) yields the following, for some separation constant $-\mu^2$:

$$\frac{\sigma_x''}{\sigma_x} = -\frac{\sigma_z''}{\sigma_z} = -\mu^2, \qquad \mu \in \mathbb{C}. \tag{3.61}$$

Analysis of the variation in the z-coordinate proceeds exactly as for the scattered potential in the exterior region and so the solutions are given by (3.29). Separation of variables in the x-coordinate using the outermost expressions in (3.61) gives the following solutions for σ_x:

$$c_1 \mathrm{e}^{\mathrm{i}k_0 x} + c_2 \mathrm{e}^{-\mathrm{i}k_0 x}, \qquad c_1, c_2 \in \mathbb{C}, \tag{3.62}$$

$$c_1 \mathrm{e}^{k_q x} + c_2 \mathrm{e}^{-k_q x}, \qquad c_1, c_2 \in \mathbb{C},\ q \geq 1, \tag{3.63}$$

where the wave numbers $k_q\,(q \geq 0)$ are given by the dispersion relations (3.27) and (3.28). The solutions for $q \geq 1$ decay or grow exponentially with distance and exhibit independent oscillations with respect to time and space. These are evanescent (standing) waves and, as we shall see, they form part of the incident wave field that originates from other bodies. However, they cannot represent a travelling wave from infinity and so will be dealt with separately. To ensure travel in the positive x-direction (other directions will be considered later), we must have $c_2 = 0$ in the remaining solution. Hence the separable potential may be reconstructed as

$$\phi^{\mathrm{A}} = C_{\mathrm{A}} \mathrm{e}^{\mathrm{i}k_0 x} N_0^{-\frac{1}{2}} \cosh k_0 z, \qquad C_{\mathrm{A}} \in \mathbb{C}. \tag{3.64}$$

Applying the dynamic boundary condition (3.8) then fixes the constant C_{A}:

$$\phi^{\mathrm{A}} = \frac{gH}{\omega} \frac{\cosh k_0 z}{\cosh k_0 d} \mathrm{e}^{\mathrm{i}k_0 x}. \tag{3.65}$$

This also forces $k = k_0$, the unique positive progressive wave number for the angular frequency. Using the identity $\mathrm{e}^{\frac{1}{2}z(t-\frac{1}{t})} = \sum_{k=-\infty}^{\infty} t^k J_k(z),\ t \neq 0$ (Abramowitz and Stegun, 1964, (9.1.41)), we may expand the exponential factor in polar coordinates, centred on the device. Replacing θ with $\theta - \beta$, the potential then represents progressive waves whose direction of travel makes an angle β with the positive x-direction:

$$\phi^{\mathrm{A}} = \frac{gH}{\omega} \frac{\cosh k_0 z}{\cosh k_0 d} \sum_{n=-\infty}^{\infty} J_n(k_0 r)\, \mathrm{e}^{in(\frac{\pi}{2}+\theta-\beta)}. \tag{3.66}$$

In an array, waves incident to the device may also come from other converters. Using coordinate transformation matrices (to be defined in Section 3.5.3), scattered and radiated waves, written in terms of the scattered basis functions (3.45) may be

reinterpreted as incident waves. Thus, ambient incident waves (3.66) and incident waves originating from other bodies may both be written as linear combinations of the following basis functions:

$$(\psi^{\mathrm{I}})_m^n = \begin{cases} \frac{gH}{\omega}\frac{\cosh k_0 z}{\cosh k_0 d} J_n(k_0 r)\mathrm{i}^n \mathrm{e}^{\mathrm{i}n\theta}, & m = 0,\ n \in \mathbb{Z}, \\ \frac{gH}{\omega}\cos k_m z I_n(k_m r)\mathrm{e}^{\mathrm{i}n\theta}, & m \geq 1,\ n \in \mathbb{Z}. \end{cases} \tag{3.67}$$

Here the $m = 0$ case corresponds to progressive waves, $m \geq 1$ to evanescent waves.

3.4.3 Diffracted wave potential

In Sections 3.4.1 and 3.4.2, we derived basis functions capable of producing the general forms of potentials scattered from the device and incident to it. We now examine how these two potentials relate to each other by studying them both in combination as the diffracted potential. Any incident potential may be dealt with by decomposing it into a linear combination of basis functions and calculating the scattered wave potentials due to each of the functions separately. Then by linearity of the governing equation and boundary conditions, the total scattered potential may be constructed as a similar linear combination of these individual scattered solutions.

In the exterior region, the incident and scattered components of the diffracted potential $\phi^{\mathrm{D}} = \phi^{\mathrm{I}} + \phi^{\mathrm{S}}$ satisfy the respective sets of boundary conditions detailed in the preceding sections. In the interior region, the incident wave potential cannot exist in its exterior form and so diffracted and scattered wave fields are indistinguishable. The potential ϕ^{D} will thus simply refer to ϕ^{S} here, satisfying the conditions imposed in Section 3.4.1 including

$$\frac{\partial \phi^{\mathrm{D}}}{\partial z} = 0, \qquad z = h,\ 0 \leq r \leq a. \tag{3.68}$$

Consider an incident wave field that is described by one of the basis functions in (3.67) of z-mode m and θ-mode n:

$$\phi^{\mathrm{I}} = (\psi^{\mathrm{I}})_m^n. \tag{3.69}$$

Since the body is radially symmetric, the scattered wave will have the same angular variation as the incident wave. Hence the diffracted wave field in the exterior region due to this disturbance may be written as

$$(\phi^{\mathrm{D}})_m^n = \frac{gH}{\omega}\chi_m^n(r, z)\mathrm{e}^{\mathrm{i}n\theta}, \qquad r \geq a. \tag{3.70}$$

The scattered wave may then be expressed as a linear combination of basis functions given by (3.45) in θ-mode n. Hence the following function describes the vertical and radial variation of the diffracted potential due to a progressive incident wave of z-mode $m = 0$:

$$\chi_0^n = \mathrm{i}^n \frac{\cosh k_0 z}{\cosh k_0 d}\left\{ J_n(k_0 r) - \frac{J_n'(k_0 a)}{H_n'(k_0 a)} H_n(k_0 r) \right\} + D_{00}^n \frac{H_n(k_0 r)}{H_n'(k_0 a)} \frac{\cosh k_0 z}{N_0^{1/2}} + \sum_{q=1}^{\infty} D_{q0}^n \frac{K_n(k_q r)}{K_n'(k_q a)} \frac{\cos k_q z}{N_q^{1/2}}. \quad (3.71)$$

This is valid for any θ-mode n, where $D_{q0}^n \in \mathbb{C}$, $(0 \leq q < \infty, -\infty < n < \infty)$ are unknown coefficients. Here, the first term in the braces represents the incident wave field, with the expression outside the braces capable of describing any resulting scattered wave field. The remaining term is included to simplify the derivation when expressions for the solution in the interior and exterior region are compared. This does not affect the nature of the solution, since the coefficient D_{00}^n may be modified accordingly. Note that the terms within the braces represent the solution surrounding a bottom-mounted cylinder, since then no evanescent waves are generated and the radial velocity on the body surface is zero (see MacCamy and Fuchs (1954) for an equivalent solution).

If the incident wave in (3.69) is evanescent, with z-mode $m \geq 1$, the radial and angular variation of the exterior potential is given by

$$\chi_m^n = \cos k_m z \left\{ I_n(k_m r) - \frac{I_n'(k_m a)}{K_n'(k_m a)} K_n(k_m r) \right\} + D_{0m}^n \frac{H_n(k_0 r)}{H_n'(k_0 a)} \frac{\cosh k_0 z}{N_0^{1/2}} + \sum_{q=1}^{\infty} D_{qm}^n \frac{K_n(k_q r)}{K_n'(k_q a)} \frac{\cos k_q z}{N_q^{1/2}} \quad (3.72)$$

in any θ-mode n, where $D_{qm}^n \in \mathbb{C}$ $(1 \leq m < \infty, 0 \leq q < \infty, -\infty < n < \infty)$ are a different set of unknown coefficients.

In the interior region, a similar representation of the potential may be formed as in the exterior region:

$$(\widetilde{\phi}^{\mathrm{D}})_m^n = \frac{gH}{\omega} \widetilde{\chi}_m^n(r, z) \mathrm{e}^{\mathrm{i}n\theta}, \qquad r \leq a. \quad (3.73)$$

The following linear combination of basis functions (3.56) then represents the vertical and radial variation of any diffracted wave field in the interior region, for all incident

z-modes ($m \geq 0$):

$$\widetilde{\chi}_m^n = \frac{C_{0m}^n}{2}\left(\frac{r}{a}\right)^{|n|} + \sum_{s=1}^{\infty} C_{sm}^n \frac{I_n(s\pi r/h)}{I_n(s\pi a/h)} \cos(s\pi z/h). \tag{3.74}$$

This holds for any θ-mode n, where $C_{sm}^n \in \mathbb{C}$ ($0 \leq m < \infty$, $0 \leq s < \infty$, $-\infty < n < \infty$). Note the equation above along with (3.71) and (3.72) corresponds exactly to equations (29), (32) and (46) respectively of Yilmaz (1998).

We now wish to express the coefficients in the interior and exterior potentials in terms of their properties on the interface between the two regions. Assuming that the integral may be exchanged with the summation in each case, orthogonality conditions on the depth functions (3.32) and (3.48) lead to the following expressions for the coefficients in expansions (3.71), (3.72) and (3.74):

$$C_{sm}^n = \frac{2}{h}\int_0^h \widetilde{\chi}_m^n(a,z)\cos(s\pi z/h)\,\mathrm{d}z, \tag{3.75}$$

$$D_{0m}^n = \frac{1}{k_0 d}\int_0^d \frac{\partial \chi_m^n}{\partial r}(a,z) N_0^{-\frac{1}{2}} \cosh k_0 z\,\mathrm{d}z, \tag{3.76}$$

$$D_{qm}^n = \frac{1}{k_q d}\int_0^d \frac{\partial \chi_m^n}{\partial r}(a,z) N_q^{-\frac{1}{2}} \cos k_q z\,\mathrm{d}z, \quad q \geq 1. \tag{3.77}$$

The simplicity of these expressions is a result of having normalised radial functions by their values and derivatives at $r = a$ and adding in a compensation term for incident waves in the expansions.

The interior and exterior potentials may be related to each other by matching properties of the solution on the boundary $r = a$. The Bernoulli equation (3.7) implies that at any depth, continuity of the potential ensures continuity of pressure. Radial velocity may be matched by insisting that the derivative of the potential with respect to r is also continuous. The boundary condition on the side of the body (3.16) gives final constraint on the exterior potential. Assuming that the velocity potential is smooth, the angular component of fluid velocity in the interior and exterior regions at their interface will be the equal. Therefore we may apply the matching conditions in each θ-mode

separately:

$$\chi_m^n = \widetilde{\chi}_m^n, \qquad r = a,\ 0 \le z \le h, \tag{3.78}$$

$$\frac{\partial \chi_m^n}{\partial r} = \frac{\partial \widetilde{\chi}_m^n}{\partial r}, \qquad r = a,\ 0 \le z \le h, \tag{3.79}$$

$$\frac{\partial \chi_m^n}{\partial r} = 0, \qquad r = a,\ h \le z \le d. \tag{3.80}$$

These matching conditions now allow the coefficients of each region to be expressed in terms of those in the other part of the domain. Hence, we insert expansions (3.71-3.72) into coefficient definition (3.75) using matching condition (3.78). Similarly, (3.74) is substituted into (3.76-3.77) using (3.79) and (3.80). Interchanging summation and integral once more, the result may be evaluated using

$$\int_0^h \cos(s\pi z/h)\cosh k_0 z \,\mathrm{d}z = \frac{k_0(-1)^s \sinh k_0 h}{k_0^2 + (s\pi/h)^2}, \tag{3.81}$$

$$\int_0^h \cos(s\pi z/h)\cos k_q z \,\mathrm{d}z = \frac{k_q(-1)^s \sin k_q h}{k_q^2 - (s\pi/h)^2}, \qquad q \ge 1, \tag{3.82}$$

which have been derived with two applications of integration by parts. Further simplification may be attained using the Wronskian identities $K_n'(x)I_n(x) - I_n'(x)K_n(x) = -\frac{1}{x}$ and $H_n'(x)J_n(x) - J_n'(x)H_n(x) = \frac{2\mathrm{i}}{\pi x}$ (Abramowitz and Stegun, 1964, (9.6.15) and (9.1.16)). These then lead to the following system of equations in the unknown coefficients:

$$C_{sm}^n + \sum_{q=0}^{\infty} E_{sq}^n D_{qm}^n = U_{sm}^n, \tag{3.83}$$

$$D_{qm}^n = \sum_{s=0}^{\infty} G_{qs}^n C_{sm}^n, \tag{3.84}$$

where

$$E_{sq}^n = \begin{cases} -\frac{2}{h}\frac{H_n(k_0 a)}{H_n'(k_0 a)}\frac{h^2 k_0 (-1)^s \sinh k_0 h}{N_0^{1/2}(s^2\pi^2 + k_0^2 h^2)}, & s \ge 0,\ q = 0, \\ -\frac{2}{h}\frac{K_n(k_q a)}{K_n'(k_q a)}\frac{h^2 k_q (-1)^s \sin k_q h}{N_q^{1/2}(-s^2\pi^2 + k_q^2 h^2)}, & s \ge 0,\ q \ge 1, \end{cases} \tag{3.85}$$

$$G^n_{qs} = \begin{cases} \frac{|n|\sinh k_0 h}{2ak_0^2 dN_0^{1/2}}, & q=0,\ s=0, \\ \frac{|n|\sin k_q h}{2ak_q^2 dN_q^{1/2}}, & q\geq 1,\ s=0, \\ \frac{I'_n(s\pi a/h)}{I_n(s\pi a/h)}\frac{s\pi h(-1)^s \sinh k_0 h}{(s^2\pi^2+k_0^2h^2)dN_0^{1/2}}, & q=0,\ s\geq 1, \\ \frac{I'_n(s\pi a/h)}{I_n(s\pi a/h)}\frac{s\pi h(-1)^s \sin k_q h}{(-s^2\pi^2+k_q^2h^2)dN_q^{1/2}}, & q\geq 1,\ s\geq 1, \end{cases} \tag{3.86}$$

$$U^n_{sm} = \begin{cases} \frac{4\mathrm{i}^{n+1}(-1)^s h\sinh k_0 h}{\pi a(s^2\pi^2+k_0^2h^2)H'_n(k_0a)\cosh k_0 d}, & s\geq 0,\ m=0, \\ \frac{2h(-1)^{s+1}\sin k_m h}{a(-s^2\pi^2+k_m^2h^2)K'_n(k_m a)}, & s\geq 0,\ m\geq 1. \end{cases} \tag{3.87}$$

The expressions above for the most part agree with equations (38a-g) of Yilmaz (1998). However, the modulus signs in the $s=0$ cases of (3.86) have been omitted in (38c,d) of that work and $\sin k_q k$ should read $\sin k_q h$ in the latter equation. Also, the evanescent ($m \geq 1$) case of (3.87) was not provided.

The system (3.83-3.84) may be solved for each incident z-mode m and θ-mode n. The diffraction solution for plane progressive wave incidence may then be reconstructed as summations of potentials (3.70) and (3.73) over θ-mode n with coefficients C^n_{s0} and D^n_{q0}. However, as we shall see in Section 3.5.5, the entire set of coefficients will define an operator that is capable of describing the diffraction behaviour under all possible incident waves.

3.4.4 Radiated wave potential

The radiation problem involves the forced motion of the body in the absence of incident waves. The method of solution follows that of the scattering problem except that (3.14-3.19) must be satisfied, with the inhomogeneous boundary condition included:

$$\frac{\partial \phi^{\mathrm{R}}}{\partial z} = X', \qquad z=h,\ 0\leq r\leq a. \tag{3.88}$$

By linearity of the governing equation and boundary conditions, the magnitude of the radiated potential is proportional to the amplitude of body velocity X'. Hence, in the exterior region we may write this potential as

$$\phi^{\mathrm{R}} = \frac{gH}{\omega}\widehat{X}R(r,z), \tag{3.89}$$

where R is a non-dimensional spatial function that depends on r and z only, since the body is axisymmetric. Here, $\widehat{X}$ is a non-dimensional complex amplitude related to those

of the vertical displacement, velocity and acceleration of the cylinder respectively by

$$X = H\widehat{X}, \tag{3.90}$$

$$X' = -\mathrm{i}\omega H\widehat{X}, \tag{3.91}$$

$$X'' = -\omega^2 H\widehat{X}. \tag{3.92}$$

Since the derivation of the exterior scattered basis functions in Section 3.4.1.1 did not require any knowledge of how the disturbance was created, it is equally applicable here. Therefore, R may be expanded as a linear combination of the radially symmetric modes for which $n = 0$ of (3.45):

$$R = D_0^{\mathrm{R}} \frac{H_0(k_0 r)}{H_0'(k_0 a)} \frac{\cosh k_0 z}{N_0^{1/2}} + \sum_{q=1}^{\infty} D_q^{\mathrm{R}} \frac{K_0(k_q r)}{K_0'(k_q a)} \frac{\cos k_q z}{N_q^{1/2}}, \tag{3.93}$$

where $D_q^{\mathrm{R}} \in \mathbb{C}$ $(0 \leq q < \infty)$. A representation similar to (3.89) may be formed which is valid in the interior region:

$$\phi^{\mathrm{R}} = \frac{gH}{\omega} \widehat{X} \widetilde{R}(r, z). \tag{3.94}$$

In this case, any particular solution $(\widetilde{R}^{\mathrm{p}})$ satisfying the condition on the moving boundary (3.88) may be augmented by a homogeneous solution $(\widetilde{R}^{\mathrm{h}})$ relating to the situation in which the body is held fixed. The general solution in this region is therefore given by the combination

$$\widetilde{R} = \widetilde{R}^{\mathrm{h}} + \widetilde{R}^{\mathrm{p}}. \tag{3.95}$$

Here, the associated homogeneous problem defined by

$$\frac{\partial \phi^{\mathrm{R}}}{\partial z} = 0, \qquad z = h, 0 \leq r \leq a \tag{3.96}$$

is exactly the same as the scattering problem described in Section 3.4.1.2. Hence the homogeneous part $\widetilde{R}^{\mathrm{h}}$ of the solution $\widetilde{R}$ may be expanded as a linear combination of the radially symmetric basis functions for which $n = 0$ of (3.56):

$$\widetilde{R}^{\mathrm{h}} = \frac{C_0^{\mathrm{R}}}{2} + \sum_{s=1}^{\infty} C_s^{\mathrm{R}} \frac{I_0(s\pi r/h)}{I_0(s\pi a/h)} \cos(s\pi z/h), \tag{3.97}$$

where $C_s^{\mathrm{R}} \in \mathbb{C}$ $(0 \leq s < \infty)$. A particular integral is then required to satisfy (3.88) along with the other boundary conditions. As may be easily verified, one such solution $\widetilde{R}^{\mathrm{p}}$ for

$\widetilde{R}$ is

$$\widetilde{R}^{\mathrm{p}} = \frac{-\mathrm{i}\omega^2}{2gh}\left(z^2 - \frac{r^2}{2}\right). \tag{3.98}$$

As explained for the diffracted wave potential (Section 3.4.3), orthogonality of the depth functions then leads to

$$C_s^{\mathrm{R}} = \frac{2}{h}\int_0^h \widetilde{R}^{\mathrm{h}}(a,z)\cos(s\pi z/h)\,\mathrm{d}z, \tag{3.99}$$

$$D_0^{\mathrm{R}} = \frac{1}{k_0 d}\int_0^d \frac{\partial R}{\partial r}(a,z)N_0^{-\frac{1}{2}}\cosh k_0 z\,\mathrm{d}z, \tag{3.100}$$

$$D_q^{\mathrm{R}} = \frac{1}{k_q d}\int_0^d \frac{\partial R}{\partial r}(a,z)N_q^{-\frac{1}{2}}\cos k_q z\,\mathrm{d}z, \quad q \geq 1. \tag{3.101}$$

Analogous matching conditions on the pressure and radial velocity at the interface $r = a$ also apply here, giving

$$R = \widetilde{R}, \qquad r = a,\ 0 \leq z \leq h, \tag{3.102}$$

$$\frac{\partial R}{\partial r} = \frac{\partial \widetilde{R}}{\partial r}, \qquad r = a,\ 0 \leq z \leq h, \tag{3.103}$$

$$\frac{\partial R}{\partial r} = 0, \qquad r = a,\ h \leq z \leq d. \tag{3.104}$$

Using decomposition (3.95) and matching condition (3.102), $\widetilde{R}^{\mathrm{h}}$ may be expressed in terms of R and $\widetilde{R}^{\mathrm{p}}$ and inserted into the integral (3.99). Also, using the matching conditions (3.103) and (3.104), the decomposition of $\widetilde{R}$ in (3.95), may be inserted into the integrals (3.100) and (3.101). The expansions (3.93) and (3.97) and the particular solution (3.98) may then be used. Much of the subsequent analysis proceeds along the same lines as in Section 3.4.3, the main difference being the integration of the particular solution. Integrating by parts twice gives

$$\int_0^h z^2\cos(s\pi z/h)\,\mathrm{d}z = \frac{2h^3(-1)^s}{(s\pi)^2}, \tag{3.105}$$

whilst the other terms are straightforwardly integrated. This leads to the following system of equations:

$$C_s^{\mathrm{R}} + \sum_{q=0}^{\infty} E_{sq}^0 D_q^{\mathrm{R}} = Q_s^{\mathrm{R}}, \tag{3.106}$$

$$D_q^{\mathrm{R}} = S_q^{\mathrm{R}} + \sum_{s=0}^{\infty} G_{qs}^0 C_s^{\mathrm{R}}, \tag{3.107}$$

where

$$Q_s^{\mathrm{R}} = \begin{cases} \frac{\mathrm{i}\omega^2}{gh}\left(\frac{h^2}{3} - \frac{a^2}{2}\right), & s = 0, \\ \frac{2\mathrm{i}\omega^2 h(-1)^s}{gs^2\pi^2}, & s \geq 1, \end{cases} \tag{3.108}$$

$$S_q^{\mathrm{R}} = \begin{cases} \frac{\mathrm{i}a\omega^2}{2k_0^2 dghN_0^{1/2}} \sinh k_0 h, & q = 0, \\ \frac{\mathrm{i}a\omega^2}{2k_q^2 dghN_q^{1/2}} \sin k_q h, & q \geq 1 \end{cases} \tag{3.109}$$

and E_{sq}^0, G_{qs}^0 are defined exactly as in equations (3.85) and (3.86). Although a different scaling of the particular solution is used here, the remainder of the expressions for the coefficients (3.108) and (3.109) agree with those given by Yilmaz (1998) in equations (60a,b) and (61a,b).

The system (3.106) and (3.107) may then be solved directly for coefficients C_s^{R} and D_q^{R}. Note that this does not involve the device motion amplitude $\widehat{X}$, so need only be performed once in order to describe any radiation from the body in question.

3.5 Hydrodynamic solution for an array of devices

In Section 3.4, the potential surrounding an isolated device was derived, incorporating different incident wave fields and motion of the body. We now consider the case of an array of N devices described in Section 3.3. The solutions relative to each body in the array will be analysed individually using knowledge of isolated device behaviour and combined together to form the complete solution. Thus the descriptions 'radiated' and 'scattered' of a wave field refer to the wave immediately emanating from a particular body.

We will first define a vector notation to represent the wave field surrounding each body, involving the basis functions derived for an isolated device (Section 3.5.1). This will first be used to represent the ambient incident wave field (Section 3.5.2). A general form of the scattered and radiated wave potentials relative to the body in question will then be derived, which will be reinterpreted as an incoming wave field at other elements of the array (Sections 3.5.3-3.5.4). The relationships between incident and scattered waves at the device (Section 3.5.5) and between forces (derived from potentials) and

motions (Section 3.5.6) then completely determine the system to be solved.

In the following, subscripts i and j will denote the numbered label of the body in the array, although these will be omitted where general results concerning any device are given. The derivation contained within this section holds in the case where devices are not necessarily identical although ultimately, the theory will be applied to devices that all have the same properties. The overarching solution structure here is due to Kagemoto and Yue (1986), with details regarding the calculation of matrices and vectors describing single body behaviour following Yilmaz (1998) closely. Some errors were found in the latter work, which will be highlighted in due course (Section 3.5.5).

3.5.1 Partial wave notation

We have seen that the basis functions contained in equation (3.45) may be linearly combined to form any scattered or radiated wave field in the exterior region. For brevity, a notation will be adopted whereby such a linear combination will be written as the scalar product of a vector of complex coefficients and a vector containing a set of spatially-dependent functions that will be termed *partial waves*. We assume that this two dimensional set, indexed by vertical and angular mode numbers, may be arranged into the single dimension of a vector. The order is not important, as long as it is kept consistent throughout the rows and columns of all relevant matrices and vectors. We may then define the element of the vector $\boldsymbol{\Psi}_i^{\mathrm{S}}(r_i, \theta_i, z)$ of scattered partial waves at Body i (distinct from the imaginary number i) corresponding to the m^{th} z-mode and the n^{th} θ-mode as

$$(\boldsymbol{\Psi}_i^{\mathrm{S}})_m^n = \begin{cases} \frac{\cosh k_0 z}{\cosh k_0 d} \frac{H_n(k_0 r_i)}{H_n(k_0 a_i)} \mathrm{e}^{\mathrm{i}n\theta_i}, & m = 0, \\ \cos k_m z \frac{K_n(k_m r_i)}{K_n(k_m a_i)} \mathrm{e}^{\mathrm{i}n\theta_i}, & m \geq 1. \end{cases} \tag{3.110}$$

These functions are capable of describing the same spatial dependence as the scattered basis functions (3.45), the only difference being the scaling of the functions. The form used here was chosen to comply more closely with the convention of Kagemoto and Yue (1986) and to assist in the accurate computation of results.

Similarly, a vector $\boldsymbol{\Psi}_i^{\mathrm{I}}(r_i, \theta_i, z)$ of incident partial waves to Body i, spanning the

same solution space as basis functions (3.67) may be defined, containing elements

$$(\mathbf{\Psi}_i^{\mathrm{I}})_m^n = \begin{cases} \frac{\cosh k_0 z}{\cosh k_0 d} \frac{J_n(k_0 r_i)}{J_n(k_0 a_i)} \mathrm{e}^{\mathrm{i}n\theta_i}, & m = 0, \\ \cos k_m z \, \frac{I_n(k_m r_i)}{I_n(k_m a_i)} \mathrm{e}^{\mathrm{i}n\theta_i}, & m \geq 1. \end{cases} \tag{3.111}$$

We have seen that in the interior region, the diffracted basis functions (3.56) span the solution space for both the scattering and homogeneous radiation problem. Hence the elements contained in the vector $\widetilde{\mathbf{\Psi}}_i^{\mathrm{D}}(r_i, \theta_i, z)$ describe the same solutions:

$$(\widetilde{\mathbf{\Psi}}_i^{\mathrm{D}})_m^n = \begin{cases} \left(\frac{r_i}{a_i}\right)^{|n|} \mathrm{e}^{\mathrm{i}n\theta_i}, & m = 0, \\ \cos(m\pi z/h_i) \frac{I_n(m\pi r_i/h_i)}{I_n(m\pi a_i/h_i)} \mathrm{e}^{\mathrm{i}n\theta_i}, & m \geq 1. \end{cases} \tag{3.112}$$

3.5.2 Ambient incident wave potential

In Section 3.4.2, the potential for an ambient incident wave making an angle β with the positive x-direction was derived in terms of polar coordinates centred on the device (3.66). This potential will take the same form when expressed in polar coordinates centred at each device within an array albeit with a phase shift. The distance from the origin in the direction of the wave to a line parallel to the wave crests through the body coordinates (x_j, y_j), has length $x_j \cos\beta + y_j \sin\beta$. Hence, the phase at body locations other than the origin may be corrected by multiplying the potential by the phase shift associated with this distance:

$$I_j = \mathrm{e}^{\mathrm{i}k_0(x_j \cos\beta + y_j \sin\beta)}. \tag{3.113}$$

Therefore, defining the elements of the vector $\mathbf{a}_j$ of complex coefficients to be

$$(\mathbf{a}_j)_m^n = \begin{cases} I_j \, J_n(k_0 a_j) \mathrm{e}^{\mathrm{i}n(\frac{\pi}{2} - \beta)}, & m = 0, \\ 0, & m \geq 1, \end{cases} \tag{3.114}$$

the ambient incident wave at Cylinder j may be expressed using the vector of incident partial waves (3.111) as

$$\phi_j^{\mathrm{A}} = \frac{gH}{\omega} \mathbf{a}_j^{\mathsf{T}} \mathbf{\Psi}_j^{\mathrm{I}}. \tag{3.115}$$

3.5.3 Scattered wave potential

In the region exterior to Cylinder i, the potential scattered by that body may be written as a linear combination of the scattered partial waves $\boldsymbol{\Psi}_i^{\mathrm{S}}(r_i, \theta_i, z)$ defined by (3.110). Hence if the vector $\mathbf{A}_i$ contains unknown coefficients $(\mathbf{A}_i)_m^n \in \mathbb{C}$ then the following expresses this potential:

$$\phi_i^{\mathrm{S}} = \frac{gH}{\omega} \mathbf{A}_i^{\mathsf{T}} \boldsymbol{\Psi}_i^{\mathrm{S}}, \qquad r_i \geq a_i. \tag{3.116}$$

After waves are scattered from one cylinder, the resulting disturbance is then considered as a set of incident waves upon the other cylinders. Graf's addition formulas (Abramowitz and Stegun, 1964, (9.1.79)) state that

$$H_n(k_0 r_i)\, \mathrm{e}^{\mathrm{i}n\theta_i} = \sum_{l=-\infty}^{\infty} H_{n+l}(k_0 L_{ij}) J_l(k_0 r_j)\, \mathrm{e}^{\mathrm{i}[\alpha_{ij}(l+n)+l(\pi-\theta_j)]}, \tag{3.117}$$

$$K_n(k_m r_i)\, \mathrm{e}^{\mathrm{i}n\theta_i} = \sum_{l=-\infty}^{\infty} K_{n+l}(k_m L_{ij}) I_l(k_m r_j)\, \mathrm{e}^{\mathrm{i}[\alpha_{ij}(l+n)+l(\pi-\theta_j)]}, \tag{3.118}$$

which hold for any integer n, and any non-negative integer m, when $r_j \leq L_{ij}$. Here L_{ij} is the distance between centres of Cylinders i and j, α_{ij} the angle at Cylinder i between the positive x-direction and line joining the centre of i to that of j in an anti-clockwise direction (See Figure 3.2). These formulas may be used to rewrite partial waves from $\boldsymbol{\Psi}_i^{\mathrm{S}}$ in terms of those belonging to $\boldsymbol{\Psi}_j^{\mathrm{I}}$, leading to a coordinate transformation matrix $\mathbf{T}_{ij}$ for every i, j pair except $i = j$. Since the depth variation is unchanged by this transformation, for fixed z-mode m, the element that multiplies incident partial waves at j of θ-mode l in the representation of scattered partial waves from i of θ-mode n is

$$(\mathbf{T}_{ij})_{mm}^{nl} = \begin{cases} \frac{J_l(k_0 a_j)}{H_n(k_0 a_i)} H_{n-l}(k_0 L_{ij})\, \mathrm{e}^{\mathrm{i}\alpha_{ij}(n-l)}, & m = 0, \\ \frac{I_l(k_m a_j)}{K_n(k_m a_i)} K_{n-l}(k_m L_{ij})\, \mathrm{e}^{\mathrm{i}\alpha_{ij}(n-l)}(-1)^l, & m \geq 1. \end{cases} \tag{3.119}$$

Thus for all i, j $(i \neq j)$,

$$\boldsymbol{\Psi}_i^{\mathrm{S}} = \mathbf{T}_{ij} \boldsymbol{\Psi}_j^{\mathrm{I}}, \tag{3.120}$$

so from equation (3.116), ϕ_i^{S} evaluated at Cylinder j is

$$\phi_i^{\mathrm{S}}\big|_j = \frac{gH}{\omega} \mathbf{A}_i^{\mathsf{T}} \mathbf{T}_{ij} \boldsymbol{\Psi}_j^{\mathrm{I}}. \tag{3.121}$$

Note that the condition $r_j \leq L_{ij}$ is automatically satisfied for the present shape of device and choice of coordinates. Since the projections of the bodies do not overlap, the spacing between two devices must be greater than the radius of the Device j (that is $L_{ij} > a_j$). The expansion of incident waves is only required to be valid on $r_j = a_j$, where the matching is performed and so the condition is automatically satisfied.

In the interior region to Cylinder i, the vector of diffracted partial waves $\widetilde{\mathbf{\Psi}}_i^{\mathrm{D}}(r_i, \theta_i, z)$ defined by (3.112) and a vector $\widetilde{\mathbf{A}}_i$ of unknown coefficients may be used to write the diffracted potential as

$$\phi_i^{\mathrm{D}} = \frac{gH}{\omega} \widetilde{\mathbf{A}}_i^{\mathsf{T}} \widetilde{\mathbf{\Psi}}_i^{\mathrm{D}}, \qquad 0 \leq r_i \leq a_i. \tag{3.122}$$

3.5.4 Radiated wave potential

The only difference between the radiation problem for a device within an array and for the same device in isolation (Section 3.4.4) is in the body velocity. Hence the radiated potential for each device i in the array may be written as the product of an unknown complex amplitude representing this velocity and a spatial function that depends only on the single body solution. This function, given by R and $\widetilde{R}$ in (3.89) and (3.94), is known as the *radiation characteristics* in the exterior and interior regions respectively (Kagemoto and Yue, 1993).

Equation (3.93) showed that the radiation characteristics may be written as a linear combination of scattered basis functions in the exterior region. Equivalently, we write the characteristics for Body i, R_i as the scalar product of a vector of complex coefficients $\mathbf{R}_i$ and a vector of scattered partial waves $\mathbf{\Psi}_i^{\mathrm{S}}$:

$$R_i = \mathbf{R}_i^{\mathsf{T}} \mathbf{\Psi}_i^{\mathrm{S}}. \tag{3.123}$$

Hence the radiated potential in this region is

$$\phi_i^{\mathrm{R}} = \frac{gH}{\omega} \widehat{X}_i \mathbf{R}_i^{\mathsf{T}} \mathbf{\Psi}_i^{\mathrm{S}}, \qquad r_i \geq a_i, \tag{3.124}$$

where $\widehat{X}_i$ is the non-dimensional body motion amplitude of Body i (See (3.90-3.92)).

Once again, T_{ij} may be used to express the radiated wave field as incident waves upon other cylinders:

$$\phi_i^{\mathrm{R}}\big|_j = \frac{gH}{\omega} \widehat{X}_i \mathbf{R}_i^{\mathsf{T}} \mathsf{T}_{ij} \mathbf{\Psi}_j^{\mathrm{I}}. \tag{3.125}$$

In the interior region, the radiated potential may be written in an analogous manner

to (3.94) using the decomposition (3.95). The homogeneous part of this solution may be expanded either as a summation of diffracted basis functions as in (3.97) or using vectors of complex coefficients $\widetilde{\mathbf{R}}_i$ and diffracted partial waves $\widetilde{\mathbf{\Psi}}_i^{\mathrm{D}}$ such that

$$\widetilde{R}_i^{\mathrm{h}} = \widetilde{\mathbf{R}}_i^{\mathsf{T}} \widetilde{\mathbf{\Psi}}_i^{\mathrm{D}}, \tag{3.126}$$

where the subscript i denotes body number. This yields the following for the radiated potential in this region:

$$\phi_i^{\mathrm{R}} = \frac{gH}{\omega} \widehat{X}_i \left[\widetilde{R}_i^{\mathrm{p}} + \widetilde{\mathbf{R}}_i^{\mathsf{T}} \widetilde{\mathbf{\Psi}}_i^{\mathrm{D}} \right], \qquad 0 \leq r_i \leq a_i. \tag{3.127}$$

Since the radiation characteristics are derived from the single device solution, we thus need to compute this for each distinct body geometry. Then to calculate $\mathbf{R}_i$ and $\widetilde{\mathbf{R}}_i$, the summations (3.93) and (3.97) must be reinterpreted in the standard partial wave notation of (3.123) and (3.126) by comparing the coefficients of spatial functions in the two representations. Thus, omitting body number i, the elements of these vectors corresponding to z-modes s, q and θ-mode l are

$$(\mathbf{R})_q^l = \begin{cases} H_0(k_0 a) \left(\dfrac{D_0^{\mathrm{R}} \cosh k_0 d}{H_0'(k_0 a) N_0^{1/2}} \right), & q = 0,\ l = 0, \\ K_0(k_q a) \left(\dfrac{D_q^{\mathrm{R}}}{K_0'(k_q a) N_q^{1/2}} \right), & q \geq 1,\ l = 0, \\ 0, & l \neq 0 \end{cases} \tag{3.128}$$

and

$$(\widetilde{\mathbf{R}})_s^l = \begin{cases} \left(\dfrac{C_0^{\mathrm{R}}}{2} \right), & s = 0,\ l = 0, \\ I_0(s\pi a/h) \left(\dfrac{C_s^{\mathrm{R}}}{I_0(s\pi a/h)} \right) = C_s^{\mathrm{R}}, & s \geq 1,\ l = 0, \\ 0, & l \neq 0. \end{cases} \tag{3.129}$$

Note that the entries are non-zero only in the radially symmetric $l = 0$ mode.

3.5.5 Scattering equations

The total potential reaching Cylinder j may be expressed as the summation of the ambient incident wave field (3.115), the waves scattered from other cylinders (3.121)

and the waves radiated by their motion (3.125):

$$\phi_j^{\mathrm{I}} = \frac{gH}{\omega}\left[\mathbf{a}_j^{\mathsf{T}} + \sum_{\substack{i=1\\ i\neq j}}^{N}(\mathbf{A}_i + \widehat{X}_i\mathbf{R}_i)^{\mathsf{T}}\mathbf{T}_{ij}\right]\boldsymbol{\Psi}_j^{\mathrm{I}}. \tag{3.130}$$

By linearity of the governing equation and boundary conditions for the diffraction problem, we may define a linear operator that transforms the coefficients of $\boldsymbol{\Psi}_j^{\mathrm{I}}$ in the above incident potential into those of $\boldsymbol{\Psi}_j^{\mathrm{S}}$ in the appropriate scattered potential (3.116). This is commonly expressed as the exterior *diffraction transfer matrix* $\mathbf{B}_j$ (Kagemoto and Yue, 1986):

$$\mathbf{A}_j = \mathbf{B}_j\left[\mathbf{a}_j + \sum_{\substack{i=1\\ i\neq j}}^{N}\mathbf{T}_{ij}^{\mathsf{T}}(\mathbf{A}_i + \widehat{X}_i\mathbf{R}_i)\right], \quad j = 1...N. \tag{3.131}$$

This matrix encapsulates the behaviour of the scattered potential for any incident wave field.

Incident waves must also be related to the interior potential, in order to calculate the heave force on the underside of the cylinder. The interior diffracted potential takes a different form to the exterior potential, so a different, *interior* diffraction transfer matrix $\widetilde{\mathbf{B}}_j$ is required to relate the coefficients of $\boldsymbol{\Psi}_j^{\mathrm{I}}$ in (3.130) and those of $\widetilde{\boldsymbol{\Psi}}_j^{\mathrm{D}}$ in the appropriate diffracted potential (3.122):

$$\widetilde{\mathbf{A}}_j = \widetilde{\mathbf{B}}_j\left[\mathbf{a}_j + \sum_{\substack{i=1\\ i\neq j}}^{N}\mathbf{T}_{ij}^{\mathsf{T}}(\mathbf{A}_i + \widehat{X}_i\mathbf{R}_i)\right], \quad j = 1...N. \tag{3.132}$$

The entry $(\mathbf{B})_{qm}^{nn}$ of the exterior diffraction transfer matrix is defined as the coefficient of the partial wave of z-mode q and θ-mode n in the scattered velocity potential exterior to the cylinder, in response to a unit incident wave of z-mode m and θ-mode n (Kagemoto and Yue, 1986). The counterpart matrix for the interior region has elements $(\widetilde{\mathbf{B}})_{sm}^{nn}$, which represents the coefficient in the interior diffracted potential in z-mode s due to the same incident disturbance.

The elements of these matrices may be determined alongside each other by solving the diffraction problem for the isolated body (Section 3.4.3). We write both the incident and scattered parts of the potentials relating to (3.71) and (3.72) as a scalar product of a vector of coefficients and a vector of partial waves by comparing coefficients in their

representations. Then $(\mathbf{B})^{nn}_{qm}$ is the ratio of the coefficient of $(\mathbf{\Psi}^{\mathrm{S}})^n_q$ to that of $(\mathbf{\Psi}^{\mathrm{I}})^n_m$. A similar definition applies for $(\widetilde{\mathbf{B}})^{nn}_{sm}$ relating to the coefficients of the diffracted partial wave vector $(\widetilde{\mathbf{\Psi}}^{\mathrm{D}})^n_s$ from (3.74) in the interior region and the same incident wave field. The calculations must be repeated for wave incidence in each mode, leading to the following expressions for elements of the diffraction transfer matrices:

$$(\mathbf{B})^{nn}_{qm} = \begin{cases} \frac{H_n(k_0a)}{J_n(k_0a)}\left(-\frac{J'_n(k_0a)}{H'_n(k_0a)} + \mathrm{i}^{-n}\frac{D^n_{00}\cosh k_0 d}{N_0^{1/2}H'_n(k_0a)}\right), & m=0,\ q=0, \\ \frac{K_n(k_qa)}{J_n(k_0a)}\left(\mathrm{i}^{-n}\frac{D^n_{q0}}{N_q^{1/2}K'_n(k_qa)}\right), & m=0,\ q\geq 1, \\ \frac{H_n(k_0a)}{I_n(k_ma)}\left(\frac{D^n_{0m}\cosh k_0 d}{N_0^{1/2}H'_n(k_0a)}\right), & m\geq 1,\ q=0, \\ \frac{K_n(k_qa)}{I_n(k_ma)}\left(\frac{D^n_{qm}}{N_q^{1/2}K'_n(k_qa)}\right), & m\geq 1,\ q\neq 0, m, \\ \frac{K_n(k_ma)}{I_n(k_ma)}\left(-\frac{I'_n(k_ma)}{K'_n(k_ma)} + \frac{D^n_{mm}}{N_m^{1/2}K'_n(k_ma)}\right), & m\geq 1,\ q=m, \end{cases} \tag{3.133}$$

$$(\widetilde{\mathbf{B}})^{nn}_{sm} = \begin{cases} \frac{a^{|n|}}{J_n(k_0a)}\left(\frac{C^n_{00}}{2\mathrm{i}^n a^{|n|}}\right) = \frac{C^n_{00}}{2\mathrm{i}^n J_n(k_0a)}, & m=0,\ s=0, \\ \frac{I_n(s\pi a/h)}{J_n(k_0a)}\left(\frac{C^n_{s0}}{\mathrm{i}^n I_n(s\pi a/h)}\right) = \frac{C^n_{s0}}{\mathrm{i}^n J_n(k_0a)}, & m=0,\ s\geq 1, \\ \frac{a^{|n|}}{I_n(k_ma)}\left(\frac{C^n_{0m}}{2a^{|n|}}\right) = \frac{C^n_{0m}}{2I_n(k_ma)}, & m\geq 1,\ s=0, \\ \frac{I_n(s\pi a/h)}{I_n(k_ma)}\left(\frac{C^n_{sm}}{I_n(s\pi a/h)}\right) = \frac{C^n_{sm}}{I_n(k_ma)}, & m\geq 1,\ s\geq 1. \end{cases} \tag{3.134}$$

All coefficients for which the angular mode of the scattered potential is not equal to that of the incident potential are zero due to the radial symmetry of the device. These calculations must be repeated for each distinct body geometry to obtain $\mathbf{B}_j$ and $\widetilde{\mathbf{B}}_j$ for all j.

We now compare these expressions with those given in Yilmaz (1998). In that paper, no scattering equations nor associated matrices are provided for the case of scattered waves in z-modes that are different to the incident mode. Since an alternative scaling for the partial wave vectors has been used here, the parts of the coefficients associated with this difference are contained outside the parentheses in the above expressions. Those inside the brackets generally agree with equations (39), (47), (40a) and (40b) given in the original work. However, the factor i^{-n} in the $m=0$, $q=0$ case of (3.133) is missing in (39) of Yilmaz (1998). This is a typographical error, the correct expressions having been used to generate the associated numerical results [Prof. Yilmaz, private communication].

The interior diffraction transfer matrix $\widetilde{\mathbf{B}}$ given here in (3.134) is analogous to $\mathbf{B}_{hj}$

defined in Yilmaz (1998) by (40a,b). Since the latter is used only in the heave force calculation, the z-dependence $\cos(s\pi z/h)$ has already been evaluated on the under surface of the cylinder $z = h$. This explains why the extra factor of $(-1)^m$ is not contained in the $s = m$ cases of (3.134). However, there is again a genuine discrepancy regarding the factor i^{-n} between the $m = 0$ case of (3.134) above and (40a) of Yilmaz (1998).

3.5.6 Equations of motion

First, we consider the forces that the fluid exerts on a body due to the pressure within it. From equation (3.7), the pressure difference between the fluid and atmosphere $p_{\mathrm{F}}^{(t)}$ satisfies

$$p_{\mathrm{F}}^{(t)} = p_{\mathrm{U}}^{(t)} + p_{\mathrm{H}}^{(t)}, \tag{3.135}$$

where $p_{\mathrm{U}}^{(t)}$ is the hydrostatic pressure and $p_{\mathrm{H}}^{(t)}$ the hydrodynamic pressure. Evaluating these on the underside S of an oscillating buoy, where $z = h + X^{(t)}$ we have

$$p_{\mathrm{U}}^{(t)} = \rho g[d - (h + X^{(t)})] \qquad \text{on } S, \tag{3.136}$$

$$p_{\mathrm{H}}^{(t)} = -\rho \left.\frac{\partial \Phi}{\partial t}\right|_{z=h} \qquad \text{on } S. \tag{3.137}$$

Here, as in Section 3.2, linearisation allows evaluation of $p_{\mathrm{H}}^{(t)}$ at $z = h$ instead of on S. The force of the fluid on the buoy in the positive vertical direction is the integral of the pressure over the surface:

$$F_{\mathrm{F}}^{(t)} = -\iint_S p_{\mathrm{F}}^{(t)}\, n_z \,\mathrm{d}S, \tag{3.138}$$

where $n_z = -1$ is the vertical component of the outward facing unit normal to S. We next evaluate the forces due to the linearised hydrostatic and hydrodynamic contributions to the pressure (3.136) and (3.137) separately. Hence, the hydrostatic upthrust on the body is given by

$$F_{\mathrm{U}}^{(t)} = \rho g \pi a^2 [d - (h + X^{(t)})]. \tag{3.139}$$

Now, since the device is assumed to be in equilibrium at rest such that weight and upthrust forces balance, its mass M satisfies

$$M = \rho \pi a^2 (d - h), \tag{3.140}$$

so that its weight is given by

$$F_{\mathrm{W}}^{(t)} = -\rho g \pi a^2 (d - h). \tag{3.141}$$

The upthrust $F_{\mathrm{U}}^{(t)}$ and the weight $F_{\mathrm{W}}^{(t)}$ may then be conveniently summed to form the buoyancy spring force. This may be written in time-independent form for each body j as

$$F_j^{\mathrm{B}} = -\rho g \pi a_j^2 X_j. \tag{3.142}$$

Also, the time-independent hydrodynamic force on each body j is

$$F_j^{\mathrm{H}} = \mathrm{i}\omega\rho \iint_{S_j} \phi_j(r_j, \theta_j, h_j)\ \mathrm{d}S, \tag{3.143}$$

where S_j is the underside of the cylinder. Using equations (3.122), (3.132) and (3.127), for each body j the total potential in the interior region may be written as the sum of the potential it diffracts and the potential it radiates.

$$\phi_j = \frac{gH}{\omega} \left\{ \left[\mathbf{a}_j^{\mathsf{T}} + \sum_{\substack{i=1 \\ i \neq j}}^{N} (\mathbf{A}_i + \widehat{X}_i \mathbf{R}_i)^{\mathsf{T}} \mathbf{T}_{ij} \right] \widetilde{\mathbf{B}}_j^{\mathsf{T}} \widetilde{\mathbf{\Psi}}_j^{\mathrm{D}} + \widehat{X}_j \left(\widetilde{R}_j^{\mathrm{p}} + \widetilde{\mathbf{R}}_j^{\mathsf{T}} \widetilde{\mathbf{\Psi}}_j^{\mathrm{D}} \right) \right\}, \qquad 0 \leq r_j \leq a_j. \tag{3.144}$$

Finally, there will be a force experienced by every element of the array due to the presence of its generator. This was assumed to have linear spring and damping components, in proportion to the displacement and velocity of the device respectively:

$$F_j^{\mathrm{G}} = -\delta_j X_j - \gamma_j X_j', \tag{3.145}$$

where $\delta_j, \gamma_j \in \mathbb{R}$ for all j. Each cylinder, j, is then governed by the following equation of motion:

$$M_j X_j'' = F_j^{\mathrm{H}} + F_j^{\mathrm{B}} + F_j^{\mathrm{G}}, \tag{3.146}$$

where M_j is the mass of Cylinder j, calculated as in (3.140).

Returning to the hydrodynamic force calculation, the only spatially dependent functions in (3.144) that require integration are $\widetilde{\mathbf{\Psi}}_j^{\mathrm{D}}$ and $\widetilde{R}_j^{\mathrm{p}}$. Defining

$$\widetilde{\mathbf{Y}}_j^{\mathrm{D}} = \int_0^{a_j} \int_0^{2\pi} \widetilde{\mathbf{\Psi}}_j^{\mathrm{D}}(r_j, \theta_j, h_j) r_j \, \mathrm{d}\theta_j \, \mathrm{d}r_j, \tag{3.147}$$

$$\widetilde{Y}_j^{\mathrm{R}} = \int_0^{a_j} \int_0^{2\pi} \widetilde{R}_j^{\mathrm{p}}(r_j, h_j) r_j \, \mathrm{d}\theta_j \, \mathrm{d}r_j + \widetilde{\mathbf{R}}_j^{\mathsf{T}} \widetilde{\mathbf{Y}}_j^{\mathrm{D}}, \tag{3.148}$$

we may separate the angular dependence from the integrands and straightforwardly integrate the resulting expressions, using $\left(\frac{1}{x}\frac{\mathrm{d}}{\mathrm{d}x}\right)\{xI_1(x)\} = I_0(x)$ (Abramowitz and Stegun, 1964, (9.6.28)). This yields

$$(\widetilde{\mathbf{Y}}_j^{\mathrm{D}})_m^n = \begin{cases} \left(\pi a_j^2\right), & m = 0,\ n = 0, \\ \frac{1}{I_0(m\pi a_j/h_j)} \left(\frac{(-1)^m 2 a_j h_j I_1(m\pi a_j/h_j)}{m}\right), & m \geq 1,\ n = 0, \\ 0, & n \neq 0, \end{cases} \tag{3.149}$$

$$\widetilde{Y}_j^{\mathrm{R}} = \left(\frac{-\mathrm{i}\omega^2\pi}{2gh_j}\right)\left(h_j^2 a_j^2 - \frac{a_j^4}{4}\right) + \widetilde{\mathbf{R}}_j^{\mathsf{T}} \widetilde{\mathbf{Y}}_j^{\mathrm{D}}. \tag{3.150}$$

Furthermore, on defining

$$W_j = \widetilde{Y}_j^{\mathrm{R}} - \frac{\mathrm{i}}{\rho g}\left(M_j\omega^2 - \pi a_j^2 \rho g + \mathrm{i}\omega\gamma_j - \delta_j\right), \tag{3.151}$$

substitution of (3.143), (3.142) and (3.145) into (3.146) results in the following system of equations:

$$\sum_{\substack{i=1 \\ i\neq j}}^{N} \left[\mathbf{R}_i^{\mathsf{T}} \mathbf{T}_{ij} \widetilde{\mathbf{B}}_j^{\mathsf{T}} \widetilde{\mathbf{Y}}_j^{\mathrm{D}}\right] \widehat{X}_i + W_j \widehat{X}_j + \sum_{\substack{i=1 \\ i\neq j}}^{N} \left[\mathbf{T}_{ij} \widetilde{\mathbf{B}}_j^{\mathsf{T}} \widetilde{\mathbf{Y}}_j^{\mathrm{D}}\right]^{\mathsf{T}} \mathbf{A}_i = -\mathbf{a}_j^{\mathsf{T}} \widetilde{\mathbf{B}}_j^{\mathsf{T}} \widetilde{\mathbf{Y}}_j^{\mathrm{D}}, \qquad j = 1...N. \tag{3.152}$$

This is a set of N scalar equations in the N scalar unknowns $\widehat{X}_i$ and the N vector unknowns $\mathbf{A}_i$. The relationship (3.131) represents a system of N vector equations in the same variables. Therefore, these two sets of equations may be solved simultaneously in order to completely determine the motion and wave amplitudes in the vicinity of the array.

3.6 Derived quantities

Now that the hydrodynamic problem has been solved, we can derive various quantities that will be useful in analysing an array. The principal forces involved in the subsequent array analysis are detailed in Section 3.6.1, whilst an expression for the power from each device is given in Section 3.6.2. Finally the interaction factor $\bar{q}$ is introduced in Section 3.6.3, that will play a central role in the assessment of arrays.

3.6.1 Forces

The expression for hydrodynamic heave force may now be fully determined from (3.143-3.144) and (3.147-3.150):

$$F_j^{\mathrm{H}} = \mathrm{i}\rho g H \left\{ \left[\mathbf{a}_j^{\mathsf{T}} + \sum_{\substack{i=1 \\ i\neq j}}^{N} (\mathbf{A}_i + \widehat{X}_i \mathbf{R}_i)^{\mathsf{T}} \mathbf{T}_{ij} \right] \widetilde{\mathbf{B}}_j^{\mathsf{T}} \widetilde{\mathbf{Y}}_j^{\mathrm{D}} + \widehat{X}_j \widetilde{Y}_j^{\mathrm{R}} \right\}. \tag{3.153}$$

The first term in the square brackets represents the force F_j^{A} due to the ambient incident wave field on the element j:

$$F_j^{\mathrm{A}} = i\rho g H \mathbf{a}_j^{\mathsf{T}} \widetilde{\mathbf{B}}_j^{\mathsf{T}} \widetilde{\mathbf{Y}}_j^{\mathrm{D}}. \tag{3.154}$$

The two terms within the sum represent the force from the waves scattered and radiated from other bodies, indexed by i, immediately before arriving at j. The final term represents the force felt by j due to its own radiation of waves:

$$F_{jj}^{\mathrm{R}} = \mathrm{i}\rho g H \widehat{X}_j \widetilde{Y}_j^{\mathrm{R}}. \tag{3.155}$$

The heave added mass m_{33} and damping b_{33} are defined in terms of this force for an isolated body j by Evans (1980):

$$F_{jj}^{\mathrm{R}} = -(m_{33} X_j'' + b_{33} X_j'). \tag{3.156}$$

Thus, using the definitions of dimensional heave velocity and acceleration, we have

$$m_{33} = \frac{1}{\omega^2 H} \mathrm{Re}\{\mathrm{i}\rho g H \widetilde{Y}_j^{\mathrm{R}}\}, \tag{3.157}$$

$$b_{33} = \frac{1}{\omega H} \mathrm{Im}\{\mathrm{i}\rho g H \widetilde{Y}_j^{\mathrm{R}}\}. \tag{3.158}$$

3.6.2 Power

The power from each device may easily be calculated using the total hydrodynamic heave force. The mean rate at which this does work on Cylinder j over one period of oscillation (duration $T = \frac{2\pi}{\omega}$) is given by (Evans, 1980)

$$P_j = \frac{1}{T} \int_0^T \mathrm{Re}\{F_j^{\mathrm{H}} \, \mathrm{e}^{-\mathrm{i}\omega t}\} \mathrm{Re}\{X_j' \, \mathrm{e}^{-\mathrm{i}\omega t}\} \, \mathrm{d}t, \tag{3.159}$$

which, using an identity (Mei, 1989, (5.10)), simplifies to

$$P_j = \frac{1}{2}\mathrm{Re}\{F_j^{\mathrm{H}}(X_j')^*\}, \tag{3.160}$$

where * denotes the complex conjugate. On rearranging (3.146) and substituting F_j^{H} into the above, only the damping term makes a non-zero contribution to the power. Hence,

$$P_j = \frac{\gamma_j}{2}|X_j'|^2 \tag{3.161}$$

$$= \frac{\gamma_j \omega^2 H^2}{2}|\widehat{X}_j|^2. \tag{3.162}$$

Using the non-dimensionalised motion amplitude $\widehat{X}_j$ for each cylinder, the power may thus be readily calculated.

3.6.3 Interaction factor

The effect of the array configuration may be more easily understood by forming the *interaction* or $\bar{q}$- *factor* as the ratio of total power from the array to that of the same number of devices in isolation. If all devices are geometrically identical, this is

$$\bar{q}(k_0,\beta) = \frac{\sum_{j=1}^{N} P_j(k_0,\beta)}{N \times P_0(k_0,\beta)}, \tag{3.163}$$

where P_0 represents the power from an isolated converter and the functional form of the variables emphasises their dependence on incident wave number and direction. Clearly the interaction factor is also dependent on the spring and damping constants applied to each member of the array and to the single body. Note that this is distinct from the commonly used q-factor:

$$q(k_0,\beta) = \frac{\max\limits_{\substack{\delta_1 \ldots \delta_N,\\ \gamma_1 \ldots \gamma_N}} \left\{\sum_{j=1}^{N} P_j(k_0,\beta)\right\}}{N \times \max\limits_{\delta_0,\gamma_0}\{P_0(k_0,\beta)\}}, \tag{3.164}$$

where for every wave number and heading, the total and isolated power have both been maximised with respect to the choice of spring and damping constants associated with the converters, $\{\delta_j, \gamma_j : j = 0 \ldots N\}$. Note that principal difference between the two measures is that $\bar{q}$ is device-specific but offers a more realistic estimate of power enhancement in a given situation whereas q is more general although may not be so easily

achieved in practice. Fitzgerald and Thomas (2007) derived the following consistency condition on the variation of q with β, under the assumptions of point absorber theory:

$$\frac{1}{2\pi}\int_0^{2\pi} q(\beta)\,\mathrm{d}\beta = 1 \tag{3.165}$$

for a fixed wave number, k_0. Whilst neither point absorber theory nor optimised individual power take-off characteristics is used in the present work, it will be instructive to form the following *consistency constant* c, by analogy with (3.165):

$$c = \frac{1}{2\pi}\int_0^{2\pi} \bar{q}(\beta)\,\mathrm{d}\beta. \tag{3.166}$$

Thus, when $c = 1$, the $\bar{q}$-factor obeys the consistency condition given above.

Chapter 4

Numerical implementation

4.1 Introduction

In this chapter, we provide some details relating to the manner in which the interaction theory of Chapter 3 has been used to produce numerical results. Firstly, the principal equations are interpreted in a format that allows direct inclusion into computer code (Section 4.2). One aspect of this process is the choice of certain scaling factors, examined in Section 4.3, that may affect the accuracy of the resulting solution. The software and hardware used in the computation of results for this thesis is subsequently described in Section 4.4. Two key parameters that govern how close the computed results are to the exact solution are analysed in Section 4.5. Finally in Section 4.6, commercial code based on an alternative method will be used to verify the accuracy of the current approach with respect to linear wave theory.

4.2 Coding

The vectors and matrices contained in equations (3.131) and (3.152) contain elements corresponding to each of the possible vertical and angular modes. Theoretically, these form infinite series and so in order to perform practical computations, they must be truncated to include only a finite number of entries. Hence let M_{T} and N_{T} be integers such that all z-modes m and θ-modes n satisfy

$$0 \leq m \leq M_{\mathrm{T}}, \tag{4.1}$$

$$-N_{\mathrm{T}} \leq n \leq N_{\mathrm{T}}. \tag{4.2}$$

Details regarding the choice of these constants will be given in Section 4.5. Solution of the system may then proceed for regular waves of different progressive wave numbers k_0 and wave headings β. Given k_0, the progressive dispersion relation (3.27) determines the angular frequency of the system ω. Note that although angular frequency could equivalently be used as the independent variable, wave number is chosen for this purpose throughout this thesis to reflect the strong spatial dependence of array interactions. The angular frequency then sets the values of the evanescent wave numbers through the relation (3.28). However, since the latter is a transcendental equation with no analytic solutions, a numerical method must be used. Hence, a local optimisation algorithm was applied to find the zeros of the following function:

$$f(k) = -\omega^2 - gk \tan kd. \tag{4.3}$$

Since there exists a solution for each branch of the tangent function, the initial values $k = [\pi/2 + \pi(q-1) + 0.1]/d$ (for $q = 1, \ldots, M_{\mathrm{T}}$) were taken to ensure that all the necessary evanescent wave numbers were captured.

Vectors that contain an element corresponding to each z-mode m were constructed using the following map to determine the row or column index of the entry in that mode:

$$m \mapsto m + 1, \qquad m = 0, \ldots, M_{\mathrm{T}}. \tag{4.4}$$

Similarly entries corresponding to each θ-mode n were mapped to an index by

$$n \mapsto n + N_{\mathrm{T}} + 1, \qquad n = -N_{\mathrm{T}}, \ldots, 0, \ldots, N_{\mathrm{T}}. \tag{4.5}$$

Where vectors (such as $\mathbf{A}$) contain elements that each correspond to a pair (m, n) of mode numbers (z-mode m and θ-mode n), the following map was adopted to determine their index in the vector:

$$(m, n) \mapsto (N_{\mathrm{T}} + n)M_{\mathrm{T}} + m + 1, \qquad \begin{array}{l} m = 0, \ldots, M_{\mathrm{T}}, \\ n = -N_{\mathrm{T}}, \ldots, 0, \ldots, N_{\mathrm{T}}. \end{array} \tag{4.6}$$

Note that this defines a bijective correspondence between mode pairs and vector indices when M_{T} and N_{T} are fixed. For matrices such as $\mathbf{B}$, where the entries within each dimension correspond to their own set of modes, the maps (4.4-4.6) were applied

separately in the rows and columns.

Most of the quantities needed to construct the relevant matrices and vectors are composed of standard functions, widely available to modern programming languages. Nonetheless, care must be taken with the evaluation of Bessel functions, since inaccuracies may be found for large order or argument. No warming messages to this effect were encountered at a representative range values in the present implementation, however. Derivatives of Bessel functions with respect to argument, may easily be computed using identities (9.6.28) and (9.1.30) of Abramowitz and Stegun (1964).

Before performing array calculations, the isolated body diffraction behaviour (governed by equations (3.83) and (3.84)) must be determined. This system may be viewed as a pair of matrix equations for every incident wave of z-mode m and θ-mode n. Fixing the incident mode numbers, we thus form column vectors $\mathbf{C}_m^n$ containing the elements C_{sm}^n, $\mathbf{D}_m^n$ containing D_{qm}^n and $\mathbf{U}_m^n$ containing U_{sm}^n. We define the matrix E^n, consisting of elements E_{sq}^n with s increasing along its rows and q increasing along its columns. Similarly, G^n is defined to be the matrix containing the entries G_{qs}^n, with q and s increasing along its rows and columns respectively. Substituting (3.84) into (3.83), we get the following solutions for the unknown vectors $\mathbf{C}_m^n$ and $\mathbf{D}_m^n$:

$$\mathbf{C}_m^n = \left[\mathsf{I} + \mathsf{E}^n\mathsf{G}^n\right]^{-1}\mathbf{U}_m^n, \tag{4.7}$$

$$\mathbf{D}_m^n = \mathsf{G}^n\mathbf{C}_m^n. \tag{4.8}$$

Here the superscript $^{-1}$ denotes the matrix inverse. This solution procedure may then be repeated in the numerical implementation for each incident wave mode pair (m, n).

For radiated waves, the equations that need to be solved are (3.106) and (3.107). As before, we define the column vectors $\mathbf{C}^{\mathrm{R}}$ containing the elements C_s^{R}, $\mathbf{D}^{\mathrm{R}}$ containing D_q^{R}, $\mathbf{Q}^{\mathrm{R}}$ containing Q_s^{R} and $\mathbf{S}^{\mathrm{R}}$ containing S_q^{R}. Then with E^0 and G^0 as above, (3.107) may be substituted into (3.106) to get the following solutions for $\mathbf{C}^{\mathrm{R}}$ and $\mathbf{D}^{\mathrm{R}}$:

$$\mathbf{C}^{\mathrm{R}} = \left[\mathsf{I} + \mathsf{E}^0\mathsf{G}^0\right]^{-1}\left[\mathbf{Q}^{\mathrm{R}} - \mathsf{E}^0\mathbf{S}^{\mathrm{R}}\right], \tag{4.9}$$

$$\mathbf{D}^{\mathrm{R}} = \mathbf{S}^{\mathrm{R}} + \mathsf{G}^0\mathbf{C}^{\mathrm{R}}. \tag{4.10}$$

After the coefficients in these matrices have been determined, the matrices B_j, $\widetilde{\mathsf{B}}_j$ and the vectors $\mathbf{R}_j$, $\widetilde{\mathbf{R}}_j$ may subsequently be formed, using equations (3.133-3.134) and (3.128-3.129), with all entries not explicitly specified taken to be zero. The remaining

necessary quantities may be formed directly from their definitions.

Both equations (3.131) and (3.152) involve the summation of products relating to each body. Where the quantities to be multiplied are scalars, we may write the sum as a matrix product of a row vector and a column vector. Similarly, the sum of products involving matrices and column vectors may equivalently be expressed by concatenating the matrices in a row and the vectors in a column to form one matrix product. This may be performed for each instance of the equations before vertically concatenating them all into a single matrix equation in the same unknown vector. We thus define the block matrix M as

$$\mathsf{M} = \left(\begin{array}{cccc|cccc} & j \longrightarrow & & & & j \longrightarrow & & \\ -\mathsf{I} & & \mathsf{B}_j\mathsf{T}_{ij}^{\mathsf{T}} & & \mathsf{0} & & \mathsf{B}_j\mathsf{T}_{ij}^{\mathsf{T}}\mathbf{R}_i & \\ & \ddots & & & & \ddots & & \downarrow i \\ \mathsf{B}_j\mathsf{T}_{ij}^{\mathsf{T}} & & -\mathsf{I} & & \mathsf{B}_j\mathsf{T}_{ij}^{\mathsf{T}}\mathbf{R}_i & & \mathsf{0} & \\ \hline \mathsf{0} & & \frac{1}{W_j}\left[\mathsf{T}_{ij}\widetilde{\mathsf{B}}_j^{\mathsf{T}}\widetilde{\mathsf{Y}}_j^{\mathrm{D}}\right]^{\mathsf{T}} & & 1 & & \frac{1}{W_j}\mathbf{R}_i^{\mathsf{T}}\mathsf{T}_{ij}\widetilde{\mathsf{B}}_j^{\mathsf{T}}\widetilde{\mathsf{Y}}_j^{\mathrm{D}} & \\ & \ddots & & & & \ddots & & \downarrow i \\ \frac{1}{W_j}\left[\mathsf{T}_{ij}\widetilde{\mathsf{B}}_j^{\mathsf{T}}\widetilde{\mathsf{Y}}_j^{\mathrm{D}}\right]^{\mathsf{T}} & & \mathsf{0} & & \frac{1}{W_j}\mathbf{R}_i^{\mathsf{T}}\mathsf{T}_{ij}\widetilde{\mathsf{B}}_j^{\mathsf{T}}\widetilde{\mathsf{Y}}_j^{\mathrm{D}} & & 1 & \end{array}\right), \tag{4.11}$$

where the vertical and horizontal lines separate four partitions. The off-diagonal expressions in each partition are to be evaluated for each pair of body numbers i and j and arranged adjacent to each other in the order indicated by the arrows. The remaining expressions represent block elements of the same size as their off-diagonal counterparts, to be placed on the diagonal $i = j$.

The unknown vectors of partial waves $\mathbf{A}_i$ and complex motion amplitudes $\widehat{X}_i$ may be formed into a single vector with an instance of each required for every i, ordered in accordance with the arrows:

$$\mathbf{z} = \left(\begin{array}{c} \mathbf{A}_i \\ \hline \widehat{X}_i \end{array}\right) \begin{array}{l} \downarrow i \\ \downarrow i \end{array}. \tag{4.12}$$

Finally the known constant terms in the system of equations may be written as a vector,

with each block element evaluated for every j and concatenated as indicated:

$$\mathbf{h} = \begin{pmatrix} -\mathbf{B}_j \mathbf{a}_j \\ -\frac{1}{W_j} \mathbf{a}_j^{\mathsf{T}} \widetilde{\mathbf{B}}_j^{\mathsf{T}} \widetilde{\mathbf{Y}}_j^{\mathrm{D}} \end{pmatrix} \begin{matrix} \downarrow j \\ \downarrow j \end{matrix} . \tag{4.13}$$

The upper partitions of (4.11) and (4.13) are derived from equation (3.131) whereas the lower ones relate to (3.152). The left-hand partitions of (4.11) and the upper partition of (4.12) are associated with unknown partial wave coefficients whereas the remaining sections in those quantities relate to unknown motion amplitudes. The whole system may therefore be written compactly as a matrix equation in the unknown $\mathbf{z}$:

$$\mathsf{M}\mathbf{z} = \mathbf{h}, \tag{4.14}$$

which has solution

$$\mathbf{z} = \mathsf{M}^{-1}\mathbf{h}. \tag{4.15}$$

From this, motion amplitudes and partial wave coefficients may be recovered using (4.12), thus solving the problem.

An alternative solution strategy (and one that is employed by the boundary element code WAMIT®[1]) is to solve various generalised hydrodynamic problems before calculating motion responses. This involves the determination of excitation forces by considering all bodies fixed under wave incidence. Furthermore, added mass and damping matrices are calculated by forcing the oscillation of each body in turn whilst the rest are held fixed. Only then are the equations of motion used (Falnes, 2002). The application of this approach to the eigenfunction expansion method would require inversion of a slightly smaller matrix than M, but also involve a greater total of matrix multiplication operations. It only represents a real advantage if the same array calculations are to be repeated with different power take-off characteristics.

All the results will be presented in non-dimensional form in the remainder of this thesis. Table 4.1 shows the physical quantity and the dimensional value by which they will be divided to become non-dimensional. The phases will be calculated relative to the free surface of the ambient incident wave at the centre of the device to which the quantity relates. Hence in this case, the argument of ζ must be subtracted from the relevant quantity Ξ instead. The power will be non-dimensionalised by that contained

[1] WAMIT is a registered trademark of WAMIT, Inc.

in an ambient incident wave of equal breadth to the device (Falnes, 2002).

Variable	Symbol	Non-dimensionalising quantity
Wave number	k	$\frac{1}{2a}$
Heave amplitude	X	H
Phase	$\arg(\Xi_j)$	$\arg(\zeta(x_j, y_j))$
Force	F	$\rho g \pi a^2 H$
Added mass	m_{33}	$\rho \pi a^2 (d-h)$
Added damping	b_{33}	$\omega \rho \pi a^2 (d-h)$
Spring constant	δ	$\rho a^3 \omega^2$
Damping constant	γ	$\rho a^3 \omega$
Power	P	$2aJ,\ J = \frac{\rho g^2 H^2 \tanh k_0 d}{4\omega} \left(1 + \frac{2k_0 d}{\sinh 2k_0 d}\right)$
Velocity potential	ϕ	$\frac{gH}{\omega}$

Table 4.1: Quantities used to non-dimensionalise variables.

4.3 Matrix scaling

Kagemoto and Yue (1986) stated that due to the disparate asymptotic nature of the Bessel functions, they should be normalised with respect to both order and argument in any numerical scheme. Siddorn and Eatock Taylor (2008) performed this by dividing all radially-dependent functions by their value at a representative distance, $r = a$. The same scaling has been employed in the present implementation, leading to the functions of device radius a in the denominators of partial wave vectors (3.110), (3.111) and (3.112).

The benefits of scaling may be understood better in terms if the condition number κ of the matrix $\mathbf{M}$ used for solving the system. This is defined as

$$\kappa(\mathbf{M}) = \frac{\|\mathbf{M}^{-1}\|}{\|\mathbf{M}\|}, \tag{4.16}$$

where $\|\,.\,\|$ is some matrix norm (Isaacson and Keller, 1994, Ch. 2, (16)). If κ is large, the matrix is said to be ill-conditioned and small errors in the numerical representation of $\mathbf{M}$ lead to large errors in the solution. If κ becomes large enough that errors in the results are likely, a warning message may be displayed by the programming environment. This occurred in a preliminary implementation where partial waves were scaled in accordance with Yilmaz (1998). Such messages were found to be more frequent for large truncation constants M_T and N_T, at lower wave numbers and at closer spacings. However, none

were displayed when the scaling of the partial waves described in Section 3.5.1 was adopted.

Suitable scaling for the purposes of accurate matrix inversion is in general hard to determine (Golub and Van Loan, 1983), although there exist strategies that may be of assistance. Stewart (1998) suggests the use of *row equilibration* where rows are scaled so that their magnitude is equal to one with respect to some norm. When the coefficients in the scattering equations (3.131) are directly entered into the matrix $\mathbf{M}$ (4.11), the associated rows have maximum modulus one (a supremum norm of one). However, if the same is applied to the equations of motion (3.152), some of the coefficients (particularly W_j) may be larger than this value by one or two orders of magnitude. Thus, row equilibration was achieved by dividing the whole equation by W_j before insertion into $\mathbf{M}$, as shown in (4.11). Along with current choice of radiation problem scaling, this resulted in a reasonable improvement in matrix condition number, especially for low wave numbers.

4.4 Software and hardware

Unless otherwise stated, all the results presented in the remainder of this thesis were generated using code written and executed in the MATLAB®[1] (Version R2008a) programming language and computing environment. Other members of the MATLAB Product Family were used to supplement functionality, namely the Optimization Toolbox™[2] (Version 4.0) and the Genetic Algorithm and Direct Search Toolbox™[3] (Version 2.3). The function `fsolve` contained in the former was used to find solutions to equation (4.3) whilst the latter provided the basis for the optimisations described in Chapter 7.

Many of the quantities that are required in the computations are one-, two- or three-dimensional numeric arrays. MATLAB code is capable of faster execution if these definitions are *vectorized*. Hence, `for` loops that sequentially provide array indices to expressions were replaced with a single input array of the appropriate dimension. Furthermore, all the solutions to matrix equations were found using the function `mldivide` instead of the `inv` function. This performs matrix left division by Gaussian elimination with partial pivoting rather than separately forming the inverse, which

[1] MATLAB is a registered trademark of The MathWorks, Inc.
[2] Optimization Toolbox is a trademark of The MathWorks, Inc.
[3] Genetic Algorithm and Direct Search Toolbox is a trademark of The MathWorks, Inc.

is considered superior in terms of execution time and numerical accuracy. Here, the underlying computations are carried out by the Linear Algebra Package (LAPACK)[1] driver routine `ZGESV` (The MathWorks, Inc., 2010c).

A standalone application was formed from the source code using the MATLAB Compiler™[2] (Version 4.8) with the Intel®[3] C++ Compiler (Version 10.1.015) and the Intel Math Kernel Library (Version 10.0.1.014). These were used instead of the default settings in order to rectify a recognised performance bug (The MathWorks, Inc., 2010b) and speed up computation times. The compiled code was then executed on a compute farm consisting of Sun®[4] machines with 2.50GHz x86 64-bit Intel Core™2 Quad[5] processors, running Scientific Linux[6] (Version 5.3). The Condor®[7] (Version 7.0.1) job management system was used to submit the compiled code for execution on one of the three slots per machine, each having access to 2.64GB of random access memory. Execution of the code was therefore undertaken in a computing environment whose specification is (at the time of writing) approximately equivalent to that of a high-end desktop computer.

Under the above conditions, a typical array of five devices as described in Section 4.5 leads to a total computation time of approximately 2.7s per wave number and heading. One of the most time-consuming parts of the computations is the solution of the matrix equation (4.14). For comparison with the MATLAB code, the time taken to compute a solution to the same equation was measured using the `ZGESV` routine in the Fortran 90[8] programming language. Here, the Intel Fortran Compiler (Version 10.1.015) was employed with the same library as before. The difference in execution times between the two implementations was found not to be significant, with the code written in Fortran running marginally faster. For reasons of convenience and compatibility, the MATLAB code was therefore used in all subsequent calculations.

The efficiency of the solution may be further explored by noting that the Gaussian elimination process requires $\mathcal{O}(n^3)$ multiplication and division operations to solve an

[1] See E. Anderson, Z. Bai, C. Bischof, S. Blackford, J. Demmel, J. Dongarra, J. Du Croz, A. Greenbaum, S. Hammarling, A. McKenney and D. Sorensen. LAPACK Users' Guide, Third Edition, 1999.

[2] MATLAB Compiler is a trademark of The MathWorks, Inc.

[3] Intel is a registered trademark of Intel Corp.

[4] Sun is a registered trademark of Sun Microsystems, Inc.

[5] Intel Core2 Quad is a trademark of Intel Corp.

[6] Scientific Linux was put together by Fermilab, CERN and other laboratories and universities

[7] Condor is a registered trademark of the University of Wisconsin-Madison

[8] Fortran was originally developed by International Business Machines Corp.

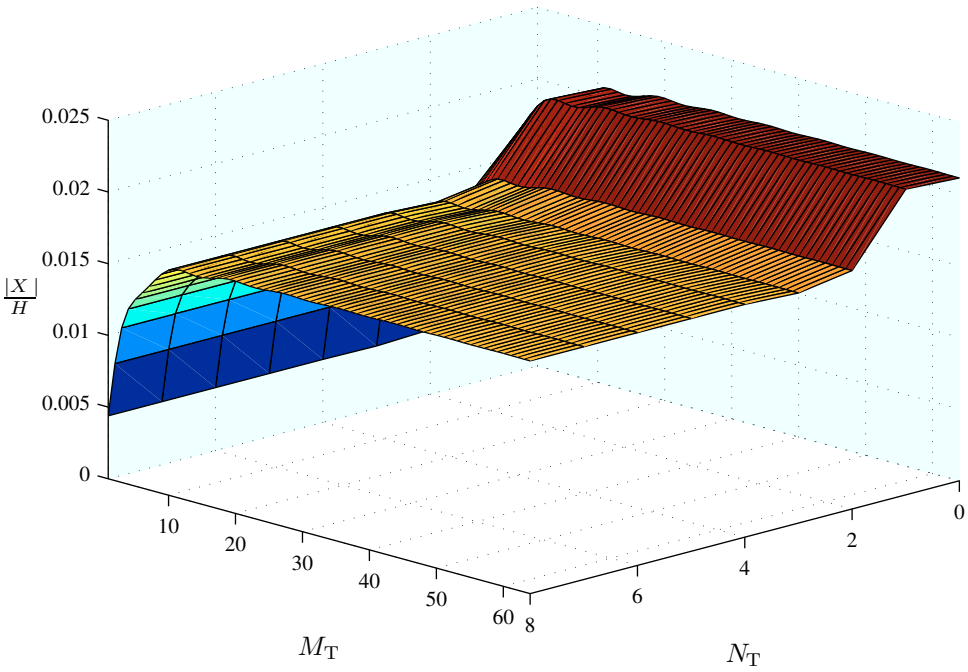

Figure 4.1: Convergence with respect to truncation constants. Variation of non-dimensional heave amplitude $|X|/H$ with M_{T} and N_{T} for the Array Convergence Test Case.

$n \times n$ system of equations (Isaacson and Keller, 1994, Ch. 2, (9)). In the present scheme, this involves the matrix $\mathbf{M}$ in equation (4.11) which is of size $N[(M_{\mathrm{T}}+1)(2N_{\mathrm{T}}+1)+1]$ and so computation times increase approximately with the cube of the number of bodies, and the vertical and angular truncation constants.

4.5 Convergence

As mentioned in Section 4.2, the infinite series of modes in the vertical and angular directions must be truncated to a finite number by constants M_{T} and N_{T} in accordance with equations (4.1-4.2). Increasing the number of modes employed means that the theoretical solution is approached and thus a greater level of accuracy achieved. However, as discussed in Section 4.4, the computation time of the code is adversely affected by such an increase. Hence we must find an acceptable compromise between accuracy and efficiency.

Figure 4.1 shows the variation of one representative solution parameter, the non-dimensional heave amplitude $|X|/H$ of a converter, as the truncation constants M_{T} and N_{T} are varied. This case involves an array of five identical devices, each of radius equal to their draught in water of depth eight times that length. The power

take-off coefficients are also identical to each other and are reactively-tuned (see Section 5.3) to a non-dimensional wave number of $2ak_0 = 0.8$. The device centres are separated by twelve radii and are in a linear formation. Only the motion of the central element will be considered here. Ambient incident waves then approach in a direction perpendicular to the line of devices, with non-dimensional wave number $2ak_0 = 4$. This will be referred to as the 'Array Convergence Test Case', for the purposes of further analysis.

The task at hand is complicated by the fact that the convergence must be considered with respect to two parameters simultaneously. However, as can be seen in Figure 4.1, it appears that the convergence behaviour with respect to M_{T} is independent of that with respect to N_{T}. Hence, we may reasonably perform convergence analysis with respect to each parameter separately, whilst holding the other at some constant value.

We shall adopt a simple approach to the convergence problem suggested by Garrett (1971). This involves setting the desired level of accuracy for the solution and then finding the minimum number of vertical and angular modes needed to achieve it. One measure of the solution is plotted against M_{T}^{-1} with N_{T} held fixed. The converged result is then estimated by extrapolation of the points to the line $M_{\mathrm{T}}^{-1} = 0$. The value of M_{T}^{-1} for which all higher mode numbers lead to a result that is within the desired level of accuracy of the converged solution is then interpolated. The corresponding truncation constant M_{T} must then be rounded upwards to form an integer, and the whole process repeated in a similar manner to find N_{T}. We take $|X|/H$ as the indicator of the solution here and aim for an accuracy of 0.5% with respect to truncation in each direction. Note that this process does not provide information as to the accuracy of computed values with respect to the true solution. Rather, correspondence is shown with the converged solution here, whilst evidence that the true solution has indeed been attained is contained in Section 4.6.

Tests were carried out for a range of different device geometries and masses; power take-off characteristics; water depths; incident wave characteristics; and configurations, separations and sizes of array. Different elements were analysed and the mode number in the direction not being considered held fixed at different values. The number of modes needed in either spatial direction proved to be independent (to within less than one mode number) of the fixed mode in the other direction, even where the extrapolated solutions differed. This appears to confirm similar observations that were made from

Figure 4.1.

No angular variation ($N_{\mathrm{T}} = 0$) was required for the case of an isolated device due to its radial symmetry. This is broken for an array of any size greater than one, although the number of modes required remains small. As regards the vertical modes, no such absolute rule seem to apply.

We now proceed to apply the convergence analysis and determine the final truncation constants using one of the worst cases studied; the Array Convergence Test Case, which required the highest truncation constants of all cases tested in both modes. The analysis is performed on M_{T} and N_{T} separately, holding the other truncation constant as $N_{\mathrm{T}} = 4$ and $M_{\mathrm{T}} = 32$ respectively. In both cases, undulations occur about the general trend line which have the potential to bias the extrapolated results. This is due to the oscillatory nature of the trigonometric and Bessel functions representing the velocity potential as their arguments incorporate increasing eigenvalues (see, for example, (3.72)). However, a smoother, more representative relationship was achieved by using every eighth mode in the vertical direction and every second one in the angular direction.

The results are plotted in Figures 4.2 and 4.3, where crosses denote results from the simulations, solid lines the smoothed trend and long dashed lines the direction of extrapolation. One horizontal dashed line represents the estimate of the converged value $\widehat{X}_e$, with those above and below it denoting the range of values that are within 0.5% of this figure. The vertical dashed lines mark the value of the truncation constant which ensures the necessary accuracy. This analysis leads to the values $M_{\mathrm{T}} = 32.18$ and $N_{\mathrm{T}} = 3.33$ which, once rounded in positive direction, consistute the truncation constants that will be used in the rest of this thesis: $M_{\mathrm{T}} = 33$, $N_{\mathrm{T}} = 4$.

Note that the rounding process has increased the accuracy of the solution, particularly in the angular direction. In fact, all mode numbers greater than or equal to the final truncation constants lead to an error of less than or equal to 0.37% and 0.02% with respect to the extrapolated values for M_{T} and N_{T}. Hence assuming independence of the two convergence processes, the total error associated with both constants is in fact less than the level desired for each one seperately. With the stated truncation constants, we therefore estimate the overall accuracy to be 0.5%.

Although linear extrapolation provides a reasonable estimate for the converged result, other more accurate methods may be more appropriate if a greater level of confidence is required. Figure 4.2 exhibits a downward overall curve as M_{T}^{-1} decreases.

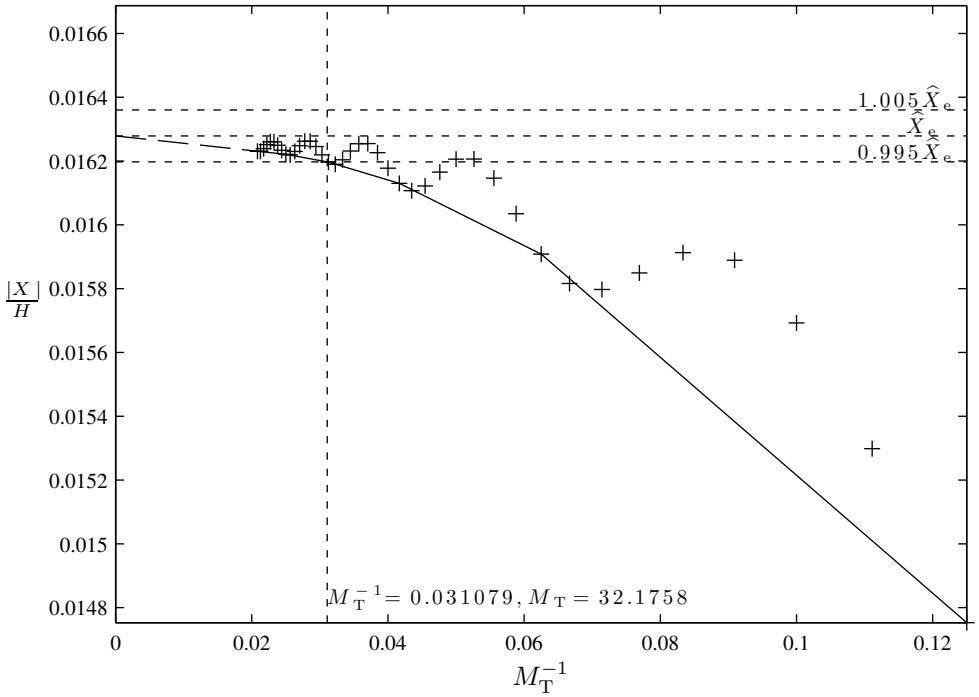

Figure 4.2: Convergence with respect to vertical truncation constant. Variation of non-dimensional heave amplitude $|X|/H$ with M_{T} for the Array Convergence Test Case ($N_{\mathrm{T}} = 4$).

This suggests that linear extrapolation may be overestimating the converged result. If that were to be the case, inspection of the figure suggests that the truncation constant $M_{\mathrm{T}} = 33$ may in fact lead to a more accurate result than the aforementioned estimate implies.

In summary the truncation constants $M_{\mathrm{T}} = 33$ and $N_{\mathrm{T}} = 4$ will be used from here on unless otherwise stated. Specifically, more angular modes will be required to determine the velocity potential at all points in the domain. Also, the calculation of hydrodynamic coefficients to determine power take-off characteristics will be performed using more modes. This is relatively inexpensive in terms of overall computation time because it only needs to be determined once for each geometry.

4.6 Verification

In this section, we wish to verify that the eigenfunction expansion method, as implemented in this thesis, converges to the true linear wave theory solution. Results will be compared against those produced by an alternative method that should converge

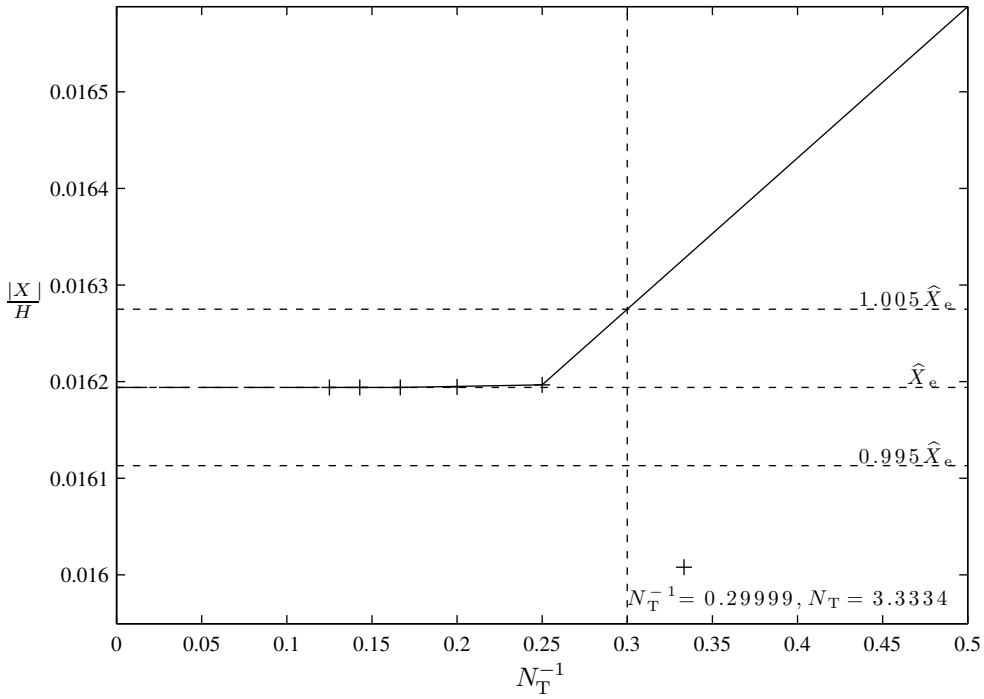

Figure 4.3: Convergence with respect to angular truncation constant. Variation of non-dimensional heave amplitude $|X|/H$ with N_T for the Array Convergence Test Case ($M_T = 32$).

on the same solution. These are computed here using the commercial boundary element code WAMIT (Version 6.03). Its application involves the discretisation of the surface of the body into elements whose size is controlled by the input parameter `PANEL_SIZE`. Decreasing the size of these panels increases the accuracy of the solution but requires more computation time. Therefore, convergence analysis was performed on this parameter in a similar way to as in the previous section with the inverse of the truncation constants. Using the Array Convergence Test Case, the parameter value `PANEL_SIZE` $= 0.317a$ was found to be required in order to reach the same 0.5% accuracy level as was acheived by the eigenfunction expansion with the chosen truncation constants.

With the respective parameters ensuring the same estimated level of accuracy, calculations were performed using the eigenfunction expansion method and the WAMIT code on the Array Convergence Test Case for a range of wave numbers. Figure 4.4 shows the non-dimensional heave amplitude of the previously specified device, derived from both approaches. This demonstrates the excellent correspondence between results from the two methods that is typical of all other cases studied. Similar comparisons were

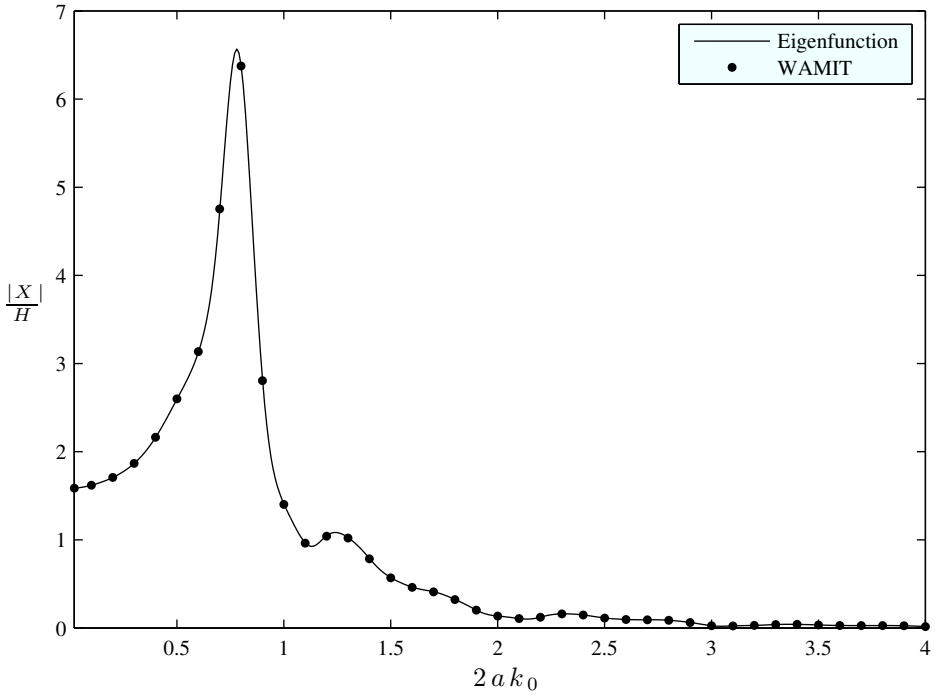

Figure 4.4: Comparison of eigenfunction expansion and WAMIT results. Variation of non-dimensional heave amplitude $|X|/H$ with non-dimensional ambient incident wave number $2ak_0$ for the Array Convergence Test Case.

performed by Cruz et al. (2009) who found some minor discrepancies between the two methods. Although these differences were not significant, they are likely to be derived from the boundary element code rather than the geometry-specific semi-analytical method presented here.

Preliminary calculations have also been made as to the relative efficiency of the two approaches. These were all performed on a Dell®[1] machine with a 3.40GHz x86 32-bit Intel Pentium® 4[2] processor and 2.00GB of random access memory, running the Microsoft®[3] Windows®[4] XP Professional operating system. The settings used for the WAMIT simulations included use of the higher-order panel method (`ILOWHI=1`, see WAMIT, Inc. (2000, Ch. 6)). Both simulations were repeated ten times, with heave motions and forces calculated and saved to disk on each iteration. The mean computation times for one wave number are shown in Table 4.2 along with the mean time to compute results for an additional wave number using the same array.

[1] Dell is a registered trademark of Dell, Inc.
[2] Intel Pentium 4 is a registered trademark of Intel Corp.
[3] Microsoft is a registered trademark of Microsoft Corp.
[4] Windows is a registered trademark of Microsoft Corp.

Method	First period (s)	Subsequent periods (s)
WAMIT	376.9	255.7
Eigenfunction	44.8	44.8

Table 4.2: Comparison of eigenfunction expansion and WAMIT efficiencies. Time taken to compute the solution for the Array Convergence Test Case.

Note that since WAMIT uses some information from the calculation of the first period in the subsequent computations, the latter may be computed more efficiently (see Table 4.2). For the eigenfunction expansion method, however, there are no such savings. Nonetheless, the method of eigenfunctions is still the fastest for initial and subsequent periods by a considerable margin. This gives an indication of the relative performance of the two methods, although it is acknowledged that there may be other settings and cases for which the efficiency of WAMIT is improved.

Chapter 5

Isolated device analysis

5.1 Introduction

In order to inform the analysis of devices within an array, we examine here the behaviour of an isolated device. Analogy with the simplified case of a second-order linear oscillator is made in Section 5.2, which provides insight into the motion of a device in water. Section 5.3 contains some established results concerning the optimal values for power take-off coefficients, along with some less well-known alternative expressions. One particular device is specified by a set of parameters in Section 5.4 and the resulting behaviour analysed. Each of these parameters is then varied in Section 5.5 in order to determine their influence on the results.

5.2 Second-order linear oscillators

As we shall see by the end of this section, the equation of motion governing the heave displacement of a converter at any given frequency is exactly that of a second-order linear differential equation with constant coefficients. This is the system which we briefly consider here, further details being available in standard texts such as Patel (1989, §8). Suppose then we have the following equation for some oscillating variable $X^{(t)}$:

$$c_{\mathrm{m}}\ddot{X}^{(t)} + c_{\mathrm{d}}\dot{X}^{(t)} + c_{\mathrm{s}}X^{(t)} = F^{(t)}, \qquad c_{\mathrm{m}},\, c_{\mathrm{d}},\, c_{\mathrm{s}} \in \mathbb{R}. \tag{5.1}$$

Here c_m, c_d and c_s are the constant coefficients and the forcing term is time-harmonic with angular frequency ω:

$$F^{(t)} = \mathrm{Re}\{F\mathrm{e}^{-\mathrm{i}\omega t}\}, \qquad F \in \mathbb{C}. \tag{5.2}$$

The solution to the homogeneous equation, with the right-hand side of (5.1) set to zero, is transient whenever damping is non-zero. This is is certainly the case in the present application, so further solutions must be sought to represent the steady state. As a particular integral we thus attempt a solution of the form

$$X^{(t)} = \mathrm{Re}\{X\mathrm{e}^{-\mathrm{i}\omega t}\}, \qquad X \in \mathbb{C}. \tag{5.3}$$

Substituting (5.2) and (5.3) into (5.1), we find that

$$X = \frac{F}{(c_\mathrm{s} - c_\mathrm{m}\omega^2) - \mathrm{i}(c_\mathrm{d}\omega)}. \tag{5.4}$$

This may be written in terms of a modulus and phase, so that the time-dependent form becomes

$$X^{(t)} = \mathrm{Re}\left\{A\mathrm{e}^{\mathrm{i}\psi}F\mathrm{e}^{-\mathrm{i}\omega t}\right\}, \tag{5.5}$$

where

$$A(\omega) = \frac{1}{\sqrt{(c_\mathrm{s} - c_\mathrm{m}\omega^2)^2 + (c_\mathrm{d}\omega)^2}}, \tag{5.6}$$

$$\psi(\omega) = \arctan\left\{\frac{c_\mathrm{d}\omega}{c_\mathrm{s} - c_\mathrm{m}\omega^2}\right\}. \tag{5.7}$$

Here, A is the amplitude of oscillations in $X^{(t)}$ relative to (divided by the amplitude of) the forcing term $F^{(t)}$ and ψ is the phase of $X^{(t)}$, relative to (minus the phase of) the same variable. Figure 5.1 illustrates the variation of these quantities with angular frequency ω in a typical case.

By differentiation of (5.6), the peak amplitude of $X^{(t)}$ and its first and second time-derivatives occur at the following frequencies respectively:

$$\omega_X^\mathrm{p} = \left\{0,\ \sqrt{\frac{c_\mathrm{s}}{c_\mathrm{m}} - \frac{c_\mathrm{d}^2}{2c_\mathrm{m}^2}}\right\}, \qquad \omega_{X'}^\mathrm{p} = \{1,\ -\mathrm{i}\}\sqrt{\frac{c_\mathrm{s}}{c_\mathrm{m}}}, \qquad \omega_{X''}^\mathrm{p} = \sqrt{\frac{c_\mathrm{s}}{c_\mathrm{m} - \frac{c_\mathrm{d}^2}{2c_\mathrm{s}}}}, \tag{5.8}$$

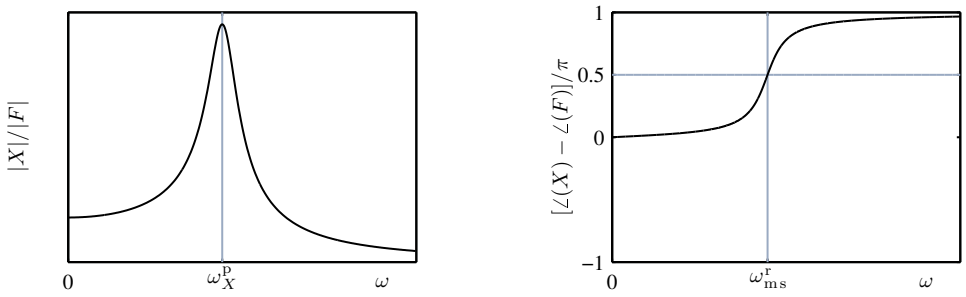

(a) Amplitude

(b) Phase

Figure 5.1: Illustration of second-order linear oscillator behaviour. Response relative to the force applied as a function of angular frequency.

provided that they are real. We also define resonant frequencies for the undamped and full systems respectively as

$$\omega_{\mathrm{ms}}^{\mathrm{r}} = \sqrt{\frac{c_{\mathrm{s}}}{c_{\mathrm{m}}}}, \qquad \omega_{\mathrm{mds}}^{\mathrm{r}} = \sqrt{\frac{c_{\mathrm{s}}}{c_{\mathrm{m}}} - \frac{c_{\mathrm{d}}^2}{4c_{\mathrm{m}}^2}}. \tag{5.9}$$

Note that amplitude A is equal to $1/c_{\mathrm{s}}$ and zero in the low and high frequency limits respectively, peaking at $\omega = \omega_X^{\mathrm{p}}$ with a value of $\left[\frac{c_{\mathrm{d}}}{c_{\mathrm{m}}}\sqrt{c_{\mathrm{s}}c_{\mathrm{m}} - \frac{c_{\mathrm{d}}^2}{4}}\right]^{-1}$. On the other hand, the phase ψ smoothly transitions from zero to π as the frequency increases, reaching a value of $\pi/2$ at $\omega = \omega_{\mathrm{ms}}^{\mathrm{r}}$.

We shall now re-examine the equation of motion for a single wave energy device floating in the water. Since no other bodies are in the vicinity, the hydrodynamic force F^{H} in (3.153) reduces to the sum of the ambient incident wave force F^{A} and the radiation force from the body itself F^{R}. Letting the buoyancy spring constant be written as $w_3 = \rho g \pi a^2$, the equation of motion (3.146) becomes

$$(M + m_{33})X'' + (\gamma + b_{33})X' + (\delta + w_3)X = F^{\mathrm{A}}. \tag{5.10}$$

This is the time-independent form of (5.1) with

$$c_{\mathrm{m}}(\omega) = M + m_{33}(\omega), \tag{5.11}$$

$$c_{\mathrm{d}}(\omega) = \gamma + b_{33}(\omega), \tag{5.12}$$

$$c_{\mathrm{s}} = \delta + w_3, \tag{5.13}$$

$$F(\omega) = F^{\mathrm{A}}(\omega). \tag{5.14}$$

Therefore, the analysis contained in this section applies to an isolated device at each frequency separately. However, because the quantities (5.11-5.14) are not all constant over angular frequency, the shape of the curves in Figure 5.1 will be deformed from those predicted from this second-order linear oscillator theory with constant coefficients. Hence these plots will retain their essential character whilst peak frequencies will not necessarily be exactly as given in (5.8).

5.3 Tuning

Before analysing isolated device behaviour, we shall give a brief account of how the power take-off characteristics will be specified. One way to determine the associated coefficients is using a method known as *tuning*. Generator characteristics are sought such that the device produces the most power possible at a given *tuning frequency* ω_0. This is often chosen to coincide with the peak of a spectrum describing the distribution of wave energy over the incident frequency range at the potential device location. However, it should be noted that the effectiveness of the technique depends on the sea-state under consideration, with narrow-banded spectra likely to be most amenable to this treatment. Most of the following analysis originates from Falnes (2002, §3.5), although other derivations exist which essentially lead to the same results.

An alternative way of writing the equation of motion (5.10) is to group together the intrinsic effects of the body and hydrodynamics separately from the effects of the generator. We thus define the intrinsic mechanical impedance Z_{M} and the impedance of the generator Z_{G} as

$$Z_{\mathrm{M}}(\omega) = -\mathrm{i}\omega[M + m_{33}(\omega)] + b_{33}(\omega) + \frac{\mathrm{i}}{\omega} w_3, \tag{5.15}$$

$$Z_{\mathrm{G}}(\omega) = \gamma + \frac{\mathrm{i}}{\omega}\delta, \tag{5.16}$$

which may be evaluated at each angular frequency ω. This quantity is henceforth fixed at the tuning frequency $\omega = \omega_0$. Since the generator impedance has been chosen in such a way as the applied force has the same time dependence as the ambient incident wave force, equation (5.10) then defines a harmonic matching between these functions of time:

$$(Z_{\mathrm{M}} + Z_{\mathrm{G}})X' = F^{\mathrm{A}}. \tag{5.17}$$

The impedances may be conveniently split into real and imaginary parts as follows:

$$Z_{\mathrm{M}} = Z_{\mathrm{MR}} + \mathrm{i}Z_{\mathrm{MI}}, \qquad Z_{\mathrm{MR}},\, Z_{\mathrm{MI}} \in \mathbb{R}, \tag{5.18}$$

$$Z_{\mathrm{G}} = Z_{\mathrm{GR}} + \mathrm{i}Z_{\mathrm{GI}}, \qquad Z_{\mathrm{GR}},\, Z_{\mathrm{GI}} \in \mathbb{R}. \tag{5.19}$$

Rearranging (5.17) for X' and substituting this into an expression for the power (3.161) along with definitions (5.18-5.19) gives

$$P = \frac{Z_{\mathrm{GR}}|F^{\mathrm{A}}|^2/2}{(Z_{\mathrm{MR}} + Z_{\mathrm{GR}})^2 + (Z_{\mathrm{MI}} + Z_{\mathrm{GI}})^2}. \tag{5.20}$$

A local maximum in the power value with respect to Z_{GR} must satisfy the condition that its partial derivative with respect to that variable is zero. This occurs when

$$Z_{\mathrm{GR}} = \sqrt{Z_{\mathrm{MR}}^2 + (Z_{\mathrm{MI}} + Z_{\mathrm{GI}})^2}, \tag{5.21}$$

which is known as the *optimum amplitude condition.* Inserting this expression into (5.20), we obtain after some manipulation

$$P = \frac{|F^{\mathrm{A}}|^2/4}{Z_{\mathrm{MR}} + \sqrt{Z_{\mathrm{MR}}^2 + (Z_{\mathrm{MI}} + Z_{\mathrm{GI}})^2}}. \tag{5.22}$$

This may be maximised by minimising the denominator, whence inspection reveals that

$$Z_{\mathrm{GI}} = -Z_{\mathrm{MI}}. \tag{5.23}$$

This is the *optimum phase condition* since it implies that the coefficient of X' in (5.17) is real and so the ambient incident wave force F^{A} is in phase with velocity X'. Hence the energy transferred to the system per unit time is maximised and we have resonance, that is $\omega_{\mathrm{ms}}^{\mathrm{r}}$ coincides with ω_0. If the amplitude condition (5.21) is used in conjunction with (5.23), it simplifies to

$$Z_{\mathrm{GR}} = Z_{\mathrm{MR}}. \tag{5.24}$$

From the last two conditions, we see that the optimum impedance of the generator is equal to the complex conjugate of the intrinsic mechanical impedance:

$$Z_{\mathrm{G}}^{\mathrm{opt}} = Z_{\mathrm{M}}^{*}. \tag{5.25}$$

This is a particularly simple way of writing the aforementioned optimum conditions and defines what is often referred to as *optimal control*.

Real (damping) tuning. The power can be partially optimised at the angular frequency ω_0 by choosing only the damping constant of the power take-off to be non-zero. In the original notation of (5.15-5.16), equation (5.21) then leads to

$$\delta_{\mathrm{d}} = 0, \tag{5.26}$$

$$\gamma_{\mathrm{d}} = \sqrt{[b_{33}(\omega_0)]^2 + \omega_0^2 \left[M + m_{33}(\omega_0) - \frac{w_3}{\omega_0^2}\right]^2}. \tag{5.27}$$

This is known as *real tuning* because only the real part of the generator impedance is utilised.

Reactive (damping-spring) tuning. Reactive tuning ensures that both conditions (5.23) and (5.24) are satisfied at the tuning frequency. That is to say both resistive and reactive (real and imaginary) parts of the impedances in (5.25) are matched. The spring and damping constants therefore satisfy

$$\delta_{\mathrm{ds}} = \omega_0^2[M + m_{33}(\omega_0)] - w_3, \tag{5.28}$$

$$\gamma_{\mathrm{ds}} = b_{33}(\omega_0). \tag{5.29}$$

Mass-damping tuning. In addition to spring and damping terms, it is also possible for the power take-off arrangement to simulate an additional mass ϵ (Price, 2009). This results in the following force on the body due to the generator, in place of (3.145):

$$F^{\mathrm{G}} = -\delta X - \gamma X' - \epsilon X''. \tag{5.30}$$

The aforementioned tuning methods do not involve such a contribution and hence for them, $\epsilon = \epsilon_{\mathrm{ds}} = \epsilon_{\mathrm{d}} = 0$.

Here, power take-off coefficients are again chosen such that the impedance of the generator is the is complex conjugate of the intrinsic impedance at ω_0 (5.25). However, there now exists some choice as to the combination of spring and mass coefficients which will be used to cancel the imaginary part of the intrinsic impedance. One option is to use the mass coefficient alone to do this, with the spring coefficient set to zero. We then

have

$$\delta_{\mathrm{md}} = 0, \tag{5.31}$$

$$\gamma_{\mathrm{md}} = b_{33}(\omega_0), \tag{5.32}$$

$$\epsilon_{\mathrm{md}} = -\left[M + m_{33}(\omega_0) - \frac{w_3}{\omega_0^2}\right]. \tag{5.33}$$

The resulting equation of motion (5.17) is identical to that for reactive tuning at the tuning frequency $\omega = \omega_0$. Hence the behaviour of the two systems is the same here, although different at other frequencies.

Mass-damping-spring tuning. If all three power take-off coefficients are used, we may do more than simply ensuring that (5.25) is satisfied at the tuning frequency. We may in fact choose the mass coefficient so that the physical mass M does not contribute to the imaginary part of the total impedance at any frequency. This occurs if

$$\delta_{\mathrm{mds}} = -w_3, \tag{5.34}$$

$$\gamma_{\mathrm{mds}} = b_{33}(\omega_0), \tag{5.35}$$

$$\epsilon_{\mathrm{mds}} = -[M + m_{33}(\omega_0)]. \tag{5.36}$$

The resulting system behaves the same as for reactive and mass-damping tuning at the tuning frequency. However, as will be seen in Section 5.5.4, it performs better at other frequencies because the velocity is more closely in phase with the ambient incident wave force.

5.4 Device Test Case

In this section, we shall analyse the behaviour of a single device in detail. The specification for the device examined here will be referred to as the 'Device Test Case.' The converter is chosen to be of radius a equal to the draught $b = d - h$ and the water to have depth eight times this length $d = 8a$, in order to represent the behaviour of a 10m wide buoy in a water depth of 40m. Reactive tuning will be used here as it is the most common method of fully optimising power production at one frequency. Choosing the tuning wave number to be $2ak_0 = 0.8$ means that peak power production of the full-scale device will coincide with the peak period (T_{p}) of a JONSWAP spectrum (Hasselmann

et al., 1973) of mean period 5.9s (McIver et al., 1996a). Note that the energy period T_e of such a spectrum could equally have been chosen as the tuning parameter (Venugopal and Smith, 2007b).

A summary of the specifications for the Device Test Case is given in Table 5.1. Values for generator constants are provided later in Table 5.3. Devices with this specification are used exclusively in the remainder of this thesis, along with real-tuned devices of the same geometry.

Property	Specification
Radius	a_T
Draught	$b_T = a_T$
Depth	$d_T = 8a_T$
PTO spring	$\delta = \delta_{ds}$
PTO damping	$\gamma = \gamma_{ds}$
PTO mass	$\epsilon = 0$

Table 5.1: Specification of the Device Test Case.

Convergence analysis was performed in Section 4.5 on the Array Convergence Test Case, consisting of five devices of the type specified by the Device Test Case. This resulted in a vertical truncation constant of $M_T = 33$ being required for an estimated accuracy of 0.5% in heave amplitudes. Here, the radial symmetry of the problem means that we need no angular modes ($N_T = 0$). These truncation constants were therefore used in the rest of this chapter unless otherwise stated.

5.4.1 Heave motion

Figure 5.2 shows added mass, added damping, ambient incident wave force amplitude and phase, all as functions of non-dimensionalised incident wave number $2ak_0$. It is evident that these quantities are not constant over frequency and thus will affect the shape of the heave amplitude plot throughout the range. The magnitude of the ambient incident wave force decreases monotonically from a finite positive value to zero as the wave number is increased from zero towards infinity. Over the same range, the force is initially in phase with the free surface at the centre point of the device, eventually lagging the incident wave at the leading edge by $\pi/4$ (Garrett, 1971). The added mass coefficient tends to a finite positive value in the high frequency limit whereas the added damping tends to zero.

The amplitude and phase of the heave motion are plotted in Figure 5.3. The

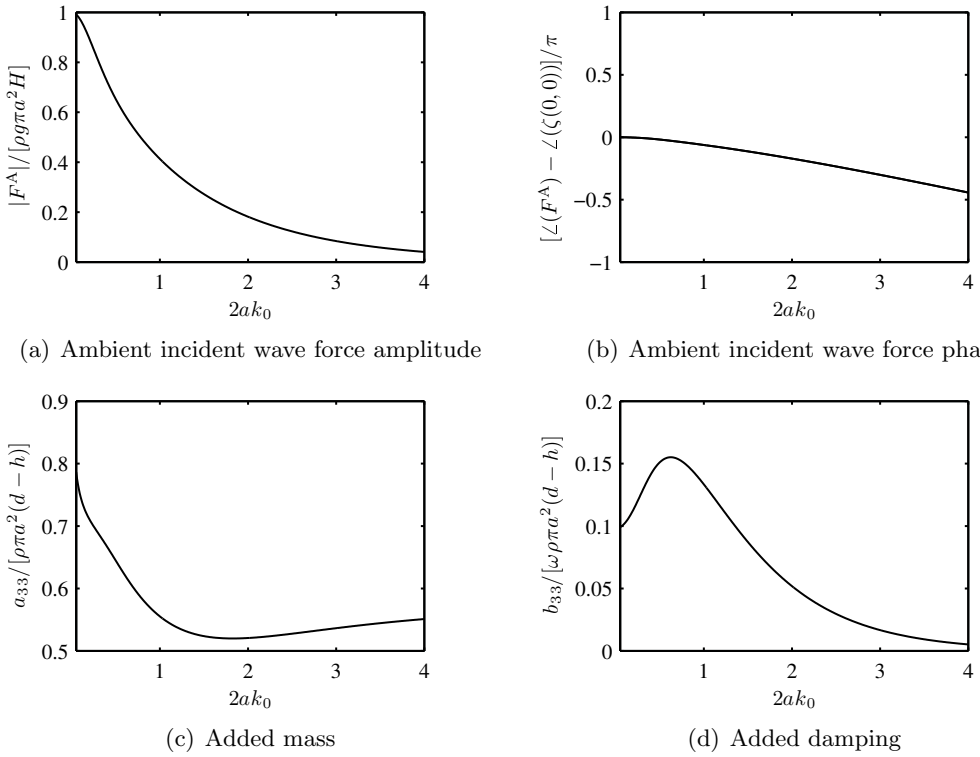

(a) Ambient incident wave force amplitude

(b) Ambient incident wave force phase

(c) Added mass

(d) Added damping

Figure 5.2: Decomposition of hydrodynamic force acting on an isolated device. Variation with wave number for the Device Test Case.

amplitude decays from a positive finite value to zero as the frequency increases, with a peak occurring in the given range. In relation to increasing frequency, the phase is initially equal to that of free surface before increasing sharply and then slowly decreasing for higher frequencies.

The heave motion plots bear a strong resemblance to those derived for a second-order linear oscillator with constant coefficients (Figure 5.1). In comparison, the plots here appear stretched in the horizontal direction due to the use of wave number as independent variable rather than angular frequency (related to each other by the progressive dispersion relation). Also, the shape of the curves is distorted by the variation with frequency of the coefficients on the left hand side of (5.10). Finally, in Figure 5.1 the dependent variable was presented relative to the ambient incident wave force, whereas here they are relative to the free surface elevation at the centre of the device. Hence the present graphs are the composition of functions that transform the free surface elevation to the ambient incident wave force and the ambient incident wave force to heave motion. This explains why both heave amplitude and phase curves

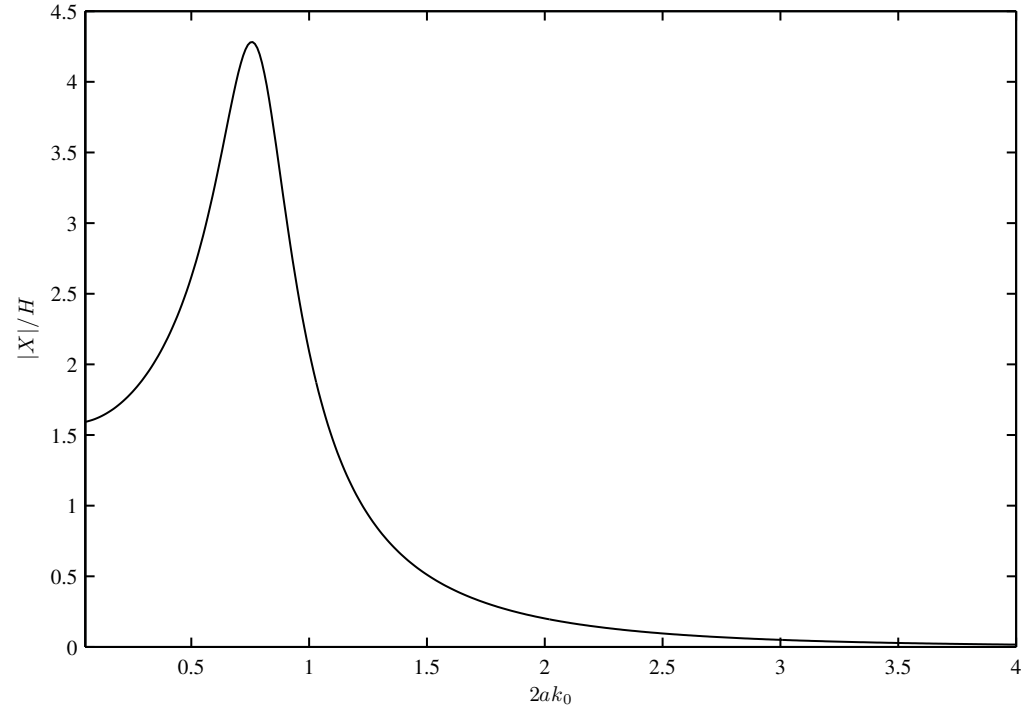

(a) Amplitude

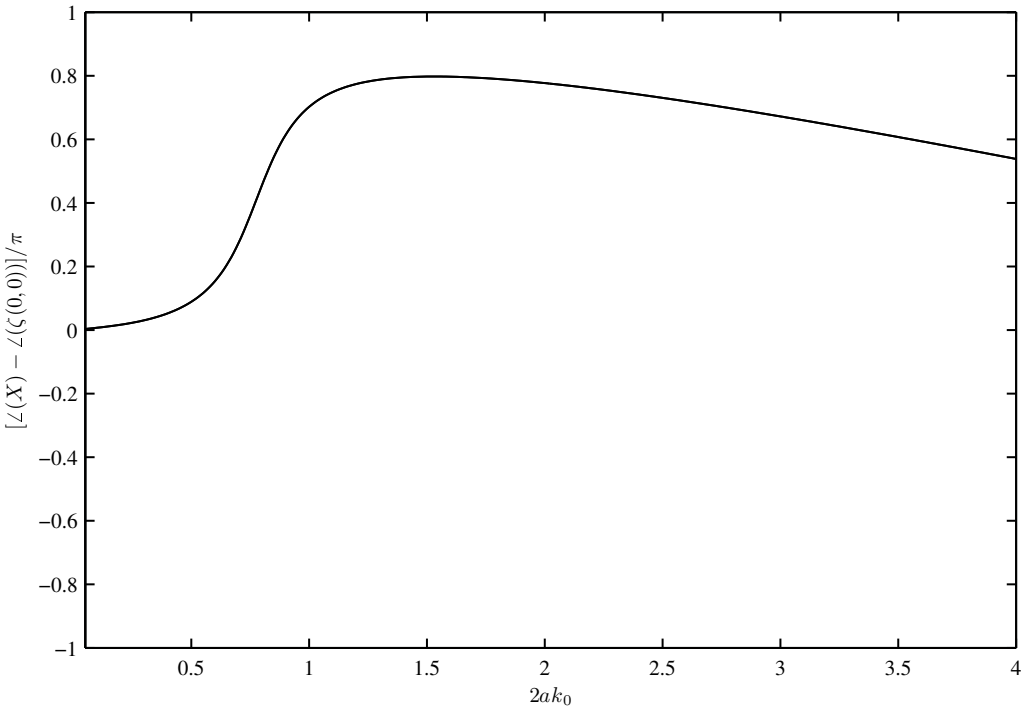

(b) Phase

Figure 5.3: Heave response of an isolated device. Variation with wave number for the Device Test Case.

have a gentle downward inclination as $2ak_0$ increases.

If the coefficients on the left hand side of (5.10) were constant, the peak in heave amplitude would occur at $\omega = \omega_X^{\mathrm{p}}$ defined by (5.8). This is close to the undamped resonant frequency $\omega_{\mathrm{ms}}^{\mathrm{r}}$ for the magnitude of coefficients under consideration here. However the differentiation required to find such a peak cannot be performed analytically here, since the frequency dependence is not explicit in the added mass, added damping and ambient incident wave force coefficients. In practice however, if these are almost constant near the tuning frequency, the expressions given for the peaks do hold approximately. Also, since the tuning frequency ω_0 satisfies the resonance condition (5.23), it coincides with the undamped resonant frequency $\omega_{\mathrm{ms}}^{\mathrm{r}}$. Hence, the peak in heave amplitude is close to the tuning wave number $2ak_0 = 0.8$. It should be noted that the values of heave amplitude attained at resonance are unlikely to be as large as those predicted here due to the presence of nonlinearities such as viscous forces. See Section 8.5 for a more thorough discussion on this topic in relation to arrays.

Velocity and acceleration plots are largely the same in form as those for the heave displacement with the present device specification. However, since the time-derivative induces a pre-factor of $-\mathrm{i}\omega$, they both pass through the origin and the location of the peaks is slightly different.

5.4.2 Decomposition of forces

Figure 5.4(a) shows the amplitude of the forces acting on the device. The ambient incident wave force has already been discussed in the previous section. The buoyancy and generator spring forces are proportional to heave displacement so the amplitude plots follow that of the displacement amplitude (Figure 5.3(a)). The remaining forces are proportional to heave velocity, acceleration or combinations of the two, so take a similar shape to that of displacement but attain the value zero for long waves. Note that in the low frequency limit, the problem becomes static and the total force on the body is zero.

The relative phases of the same forces are shown in Figure 5.4(b). The buoyancy force opposes the displacement, which gives rise to a phase difference of π between the two plots. The total force is in phase with acceleration which is also out of phase with displacement, so shares its curve with the buoyancy force. The generator spring force,

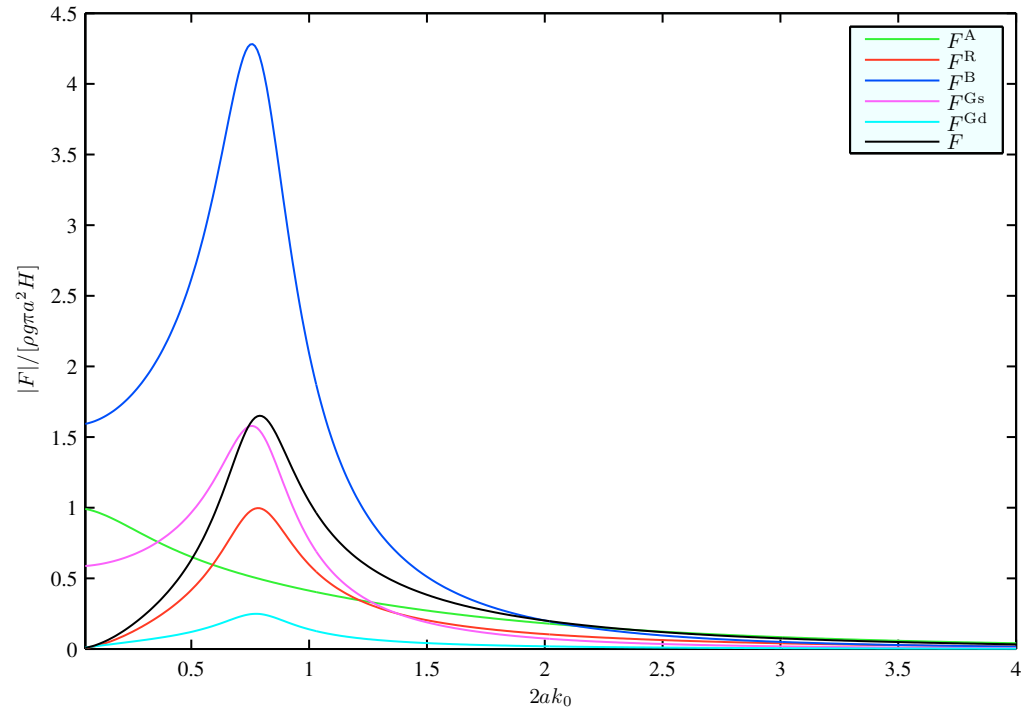

(a) Amplitude

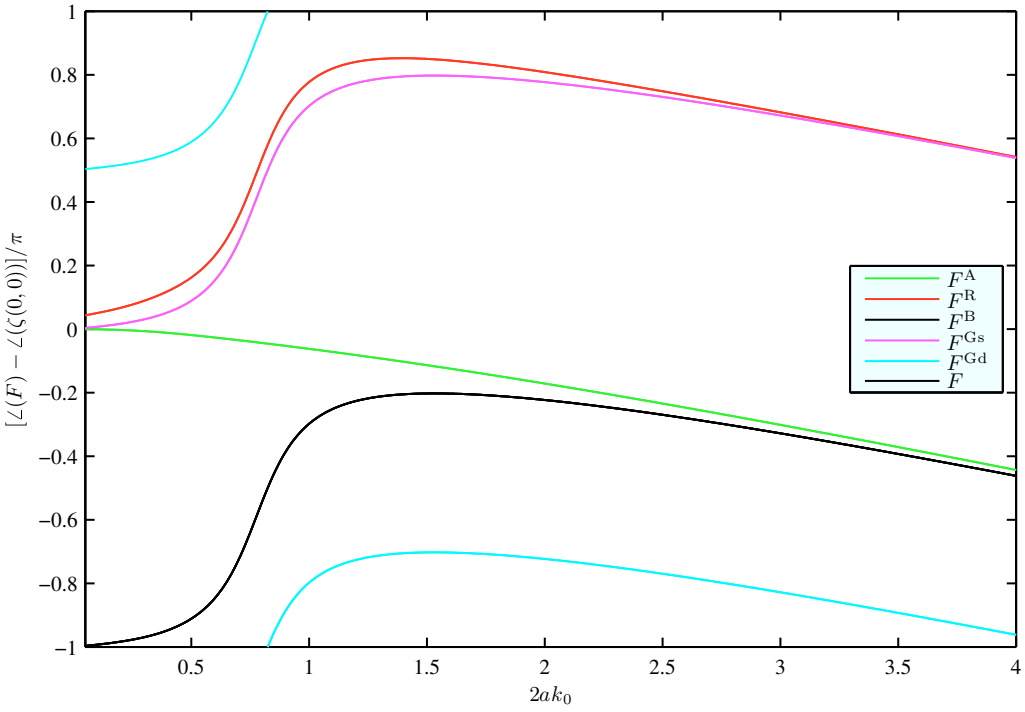

(b) Phase

Figure 5.4: Decomposition of total force acting on an isolated device. Variation with wave number for the Device Test Case. Forces: Ambient (F^{A}), Radiation (F^{R}), Buoyancy (F^{B}), Generator spring (F^{Gs}), Generator damper (F^{Gd}), Total (F).

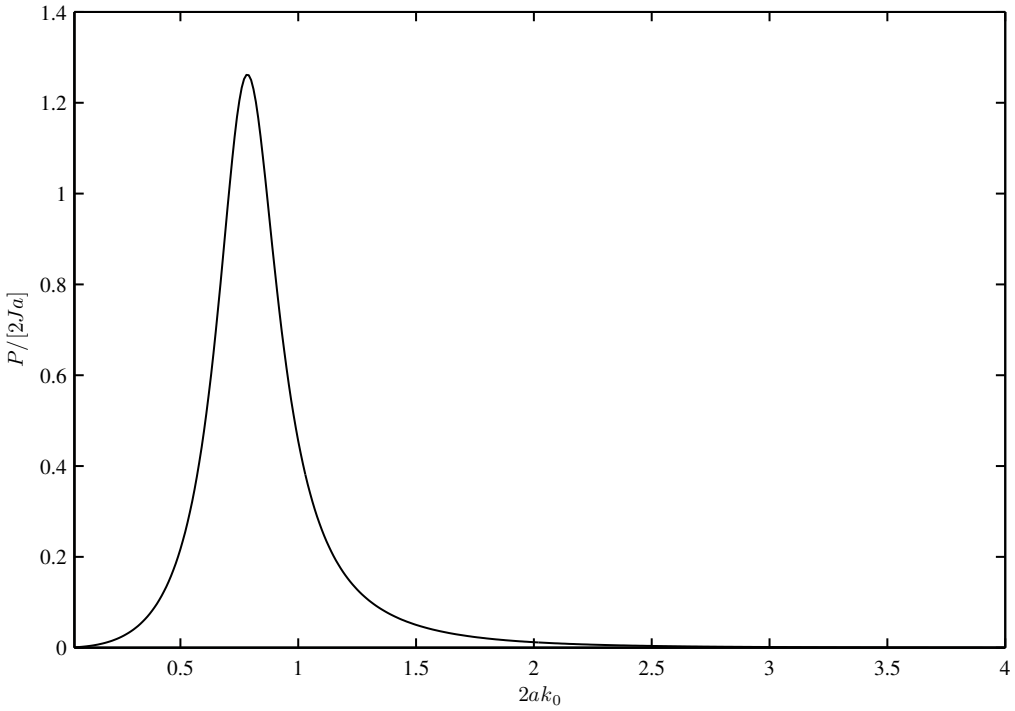

Figure 5.5: Power absorbed by an isolated device. Variation with wave number for the Device Test Case.

however, is in phase with the displacement due to the negative spring constant used here (see Table 5.3). The generator damping force has a phase difference of $\pi/2$ to this since it is out of phase with velocity. The radiation force has components out of phase with acceleration and velocity so the curve sits between generator spring and damping forces, tending to the former at higher wave numbers as the added damping decays.

5.4.3 Power

Power production from the device is shown in Figure 5.5. Since this is proportional to the square of velocity, we have a similar shaped curve to that of the heave amplitude (Figure 5.3(a)), with a peak in the range but producing no power in the low frequency limit.

We have seen in Section 5.3 that reactive tuning has ensured that power is at a maximum with respect to the choice of generator constants at the tuning frequency. However, this does not necessarily ensure that P is maximum with respect to ω at this point. In fact the peak in power occurs at the peak in velocity, which may be altered from the predicted value given by $\omega_{X'}^{\mathrm{p}} = \omega_{\mathrm{ms}}^{\mathrm{r}} = \omega_0$ of (5.8) in the same way as

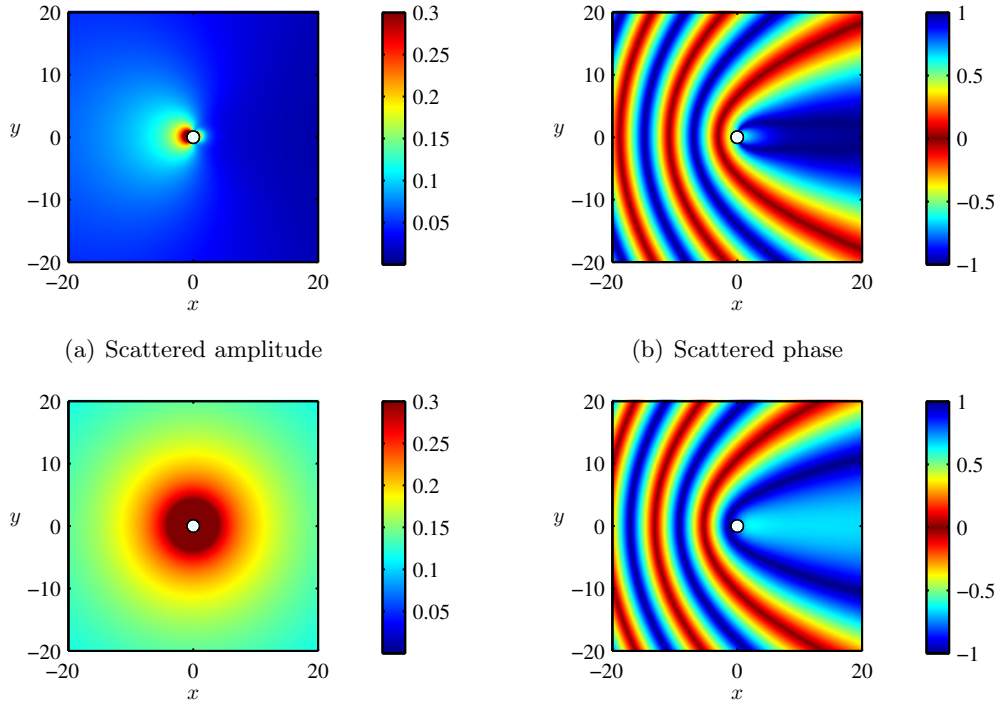

(a) Scattered amplitude

(b) Scattered phase

(c) Radiated amplitude

(d) Radiated phase

Figure 5.6: Decomposition of velocity potential surrounding an isolated device. Scattered and radiated potentials at the free surface for the Device Test Case. Amplitudes normalised by that of the ambient incident wave field (see colour bar). Phases given relative to that of ambient incident wave field, normalised by π (see colour bar).

the displacement is. Scaling the power by $1/(2aJ(\omega))$ for plotting here also moves the position of the peak slightly. Hence we expect and indeed observe the peak to be near but not at tuning frequency $2ak_0 = 0.8$.

5.4.4 Velocity potential in the domain

The velocity potential at points surrounding an isolated device is examined in this section by plotting its amplitude and phase at the free surface, as shown in Figure 5.6. Here the radiated and scattered components are plotted separately. All depict an aerial view of the device as a white circle in the centre, encountering plane waves travelling in the positive x-direction of wave number $2ak_0 = 0.8$. The amplitude and phase are both relative to those of the ambient incident wave.

Both radiated and scattered waves are stronger close to the device because the further away they travel, the greater the area over which a given amount of energy is spread. Radiated waves are generally stronger than scattered waves for this device

near its resonant wave number, due to large associated motion amplitudes. Since the radiation problem in the heave mode is entirely radially symmetric, the same property also applies to the resulting radiated wave amplitude relative to the constant ambient incident wave amplitude. On the other hand, it is apparent that the scattered wave field is strongest along the line of wave incidence. This is because on the sides of the device that are in a cross-wave direction from the centre, the path of the incoming wave is tangential to the body surface and so is not significantly modified by its presence. Conversely on the point that is directly up-wave from the centre, the incident wave field is normal to the body surface giving rise to a strong reflected wave. Down-wave of the device there is also some amplitude modification, although this corresponds to energy being taken out of the total wave field there, as the body shadows the area in its lee. Both phase plots reveal bands of points where incoming and outgoing waves are in or out of phase with each other, as will be explained in detail in Section 7.3.1.

5.5 Variation of device parameters

We now turn our attention to how the parameters in the device specification affect the isolated device behaviour. The Device Test Case (summarised in Table 5.1) will provide the basis for the definition of each device and one of the parameters will then be varied at a time. For easy comparisons between plots, the original set-up will be denoted by a black curve. Additionally, the plot corresponding to the zero value of each quantity is marked as a dashed line.

The number of modes needed for sufficient accuracy was not found to depend heavily on the values of the power take-off coefficients. Hence in Sections 5.5.1-5.5.4, the same truncation constants will be used as were employed in the analysis of the Device Test Case ($M_{\mathrm{T}} = 33$, $N_{\mathrm{T}} = 0$).

However, the variation of convergence rate with geometry meant that individual analysis was needed for each case studied in Section 5.5.5. The angular truncation constant was set at $N_{\mathrm{T}} = 0$, the incident wave number to the worst case of $2ak_0 = 4$ and the procedure outlined in Section 4.5 carried out on each geometry. Because the matrix to be solved is reduced in size by having only one body and no angular modes, it was possible to test every vertical mode from 1 to 256.

The undulations in heave amplitude with mode number appeared to have a period of approximately d/b. Thus, as before, the accuracy of the method was increased by

using only the mode numbers that are whole multiples of such a period. This procedure produces the truncation constants shown in Table 5.2, which were then used to calculate the relevant results.

Note that the increased number of trial modes used here has revealed a better estimate of the converged value. Fewer modes ($M_{\mathrm{T}} = 24$ rather than $M_{\mathrm{T}} = 33$) are in fact necessary to achieve an estimated accuracy in of 0.5% for the Device Test Case ($d/d_{\mathrm{T}} = 1$, $a/a_{\mathrm{T}} = 1$ or $b/b_{\mathrm{T}} = 1$). This was conjectured in Section 4.5, but makes little difference to the results themselves.

d/d_{T}	M_{T}	a/a_{T}	M_{T}	b/b_{T}	M_{T}
2/8=0.25	1	0.25	95	0.25	50
4/8=0.5	28	0.5	46	0.5	39
8/8=1	24	1	24	1	24
16/8=2	72	2	14	2	50
32/8=4	255	4	1	4	85

Table 5.2: Vertical truncation constants for required for different device geometries. Water depth, device radius and draught individually varied whilst all other parameters fixed using the Device Test Case specification.

5.5.1 Generator spring coefficient

In this section, the generator spring constant is varied as a proportion of the modulus of the reactively-tuned value δ_{ds} used in the Device Test Case. This range includes positive, negative and zero values as well as the original quantity $\delta_{\mathrm{ds}} = -|\delta_{\mathrm{ds}}|$. Note that because of the additional buoyancy spring, cancellation of the total spring force occurs for some negative δ (not shown). From the results in Figure 5.7, we may see that all plots qualitatively conform to that of the Device Test Case.

As the spring coefficient increases, the frequency at which the peak in heave amplitude occurs increases, whilst the value attained decreases. This is predicted by the second-order linear oscillator theory of Section 5.2 and accentuated by the effect of the ambient incident wave force included here, which increases heave amplitudes relative to the free surface at lower frequencies.

Increasing the spring coefficient shifts the entire phase plot to higher frequencies. This is consistent with a linear oscillator attaining a phase of $\pi/2$ at the undamped resonant frequency, which increases with the spring constant.

The frequency at which there is a peak in power increases with spring constant.

This too is consistent with linear oscillator theory, since power is proportional to the square of velocity whose plot is altered in a similar way to that of displacement. It is the effect of the ambient incident wave force on the velocity amplitude that means peaks at lower frequencies attain higher power values. For the spring constant $\delta = -|\delta_{\mathrm{ds}}| = \delta_{\mathrm{ds}}$, the peak occurs near the wave number $2ak_0 = 0.8$ to which the power take-off has been reactively-tuned. This is enough to ensure that at that wave number, the reactively-tuned spring constant produces more power than other coefficients.

5.5.2 Generator damping coefficient

Here the generator damping constant is varied as a proportion of the modulus of that used for the Device Test Case. The range considered includes zero but not negative values since these correspond to an overall input of electrical energy into the sea. Note that because the added damping is positive here, the overall damping is never zero, so the amplitudes at resonance are always finite.

Results from these calculations are shown in Figure 5.8. All plots conform qualitatively to that of the Device Test Case except those with higher damping values. For these, the peak in heave amplitude disappears, partly due to the fact that (5.8) no longer predicts a real peak frequency and partly because weak local maxima are obscured by the downward curve of the ambient incident wave force.

The frequency at which the peak in heave amplitude occurs and the value it attains there both decrease with increasing damping, as predicted by the linear second-order oscillator theory.

From Figure 5.8, we can see that all phase plots cross over at a particular wave number. Because the undamped resonant frequency $\omega_{\mathrm{ms}}^{\mathrm{r}}$ in (5.9) is independent of the damping constant used, linear oscillator theory predicts that the associated curves attain the same value at this frequency. They reach a phase of close to but not exactly $\pi/2$, because the effect of the ambient incident wave force is included here. Below the undamped resonant frequency, a higher damping coefficient makes the argument of the arctan function in (5.7) rise more quickly with respect to ω towards positive infinity, making ψ increase faster. However, above that frequency, as the argument descends from negative infinity, a higher damping constant slows down the resulting further increase in ψ.

The peak power production does not vary monotonically with damping constant.

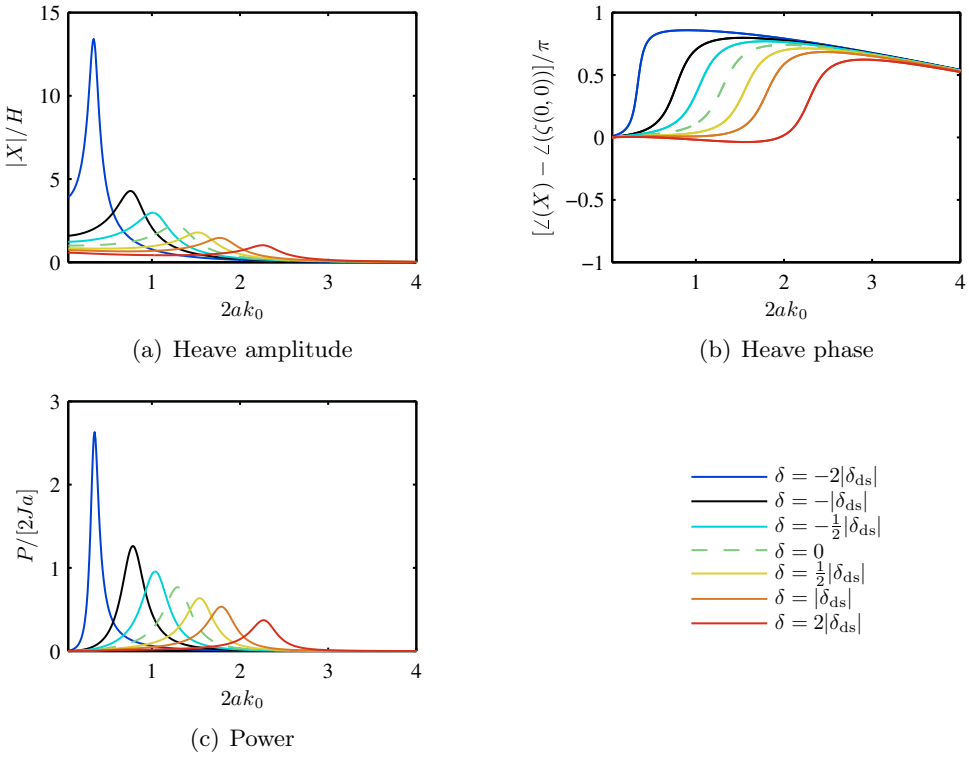

Figure 5.7: Isolated device behaviour with different PTO spring coefficients.

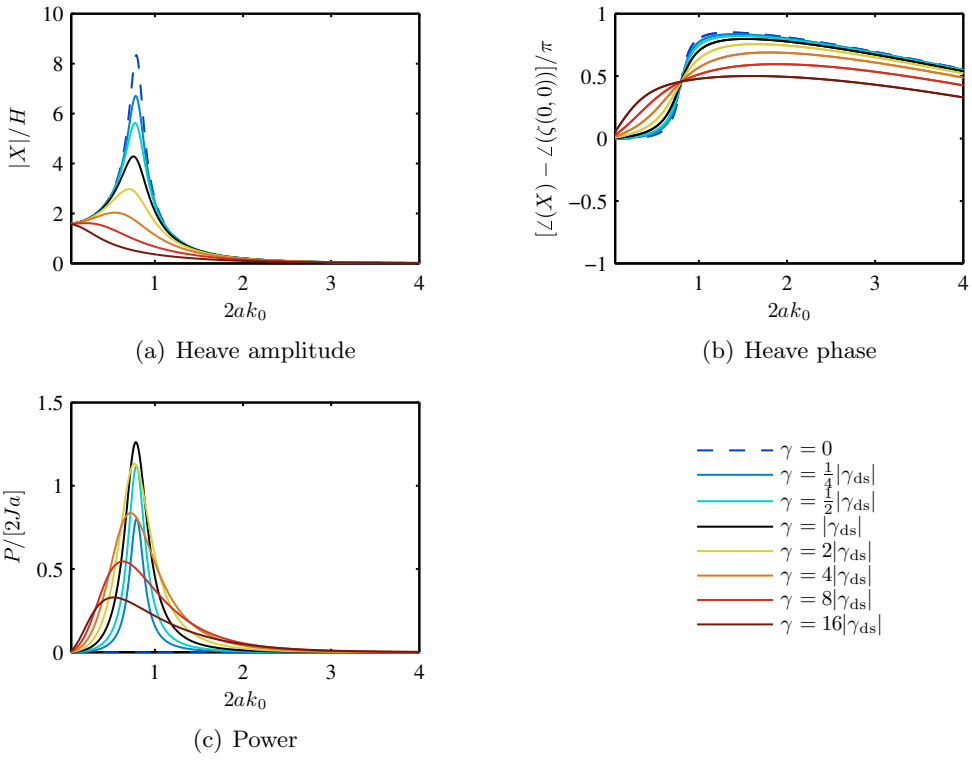

Figure 5.8: Isolated device behaviour with different PTO damping coefficients.

There is an optimum damping coefficient that produces the largest peak, which in this case is the reactively-tuned value γ_{ds}. As intended, this value of damping certainly produces the most power at the tuning wave number of $2ak_0 = 0.8$. Linear oscillator theory predicts that the peak frequency $\omega^{\mathrm{p}}_{X'}$ is independent of γ. However, the ambient incident wave force enhances velocity amplitudes in long waves, shifting broad peaks to lower frequencies. Note that despite providing largest heave amplitude, no power is produced when $\gamma = 0$.

5.5.3 Generator mass coefficient

The generator mass coefficient is now varied as a proportion of the physical mass M, including positive negative and zero values. Note that when $\epsilon = -M$, we only have the added mass functioning as a mass term in the system. The results in Figure 5.9 show all plots conforming qualitatively to that of the Device Test Case.

The frequency at which the peak in heave amplitude occurs gets lower with an increasing generator mass term, as predicted from second-order linear oscillator theory. However, the peak amplitude gets higher with increasing mass, which is accentuated by the low-frequency enhancement of the ambient incident wave force.

In common with the peak in displacement amplitude, the frequency at which the phase difference between the displacement and the ambient incident wave force reaches $\pi/2$ becomes smaller with an increased mass coefficient. The plot also changes more rapidly with respect to frequency for higher mass constants because this speeds up the rate at which the argument in (5.7) changes with ω either side of the damped resonant frequency.

The peak in power occurs at lower frequencies with increasing mass. This agrees with second-order linear oscillator theory that predicts a peak at $\omega = \omega^{\mathrm{p}}_{X'}$ given by (5.8). The same theory predicts that the value attained at the peak is independent of mass. However, this is relative to ambient incident wave force which decreases in amplitude with frequency, so the height of the peak in power decreases with frequency. At the tuning wave number $2ak_0 = 0.8$, the spring and damping constants have been optimised without an additional generator mass term, so it is the curve corresponding to $\epsilon = 0$ that attains the most power here.

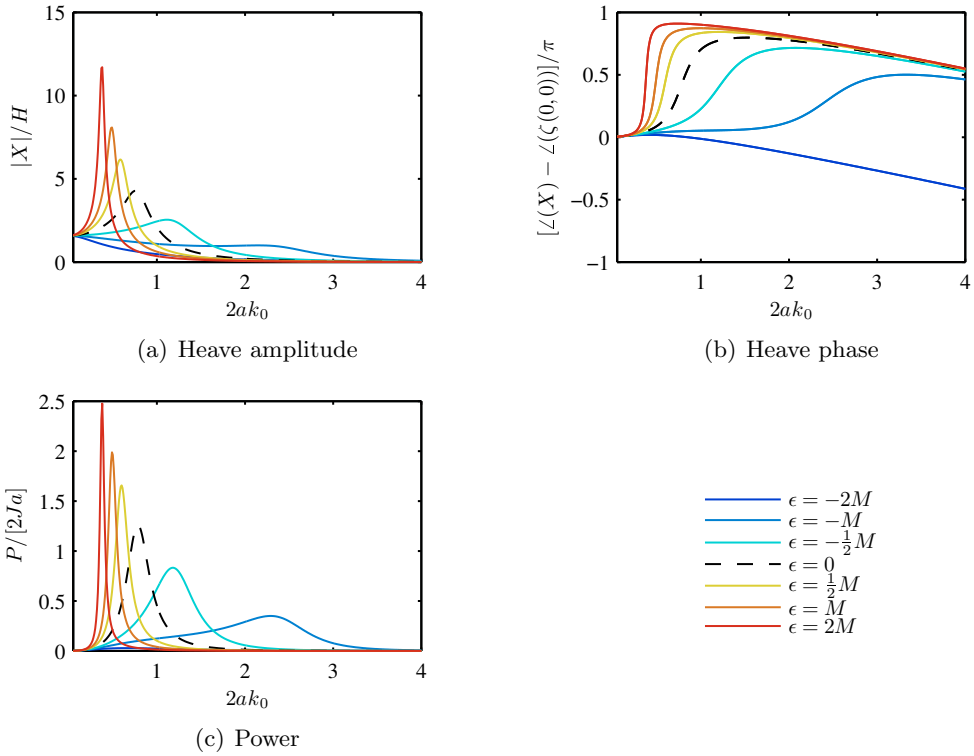

(a) Heave amplitude

(b) Heave phase

(c) Power

Figure 5.9: Isolated device behaviour with different PTO mass coefficients.

5.5.4 Generator tuning regime

In this section we consider different combinations of generator spring, damping and mass coefficients. All of the tuning regimes described in Section 5.3 are examined here, along with one involving no forces from the generator. Power take-off coefficients for each regime are given in Table 5.3 and the associated results shown in Figure 5.10. In general, the characteristics of these plots differ from the Device Test Case in accordance with the trends described in the preceding three sections.

Regime	$\delta/(\rho a^3\omega_0^2)$	$\gamma/(\rho a^3\omega_0)$	$\epsilon/(\rho a^3)$
Real tuning (damping)	0	2.94	0
Reactive tuning (damping-spring)	-2.91	0.468	0
Mass-damping tuning	0	0.468	2.91
Mass-damping-spring tuning	-7.88	0.468	-4.97

Table 5.3: Power take-off coefficients under different tuning regimes.

For tuning regimes where both optimum conditions (5.23-5.24) are satisfied at tuning wave number $2ak_0 = 0.8$ (reactive, mass-damping, mass-damping-spring), the associated power plots all attain the same value there. This wave number is near the peak of each

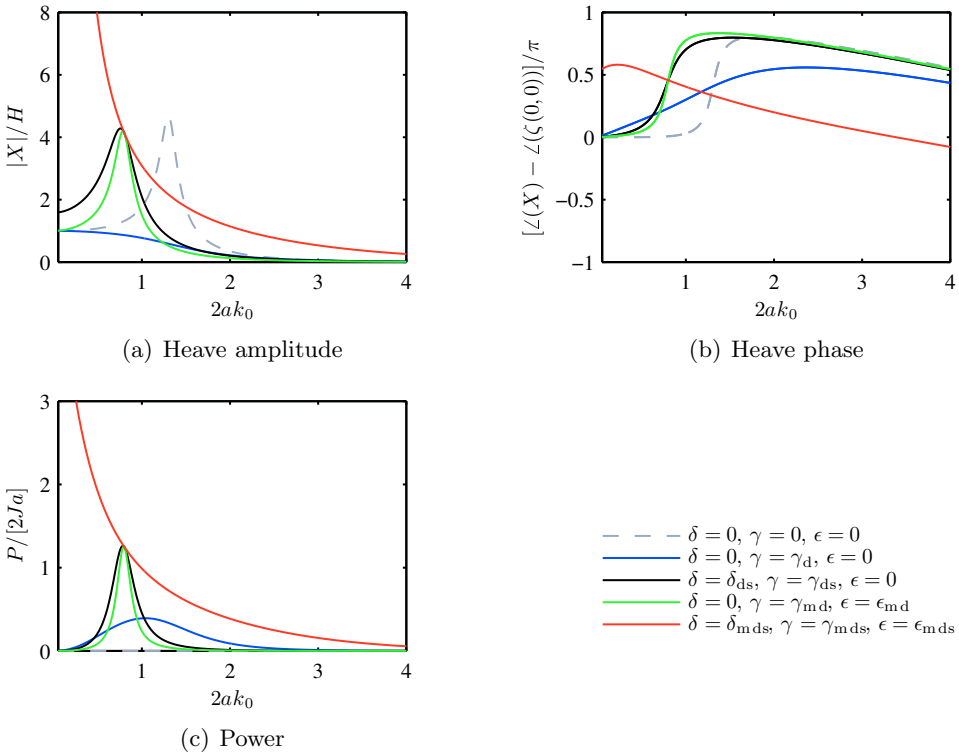

Figure 5.10: Isolated device behaviour with different PTO tuning regimes

plot if it exists, as previously discussed.

No tuning at all was carried out for the case with no power take-off forces, so the peak frequency is not at $2ak_0 = 0.8$. No power is produced for any wave number in this situation because no generator damping coefficient is included.

The real-tuned case does not produce a peak in heave amplitude because it involves a high damping coefficient, as discussed in Section 5.5.2. Note that the power does not reach the optimal value at $2ak_0 = 0.8$ that the other tuning regimes do because the optimum phase condition (5.24) was not used. The associated velocity potential at the free surface in the domain surrounding the device is shown in Figure 5.11. We consider it here because the real tuning regime will be used extensively in subsequent chapters. The scattered potential is not given since it is exactly the same as for the reactively-tuned device (Figure 5.6). Because resonance has not been forced to occur at $2ak_0 = 0.8$, the device motion is diminished and thus the radiated wave field weaker than in the reactively-tuned case.

The regime involving the mass and damping coefficients alone produces curves that are similar in character to those arising from reactive (damping-spring) tuning. This

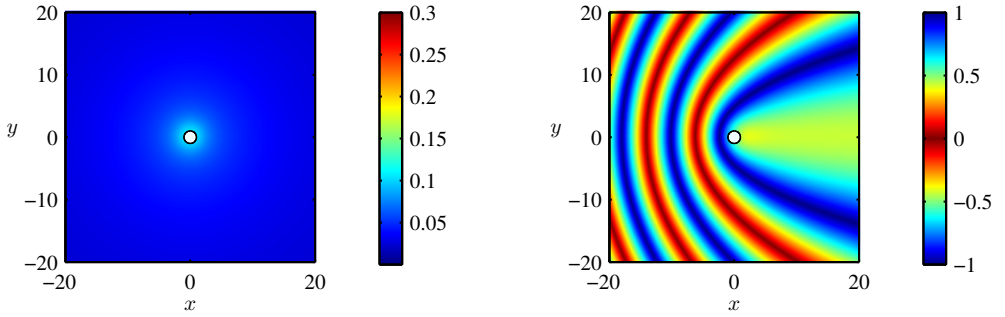

(a) Radiated amplitude

(b) Radiated phase

Figure 5.11: Decomposition of velocity potential surrounding a real-tuned isolated device. Radiated potentials at the free surface for the Device Test Case with real tuning. Amplitude normalised by that of the ambient incident wave field (see colour bar). Phase given relative to that of ambient incident wave field, normalised by π (see colour bar).

behaviour has been analysed in detail in Section 5.4.

There is no peak in the heave amplitude or power plots where all three generator coefficients have been used. This is because the total spring force is zero throughout the range. Hence, from (5.8) there is no real peak in heave amplitude relative to force amplitude and the stationary point in velocity at $\omega = 0$ disappears once the ambient incident wave force amplitude is taken into account. Equation (5.7) predicts that the phase of the heave displacement relative to the ambient incident wave force is $\pi/2$ throughout the frequency range. Once the effect of the ambient incident wave force is accounted for, there is in fact a downward slope from this value with increasing frequency in the phase plot. The shape of the power curve means that this arrangement may capture much more energy than reactive or mass-damping tuning for wave numbers other than at the tuning frequency. In fact this plot resembles that of the theoretical maximum for any device absorbing in heave, which is inversely proportional to wave number (Evans, 1981a, (4.5)).

Although there is no intuitive physical equivalent, negative power take-off coefficients may be nonetheless achievable with appropriate control of the generator. However, this can involve large variations in power flow over one wave period, requiring expensive machinery. Furthermore, significant energy losses can result, reducing efficiency. Thus real tuning is often given serious consideration, as an alternative that does not require negative generator constants despite the associated power production not being optimal. Tuning with all three coefficients produced some very large displacement amplitudes in these results that are clearly not feasible in practice, especially for low wave numbers.

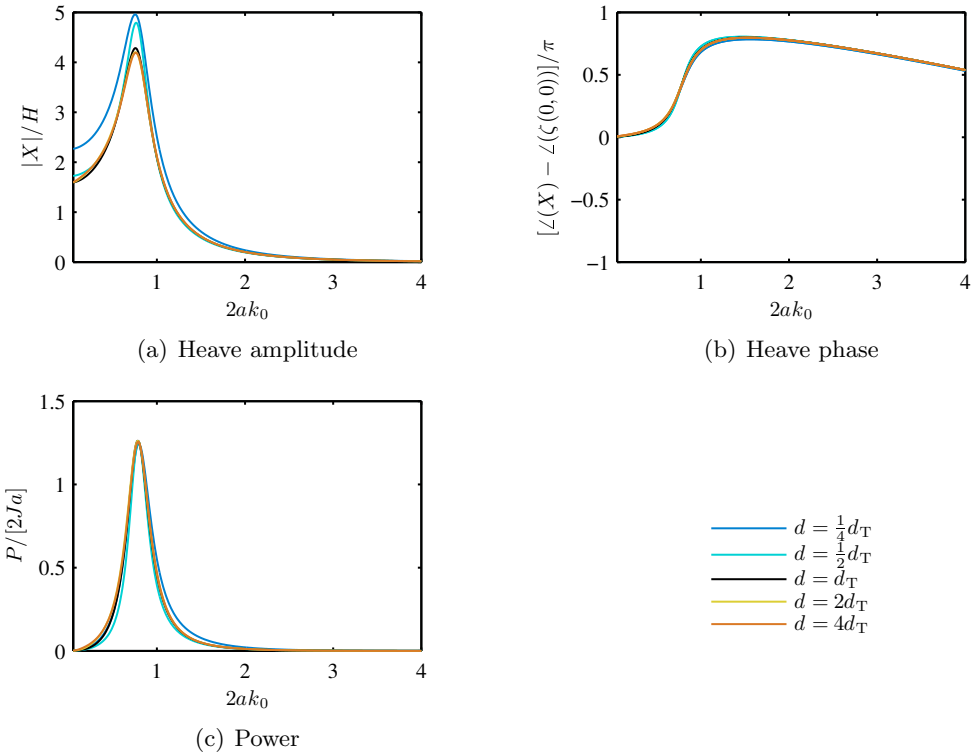

(a) Heave amplitude

(b) Heave phase

(c) Power

Figure 5.12: Isolated device behaviour with different water depths.

Moreover, tuning regimes involving generator mass coefficients are not widely used so will not be considered in the remainder of this thesis.

5.5.5 Geometry

In this final subsection of the chapter, the geometry of an isolated device will be varied and the behaviour analysed. Power take-off coefficients have been calculated individually for each geometry using reactive tuning with the non-dimensional wave number $2ak_0 = 0.8$. One consequence of this is that all heave phase plots pass through the same value near the tuning frequency where resonance has been forced to occur.

First the depth is varied as a proportion of that used for the Device Test Case d_T. The heave motion, forces and power output shown in Figure 5.12 do not appear to be significantly affected by changes to the water depth. In fact, for depths greater than or equal to d_T, there is minimal appreciable difference between the associated curves and the behaviour in the infinite-depth limit is approached rapidly. The most significant deviations are for long waves (low wave numbers), in which case the depth is proportionally smaller in comparison to the wavelength.

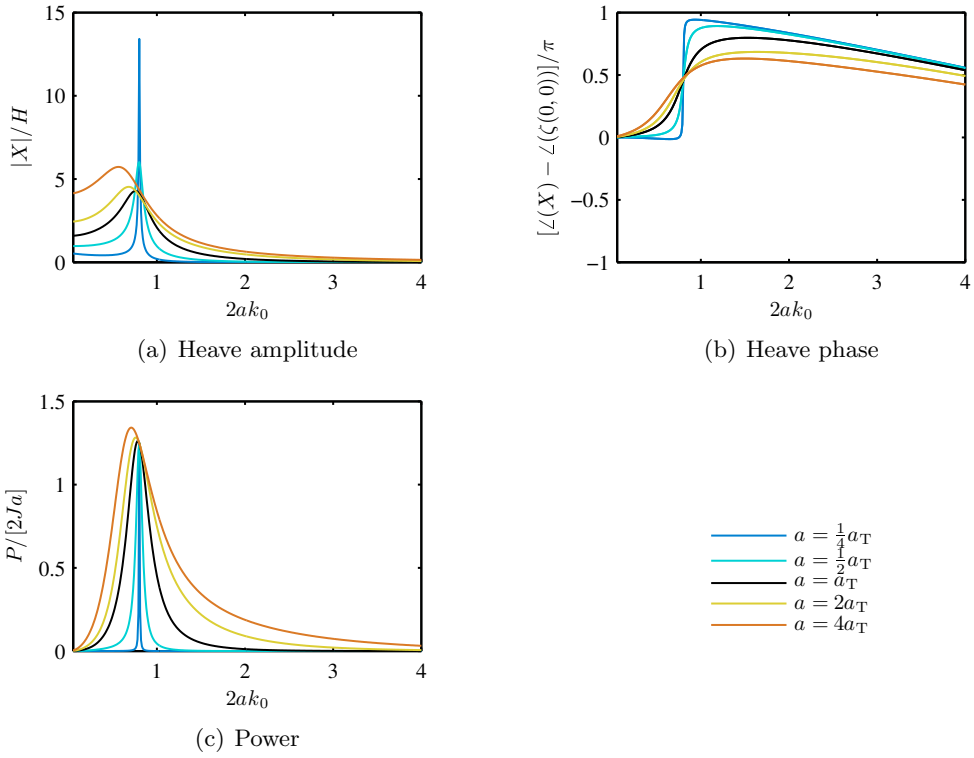

(a) Heave amplitude

(b) Heave phase

(c) Power

Figure 5.13: Isolated device behaviour with different device radii.

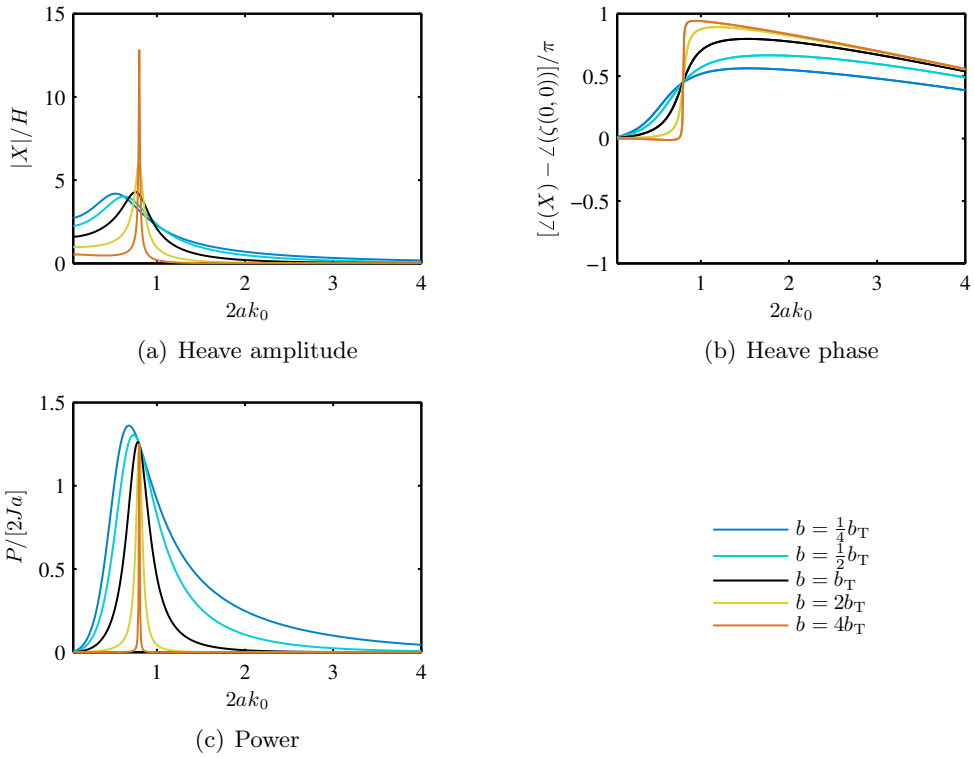

(a) Heave amplitude

(b) Heave phase

(c) Power

Figure 5.14: Isolated device behaviour with different device draughts.

Figures 5.13 and 5.14 respectively show the device behaviour as the radius and draught of the buoy is varied as a proportion of those used for the Device Test Case a_{T} and b_{T}. Altering these parameters has an effect on the ambient incident wave forces, added mass and added damping, whilst the mass of the device and the reactively-tuned generator parameters also change as a result. Each of these modifications may individually be related to the behaviour observed in the preceding sections. However, the combination of all the factors has given rise in this case to a more peaked response for smaller radii and larger draughts.

It is interesting to note that the curves in Figure 5.13 are almost exactly replicated by those in Figure 5.14, with small radii corresponding to large draughts and *vice-versa*. As discussed earlier, at this depth ($d = d_{\mathrm{T}}$) the behaviour is largely the same as for infinite water depth. Hence, the only relevant lengths are those of wavelength and radius and draught of the device. The behaviour with respect to the non-dimensional independent and dependent variables is therefore replicated when all of these lengths except depth are scaled by the same factor. Thus, for example, a device for which $a = 1$ and $b = 2$ gives rise to a similar curve as one for which $a = 0.5$ and $b = 1$.

5.6 Summary

In this chapter, the behaviour of an isolated point absorber has been overviewed, in order that array effects may be distinguished more clearly in the subsequent analysis. The well-used parallel of a second-order linear oscillator has been employed in order to lend an intuitive interpretation to the results, as well as to derive the power take-off regimes used in the remainder of this thesis. Furthermore, the decomposition of velocity potential in the domain surrounding an isolated device presented here forms the basis for one of the array optimisation procedures described in Chapter 7. Finally, the majority of the parameters analysed in this chapter will not henceforth be varied, in order that a more thorough analysis of the array-related parameters may be performed. Hence this chapter may serve as a starting point for those wishing infer array results for a different description of device.

Chapter 6

Principles of array analysis

6.1 Introduction

In order to gain an understanding of wave energy device array performance, its fundamental influencing factors are examined in this chapter. A simple test case is first defined in Section 6.2 and the resulting behaviour as a function of wave number studied. In the course of this discussion, the key concept of the *interaction distance* is introduced. The work contained in this chapter is based on Child and Venugopal (2008).

The defining characteristics of the array are then altered in turn to determine their effect on performance, measured by the interaction factor introduced in Chapter 3. The spacing between devices is analysed in Section 6.3 whilst Section 6.4 examines the effects of changing the direction of incident waves. The number of devices in a linear array is varied in Section 6.5 and finally some alternative configurations of devices are explored in Section 6.6.

In order to aid the description of the arrays and their behaviour, we first define some terminology. Where waves arrive at Device i and undergo some interaction before encountering another converter, j, we label this process i-j. Here, i is the *originating device* and j is the *receiving device* and passed between them are *interacted* waves.

6.2 Elementary Array Test Case

We begin by defining a simple array that is capable of demonstrating the basic principles of wave interaction. Thus the 'Elementary Array Test Case' consists of two devices in a

line parallel to that of the ambient incident waves. These are separated by a distance L of eight radii so that Device 1 has coordinates $(-L/2, 0)$ and Device 2 is located at $(L/2, 0)$. Each converter is of the type defined by the 'Device Test Case' in Section 5.4. Real tuning of devices is considered alongside reactive tuning, since together they constitute the most widely used regimes. The specification for the Elementary Array Test Case is summarised in Table 6.1.

Property	Specification
Radius	a
Draught	$b = a$
Depth	$d = 8a$
Tuning	*real*, *reactive*
Separation	$L = 8a$
Wave heading angle	$\beta = 0$
Array size	$N = 2$
Array configuration	*linear*

Table 6.1: Specification of the Elementary Array Test Case.

6.2.1 Real-tuned devices

Array behaviour

Here we analyse the behaviour of the Elementary Array Test Case, where the devices are real-tuned. Heave amplitude and phase, along with power production, are plotted as functions of ambient incident wave number in Figure 6.1 for each device in the array as well as for an isolated device. As can be clearly seen, the devices within the array experience certain alterations to their behaviour due to interference effects. The up-wave device (Device 1) exhibits strong fluctuations about the isolated device curve in each plot. The down-wave device (Device 2) has much weaker deviations and leads to a diminished power output over most of the frequency range compared with a single converter.

Also included in Figure 6.1, is the $\bar{q}$-factor, defined by equation (3.163) as the ratio of total array power to that from the same number of isolated devices. This is a crucial quantity since it determines whether or not on average the array has a beneficial effect on the performance of its members. A line is marked at the value $\bar{q} = 1$, above which the array produces a net increase in power whilst the converse is true below this. Fluctuations are also apparent in this plot with a reasonably regular increment in wave

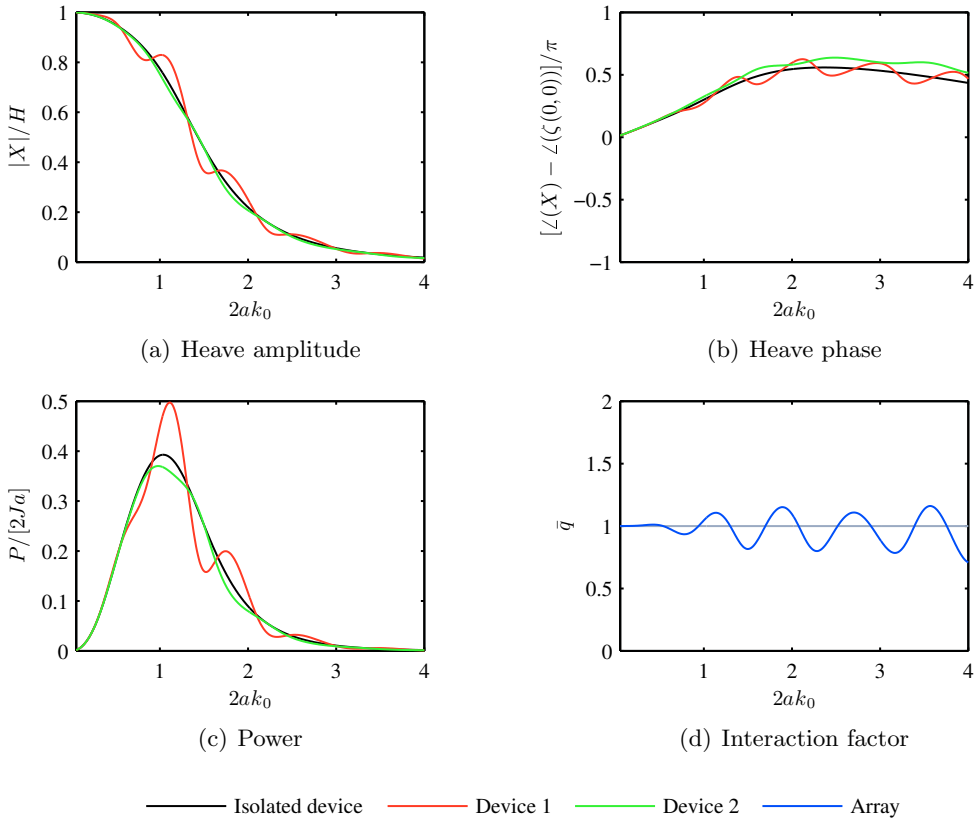

Figure 6.1: Array behaviour. Elementary Array Test Case with real-tuned devices.

number needed to move between consecutive peaks in the $\bar{q}$-factor. As the wave number tends to zero, that is to say for long waves, the interaction factor tends towards unity.

We now seek to answer the question: What determines the characteristics of the $\bar{q}$-factor? Although a method has been derived in the present work that is capable of computing the 'exact' solution, this does not on its own provide sufficient insight into the phenomena involved. We therefore attempt to provide an intuitive explanation of ways in which the interaction factor may be modified. Because there will be some simplifying assumptions made, the following phase argument can by no means account for every feature of the results.

Consider the wave field incident to each device in the array as the sum of the ambient incident waves and those scattered and radiated by other converters. Although wave interactions may be significant, these interacted wave fields are in general much smaller than that of the ambient incident waves. This can be seen, for example, from the amplitude of the associated potentials around an isolated device (Figure 5.6 and

Figure 5.11). For the purposes of simplicity, it is often possible to disregard one of the interacted wave fields with reference to the dominant magnitude of the other, leaving just two *principal* incident wave fields. We then propose that the following chain of events leads to an enhancement of the power production at one of the devices:

1. The velocity potentials of the principal wave fields on the surface are in phase with each other at the centre of the receiving device.

2. The forces due to the principal wave fields are in phase with each other. This follows from equation (3.143) in an approximate sense, especially if the device is of small radius.

3. The amplitude of the incident wave force (i.e. the sum of the forces from the principal wave fields) on the receiving body is larger than that of the ambient incident wave force. The total hydrodynamic force, the largest component of which is the incident wave force, is also generally increased in amplitude.

4. The amplitudes of motion (i.e. displacement and velocity) are enhanced, compared with those of an isolated device. The relationship between motion amplitudes (3.90-3.92) and second-order linear oscillator theory account for this behaviour when the amplitude of F is increased in equation (5.5).

5. The power output from the device is increased compared to that from the device in isolation. This follows from (3.161).

Where the last event takes place at one of the devices, a larger $\bar{q}$-factor results, provided power production from the other devices is not also reduced significantly. Conversely, where the principal wave fields are out of phase with each other at the receiving device, a diminished $\bar{q}$-factor is likely. Furthermore, if as the relative phases described here change, the associated amplitudes do not vary significantly, then we can expect peaks and troughs instead of merely increases and decreases in the relevant quantities.

Force decomposition

The processes involved in wave interaction may be further illuminated by decomposing the incident wave force acting on each body in the array with respect to the type and origin of the associated wave field (Figure 6.2). These precisely correspond to terms in the expression of the hydrodynamic force (3.153). Thus, the 'radiated force from i to j'

is the component of the force on j that results purely from the motion of Device i given in the solution of the full system. Equally, the 'scattered force from i to j' is derived from the scattering of all incident waves to i in the same solution. Note that these definitions differ from the more conventional exciting force and added mass and damping matrices of, for example, Falnes (2002). For each force component, the amplitude and phase is plotted on the same set of axes. The latter is calculated relative to the phase of the force from the ambient incident wave field. Hence the horizontal grey line at zero denotes where interacted and ambient wave forces are in phase with each other.

We turn firstly to the up-wave interactions, labelled 2-1. The phase plots of both scattered and radiated wave forces in this direction have a steep inclination, the gradient of which is reasonably constant as the wave number varies. The amplitudes of these forces generally follow a skewed bell-shaped curve, with some small deviations to this over the frequency range. Note that the scattered wave force is larger in amplitude than the radiated wave force, especially for higher wave numbers. Hence the principal wave fields experienced by Device 1 are those of the scattered and ambient incident waves. Moreover, the amplitude of the interacted wave forces in this direction are larger than those for the down-wave interaction, so we may justifiably expect Device 1 to have a stronger influence on the $\bar{q}$-factor than Device 2.

The steep gradient of the phase plots means that the scattered wave force goes rapidly in and out of phase with the ambient incident wave force at Device 1. The phase argument above then predicts rapid fluctuations in hydrodynamic force, heave motion, power and $\bar{q}$-factor with respect to wave number, which are indeed observed. Note that where there is a peak in hydrodynamic force amplitude on Device 1, the phase of this force crosses the isolated device curve in an upward direction. This is because the additional force from the interaction has maximum effect on the combined force amplitude when it is in phase with the original force on an isolated device. This leads to a similar relationship between heave amplitude and phase.

Further confirmation of the correlation between the proposed phenomena involved in the phase argument may be obtained by comparing the wave numbers at which they occur (Table 6.2). Where appropriate, calculation of the position of the peaks is preceded by division of the respective quantity by that for an isolated device. For each peak in $\bar{q}$-factor, the wave numbers at which the listed events occur match very well. The correspondence is especially close at higher frequencies where radiation becomes

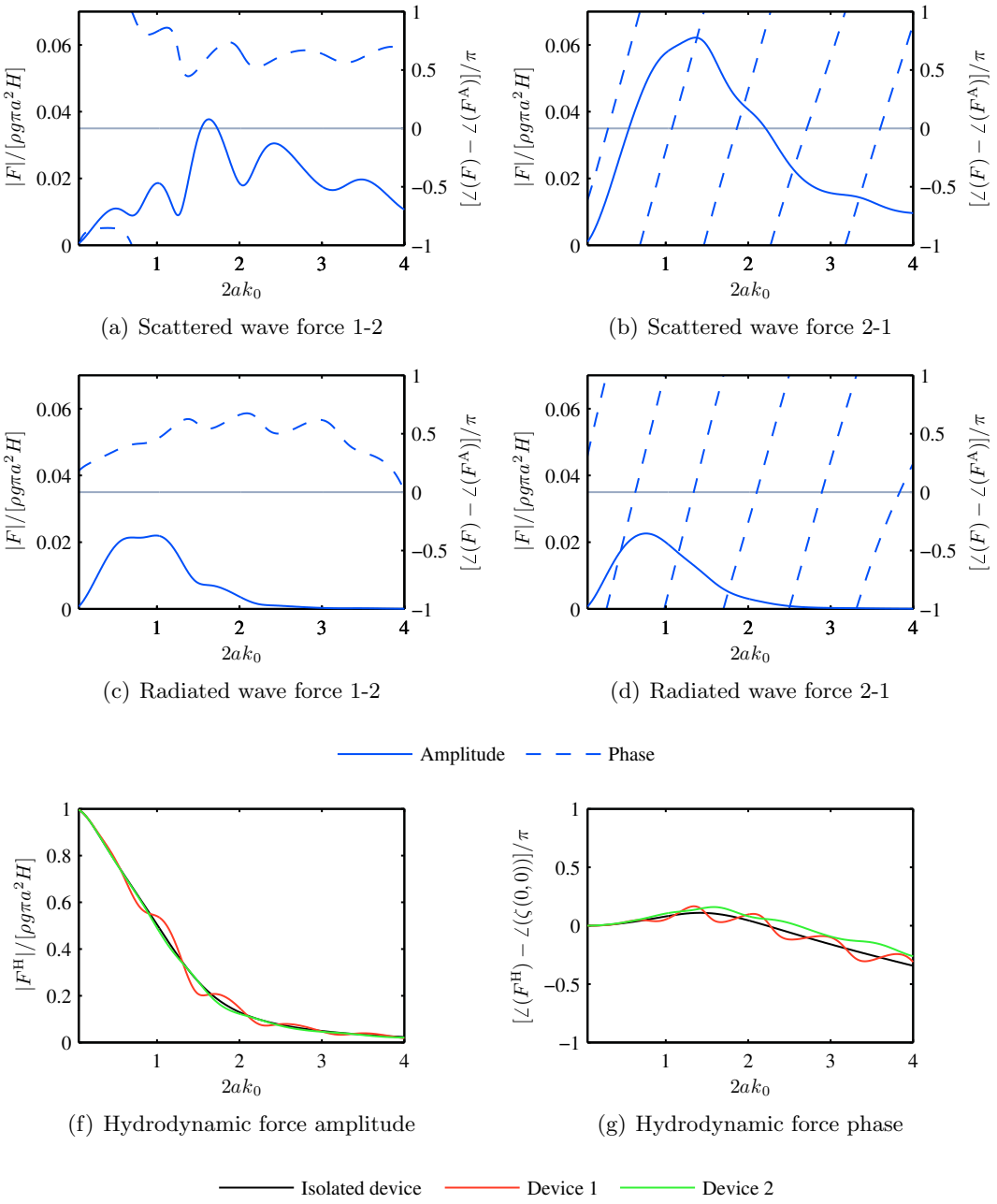

Figure 6.2: Forces. Elementary Array Test Case with real-tuned devices.

much weaker in comparison to scattering processes.

Now we consider the down-wave interaction, labelled 1-2. Here we have large fluctuations in both the amplitude and phase of the wave forces originating at Device 1. This is because the up-wave device is passing on the variations in wave force that it experiences from the down-wave device as the wave number changes. Neither radiation

Event [Item number]	1	2	3	4	5
Scattered and ambient forces in phase [2]	0.30	1.08	1.86	2.71	3.60
Hydrodynamic force amplitude peak [3]	0.44	1.13	1.88	2.71	3.60
Hydrodynamic force phase up-crossing	0.35	1.11	1.87	2.72	3.60
Heave amplitude peak [4]	0.44	1.13	1.88	2.71	3.60
Heave phase up-crossing	0.35	1.11	1.87	2.72	3.60
Device power peak [5]	0.44	1.13	1.88	2.71	3.60
$\bar{q}$-factor peak	0.43	1.14	1.89	2.70	3.57
Difference between $\bar{q}$-factor peaks	-	0.71	0.75	0.81	0.87

Table 6.2: Non-dimensional wave numbers $2ak_0$ at which events described in the phase argument on p.112, along with others defined in the text, occur for the Elementary Array Test Case with real-tuned devices. Where appropriate, data is derived from Device 1 in relation to isolated device behaviour.

nor scattering dominates over the whole range in the down-wave direction, although as previously stated, they both have little effect compared with the up-wave interactions. Also both the scattered and the radiated wave force phases do not change rapidly with respect to wave number, rarely becoming exactly in or out of phase with the ambient incident wave force. Thus, the modifications to the isolated device behaviour are smaller for Device 2 than for Device 1.

A phase argument again provides some insight into the behaviour here. Note that the relative phase between the down-wave scattered wave force and the ambient incident wave force stays between $\pi/2$ and $3\pi/2$ for almost all of the frequency range. This means that scattered waves at Device 2 are interfering in at least a partially destructive manner. Hence the performance of this device is diminished for most frequencies, as has already been observed. Intuitively, the down-wave device is in the shadow of its up-wave counterpart and thus receives less wave energy than one would if it were in isolation.

In both directions, long ambient incident waves lead to very weak scattered and radiated waves. Therefore power modifications due to interactions also decay and the $\bar{q}$-factor tends to unity as $2ak_0$ tends to zero, as can be seen in Figure 6.1(d).

Due to the simplifying assumptions used, not all peaks in the $\bar{q}$-factor necessarily result from the sequence of events in the phase argument outlined above. However, most examples of such constructive interference do seem to coincide with principal velocity potentials being in phase with each other at key devices. To illustrate this, one peak ($2ak_0 = 1.89$) and one trough ($2ak_0 = 1.50$) is selected from the $\bar{q}$-factor plot. The phase of the scattered potentials from each device at those wave numbers is given, relative to

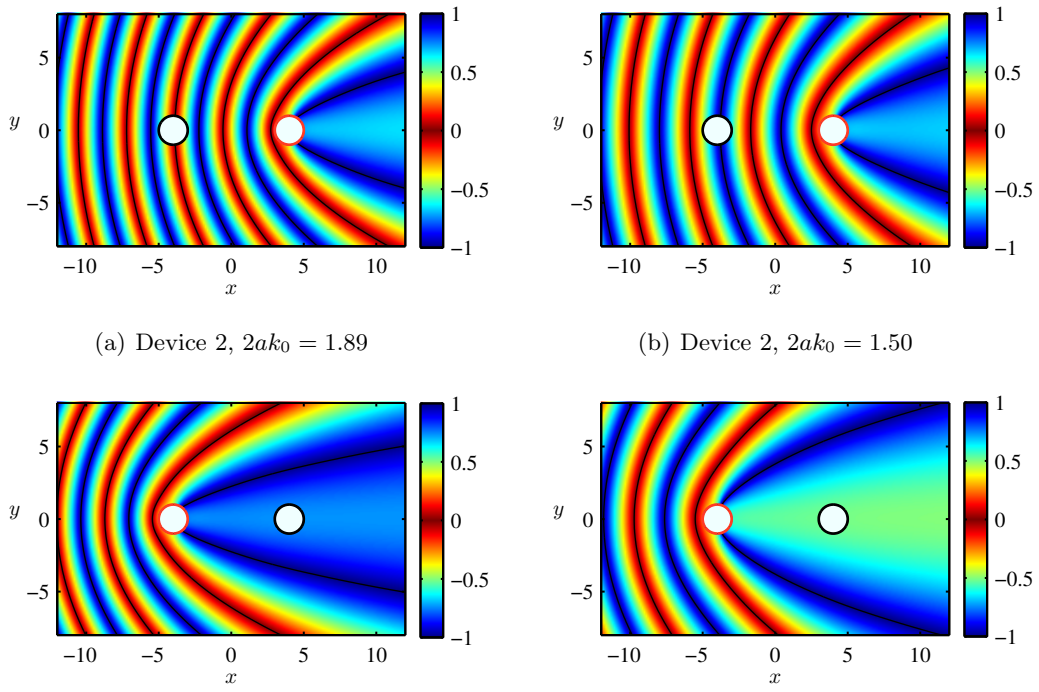

(a) Device 2, $2ak_0 = 1.89$

(b) Device 2, $2ak_0 = 1.50$

(c) Device 1, $2ak_0 = 1.89$

(d) Device 1, $2ak_0 = 1.50$

Figure 6.3: Phase of scattered velocity potential from each device (red circle) at the free surface, relative to that of ambient incident wave field and normalised by π (see colour bar). Elementary Array Test Case with real-tuned devices.

the ambient incident wave potential, by the colour maps in Figure 6.3. The originating body is denoted by a red circle. Indeed at the peak in $\bar{q}$-factor, the plot of the wave field scattered from the down-wave device shows that it is in phase with the ambient incident wave field at the up-wave converter. Conversely at the trough, the relevant wave fields are out of phase with each other. Note that in both cases, the down-wave body lies in an area of neutral or destructive interference from the up-wave one.

The interaction distance

We have seen that the nature of interference is principally determined by the shape of the relative phase plot between the scattered and ambient incident wave forces. Hence it is important to obtain a greater understanding of what influences these plots in the general case. An explanation is presented in the following paragraphs to do precisely this, making more simplifying assumptions along the way.

Suppose two devices i and j within an array are undergoing some interaction, dominated by scattered waves. Let the distance between these converters be L_{ij} and

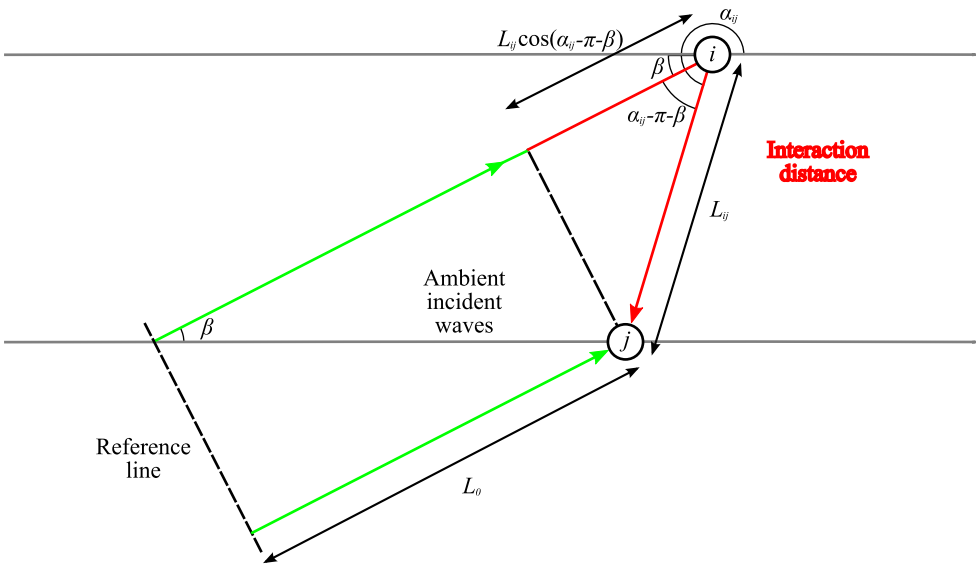

Figure 6.4: Illustration of the interaction distance for interference from i to j.

the angle between the positive x-axis at i and Device j be α_{ij}, as represented in Figure 6.4. Ambient incident waves arrive at an angle β to the positive x-direction and have progressive wave number k_0. Define some reference line up-wave of the array, parallel to the crests of the ambient incident wave field and let the distance from this to j be L_0.

Evanescent waves are ignored in the following, since they generally have small amplitude in comparison with progressive waves. The dimensions of the devices are also neglected with reference to the other lengths used. Consider the complete path of a progressive incident wave as it travels from the reference line, and is then scattered from body i towards the other body, j. The distance that this wave has travelled is $L_0 + L_{ij}\cos(\alpha_{ij} - \beta - \pi) + L_{ij}$. At the receiving body, j, ambient incident waves also arrive directly from the reference line having travelled distance L_0. The difference between these two distances is defined to be the *interaction distance*, D shown by the red line in the diagram. For the interaction, i-j, this is then

$$D_{ij} = L_{ij}[1 - \cos(\alpha_{ij} - \beta)]. \tag{6.1}$$

Note that this distance is defined and correctly calculated by the above equation for

all angles α_{ij} and β. The phase shift associated with the interaction at the body is neglected with reference to other phases involved in the calculation. Thus the phase of a progressive wave increases at a rate of k_0 with respect to the total distance it has travelled along its path. Since all waves shared a common phase at the reference line, the difference in phase between scattered and ambient wave fields is proportional to the difference in distance travelled. At the receiving body, j, this is given by the *interaction phase* η_{ij}:

$$\eta_{ij} = D_{ij}k_0 \tag{6.2}$$

$$= L_{ij}[1 - \cos(\alpha_{ij} - \beta)]k_0. \tag{6.3}$$

Hence under these assumptions, the relative phase between scattered and ambient wave forces also has a gradient of approximately D_{ij} with respect to k_0. This accounts for the sloped plots in Figure 6.2(b) and Figure 6.2(d), and gives a reasonable prediction of their gradients. Note that the larger the interaction distance, the more rapid the change in relative phase between these forces.

The phase argument outlined earlier in this section implies that if there are two situations in which the relative phase between scattered and ambient incident waves at a device are the same, the interference is likely to have similar qualities. This must also be true therefore if that relative phase is incremented by a whole multiple of 2π. Hence if we have interaction phases $\eta_{ij}^{(1)}$ and $\eta_{ij}^{(2)}$ corresponding to two cases, then the condition is

$$\eta_{ij}^{(2)} - \eta_{ij}^{(1)} = 2\pi P, \qquad P \in \mathbb{Z}. \tag{6.4}$$

The change in interaction phase may be achieved by altering the ambient incident wave number alone. The smallest such increment k_R is defined to be the wave number *repeat value* for that interaction. Equations (6.2) and (6.4) with $P = 1$ then yield this quantity:

$$k_\mathrm{R} = \frac{2\pi}{D_{ij}}. \tag{6.5}$$

Since the difference in interaction phases in (6.4) is proportional to the difference in the associated wave numbers, increments to the wave number of whole multiples of the repeat value will also give interference that shares some qualities with the initial case. What this means is that the repeat value has effectively defined the 'period' of the fluctuations of power from a device with respect to wave number. Where more than one

interaction occurs in an array, the plot of interaction factor with respect to wave number will resemble a superposition of many different fluctuating patterns, each corresponding to a particular interaction with its own repeat value.

The repeat value for the up-wave interaction in the Elementary Array Test Case is $2ak_{\mathrm{R}} = 0.79$. This corresponds approximately with the observed difference in wave numbers at consecutive peaks in the $\bar{q}$-factor (see Table 6.2). For the down-wave interaction, the interaction distance is zero, since the ambient incident wave field at Device 2 travels approximately the same distance as that which has been scattered before arriving there. The repeat value is therefore not defined for this interaction, and correspondingly, there are no strong fluctuations in power output from Device 2 with respect to wave number. Although it must be emphasised that the repeat value calculation does not take all relevant factors into account, it does provide a good indicator of the likely interference characteristics.

6.2.2 Reactively-tuned devices

The Elementary Array Test Case involving reactively-tuned devices is now examined. Heave amplitude and phase, power and the $\bar{q}$-factor are shown in Figure 6.5 as functions of wave number. The isolated device behaviour is quite different to that of real-tuned devices, as discussed in Chapter 5. However, the relationship between the behaviour of array elements and an isolated device has similar characteristics to those for real-tuned devices described in Section 6.2.1. The main difference here is around the tuning frequency $2ak_0 = 0.8$, where there is now a larger range of $\bar{q}$-factor values.

Figure 6.6 shows the incident wave force on each device, decomposed in the same way as in Figure 6.2. The main difference here is that radiated wave forces are much larger around the tuning frequency than they are for real-tuned devices. This is because reactive tuning forces resonance to occur near the tuning frequency ($2ak_0 = 0.8$) which leads to large body motion amplitudes and hence large radiated waves. Hence, much stronger interactions are possible in this wave number range, leading to more variation in the $\bar{q}$-factor. Note that up- and down-wave radiated force amplitudes are approximately equal, since this process is radially symmetric and the devices are moving with roughly the same amplitude.

The wave forces resulting from scattered waves are largely unchanged from the real-tuned case. The differences that do exist again occur around the tuning frequency,

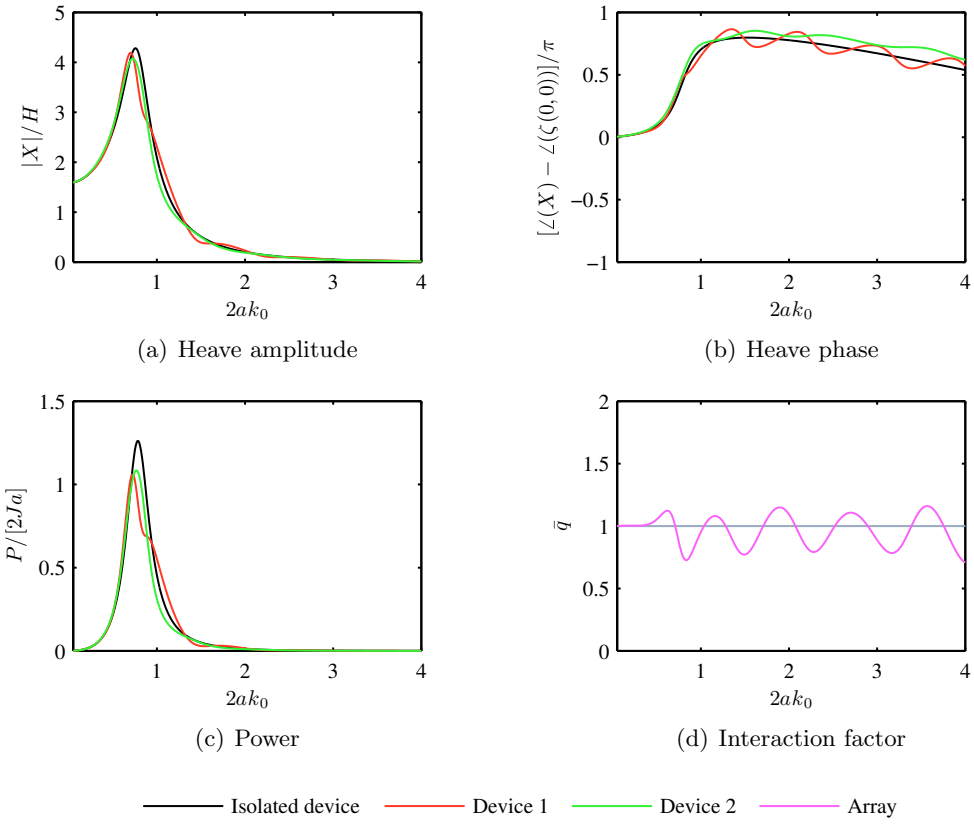

Figure 6.5: Array behaviour. Elementary Array Test Case with reactively-tuned devices.

where large radiated waves are being sent from the device that receives scattered waves towards the device at which they originate. This modified wave field is finally scattered back to the receiving device producing an alteration in the scattered wave force in that direction.

For the array of real-tuned devices, scattering is the dominant effect throughout the frequency range, at least in the up-wave direction. However, in the present array, radiation dominates near resonance ($0 < 2ak_0 \lesssim 1$) whilst scattering is most significant again in the rest of the range ($2ak_0 \gtrsim 1$) in both directions. For these higher frequencies, where both real and reactively-tuned arrays are dominated by scattering, the behaviour is very similar.

In common with the case of real-tuned devices, the radiated and scattered wave force phases in the down-wave direction do not change significantly with wave number here, staying for the most part in the range $\pi/2$ to $3\pi/2$ relative to the ambient incident wave force. Hence the power obtained from Device 2 is not considerably different to

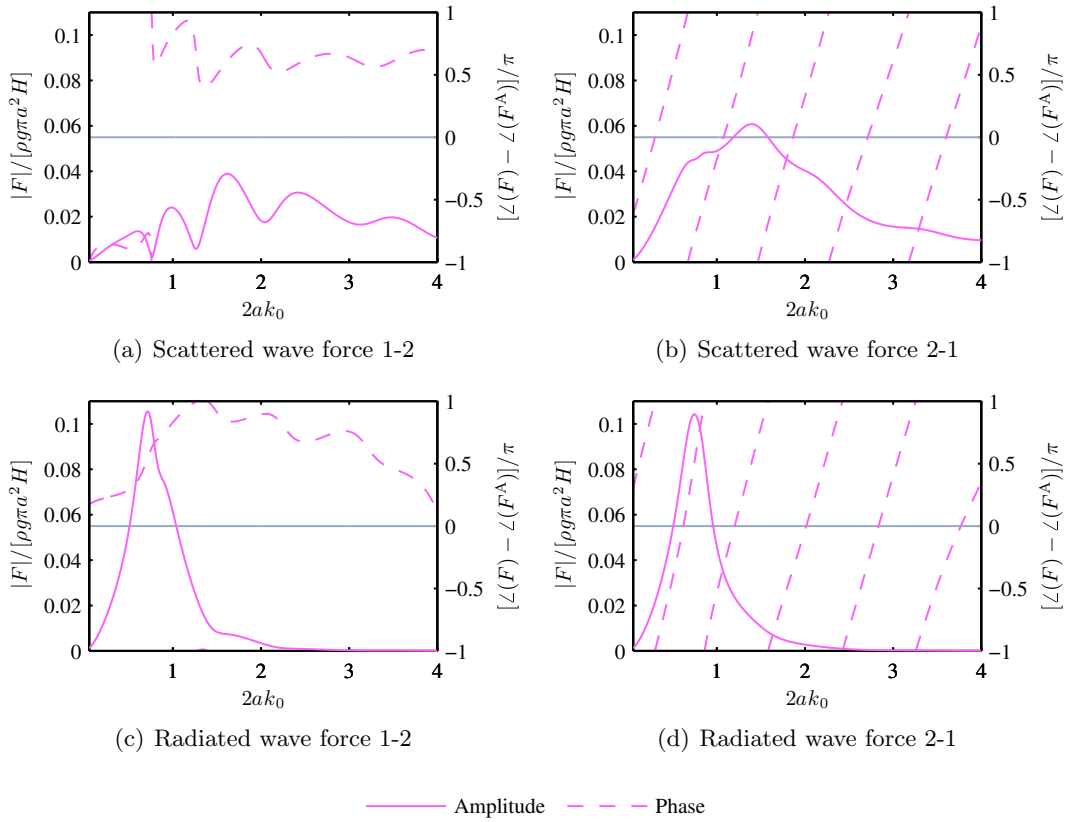

(a) Scattered wave force 1-2

(b) Scattered wave force 2-1

(c) Radiated wave force 1-2

(d) Radiated wave force 2-1

Figure 6.6: Forces. Elementary Array Test Case with reactively-tuned devices.

that from an isolated device and is, if anything, smaller for most of the frequency range.

For the frequency range where radiation dominates, we now wish understand why we have positive and negative interference in the $\bar{q}$-factor. Since down-wave interactions do not produce strong fluctuations in the power output, up-wave interference must be closely examined to find the cause. The same phase argument as for real-tuned devices may be applied here, with radiated and ambient incident wave potentials constituting the principal wave fields required. Hence, where they are in phase with each other, we expect a peak in the $\bar{q}$-factor and *vice-versa*. Indeed they are in and out of phase with each other at wave numbers $2ak_0 = 0.62$ and $2ak_0 = 0.86$, which match very well with a peak and trough in the $\bar{q}$-factor at $2ak_0 = 0.62$ and $2ak_0 = 0.83$ respectively. For wave numbers where both scattering and radiation are significant, it is possible to have effects of both interaction processes evident in the $\bar{q}$-factor.

The key to understanding the interactions that occur in the array therefore lies finding out what determines the shape of the radiated force phase plots. In Section 6.2.1,

an approximation was made asserting that scattering merely redirects progressive incident waves, obtaining a good approximation of the shape of the relevant plot. Here, ambient incident waves are absorbed by the device, which then moves and radiates them back out again. Hence this may also be thought of as a redirection of incident waves, provided the interaction processes at the interacting body are ignored. This allows radiated waves to be used instead of scattered waves in the argument, giving rise to the same predicted repeat values in every case.

As for interactions dominated by scattered waves, the repeat values for radiated waves are $2ak_{\mathrm{R}} = 0.79$ and 0 for up- and down-wave interactions respectively. This is evident from the comparable gradients of scattered and radiated wave force phase plots in Figure 6.6. Note, however, that the actual wave numbers where the wave fields are in or out of phase are likely to be different for scattering and radiation, due to the differing interaction processes.

As an example of the causes of interference, a peak ($2ak_0 = 0.62$) and a trough ($2ak_0 = 0.83$) in the $\bar{q}$-factor are first selected near the tuning frequency. The phase of the up-wave radiated wave field with respect to the ambient incident wave field is then plotted as a colour map in Figure 6.7. These confirm that the principal wave fields are indeed approximately in and out of phase with each other at the peak and trough respectively.

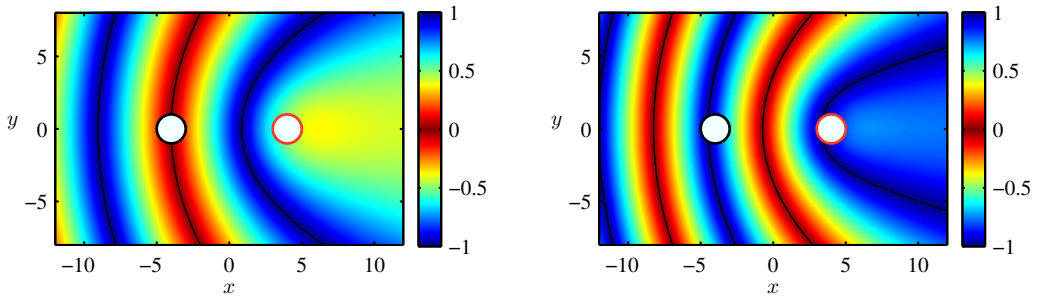

(a) $2ak_0 = 0.62$ (b) $2ak_0 = 0.83$

Figure 6.7: Phase of radiated velocity potential from Device 2 (red circle) at the free surface, relative to that of ambient incident wave field and normalised by π (see colour bar). Elementary Array Test Case with reactively-tuned devices.

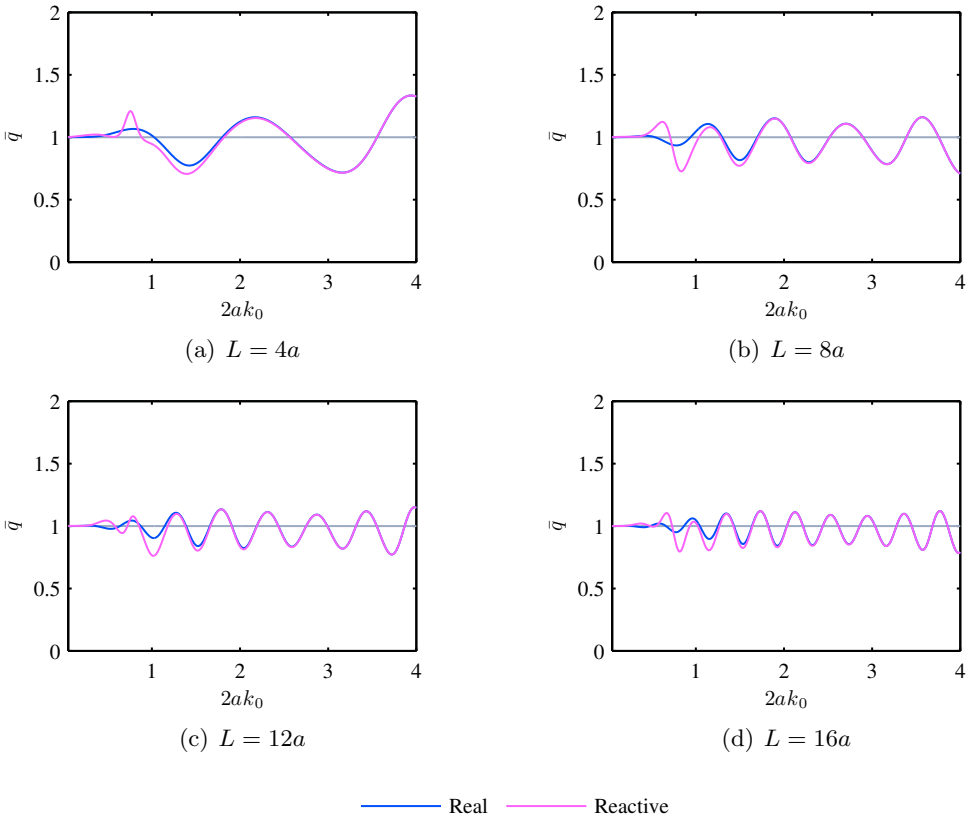

Figure 6.8: Interaction factor $\bar{q}$. Elementary Array Test Case with different device separations L.

6.3 Device separation

In this section, the Elementary Array Test Case is examined and the spacing between devices varied. Separation distances from $L = 4a$ to $L = 16a$ are considered here. The $\bar{q}$-factor is plotted as a function of wave number for some of these cases in Figure 6.8. Each of these gives rise to reasonably regular fluctuations about $\bar{q} = 1$ for most of the frequency range.

From these subfigures, it is clear that as the spacing between devices is increased, the number of fluctuations in $\bar{q}$-factor about $\bar{q} = 1$ over the frequency range increases. As discussed earlier in this chapter, the factor that primarily determines the characteristics of these undulations is whether or not the progressive waves arriving at each device from other elements in the array are in phase with the ambient incident wave field. The wave number for a progressive wave, by definition is the rate of change of phase with distance. Hence, if the additional distance that interacted waves must travel is increased, a given

increment in wave number will have a much greater effect on the relative phases at the receiving body. This means that each body will change from experiencing positive to negative interference with a smaller change in wave number.

The relationship between spacing and interaction factor may be conveniently expressed in terms of the quantities introduced in the previous section. Large inter-body spacings mean the interaction distances D_{ij} between devices will also be large (see equation (6.1)) and hence the repeat values in the wave number will be small (see equation (6.5)). The repeat values for the separations $L = 4a$, $8a$, $12a$, $16a$ are calculated as $2ak_{\mathrm{R}} = 1.57$, 0.79, 0.52, 0.39 respectively. Values taken from the $\bar{q}$-factor plots themselves are $2ak_{\mathrm{R}} = 1.64$, 0.80, 0.53, 0.40 respectively, demonstrating an excellent correspondence especially for wider separations. When devices are closer together, the phase difference associated with interaction at each device becomes larger in comparison with that relating to waves travelling between devices, and as such is less readily neglected. Also evanescent waves become more significant closer to the devices. Hence the repeat value calculation is not as accurate here.

Since the amplitude of waves emanating from any body decays with distance, the interactions are correspondingly weaker at larger separations. This applies to both up- and down-wave interactions. Hence, in this situation, we see that the $\bar{q}$-factor is on average closer to unity. This is consistent with the expectation that as the separation approaches infinity, each device behaves more like an isolated converter. Note that all of the principles outlined in this section also apply to a pair of devices in a more complex array. Investigations have been carried out by Babarit (2010) into the manner in which the performance of a similar array recovers with increasing separation. They found that interference effects decay approximately with the inverse square root of device separation and may still be significant for large values of that distance. This observation is reflected in the present set of results (Figure 6.8) where the range of $\bar{q}$-factors over the frequency range decreases more appreciably between separations $L = 4a$ and $L = 8a$ than between $L = 12a$ and $L = 16a$.

The variation of $\bar{q}$-factor with separation may be seen by plotting these two variables directly against each other. Figure 6.9(a) is just such a graph for real-tuned devices, where the wave number has been fixed at a value ($2ak_0 = 1.89$) for which there is a peak in the graph of $\bar{q}$ with respect to $2ak_0$ when $L = 8a$. From equation (6.3), it can be seen that as L_{ij} increases, the interaction phase increases and so the interacted

wave field goes in and out of phase with ambient incident wave field. This causes constructive and destructive interference and hence fluctuations in the $\bar{q}$-factor with respect to spacing. The scenario is analogous to the fluctuations with respect to wave number. In a similar way, therefore, we may define the *separation repeat value* L_{R} to be the smallest increment in separation such that the interaction phase is unchanged (*modulo* 2π). Using equations (6.3) and (6.4), this yields

$$L_{\mathrm{R}} = \frac{2\pi}{[1 - \cos(\alpha_{ij} - \beta)]k_0}. \tag{6.6}$$

For the case plotted, the distance between consecutive peaks along the L/a-axis is very close to the value predicted by this equation, $L_{\mathrm{R}}/a = 3.32$. Note that the separation repeat value decreases as the wave number increases.

To see how separation and wave number jointly affect the nature of interference, Figure 6.9(b) shows a colour map plot of the $\bar{q}$-factor for real-tuned devices. The patterns can be explained by considering characteristic lines along which the interaction phase is a constant c. From equation (6.3), this gives the relationship:

$$L_{ij} = \left(\frac{c}{1 - \cos(\alpha_{ij} - \beta)}\right)\frac{1}{k_0}. \tag{6.7}$$

These characteristic lines therefore predict a set of hyperbolas along which the nature of interference is comparable. Such lines can clearly be seen as bands of colour in the figure. Note that adding 2π to the constant c is equivalent to moving to a different hyperbola for which the interference is similar. This plot clearly confirms that more rapid variations in the $\bar{q}$-factor with respect to wave number result from wider spacing, and the same occurs with respect to spacing for higher wave numbers.

In order to draw some comparisons with earlier work on arrays, we now briefly consider the motions of devices. Figure 6.10 shows heave amplitudes as functions of spacing between two devices in an array that is aligned with the incident wave direction (that is to say in 'head seas' or an 'attenuator' configuration). The wave number is held at the device tuning wave number of $2ak_0 = 0.8$.

In the first case, the power take-off coefficients of the devices are reactively-tuned using the hydrodynamic properties of a single device, in the same way as in the rest of this thesis. A second case is also considered in which the power take-off coefficients have effectively been determined by imposing a condition for optimal absorption on the array

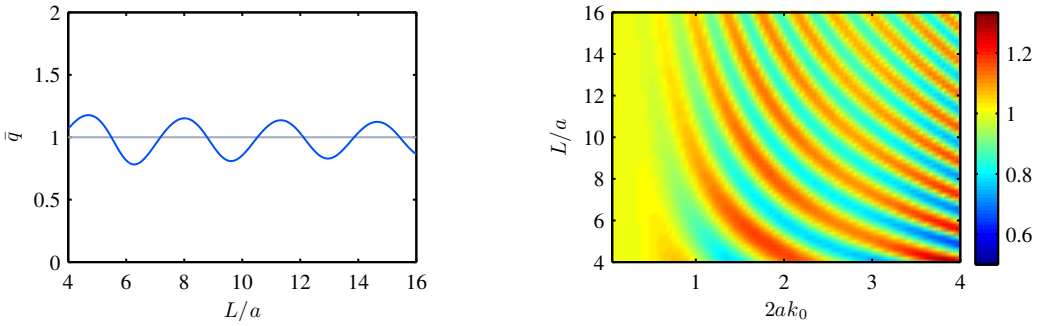

(a) $2ak_0 = 1.89$ (b) $\bar{q}$ (colour bar), varying L and k_0.

Figure 6.9: Interaction factor $\bar{q}$. Elementary Array Test Case with real-tuned devices, varying device separation L.

at each spacing. This relationship, which follows from an analogue of equation (5.25) for arrays was given by Evans (1980) in the form

$$\mathbf{U}_0 = \frac{1}{2}\mathbf{B}^{-1}\mathbf{X}_\mathrm{S}, \tag{6.8}$$

where (here only) $\mathbf{U}_0$ is the vector of complex velocity amplitudes, $\mathbf{B}$ is the added damping matrix and $\mathbf{X}_\mathrm{S}$ is the vector of complex excitation force amplitudes. The latter two array-dependent quantities (which are also used in the alternative solution procedure outlined towards the end of Section 4.2) were computed using the eigenfunction expansion described in Chapter 3.

It can be seen that where each of the power take-off coefficients have been optimised for the array configuration under consideration, the up- and -down-wave devices (labelled 1 and 2 respectively) move with approximately the same amplitude. This remarkable symmetry, first observed by Evans (1979) using the point absorber approximation, does not appear to have an intuitive physical explanation. The result was also noted by Thomas and Evans (1981) using the same approximation and recorded by Justino and Clément (2003) (in Figure 6) following application of a boundary element method (AQUADYN).

However, where devices have been tuned in isolation before array calculations are performed, this symmetry is clearly broken. Here, the down-wave device plainly exhibits more moderate motions than the up-wave device for most separations and behaves similarly with respect to the isolated device for all spacings. Note that the up-wave device follows a similar trend to both those devices that have been tuned as an array.

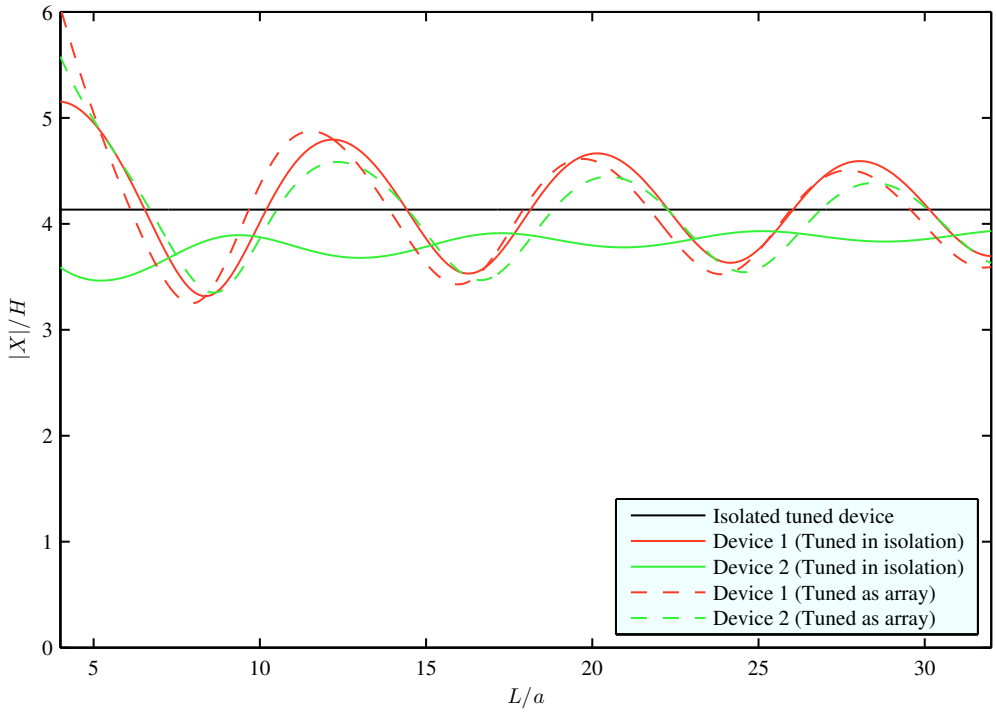

Figure 6.10: Heave response of an array of two devices in waves approaching parallel to the line joining them ($\beta = 0$) with wave number $2ak_0 = 0.8$. Power take-off settings determined as optimal for an isolated device (Tuned in isolation) and optimal for the array (Tuned as array). Isolated reactively-tuned device behaviour also shown.

These results imply that symmetry of motion amplitudes for devices in an 'attenuator' configuration is not an intrinsic property of array behaviour but rather a property of the optimal solution in which devices can be controlled in a specific manner. In the present situation, the added damping matrix (and therefore its inverse) is symmetric due to the symmetry of the problem and furthermore, if multiple wave scattering is not significant then the excitation forces on each element are approximately equal. Hence equation (6.8) leads to symmetry in the velocity amplitudes down the line of devices. However, if scattering is a significant effect and 'shadowing' diminishes excitation forces on the down-wave devices, then motion symmetry will be broken even in the case of optimal array tuning.

Therefore we may expect symmetry not to be present in the general case of 'attenuator' configurations, especially where the power take-off coefficients differ from optimal array values and where scattering is significant. Babarit (2010) previously found asymmetry in similar arrays using sub-optimal power take-off coefficients and hydrodynamic data from AQUADYN.

For further comparisons between results derived using different theories, see Mavrakos and McIver (1997). Note that results of the 'multiple scattering' technique described therein will in principle correspond precisely with 'exact' results from the present method. Compared with the former method, the 'point absorber' approximation was found to break down for wave numbers $2ak_0 > 1.6$, especially for closely spaced devices. Indeed, the results presented in this chapter for real- and reactively-tuned devices are well matched for such wave numbers, indicating that scattering and not radiation is the dominant process here.

6.4 Wave heading angle

The effect of changing the angle at which ambient incident waves approach the Elementary Array Test Case is now investigated. The symmetries that exist for the special case of a two-device array mean that only a restricted range of angles is necessary here, although this does not necessarily hold for larger arrays. Firstly, because the pair of devices has rotational symmetry of order two, every interaction from i to j for $\beta = \beta_0$ occurs from j to i for $\beta = \beta_0 + \pi$. Hence the total performance is unchanged: $\bar{q}(\beta_0) = \bar{q}(\beta_0 + \pi)$, a result that holds approximately even for arrays with no such symmetry (see Chapter 8). Secondly, any pair of identical devices has reflectional symmetry about the line joining their centre points, and also about the perpendicular bisector of this. Therefore, the behaviour must be replicated for wave headings making the same angle with these lines. Thus $\bar{q}(\alpha_0 + \beta_0) = \bar{q}(\alpha_0 - \beta_0)$, where $\alpha_0 = \alpha_{ij},\ \alpha_{ij} + \pi/2,\ \alpha_{ij} + \pi,\ \alpha_{ij} + 3\pi/2$. Since $\alpha_{12} = 0$ here, only wave headings β between 0 and $\pi/2$ need to be examined.

The $\bar{q}$-factor is shown as a function of wave number for selected wave heading angles in Figure 6.11. In common with the arrays studied up to this point, all of these plots exhibit fluctuations as the independent variable increases. However, the magnitude of the undulations varies with wave number for some angles.

Having discussed array behaviour for the case where $\beta = 0$ in Section 6.2, we next consider ambient incident waves approaching in a line perpendicular to that between the devices ($\beta = \pi/2$). In this situation, symmetry dictates that each device experiences exactly the same interacted wave field as the other for every wave number. Hence both positive and negative interaction effects are magnified, leading to the large range of $\bar{q}$-factor values seen in Figure 6.11(d). This also means that the plot maintains a

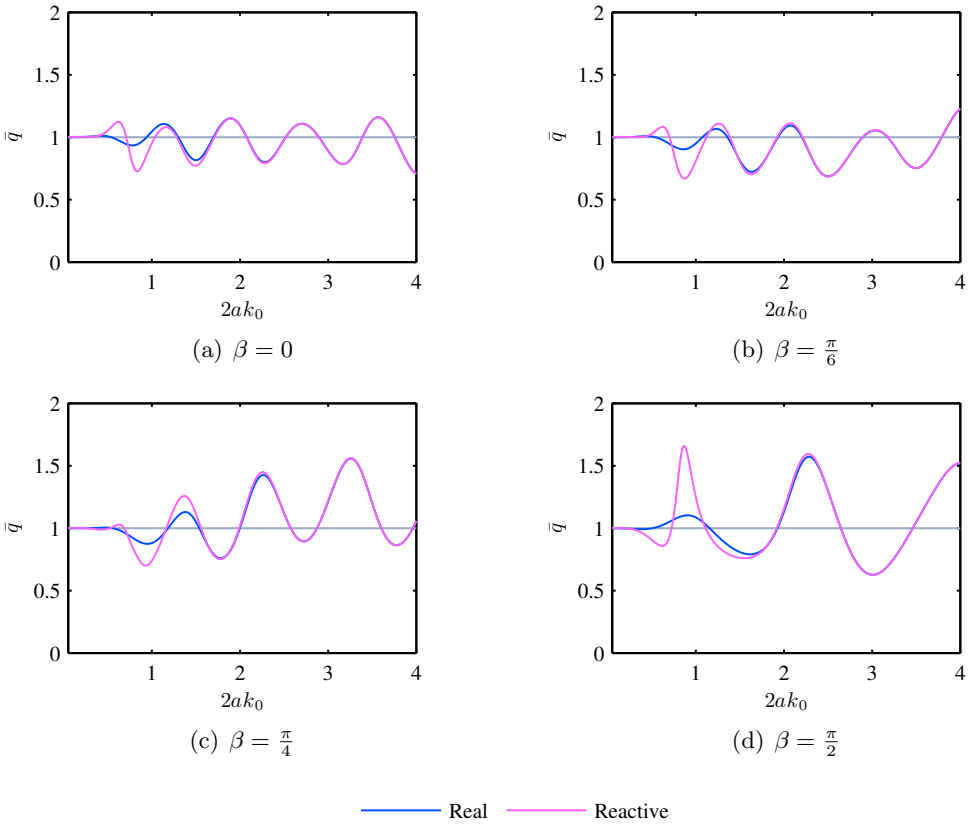

Figure 6.11: Interaction factor $\bar{q}$. Elementary Array Test Case with different wave heading angles β.

particularly simple, fluctuating appearance.

The interaction distance for the wave heading $\beta = \pi/2$ is half that for $\beta = 0$, so the repeat value is doubled to give $2ak_{\mathrm{R}} = 1.57$. This corresponds well with the behaviour observed in Figure 6.11(d), which exhibits a slower variation of the $\bar{q}$-factor with respect to wave number. In contrast with the $\beta = 0$ case, waves leaving each device interfere both constructively and destructively at the other converter over the wave number range, meaning that there are no shadowing effects (general degradation of down-wave device performance) observed.

The tuning regime makes a significant difference to the $\bar{q}$-factor near to the tuning frequency for $\beta = \pi/2$. For reactively-tuned devices, there is a large peak in the amplitude of radiated wave force near the tuning frequency $2ak_0 = 0.8$. Near to this wave number, the same force becomes in phase with the ambient incident wave force (not shown), and so there is a large modification in performance. The consequence of this is that the array of reactively-tuned devices exhibits a sharp peak near the tuning

frequency that the array of real-tuned devices does not.

In the case where $\beta = 0$, there is only one non-zero interaction distance and this largely governs the variation of the $\bar{q}$-factor with respect to wave number. When $\beta = \pi/2$, interactions in each direction share the same interaction distance, so there is only one distinct value that determines this behaviour. From equation (6.1), it is clear that for wave headings in between 0 and $\pi/2$ there are two distinct non-zero interaction distances, one relating to each direction. These lead to two different repeat values, each producing a significant increase in receiving device power that reoccurs when the wave number is incremented by that value. When the power contributions are added together, as in the $\bar{q}$-factor, a superposition of these two fluctuation patterns results. Since the two interaction processes are not coordinated at every wave number if $\beta \neq \pi/2$, the variations in $\bar{q}$-factor may not be as large as if that were to be the case.

As β is increased or decreased from $\pi/2$, one interaction distance increases and one decreases from their initially equal values. The up-wave interaction produces the longer distance and therefore the smaller repeat value than its down-wave counterpart. It is the former process that leads to the densest and hence most noticeable fluctuations of the $\bar{q}$-factor with respect to wave number. This means that the undulations appear to be more rapid with respect to wave number for any wave heading angle other than $\beta = \pi/2$, as can be seen from Figure 6.11. For the two angles in the middle of the range $\beta = \pi/6$, $\pi/4$, the larger of the repeat values in each array defines a broad trend curve about which the $\bar{q}$-factor fluctuates in accordance with the smaller value. In the case of $\beta = \pi/6$ these are calculated to be $2ak_{\mathrm{R}} = 11.72$ and 0.84, whilst for $\beta = \pi/4$ they are $2ak_{\mathrm{R}} = 5.36$ and 0.92. In both situations the smaller value matches well with that observed in the figures and some effects of the larger one (which exceeds the given wave number range) may be seen. Note also that as the wave heading approaches the direction joining converters, partial shadowing of the down-wave device is possible.

The variation of $\bar{q}$-factor with angle at a wave number of $2ak_0 = 1.89$ for devices that are real-tuned is shown in Figure 6.13(a). As with wave number and device separation variables, it is possible to replicate the same interaction phase and therefore type of interference at the receiving device for different wave heading angles. However, the matter is complicated by the fact that the difference in interaction phase is not proportional to the difference in wave heading angle. To aid understanding of the principles involved, the general case is simplified here. First, we assume that two devices

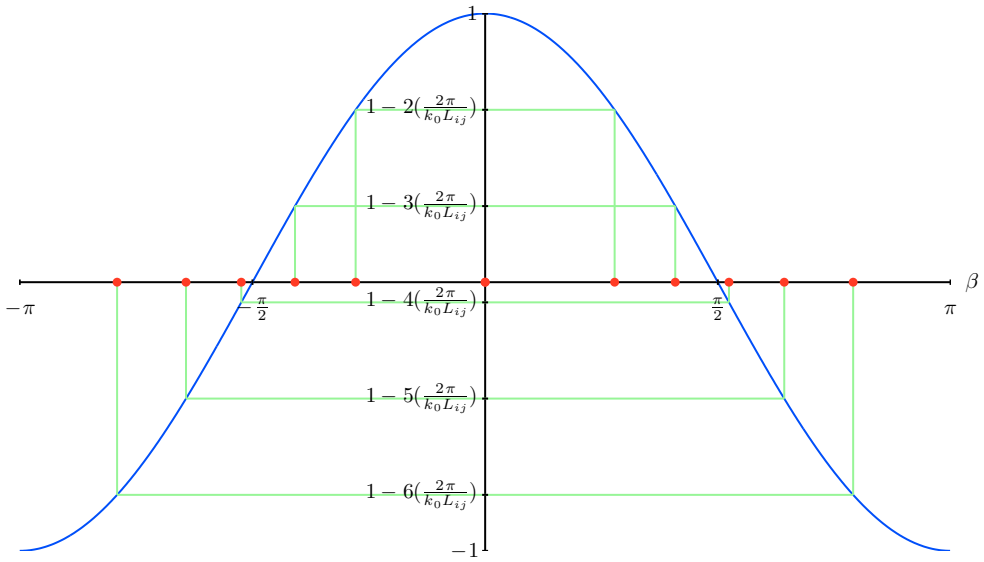

Figure 6.12: Illustration of wave heading angles β (red dots) for which the nature of interference at a device is qualitatively the same.

are in-line with the x-axis, such that $\alpha_{ij} = 0$. Suppose further that we wish to replicate the nature of interference that occurs at Device j when the ambient incident waves approach in the positive x-direction ($\beta = \beta^{(1)} = 0$) at some other heading ($\beta = \beta^{(2)}$). Then equations (6.3) and (6.4) give

$$\cos\beta^{(2)} = 1 - \frac{2\pi P}{k_0 L_{ij}}, \qquad P \in \mathbb{Z}. \tag{6.9}$$

The wave heading angles that satisfy this equation can be visualised as the values of β for which horizontal lines at the values $1 - \frac{2\pi P}{k_0 L_{ij}}$ ($P \in \mathbb{Z}$) intersect the plot of $\cos\beta$, as illustrated by the red dots on the β-axis in Figure 6.12. Hence if there is a peak in the power when wave incidence is parallel to the line between devices, then there are also likely to be peaks near the given angles.

A similar procedure may be applied to interactions occurring in the opposite direction to get another set of predicted peaks in power which will be combined with the first set to define the shape of the $\bar{q}$-factor plot. This process may be used to explain the shape of plots like Figure 6.13(a), which shows a peak in the $\bar{q}$-factor at $\beta = 0$, with a secondary example at $\beta = 0.40\pi$.

Note that from equation (6.9), as the spacing L_{ij} increases, more solutions for the angle exist and so the fluctuations in the power with respect to β become more dense. In arrays with more devices, the principles outlined above still hold, although the $\bar{q}$-factor

will resemble a superposition of more fluctuating patterns relating to the interacting pairs.

The variation of the $\bar{q}$-factor with both wave number and heading angle for real-tuned devices is shown in Figure 6.13(b). Characteristic contours of the resulting colour map may again be derived for any constant c, along which one of the interaction phases stays the same. Unlike with the varying of device spacing at $\beta = 0$, here the two interaction distances both change with each variable. From equation (6.3), the variables on characteristic lines are thus related by

$$k_0 = \frac{c}{L_{ij}(1 \pm \cos\beta)}. \tag{6.10}$$

This gives two sets of hyperbola-like curves in k_0 as a function of β which cross over, forming the patchwork pattern in Figure 6.13(b). Note that there is more rapid variation of the $\bar{q}$-factor with β for higher wave numbers k_0, as predicted by equation (6.9).

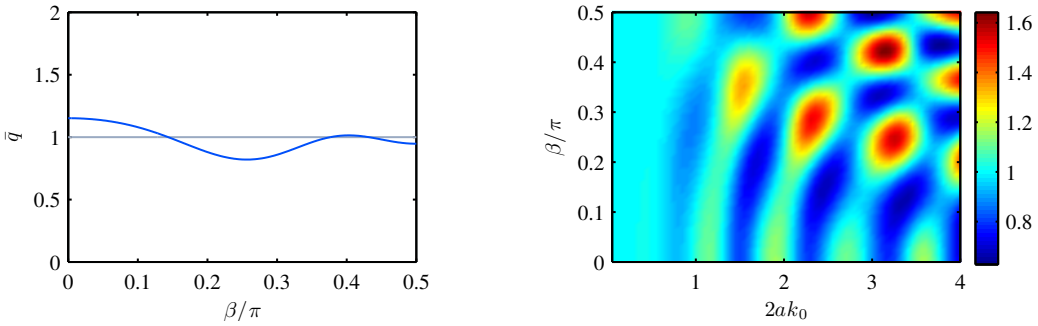

(a) $2ak_0 = 1.89$ (b) $\bar{q}$ (colour bar), varying β and k_0.

Figure 6.13: Interaction factor $\bar{q}$. Elementary Array Test Case with real-tuned devices, varying wave heading angle β.

6.5 Array size

In order to analyse collections of more than two devices, the Elementary Array Test Case is generalised to define any regular linear arrangement involving devices of the type specified by the Device Test Case (see Section 5.4). This consists of N converters, separated by a centre-to-centre distance L, aligned on the x-axis and with the centre of the array on the y-axis (shown in Figure 6.14 for five elements). The $\bar{q}$-factor as a function of wave number is shown in Figure 6.15 for each arrangement of up to five bodies, along with a ten-body array. Note that the simple shape of the curve gets

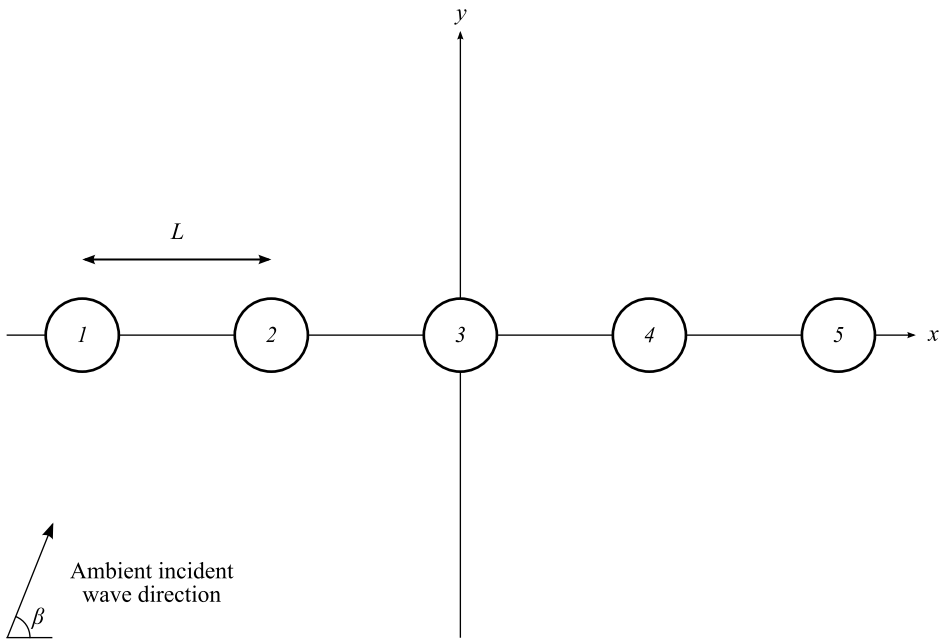

Figure 6.14: Illustration of linear array configuration for five devices.

increasingly deformed as the number of devices increases.

Increasing the number of devices in an array means that there are more combinations of body pairs that undergo interaction, and hence a potentially greater number of repeat values. The $\bar{q}$-factor plot then resembles the superposition of an increasing number of fluctuating curves. With the addition of devices to the Elementary Array Test Case, the new interaction distances are greater than or equal to those already present. Hence the repeat values that are distinct from the existing ones are smaller, leading to deformations of the plot that are of a finer character than the previously observed fluctuations.

From the isolated body velocity potential plots (Figures 5.6 and 5.11) the magnitude of interacted waves clearly decreases with distance from the originating device. This means that weaker interference occurs for arrays with larger inter-body separation. Also, the effect of any interaction process is enhanced if it occurs between more than one pair of devices. Therefore, since the most common interaction is between adjacent bodies in the array, the associated undulation dominates the appearance of the $\bar{q}$-factor plots for all N. Conversely, the rapid fluctuations associated with the up-wave interactions between more distant devices individually have a lesser influence on the shape of the curve.

We have already seen that for $\beta = \alpha_{ij}$, the wave energy reaching the down-wave

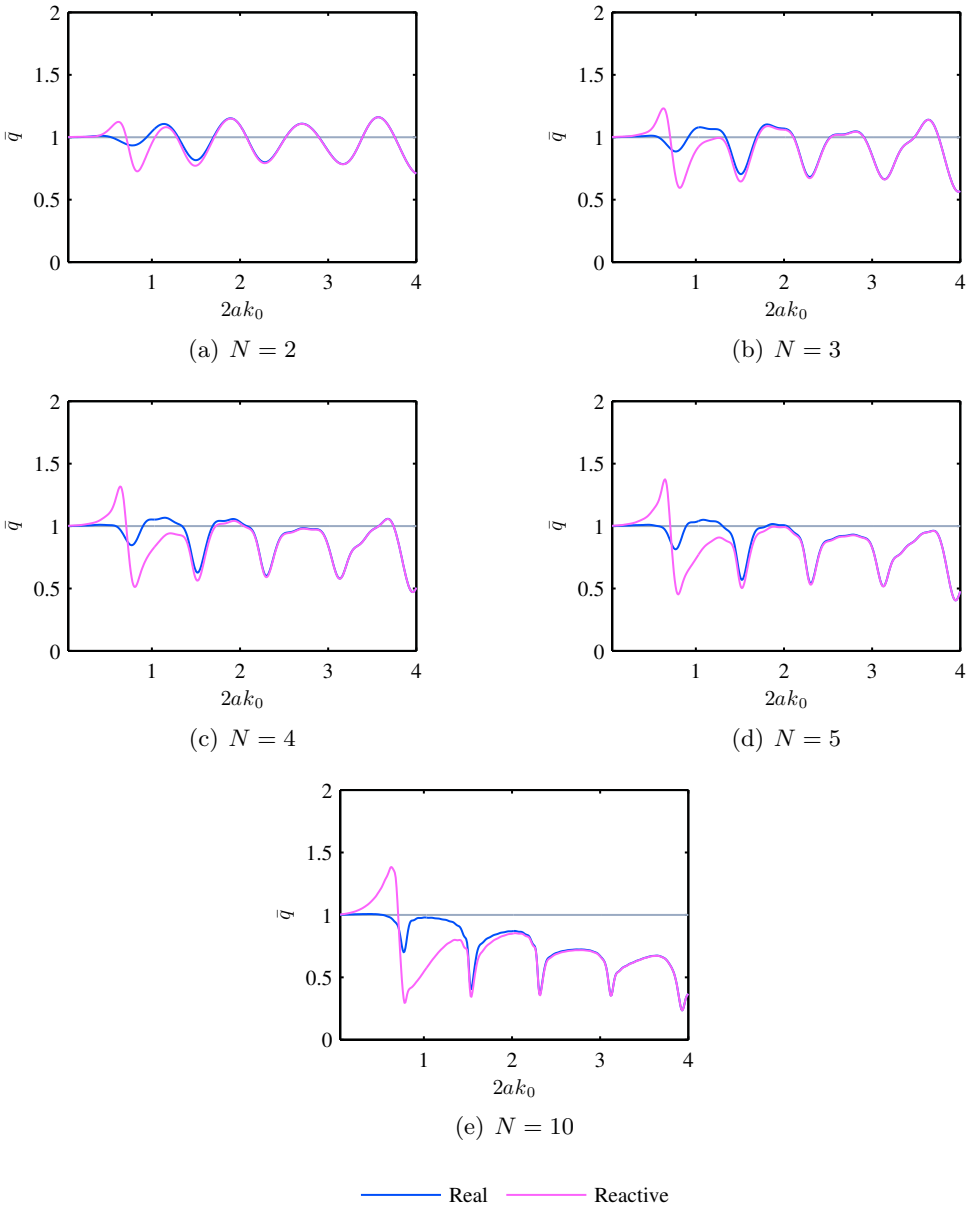

Figure 6.15: Interaction factor $\bar{q}$. Linear array configuration with device separation $L = 8a$, wave heading angle $\beta = 0$ and different array sizes N.

device of a pair may be attenuated, leading to diminished overall performance. When more than two devices are arranged in a linear formation, this effect is accentuated. From Figure 6.15, it is clear that as the number of devices increases, the $\bar{q}$-factor generally deteriorates, especially for higher wave numbers. To illustrate this further, Figure 6.16 shows the amplitude of total velocity potential surrounding an array of five real-tuned devices, relative to that of the ambient incident wave field at a wave number

for which there is a peak in the $\bar{q}$-factor ($2ak_0 = 1.87$). We see that there is a general decrease in wave amplitude further down-wave (towards the right of the figure). This means less energy is available for devices at the rear of the arrangement, even here where the overall performance is better than for neighbouring wave numbers. No such shadowing occurs for larger linear arrays when $\beta = \pi/2$.

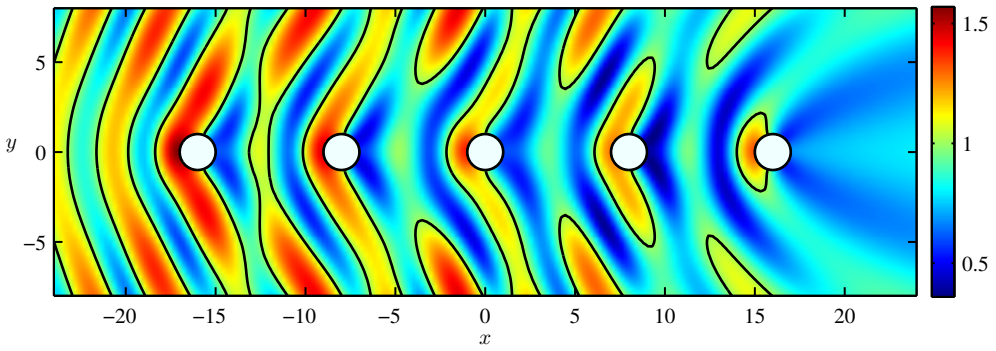

Figure 6.16: Amplitude of total velocity potential relative to that of ambient incident wave field (see colour bar). Linear array configuration of real-tuned converters with device separation $L = 8a$, non-dimensional wave number $2ak_0 = 1.87$, wave heading angle $\beta = 0$ and array size $N = 5$.

In Section 6.3, it was mentioned that 'attenuator' arrays such as the ones described here do not necessarily exhibit symmetry in the motion amplitudes between up- and down-wave elements. This is confirmed by the heave amplitude plots for the arrays described in this section, shown in Figures A.1 and A.2 of the appendix. It is also clear that the down-wave devices generally have more moderate motions than an isolated device, especially in the real-tuned case and for reactively-tuned devices at higher wave numbers where scattering effects dominate.

6.6 Array configuration

Arrangements other than the linear formation previously considered are analysed in this section, again involving devices of the type specified by the Device Test Case (see Section 5.4). The first of these is a circular configuration, formed such that the N devices lie evenly distributed around the circumference of a circle which is centred on the origin. Each element is separated from its nearest neighbours by a distance L, as

shown in Figure 6.17(a) for five devices.

Secondly a staggered array is formed by the addition of bodies at increasing y-coordinates to alternate sides of the three-device circular arrangement, starting with the side having negative x-coordinate. This is done in such a way as to make two rows of bodies parallel to the y-axis, with each body separated from the ones closest to it within the same row by a distance L. The median position of all the elements is then arbitrarily centred on the origin. This arrangement is shown in Figure 6.17(b) for five devices.

Figure 6.18 shows plots of the $\bar{q}$-factor as a function of wave number for circular arrays of up to five devices. The wave heading angle used in the calculations is $\beta = 0$ for all except the two-body arrangement, where it is set at $\beta = \pi/2$. The latter case, covered in detail in Section 6.4 is included here for comparison. As with the linear arrays, understanding of the results can be built up from consideration of the interactions between constituent body pairs.

The two down-wave devices in the array of size three interact with each other in much the same way as do the elements of the two-body array in waves normally incident to their connecting line. We therefore observe that two large peaks in the $\bar{q}$-factor close to $2ak_0 \simeq 2.2$ and $2ak_0 \simeq 4$, corresponding to waves scattered from one device to the other, are common to both cases (Figures 6.18(a) and 6.18(b)). Note that the interactions that occur in the three-device array also share similarities with those in an array where one of the down-wave cylinders is removed, that is to say the results given in Figure 6.11(b). In particular, there is an increase in the $\bar{q}$-factor around $2ak_0 \simeq 3$ that leads to the deformation of the trough occupying $2.2 \lesssim 2ak_0 \lesssim 4$ in Figure 6.18(a) that is observed in Figure 6.18(b).

Most of the body pair combinations in the circular array of four devices are equivalent to the case where waves meet a two-body linear array at an angle of $\beta = \pi/4$. Hence the overall interaction effects in the circular array are similar in nature but more accentuated due to replication of the phenomena (compare Figures 6.11(c) and 6.18(c)). This is in contrast to the circular array of five devices, which has more device pairs with different relative coordinates and hence repeat values. A $\bar{q}$-factor curve with a complicated fluctuating appearance therefore results (Figure 6.18(d)).

Moving on to the staggered arrangements, we see that for the same wave heading and separation distance, the $\bar{q}$-factor plots (Figure 6.19) show a striking resemblance

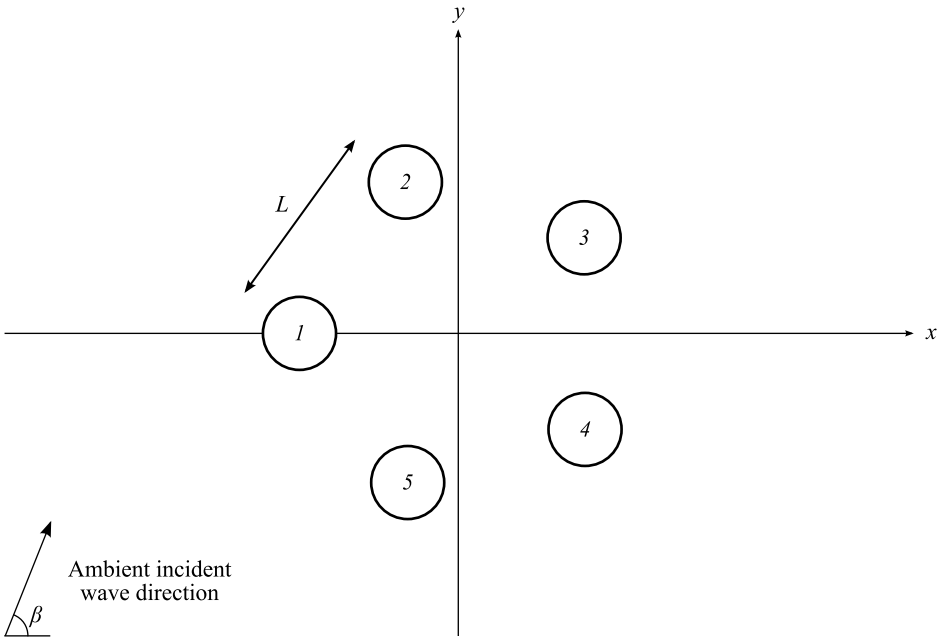

(a) Circular

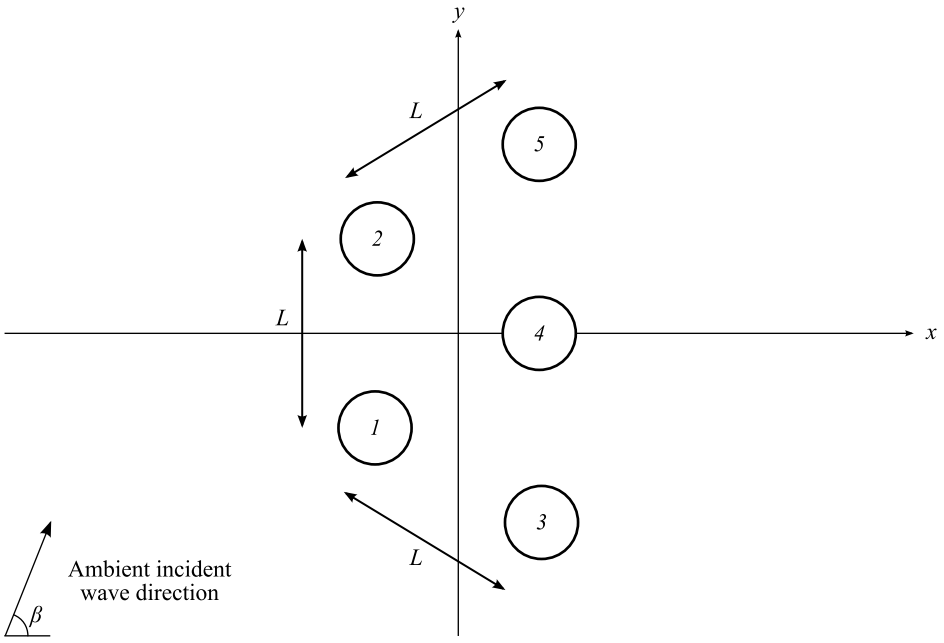

(b) Staggered

Figure 6.17: Illustration of alternative array configurations of five devices.

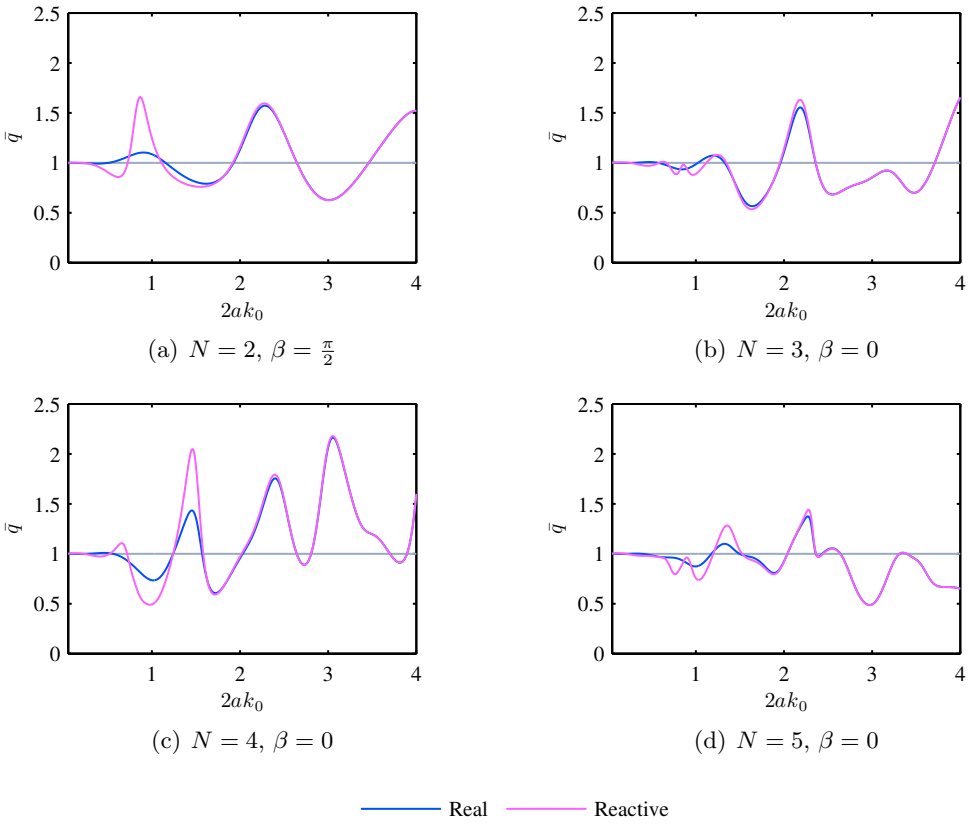

(a) $N = 2$, $\beta = \frac{\pi}{2}$ (b) $N = 3$, $\beta = 0$

(c) $N = 4$, $\beta = 0$ (d) $N = 5$, $\beta = 0$

Figure 6.18: Interaction factor $\bar{q}$. Circular array with device separation $L = 8a$ and different array sizes N.

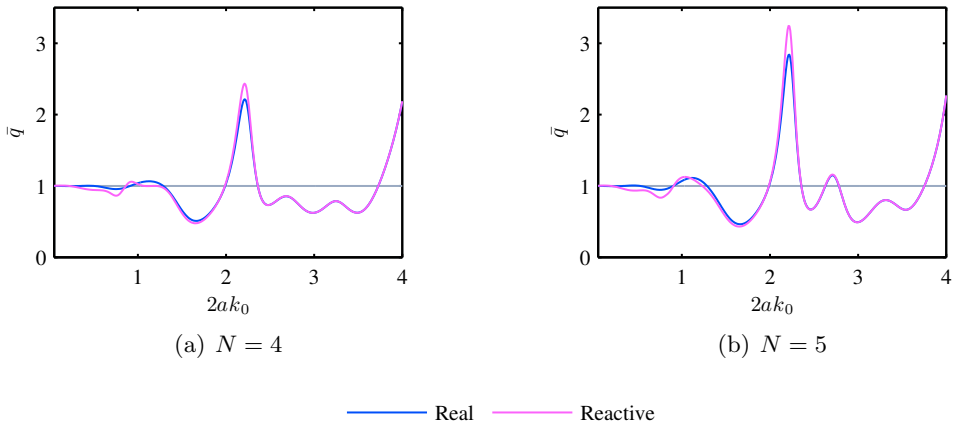

(a) $N = 4$ (b) $N = 5$

Figure 6.19: Interaction factor $\bar{q}$. Staggered array with device separation $L = 8a$, wave heading angle $\beta = 0$ and different array sizes N.

to the graph of the three-device circular array (Figure 6.18(b)). This is because the staggered configurations can be seen as an amalgamation of 'sub-arrays' consisting of three devices in a circular formation. The major difference between the plots for these circular and staggered cases is that the two large peaks corresponding to interaction between bodies with the same x-coordinate are enhanced in the four- and, to a greater degree, five-device arrangements. These peaks are derived from interactions between the pairs of bodies separated by $L = 8a$ for wave heading angle $\beta = \pi/2$, of which two and three are contained in the four- and five-body arrangements respectively. This effect is therefore exaggerated in larger staggered arrays. A feature of the four-device staggered arrangement that is not clearly exhibited in the three-converter array is the two smaller peaks in the $\bar{q}$-factor at $2ak_0 \simeq 2.7$ and $2ak_0 \simeq 3.3$. These correspond to constructive interaction between the devices across the long diagonal of the array and are magnified in the five-device case where two such paths exist.

Chapter 7

Array optimisation in regular waves

7.1 Introduction

We have seen in Chapter 6 how the layout of an array of wave energy converters can influence the overall performance. Now we consider the complimentary problem of seeking arrangements such that the array exhibits desired modifications in performance. Specifically, power output from a given set of devices is optimised at one incident wave frequency and direction in three different situations, as described in Section 7.2. The optimisation is applied using two different approaches in each case: the Parabolic Intersection (PI) method and a Genetic Algorithm (GA). The former is a heuristic technique that has been devised here to enable rapid array construction using only simple calculations (Section 7.3). The latter is an existing method, applied here with a novel crossover operator (Section 7.4). The resulting arrays will be analysed in detail in Chapter 8, and the optimisation techniques evaluated.

Since most optimisation processes require numerous calls to the objective function, calculation of the hydrodynamic interactions must be rapid. Whilst Fitzgerald and Thomas (2007) used the 'point absorber' approximation to enable this, the efficiency of the interaction procedure contained within this thesis allows scattering effects to be included along with those of radiation for the first time in a free optimisation of layout. Preliminary methodologies for the present techniques are contained in a paper by the author (Child and Venugopal, 2009) with the final approach summarised in a further publication (Child and Venugopal, 2010).

7.2 Problem definitions

Once wave energy devices have been designed and built, the primary concern for a project developer is to maximise output from the installed converters whilst minimising cost. The latter criterion will almost always lead to several devices being deployed in the same vicinity, in order to exploit the associated economies of scale. A similar physical situation also arises with a multiple-float device that itself consists of many absorbers. In both cases, this leaves the problem of maximising the power output from the converters, which will be solved in this chapter using the layout of the array only. It may also be useful to know the extent of the deterioration in performance when the array is arranged the worst possible manner. Even if the optimal solution could not be implemented in practice, this would provide some guidance as to which arrangements should be avoided.

The optimisation processes are demonstrated here by forming arrays of five devices, although both the PI method and the GA are still feasible with a larger number of converters. To reflect likely economic constraints of mass production, all devices are considered to be identical. Their geometry is chosen to be that of the Device Test Case specified in Table 5.1. Characteristics of the power take-off are determined in advance of array formation by using real and reactive tuning (see Section 5.3) at the pre-assigned *device tuning wave number* $2ak_0 = 0.8$. Optimisation with respect to array layout is intended to further modify the overall performance at incident wave parameters specified by the *array tuning wave number* and *direction*. For simplicity, these wave numbers will be taken to be equal and the wave direction taken to be that of the positive x-axis.

In the next chapter, both the array layout and power take-off characteristics are considered fixed under wave incidence of different frequencies and directions. These results are combined in Chapter 9 to predict performance in several irregular sea-states. In both sets of analysis, the spring and damping constants are sub-optimal in that power is only optimised at one wave frequency. However, it is in fact impossible for a device operating in a real sea to achieve optimal absorption of each frequency component without some knowledge of the future state of the system (Price, 2009). The effectiveness of a sub-optimal control strategy depends upon the wave energy spectrum under consideration, with narrow-banded spectra likely to produce the best results with its use.

The layout of the array is also sub-optimal in the sense that it cannot physically

represent the separate optima for all wave components simultaneously. Nevertheless, irregular waves are dealt with in this chapter by taking the peak frequency and mean direction from a representative spectrum before tuning the device and array to those parameters. This approach allows the optimisation to be performed efficiently, as each array only need be evaluated using one regular wave component. A more thorough yet time-consuming optimisation in the irregular wave case is presented in Chapter 9.

A quantity that plays an important role in the calculations is the interaction factor ($\bar{q}$ in equation (3.163)), since it is proportional to the total power output of the array. This value is used to assess the fitness of the arrays in the layout optimisation process and to analyse the resulting configurations in a meaningful manner (as in Chapter 6). A minimum separation distance of one diameter between body surfaces is imposed in the optimisation to reduce the likelihood of device collisions in practical applications. We thus seek to optimise

$$\bar{q}(x_1, y_1, \ldots, x_N, y_N), \tag{7.1}$$

where the $\bar{q}$-factor is expressed as a function of the device coordinates in the array, subject to the condition

$$\min_{i,j}\{L_{ij}\} \geq 4a, \tag{7.2}$$

where L_{ij} is the distance between i and j and a is the device radius.

Three problems optimisation problems are defined here. The first two concern achieving the best possible array performance under different regimes. The case in which scattered waves mostly dominate over those from radiation is considered in Problem 1. As we shall see in the next section, this can be achieved for the geometry and tuning wave number specified by using real tuning to determine the power take-off coefficients. Conversely, Problem 2 concerns radiated waves being dominant. This occurs when devices are reactively-tuned since then resonance ensures large motion amplitudes. In Problem 3, the capacity of array-related effects to diminish power output are investigated by minimising that quantity. Given that devices are tuned to a particular wave number, array layout is therefore optimised under incident waves of the same wave number and zero wave heading, with the following objectives:

Problem 1 Maximise power in an array of real-tuned devices

Problem 2 Maximise power in an array of reactively-tuned devices

Problem 3 Minimise power in an array of reactively-tuned devices

7.3 Parabolic Intersection

7.3.1 Method

The Parabolic Intersection method is a framework, devised in the course of this research, that assists its user in the design of arrays. The aim is to construct array configurations exhibiting desired properties, using only the simplest calculations. This approach facilitates rapid assessment of the most fundamental interaction processes, in terms of their contribution to array performance. As we have seen in the previous chapter, a good level of understanding may be gained by forming some strong assumptions about the nature of interactions. Making similar assumptions here therefore allows the effective assessment and construction of array configurations.

The present technique involves the analysis of the interference pattern surrounding each body in the array. By the time they reach other bodies in the array, radiated and scattered waves are generally smaller in amplitude than the ambient incident wave field. The incoming (and therefore outgoing) waves at each body may then be approximated by those surrounding an isolated body. It can be seen by comparing, for example, Figures 5.6(d) and 6.7(b) that such an approximation is a reasonable one. Furthermore, the isolated device potentials may be computed much more quickly and easily than the full wave fields.

The wave field surrounding an isolated device, tuned to the wave number $2ak_0 = 0.8$, has already been considered in Chapter 5, with Figures 5.6 and 5.11 showing the scattered and radiated velocity potentials at the free surface. Here, we further decompose each of these into the progressive part and the remaining evanescent part. Figure 7.1 shows the scattered wave field from both a real- and reactively-tuned device, since they are in fact equal. Figures 7.2 and 7.3 show the radiated wave field from a real- and reactively-tuned device respectively. In all cases, the amplitude of the evanescent component is much smaller than the progressive part, especially further away from the device. This means that the amplitude and phase of the total wave field is approximately equal to that of the progressive part. Note that the amplitude of the radiated wave field from the reactively-tuned converter is larger than that of the scattered wave field throughout the domain. Conversely for real-tuned devices, the scattered wave field is the largest in most areas, especially up-wave of the body.

Only the wave field that contributes most to the interactions will be subsequently

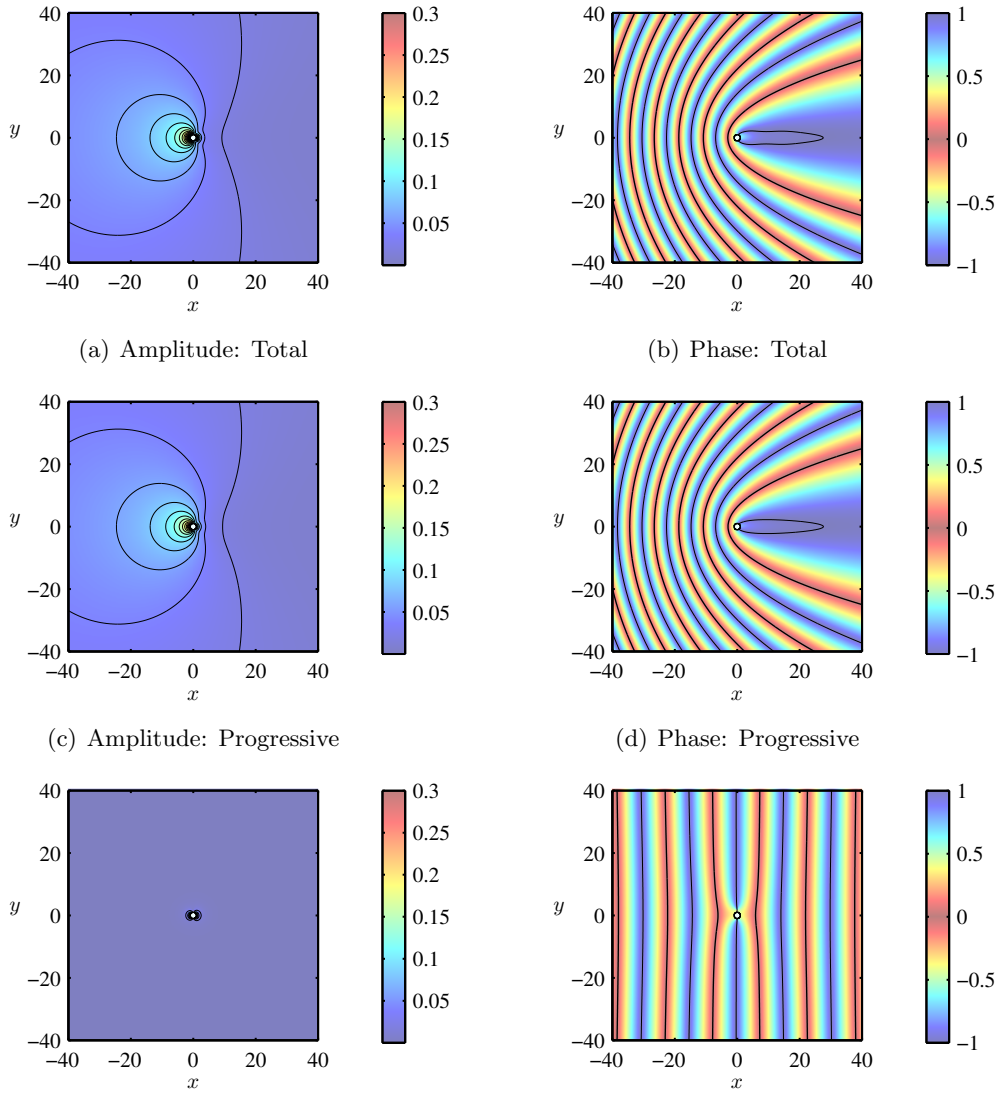

(a) Amplitude: Total

(b) Phase: Total

(c) Amplitude: Progressive

(d) Phase: Progressive

(e) Amplitude: Evanescent

(f) Phase: Evanescent

Figure 7.1: Scattered velocity potential surrounding isolated real-tuned (or reactively-tuned) device at the free surface. Amplitude normalised by that of the ambient incident wave field (see colour bar). Phase given relative to that of ambient incident wave field, normalised by π (see colour bar). Total potential further decomposed into the progressive part and the remaining non-progressive (evanescent) part.

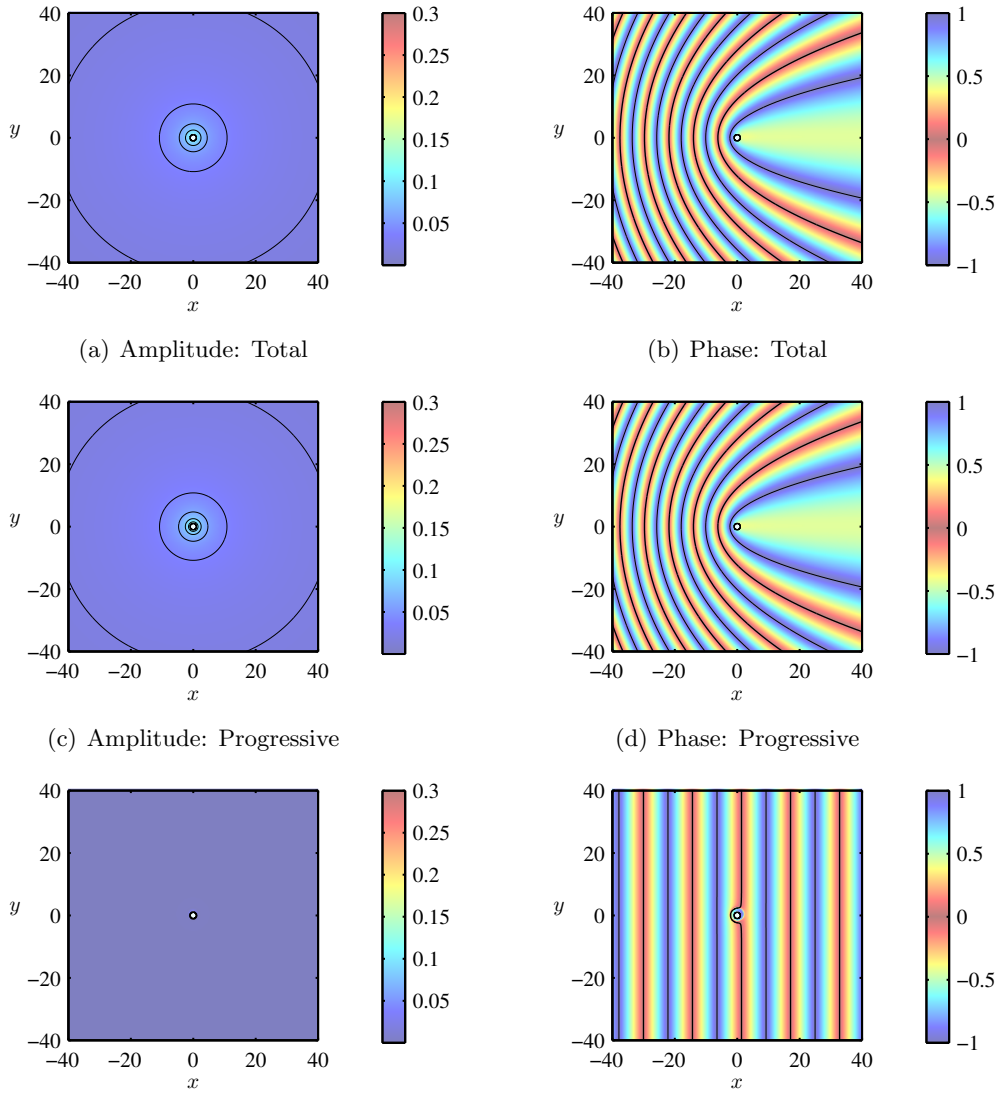

(a) Amplitude: Total

(b) Phase: Total

(c) Amplitude: Progressive

(d) Phase: Progressive

(e) Amplitude: Evanescent

(f) Phase: Evanescent

Figure 7.2: Radiated velocity potential surrounding isolated real-tuned device at the free surface. Amplitude normalised by that of the ambient incident wave field (see colour bar). Phase given relative to that of ambient incident wave field, normalised by π (see colour bar). Total potential further decomposed into the progressive part and the remaining non-progressive (evanescent) part.

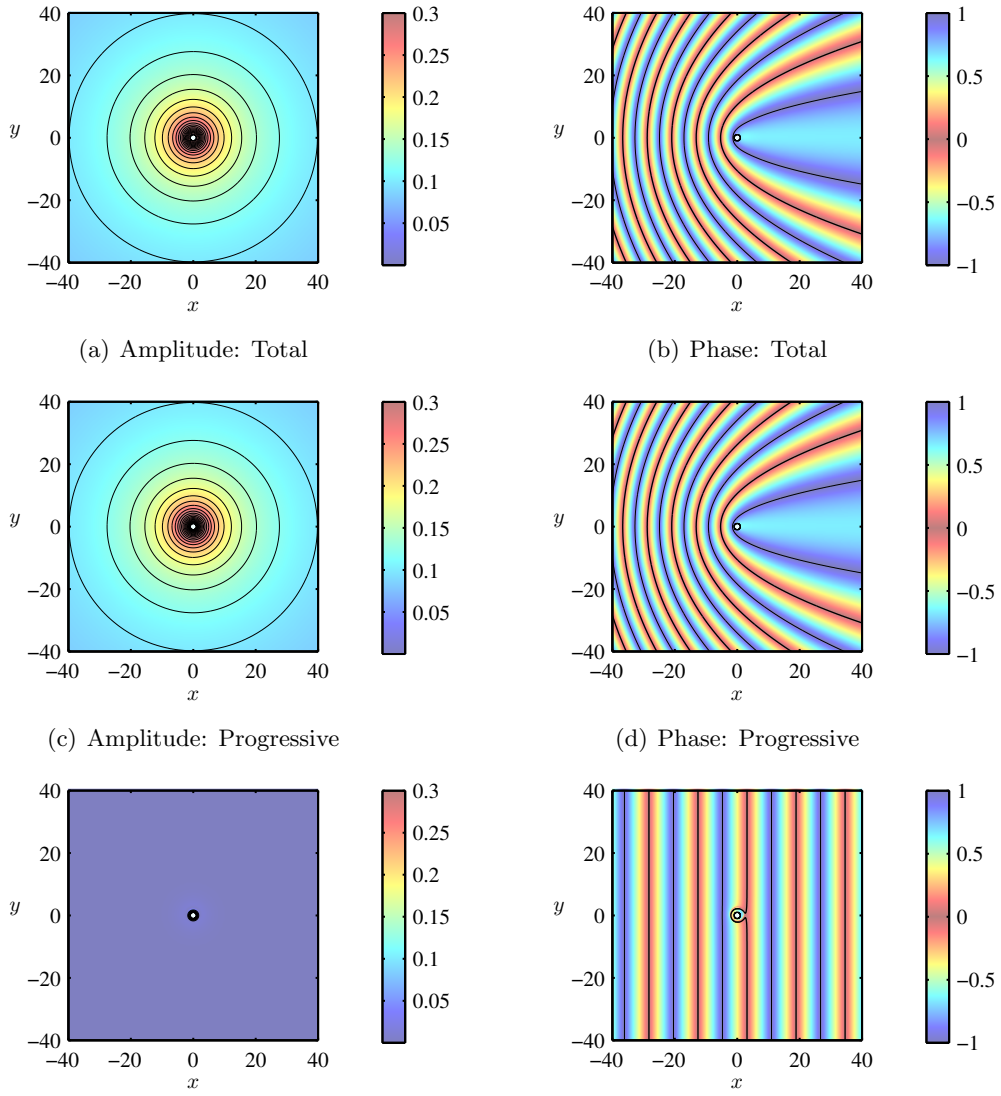

(a) Amplitude: Total

(b) Phase: Total

(c) Amplitude: Progressive

(d) Phase: Progressive

(e) Amplitude: Evanescent

(f) Phase: Evanescent

Figure 7.3: Radiated velocity potential surrounding isolated reactively-tuned device at the free surface. Amplitude normalised by that of the ambient incident wave field (see colour bar). Phase given relative to that of ambient incident wave field, normalised by π (see colour bar). Total potential further decomposed into the progressive part and the remaining non-progressive (evanescent) part.

used. For real-tuned devices, the progressive part of the scattered wave field will be retained. In the case of reactively-tuned devices, however, it is the progressive part of the radiated wave field that is kept.

We now attempt to explain the important features of the progressive scattered and radiated wave field phase plots that form the basis of the current method. Suppose there is a single device located at the origin O with waves approaching in the positive x-direction and we wish to know the points $(x_\mathrm{p}, y_\mathrm{p})$ where the interacted waves are in phase with ambient incident wave field. Assuming momentarily that there is no phase shift at the body, the case reduces to that under which the interaction distance of Chapter 6 was derived. Instead of finding different wave numbers that give rise to the same interaction distance, here we wish to find different points at which the interference is similar. Consider the interaction distance associated with waves scattered or radiated from O to $(x_\mathrm{p}, y_\mathrm{p})$. From the definition, this is given by the total distance that interacted waves have travelled less the distance that ambient waves have travelled at $(x_\mathrm{p}, y_\mathrm{p})$, both measured from some common reference line. The interaction distance, shown by the red line in Figure 7.4, is therefore

$$D = \sqrt{x_\mathrm{p}^2 + y_\mathrm{p}^2} - x_\mathrm{p}, \tag{7.3}$$

which is an expression of the equation (6.1). For interacted and ambient waves to be in phase at $(x_\mathrm{p}, y_\mathrm{p})$, we require that the phase associated with the interaction distance (the interaction phase given by (6.2)) is a whole multiple of 2π:

$$Dk_0 = 2\pi P, \qquad P \in \mathbb{Z}. \tag{7.4}$$

Inserting (7.3) into the equation above and rearranging results in the following loci of points where the two wave fields are in phase:

$$y_\mathrm{p}^2 = 4\left(\frac{P\pi}{k_0}\right)\left[x_\mathrm{p} + \left(\frac{P\pi}{k_0}\right)\right]. \tag{7.5}$$

This describes a family of parabolas (indexed by P and correspondingly numbered in Figure 7.4), sharing the centre of the interacting body as their focus (Courant and John, 1989, pp. 244–5, 248). Similarly, the points where the two wave fields are out of phase with each other will form a family of parabolas with the same focus, between the original set of curves. A similar argument applies for other angles of attack, with the device at

locations other than the origin and where the phase shift at the body in non-zero but constant over the angular range.

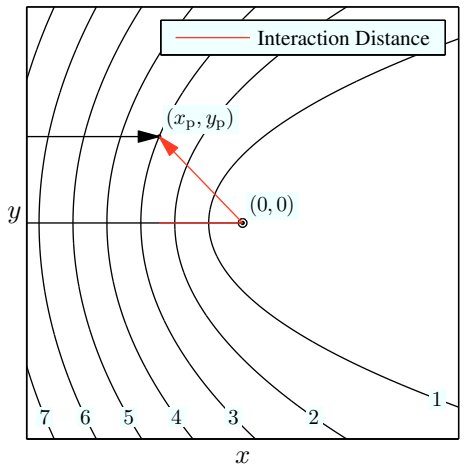

Figure 7.4: Illustration of parabolic curves of interference from a device at $(x_0, y_0) = (0, 0)$. Parabolas are labelled consecutively away from the device. The paths of ambient and interacted waves from the left hand side of the diagram to the point (x_p, y_p) are shown by solid and dashed arrows respectively.

In Figures 7.1, 7.2 and 7.3, the actual curves of minimum and maximum phase difference between the wave fields are shown in the phase plots by thick and thin contours respectively. Clearly the phase shift at the device is not as simple in practice as has been assumed in the derivation of the parabolic curves above. However, despite slight deviations to their shape, the actual curves are approximately parabolic in form, as predicted. They will therefore simply be referred to as *parabolas* from here on and numbered in ascending order ($p = 1, 2, \ldots$) outwards from the device for the two sets of parabolas separately.

The PI method works iteratively by adding further devices to an existing array. As we have seen in Chapter 6, devices at which interacted and ambient wave fields are in phase with each other experience constructive wave interference and so generally perform better than they would do otherwise. Hence for Problems 1 and 2, desirable locations to situate converters are points on the curves of maximum constructive interference. Thus, if the set of thick parabolas from the dominant wave field (Figure 7.1(d) or 7.3(d)) is superimposed around a device in the array, potential locations may be identified as those lying on one of these curves. Points at which parabolas surrounding two existing devices intersect are even more advantageous and so one of the main tasks in this method is to find points of parabolic intersection. A similar process may be performed using a set

of thin parabolas from the dominant wave field of Figure 7.3(d) to create destructive interference in Problem 3.

7.3.2 Implementation

Although the PI procedure vastly reduces the number of potential body locations available, many options in the design of the array still remain. A strategy for construction is therefore required. In this section, three formation types are introduced that will guide the process of array creation: *linear*, *pentagonal* and *staggered*. Each of these may then be applied to the three problems at hand by selecting the appropriate set of parabolas from the dominant wave field.

Linear: A line of equally spaced devices is perhaps the simplest practical array configuration. Furthermore, it allows converters to both cause and experience the desired variety of interference in partnership with the adjacent elements in the row. The construction of a linear array may be carried out in the following manner, as illustrated by Figure 7.5. First select two natural numbers $p_\mathrm{a}, p_\mathrm{b} = 1, 2, \ldots$ relating to parabolas in the interference pattern of the dominant wave field. Then:

1. Place the first device at the origin.
2. Overlay the p_a^th parabola around the first device. Place a second device on this parabola such that the first also lies on the p_b^th parabola overlaid around the second.
3. Repeat step 2, starting with the second device and so on, until all five devices are situated in a line.

Pentagonal: As can be seen in Figure 7.1, scattered waves are strongest up-wave of an isolated device. Hence, in the case of real tuning (and to some extent reactive tuning), this region may be a valuable place to situate further converters and take advantage of the increased capacity for interaction. The pentagonal array formation is therefore designed to incorporate many instances of up-wave interaction. The procedure is simplified here by insisting that the final array is symmetric with respect to the incident wave direction. Construction proceeds as follows, as shown in Figure 7.6. First select four natural numbers $p_\mathrm{a}, p_\mathrm{b}, p_\mathrm{c}, p_\mathrm{d} = 1, 2, \ldots$ relating to parabolas in the interference pattern of the dominant wave field. Then:

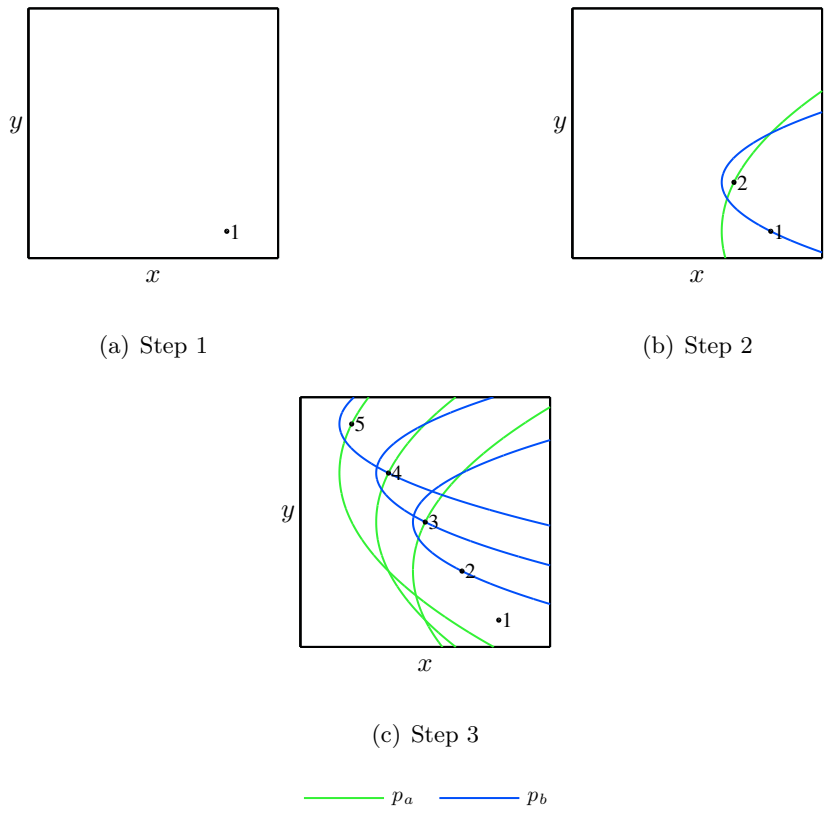

(a) Step 1

(b) Step 2

(c) Step 3

Figure 7.5: Linear array construction using the PI method.

1. Place the first device at the origin.

2. Overlay the $p_{\mathrm{a}}^{\mathrm{th}}$ parabola around the first device. Place a second device on this parabola such that the first also lies on the $p_{\mathrm{a}}^{\mathrm{th}}$ parabola overlaid around the second.

3. Overlay the $p_{\mathrm{b}}^{\mathrm{th}}$ parabola around the first device and the $p_{\mathrm{c}}^{\mathrm{th}}$ parabola around the second. Place the third device at the intersection of these two parabolas.

4. Repeat step 3, interchanging p_{b} and p_{c}, to determine the location of the fourth device.

5. Overlay the $p_{\mathrm{d}}^{\mathrm{th}}$ parabola around the third and fourth devices. Place the fifth device at the intersection of these two parabolas.

Staggered: One intuitively appealing layout involves the offsetting of one row of machines from another with respect to the principle direction of energy transfer. This

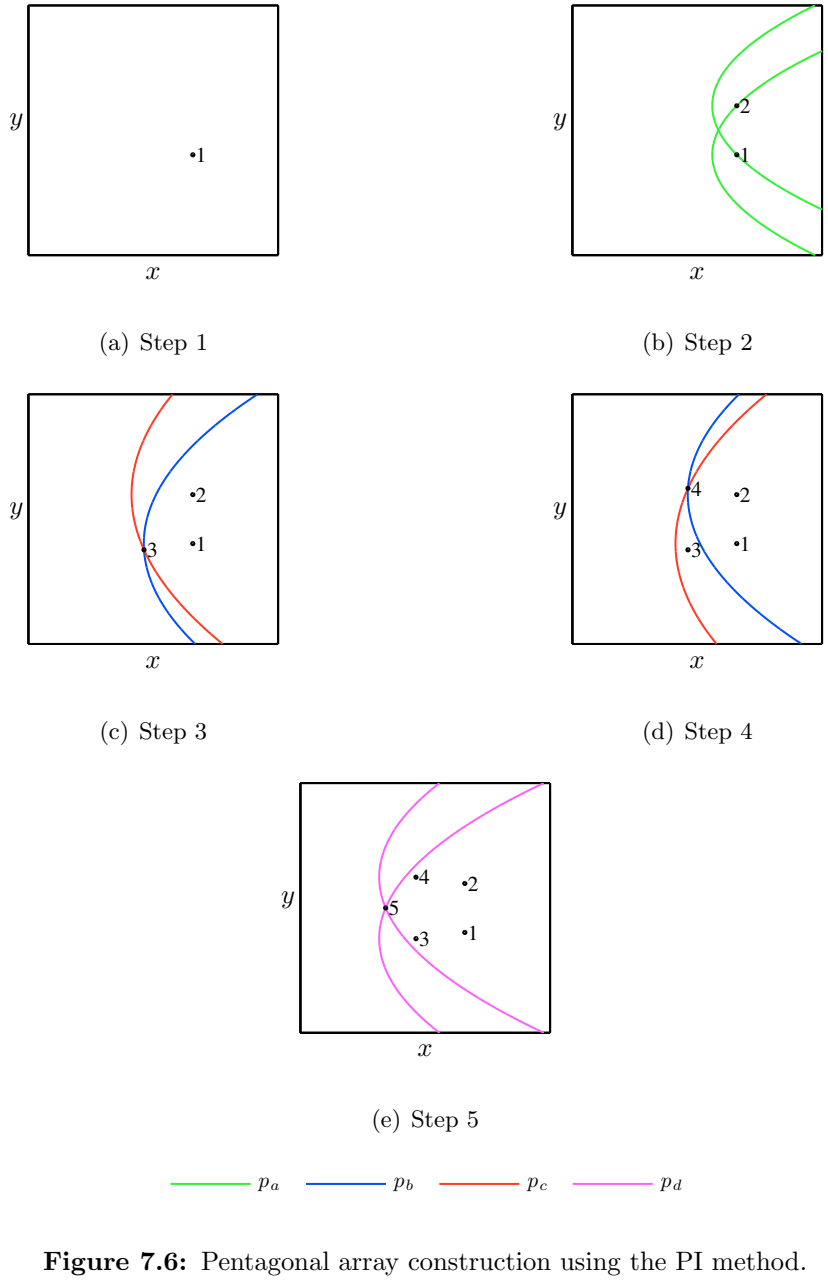

(a) Step 1

(b) Step 2

(c) Step 3

(d) Step 4

(e) Step 5

Figure 7.6: Pentagonal array construction using the PI method.

allows the array to be fairly compact whilst hopefully minimising the worst of the possible shadowing effects. The staggered formation also permits desirable interference processes between devices in the same row as well as between elements in different rows. The construction process (see Figure 7.7) is thus carried out as follows. First select two natural numbers $p_{\mathrm{a}}, p_{\mathrm{b}} = 1, 2, \ldots$ relating to parabolas in the interference pattern of the dominant wave field. Then:

1. Place the first device at the origin.
2. Overlay the $p_{\mathrm{a}}^{\mathrm{th}}$ parabola around the first device. Place a second device on this parabola such that the first also lies on the $p_{\mathrm{a}}^{\mathrm{th}}$ parabola overlaid around the second.
3. Overlay the $p_{\mathrm{b}}^{\mathrm{th}}$ parabola around the first and second devices. Place the third device at the intersection of these two parabolas.
4. Repeat steps 2 and 3, using the same choices for p_{a} and p_{b}, such that the fourth and fifth devices are the mirror images of the second and third with respect to the x-axis.

In order to assist the array construction process, a graphical user interface (GUI) was created (see Figure 7.8) in the MATLAB computing environment. The user is required to arrange the devices in approximately the correct positions using appropriate sets of parabolas from the isolated device potential that may be made visible on the screen. The device pairs between which interference is desired may be selected and the resulting directions displayed as arrows. The programme will then 'snap' the bodies that are to receive interacted waves to the nearest parabola from the appropriate interference patterns, using a fast local optimisation routine. Extra savings in computation time may be achieved by stipulating that the array is required to be symmetric with respect to the incident wave direction. The resulting coordinates and $\bar{q}$-factor for the arrangement may finally be saved to a file. This programme facilitates a rapid, intuitive way of designing arrays in which any number of other design constraints may be incorporated by the user.

The GUI was used to create linear, pentagonal and staggered arrays for each of Problems 1, 2 and 3. Furthermore, this was performed for different selections of the parabola indices involved in the designs. However, only arrangements that satisfied the minimum body separation condition (7.2) were constructed. Additionally, a maximum

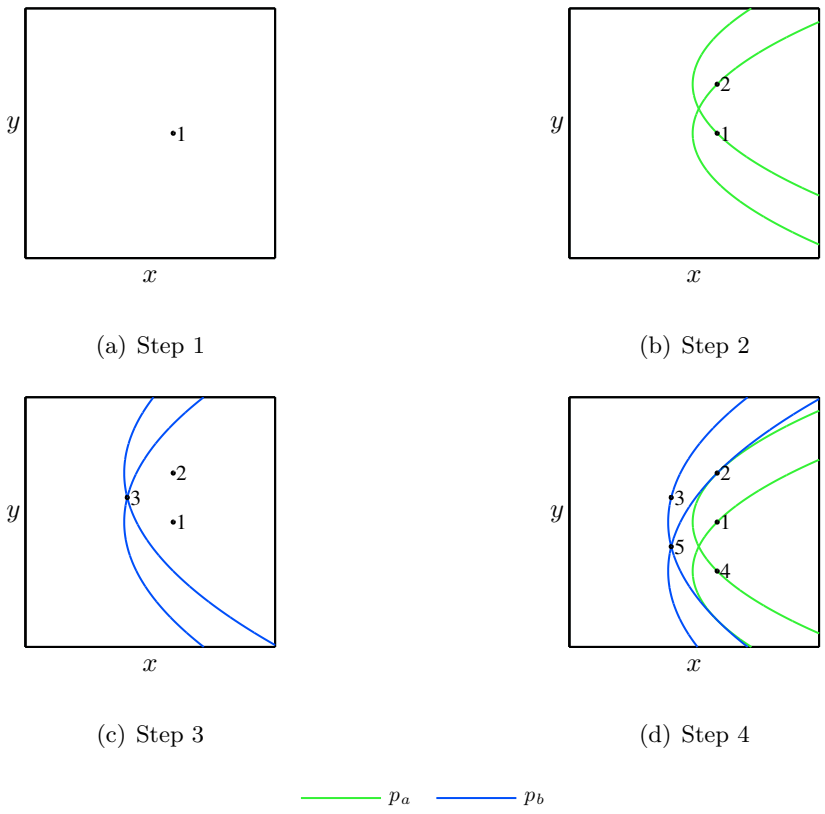

(a) Step 1 (b) Step 2

(c) Step 3 (d) Step 4

Figure 7.7: Staggered array construction using the PI method.

separation of $40a$ in the x- or y-direction between interacting body pairs was imposed in order to limit the number of array candidates. This is not likely to exclude any configurations that exhibit strong interference, since interaction strength generally decreases with separation.

Due to their symmetry, the reflections of linear arrangements in axes parallel or perpendicular to the incident wave direction are equivalent in terms of performance. Therefore, only layouts for which $p_\mathrm{b} \leq p_\mathrm{a}$ and the device number increases with the y-coordinate were created. The special case of $p_\mathrm{a} = p_\mathrm{b}$ implies that the line of devices is perpendicular to the direction of oncoming waves. The $\bar{q}$-factor for all eligible linear arrangements is shown in Tables A.1(a), A.2(a) and A.3(a) of the appendix for Problems 1, 2 and 3, labelled PL followed by the problem number and the subscript $p_\mathrm{a}p_\mathrm{b}$.

For the pentagonal formation, only arrangements where the x-coordinate decreases from the first to the third and the third to the fifth device were considered. These are shown in Tables A.1(b), A.2(b) and A.3(b) of the appendix for Problems 1, 2 and 3,

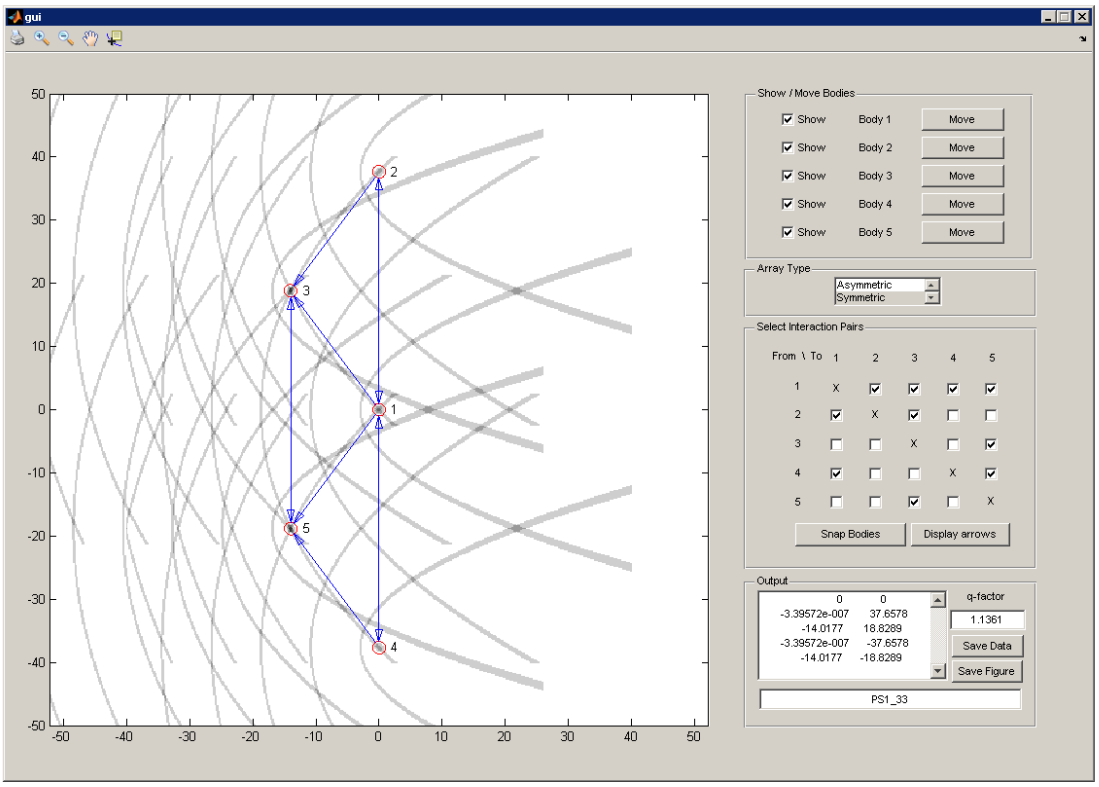

Figure 7.8: Graphical User Interface to assist in the construction of arrays using the PI method.

with the label beginning PP and the subscript $p_{\mathrm{a}}p_{\mathrm{b}}p_{\mathrm{c}}p_{\mathrm{d}}$.

Only staggered configurations where the x-coordinate decreases from the first to the third device were considered. Such arrangements are shown in Tables A.1(c), A.2(c) and A.3(c) of the appendix for Problems 1, 2 and 3, with the label beginning PS and the subscript $p_{\mathrm{a}}p_{\mathrm{b}}$.

Although the desired interference is likely to be stronger for more closely spaced arrays, unintended interactions may mean that a configuration does not attain the expected level of performance. Therefore the array candidates are ranked by their $\bar{q}$-factor and the most highly optimised configuration (highest $\bar{q}$-factor for Problems 1 and 2, lowest for Problem 3) selected for each problem to receive further analysis in the next chapter. These arrays are shown in bold type in the appropriate table; $\mathrm{PS1}_{33}$ is chosen and renamed P1, $\mathrm{PS2}_{22}$ as P2 and $\mathrm{PS3}_{22}$ as P3.

Note that there is a significant discrepancy between the top and bottom of each table, which shows that many other factors not taken into account in this process can have an influence on array performance. However, the nature of interference (that is to say, constructive or destructive) is the same for most examples within each problem.

This suggests that the dominant factors have indeed been taken into account in the construction procedure.

7.4 Genetic Algorithm

7.4.1 Method

A Genetic Algorithm (GA) is a type of optimisation routine that takes its inspiration (and much of its terminology) from the theory of evolution. Rather than performing deterministic iterations on one solution, GAs work with a collection of solutions that are allowed to develop towards an optimum in a controlled random manner.

GAs are well suited to problems where the search space is large, not unimodal, not well understood and no absolute global optimum is required (Mitchell, 1996). In the present application, the dimension of the solution space increases by two with each additional body and so may quickly become large. Additionally, the spatial periodicity of the waves leads to a multi-peaked search space, yet not enough is known about the solution to easily apply a more specific algorithm. Finally, the practical nature of the engineering application means that a solution may satisfactorily be judged on its own performance without undue concern regarding its global optimality. GAs have already been applied effectively in a number of array-related problems, such as the design of acoustic lenses (Håkansson et al., 2004), electromagnetic antennas (Haupt, 1995) and communication transmitter networks (Chopard et al., 1997). Whilst these applications may inform the choice of algorithm, it should be noted that the problems are not equivalent since both scattering and radiation occur in arrays of wave energy devices.

In general, Genetic Algorithms involve representing the defining characteristics of solution candidates (termed *individuals*) as encoded *genes*. The first step is then to create a set of individuals (usually at random) which forms the initial *population*. A number of iterations (*generations*) then follow in which new populations are created. At each stage, the aptitude of the individuals in solving the problem is assessed by assigning each a real number (*fitness*) using a pre-defined function. These values are *scaled* to a more convenient range with the fittest individuals more likely to be chosen (*selected*) to pass on some of their characteristics to the next generation. This occurs by one of three methods: *elitism*, *mutation* or *crossover*. Elitism involves the very fittest individuals being transferred to the next generation unchanged. Individuals that are

mutated have their genetic definition randomly perturbed before entering the population of the following generation. Crossover entails taking more than one *parent* individual from the population and combining their genes in some way to form new individuals (*offspring*). The population size stays constant over the generations and so generally the least fit individuals for whom there is not space in the new population will die. This process is repeated over a number of generations with the best individual at the final iteration becoming the overall solution. For further details on GAs and variations on the method, see for example Mitchell (1996).

7.4.2 Implementation

The optimisation was implemented using the Genetic Algorithm and Direct Search toolbox (Version 4.0) from the MATLAB Product Family. Each problem was expressed as a minimisation with respect to array layout by taking the fitness function to be $-\bar{q}$ in Problems 1 and 2, and to be $\bar{q}$ in Problem 3, with array layouts constituting the individuals. The fitness function was then adapted by forcing the output to be zero whenever the minimum device spacing condition (7.2) is violated. This is one way to encourage the formation of arrays that satisfy the constraint.

An array layout can be defined using a pair of coordinates for each body. However, interactions are independent of the position of the entire array within the domain, so one pair of coordinates may in fact be eliminated. Devices are therefore numbered consecutively and all body coordinates (except those of body 1) defined relative to an origin at the one labelled with the preceding number. Since there are five bodies considered in these examples, a sequence of eight real numbers therefore represents each array. The main alternative, that is to say discretisation and binary encoding of these coordinates, is not the necessary or natural choice. In fact, the choice of representation is not critical here since each component operator in this GA implementation may first express the genes of the individual in a more convenient form before acting upon it.

The choice of the remaining parameters and operators to use in the algorithm can have a significant effect on the rate of convergence and the eventual solution, although there is no accepted methodology as to how these should be determined (Mitchell, 1996). In fact, the question of finding the best settings represents a complex optimisation problem in itself. We opt here for a simple technique that will in practice almost always lead to some performance improvement without the need for extensive additional coding.

The parameter setting algorithm involves grouping the available options together by their function within the GA. Options are then taken from the first group in turn and used to replace those in a pre-determined complete set of options. Under these modified option sets, the GA is executed a number of times with different initial random seeds. The setting from the first group that leads to the best GA performance is then selected to replace the existing option in the complete set, which is subsequently passed to the next group. The process thus repeats until all option groups have been tested. This strategy is by no means a full optimisation of parameters but if the initial complete set of options is a subset of those belonging to the option groups, then at every stage one option represents no change from the previous stage. Hence the performance of the GA cannot get worse as the algorithm proceeds.

The performance of each option set is rated by taking the mean of the fitness values that are output from fifty trials of the GA, with the lowest value being preferable. An exception to this is in stage 8 below, where the long computation times dictate that only one trial is feasible. This parameter setting algorithm has only been performed using the criteria of Problem 1 to assess the array configurations. The resulting options are ultimately employed in the optimisation of array layout for all three problems, although a fuller treatment might involve individual parameter setting.

The option groups are listed below, numbered in the order in which the algorithm progresses. Within each option type, delimited by semi-colons, there may be one or more lists of additional parameters. In this case, distinct options are defined by a single choice from each list of parameters.

1. **Constraints:** *Minimum spacing* constrained and unconstrained with *maximum spacing* constrained and unconstrained.

2. **Crossover:** *Scattered*; *Single point*; *Two point*; *Intermediate* with *ratio* parameters 0.5, 1, 1.5; *Heuristic* with *ratio* parameters 1.1, 1.2, 1.3; *Arithmetic*; *Custom*.

3. **Mutation:** *Gaussian* (*relative* and *absolute*) with *scale* parameters 0.5, 1, 2 and *shrink* parameters 0, 0.5, 1; *Uniform* (*relative* and *absolute*) with *rate* parameters 0.005, 0.01, 0.02; *Adaptive feasible* (*relative* and *absolute*).

4. **Reproduction proportions:** *Elite count* parameters 1, 2, 4, 8 with *crossover fraction* parameters 0, 0.7, 0.8, 0.9, 1.

5. **Selection:** *Stochastic uniform*; *Remainder*; *Uniform*; *Roulette*; *Tournament* with *tournament size* parameters 2, 4, 8.

6. **Scaling:** *Rank*; *Proportional*; *Top* with *quantity* parameters 0.2, 0.4, 0.6; *Shift linear* with *max survival rate* parameters 1.5, 2, 3.

7. **Creation:** *Uniform* (*relative* and *absolute*) with *initial range* parameters [-5,5], [-10,10], [-50,50].

8. **Simulation size:** *Population size* parameters 20, 50, 100 with *generations* parameters 20, 50, 100.

In this list of options, '*minimum spacing* constrained' means an insistence that arrays created at every stage of the GA satisfy the condition (7.2). Similarly, '*maximum spacing* constrained' means that all relevant arrays contain devices that are no further than $40a$ from the centroid of the arrangement. Note that even if the minimum spacing condition is not imposed, the fitness of the arrangement is defined to be zero for arrays that violate condition (7.2). The option *relative* or *absolute* denotes whether the function acts upon the coordinates of the devices expressed relative to each other (as described earlier) or on the set of absolute coordinates. Apart from the *custom* crossover which will be described below, all other options are detailed in the documentation for the toolbox that is used here (The MathWorks, Inc., 2010a).

The initial set of options is underlined once in the list above, with the final options marked underneath with a double line. Where these coincide with each other, only the latter is shown. Note that the constraint on the maximum spacing is not needed, presumably because the interactions are weaker and so the fitness inferior for widely spaced arrays. On the other hand, the minimum spacing condition was found to be beneficial in comparison with just altering the fitness value for unacceptably closely spaced arrays. We may reasonably predict that increasing either of the final two parameters will enhance the performance of the GA, at the expense of computation time. However, it was found that in the single trial performed with the other options fixed, no improvement was made by increasing the number of generations from 50 to 100. The smaller value was therefore taken.

Figure 7.9 graphically depicts the progress of the parameter setting algorithm. On the independent variable axis is marked the option groups as listed above. On the dependent variable axis is the mean of the fitness values produced by the trials of the

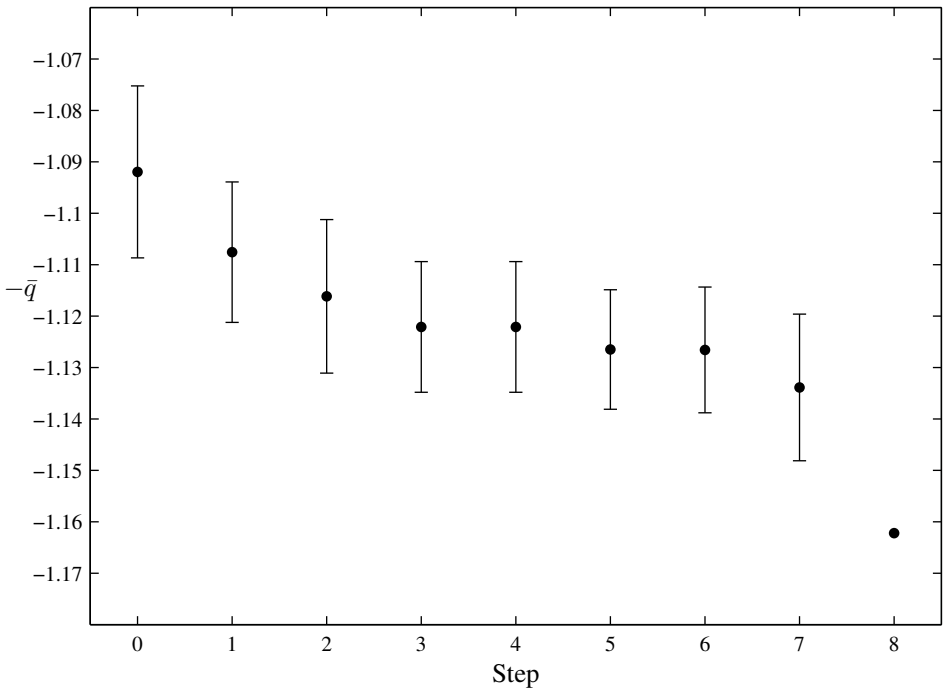

Figure 7.9: Performance of the GA with different parameter settings. Mean (points) and standard deviation (bars) of fitness values at each step of parameter optimisation algorithm. Fifty trials for Steps 1-7, one for Step 8 (and so no bars shown).

GA with the final option from that group applied. Group 0 denotes the initial set of options. The bars mark one standard deviation of the fitness values above and below the mean, with none shown in group 8 where only one trial was performed. This graph shows a clear improvement in the performance of the GA as the parameter setting algorithm progresses and hence the arrays that it produces are likely to be improved.

This parameter setting algorithm could be repeated, starting with the final set of parameters as the initial set if improved performance is desired. The efficacy of the GA could also be measured with different indicators, such as the *on-line* and *off-line performance* (see Mitchell (1996)), although this is not explored here. In the next paragraphs, the final options determined by the algorithm are described in more detail, including the new crossover operator.

.

Crossover: *Custom.* Crossover is a crucial operator in a GA because it allows beneficial features from different arrays to be combined, potentially producing a fitter individual than either parent. It is also important that these features have the chance to be inherited without being significantly altered. From the single body interference

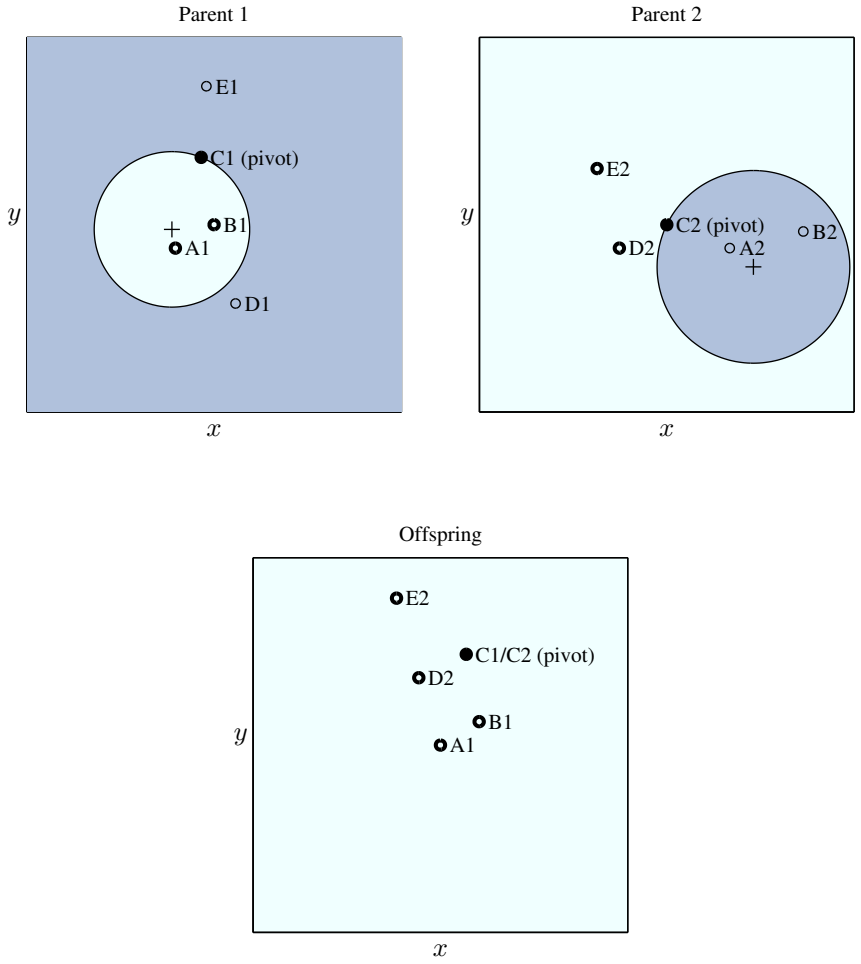

Figure 7.10: Illustration of the custom crossover operator. White area in each parent array contains the body locations that will be inherited, which are denoted by the thicker circles. The solid black dot represents the pivot body and the other devices are shown with thin circles. Body labels in the offspring relate to those in the parents from whom their position is inherited.

patterns in Figures 7.1, 7.2 and 7.3, it is clear that interactions between devices depend mainly on their positions relative to one another. However, in a given array it is not known which of these interactions are the most advantageous to overall performance. Hence the crossover operator will take some subset of devices from the first parent and use their relative positions to arrange bodies in the offspring array, in the hope that beneficial interactions will be preserved. Interactions are likely to be strongest for devices within the same vicinity of the array, so those enclosed by a randomly placed circle within the array are chosen. The relative positions of the remaining bodies in the offspring array will be determined by the bodies outside another such circle in the second parent, thus maintaining the average spacing between devices. It is important to note that this crossover operator merely allows beneficial interactions in arrays to be combined. It may be that it creates arrays that are successful as a result of unintended interactions between bodies from each parent, or indeed that are unsuccessful. The procedure, illustrated in Figure 7.10, is therefore as follows:

1. Randomly select the number of bodies ($n_1 = 2...N-1$) that will be used from Parent 1. The number of bodies from Parent 2 will then be $n_2 = N + 1 - n_1$.

2. In Parent 1, choose a point with coordinates taken from a uniform random distribution of range $[-20a, 20a]$. Expand a circle around this point until it encloses exactly $n_1 - 1$ body centres and intersects a further *pivot* body. Select these bodies for inheritance.

3. Repeat the previous step with Parent 2 until the circle excludes exactly $n_2 - 1$ body centres and intersects a further *pivot* body. Select these bodies for inheritance.

4. Form the offspring array such that the first n_1 bodies have the same coordinates relative to each other as those selected from Parent 1. Arrange the remaining bodies using the relative positions of the n_2 bodies from Parent 2, such that the pivot elements from each parent are aligned.

Mutation: *Adaptive Feasible (absolute).* The genes of the parents are perturbed by a random set of coordinates whose magnitudes change with respect to the success of the previous generation. If the most recent best fitness value in the population improved upon that from the preceding generation, the size of the mutation is increased. Otherwise the step size is decreased.

Reproduction proportions: *Elite count*=2, *Crossover fraction*=0.8. The fittest two individuals from each generation are copied exactly as they are into the next generation. Of the remaining places in the new population, 80% are filled by crossover and 20% by mutation.

Selection: *Tournament* with *tournament size* 4. Each parent of an individual in the new generation is selected by first randomly choosing four individuals from the current generation. The individual with the highest expected number of offspring from this group is taken as the new parent.

Scaling: *Proportional*. The expected number of offspring for an individual, less one, is proportional the amount its fitness is below the mean for that generation.

Creation: *Uniform (absolute)*. The bodies are initially chosen to lie in a square area such that all absolute Cartesian coordinates with respect to the origin are taken from a uniform distribution with minimum $-20a$ and maximum $20a$.

Having determined the parameter settings, all that remains is to employ them within an execution of the GA for each problem. The final generation of this process produces a population from which the fittest is selected as the solution. The $\bar{q}$-factors for these individuals are given in Tables A.4, A.5 and A.6 for Problems 1, 2 and 3, and the fittest one highlighted in bold for each. Thus we select the Array G1 as $G1_1$, G2 as $G2_1$ and G3 as $G3_1$. These will be analysed in more detail, along with Arrays P1, P2 and P3 generated by the PI method in the next chapter.

Chapter 8

Optimised array analysis

8.1 Introduction

In this chapter, we analyse the arrays produced in regular waves by the two optimisation methods detailed in Chapter 7; namely the Parabolic Intersection (PI) method and the Genetic Algorithm (GA). Our aim is to discover just how well the configurations perform in the conditions under which they were optimised, what factors contribute to this behaviour and how they perform in other regular wave climates. On the basis of this information, the optimisation methods themselves are subsequently evaluated. The main results and analysis presented here are contained in Child and Venugopal (2010).

We begin in Section 8.2 by analysing the layout of the given array configurations. The velocity potential in the domain surrounding the arrays is then considered in Section 8.3, in order to better understand the related interaction processes. Section 8.4 contains analysis of the array performance under a range of different wave numbers and heading angles, whilst in Section 8.5, the associated motions of the devices are considered. Other arrays produced by the two optimisation procedures are briefly considered in Section 8.6, some of which correspond to those manufactured with the preliminary methodology of Child and Venugopal (2009). Finally, in Section 8.7, some general remarks are given and the two methods evaluated.

8.2 Array layout

Array configurations solving Problems 1, 2 and 3 of Section 7.2 using the PI method were defined in Section 7.3.2 with the labels P1, P2, P3 whilst those produced by the

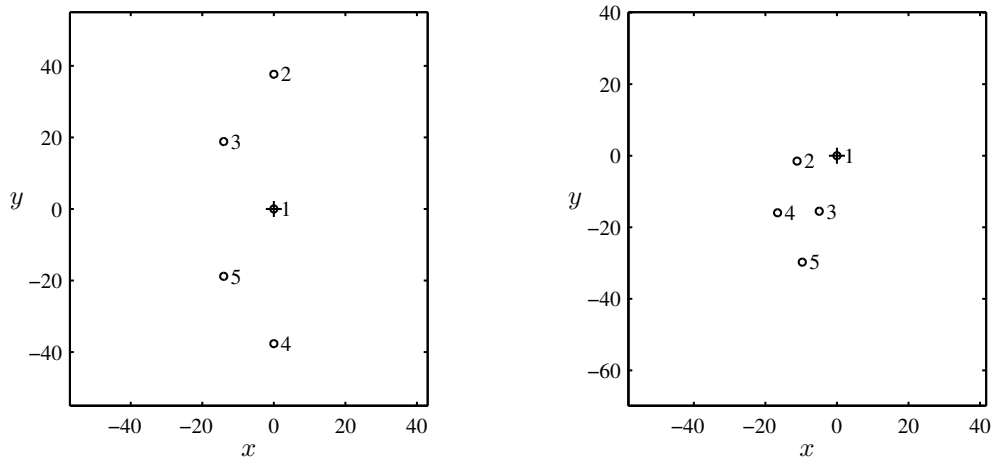

(a) P1 ($\bar{q}$=1.136)

(d) G1 ($\bar{q}$=1.163)

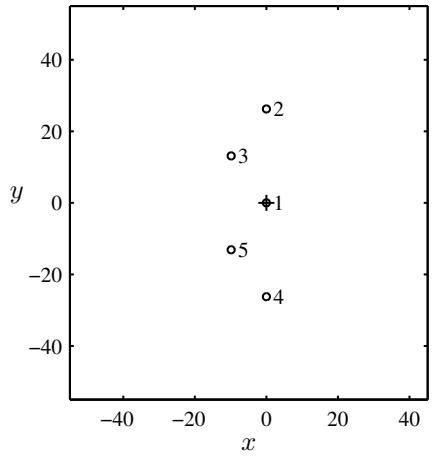

(b) P2 ($\bar{q}$=1.787)

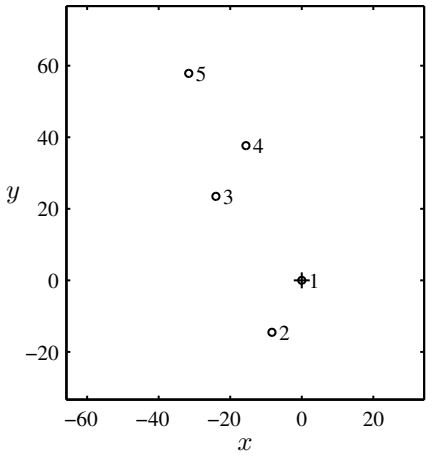

(e) G2 ($\bar{q}$=2.010)

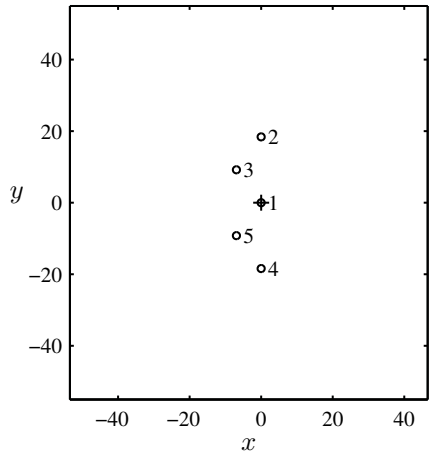

(c) P3 ($\bar{q}$=0.453)

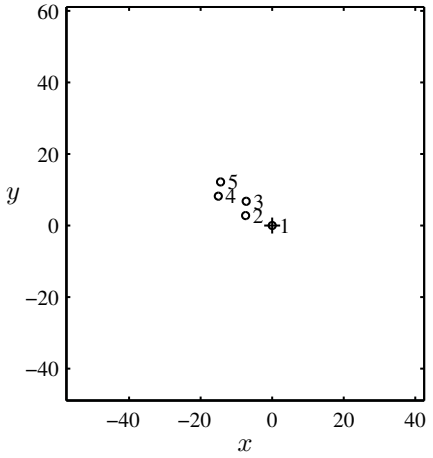

(f) G3 ($\bar{q}$=0.326)

Figure 8.1: Array configurations optimised in regular waves of wave number $2ak_0 = 0.8$ and heading $\beta = 0$. Labels: Parabolic Intersection method (P), Genetic Algorithm (G), Problem (1,2,3).

GA were denoted G1, G2, G3 respectively in Section 7.4.2. These layouts are displayed in Figure 8.1 with the Cartesian coordinates of each device (except the first, which is always located at the origin) given in Table 8.1.

Array	$(x_2/a, y_2/a)$	$(x_3/a, y_3/a)$	$(x_4/a, y_4/a)$	$(x_5/a, y_5/a)$
P1	(0.00,37.66)	(-14.02,18.83)	(0.00,-37.66)	(-14.02,-18.83)
P2	(0.00,26.24)	(-9.85,13.12)	(0.00,-26.24)	(-9.85,-13.12)
P3	(0.00,18.40)	(-6.92,9.20)	(0.00,-18.40)	(-6.92,-9.20)
G1	(-11.15,-1.51)	(-4.95,-15.52)	(-16.60,-15.94)	(-9.69,-29.75)
G2	(-8.34,-14.52)	(-24.01,23.48)	(-15.61,37.65)	(-31.60,57.86)
G3	(-7.44,2.78)	(-7.27,6.77)	(-15.07,8.21)	(-14.44,12.18)

Table 8.1: Global Cartesian coordinates of devices belonging to arrays optimised in regular waves.

The arrays constructed using the GA display an almost regular pattern in their layout. That is to say, many of the relative coordinates of one body with respect to another are approximately equal. The GA contains a mechanism that in fact enables exact repetition, since the relative positions of some of the bodies may be passed from one parent to more than one offspring. Later, an individual may inherit this configuration from both parents with each copy of the pattern involving a different subset of the bodies in the offspring. However, such features will generally only persist through the generations if they are particularly advantageous to the performance of the array as a whole.

Regularity in the configuration has manifested itself in the arrays produced by the GA as rows of devices, roughly parallel to each other. Down- and up-wave rows of Array G1 can be defined as consisting of Devices 1, 3 & 5 and 2 & 4 respectively; those of G2 as 1, 4 & 5 and 2 & 3; and those of G3 as 1, 3 & 5 and 2 & 4. In each case, the up-wave row is slightly offset from the down-wave row. In this respect, these arrays are qualitatively the same as the staggered arrays produced by the PI method, where down- and up-wave rows consist of bodies 2, 1 & 4 and 3 & 5 respectively.

As before, interactions are labelled as *i-j* where Device i leads to interference in the wave field experienced by Device j. *Adjacent intra-row* interactions will be defined as those occurring between a device and its closest neighbour either side, within the same row (for example, 3-1, 3-5 of G1). *Adjacent inter-row* interactions will involve the closest body either side of the projection of the originating body (perpendicular to the row) into the row to which it does not belong (for example, 2-1, 2-3 of G1). Adjacent

inter- and intra-row interaction will be referred to simply as *adjacent* interactions.

Within arrays produced by the GA, adjacent body pairs in each row (for example, 1 & 3 of G1) all have approximately the same relative positions. Furthermore, the position of bodies relative to elements in the row to which they do not belong (for example, 2 & 1 or 2 & 3 of G1) is repeated in these configurations. One exception to these observations is provided by Device 5 of Array G2 whose location with respect to the other bodies in the array is not replicated in any of the remaining body pairs.

8.3 Velocity potential

Figure 8.2 shows the relative phase between the ambient incident wave field and the total outgoing wave field (scattered and radiated) from bodies within each array. The outgoing potential from each body is plotted separately, with the interacting body shown as a solid black dot in the appropriate diagram. Here the full potential around all bodies, including the effects of every interaction was calculated before the relevant components extracted for plotting. The deep red bands show points in the domain where the incident and outgoing potentials are in phase with each other, the deep blue bands showing where they are out of phase. In the case of a body lying in a red (*resp.* blue) coloured band emanating from another body, there is constructive (*resp.* destructive) interference between the wave fields. By the phase argument on p.112, we therefore expect an appropriate modification to the performance of the receiving device.

The PI method uses the assumption that bodies lying on a curve of maximum interference in the progressive radiation or scattering potential surrounding an isolated body still receive this interference if the full potential around a body in the array is calculated. This hypothesis appears to hold for the Arrays P1, P2 and P3 in Figure 8.2, where the relevant bodies do indeed lie on the appropriate curves of interference.

For the arrays produced by the GA, no specific interactions between body pairs were sought, yet strong interference between incoming and outgoing potentials may still be observed at key devices. In the case of Array G1, the dominant scattered waves would be expected to produce the most valuable interactions a short distance up-wave of the originating body. Most of these result in the curve of maximum constructive interference intersecting the receiving body. In Array G2 the dominant radiated potential does not favour any particular direction, so the most significant interactions are simply between closely spaced body pairs. Of these, the majority result in the receiving body lying on

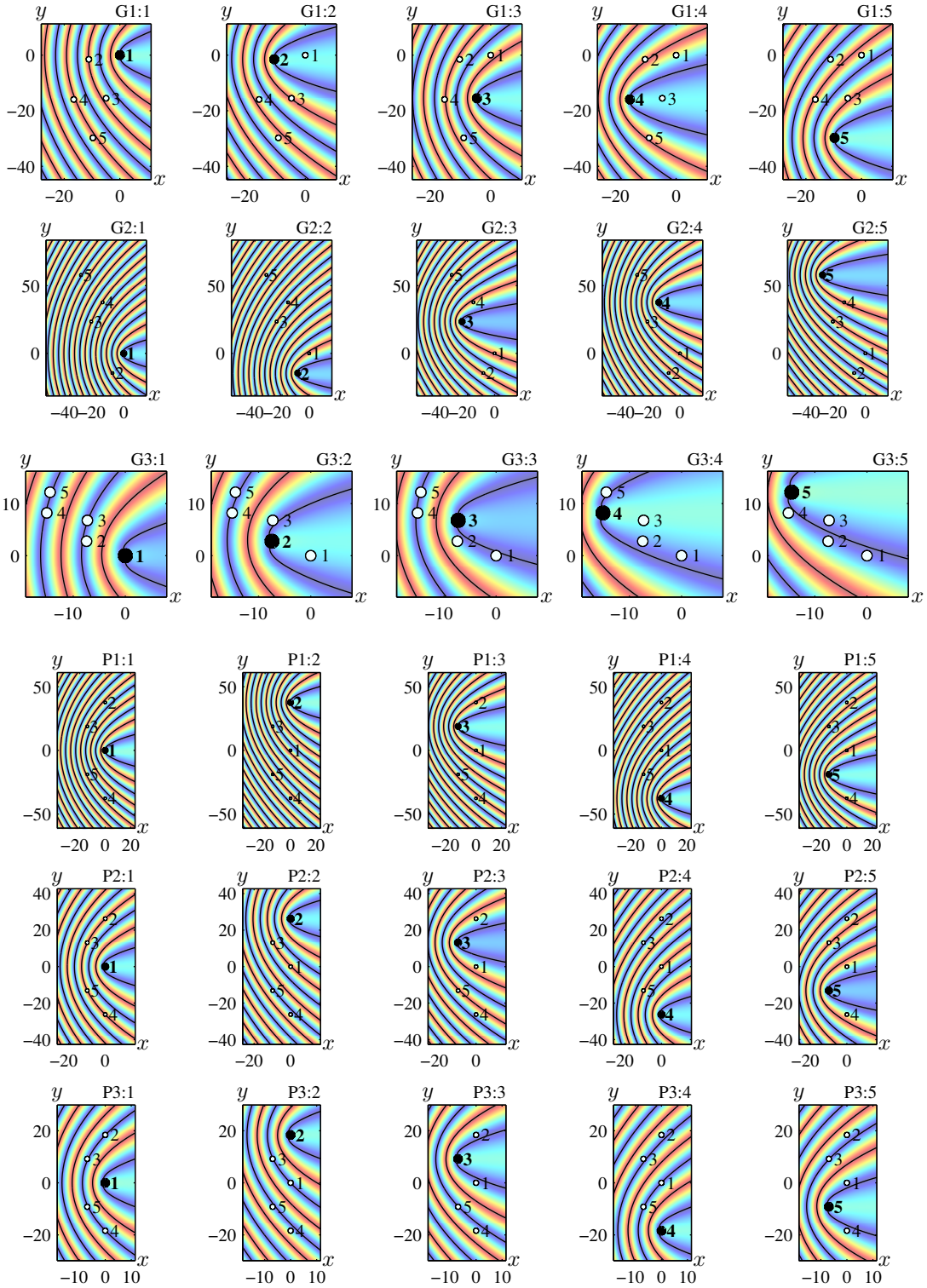

Figure 8.2: Relative phase between ambient incident wave potential and total outgoing potential ($= \phi^{\mathrm{R}} + \phi^{\mathrm{S}}$) from each body at the free surface. Red: In phase. Blue: Out of phase. Each row relates to a different array and each column represents waves originating from a different body (coloured solid black). Plots are labelled 'Array:Body'.

a line of maximum constructive interference, with the remaining devices situated close by. Radiation also dominates in Array G3 and in most of the cases, the receiving body lies on a line of maximum destructive interference as might be expected. In fact, all of the interactions in this array result in the receiving body lying in a zone of at least partially destructive interference.

8.4 Interaction factor

Figures 8.3(a), 8.4(a) and 8.5(a) show the variation of $\bar{q}$ with non-dimensional incident wave number for arrays solving Problems 1, 2 and 3 respectively. Here, the wave heading angle has been fixed at the tuning direction of $\beta = 0$. Figures 8.3(b), 8.4(b) and 8.5(b) show the variation of $\bar{q}$ with incident wave heading angle, β where the wave number has been fixed at the value to which the devices and array are tuned, $2ak_0 = 0.8$. In each plot, the value of the independent variable at the tuning parameters is marked with a vertical grey line. The critical value of $\bar{q} = 1$, about which the overall effect of interferences changes between being constructive and destructive, is marked with a horizontal grey line.

The $\bar{q}$-factor values at the tuning parameters (see Table 8.2) clearly show that the arrays produced by the GA all perform better in terms of the stated objectives than those constructed using the PI method. That is to say, G1 and G2 attain a higher $\bar{q}$-factor than P1 and P2 respectively, whilst G3 gives rise to a lower value than P3. Nevertheless, the PI method still achieves an interaction strength of magnitude comparable to the GA in all cases. Hence, whilst PI can be an effective optimisation technique there are some factors affecting array performance that cannot be understood by these simple means alone. Note also that even greater differences in behaviour may be observed away from the tuning parameters between arrays that have been optimised under the same conditions but using different algorithms (see Figures 8.3, 8.4 and 8.5).

From the figures in this section, it can be seen that there is a local maximum or minimum very close to the tuning frequency and angle for all arrays. It should be noted that in general a local maximum/minimum with respect to array configuration does not necessarily imply the same property exists with respect to wave number or angle of attack. However, optimised arrangements will usually exhibit a stationary point in the $\bar{q}$-factor in the immediate vicinity of the tuning parameters, by the argument contained in the following paragraphs.

Array	$\bar{q}(0.8, 0)$	w	c
G1	1.163	0.20π	0.96
G2	2.010	0.11π	0.93
G3	0.326	0.64π	0.85
P1	1.136	0.10π	0.98
P2	1.787	0.16π	0.92
P3	0.453	0.17π	0.93

Table 8.2: Optimised array properties. Interaction factor at the tuning wave number and heading ($2ak_0 = 0.8$, $\beta = 0$); Continuous angular range, w, about $\beta = 0$ for which $\bar{q} \neq 1$; Consistency constant $c = \frac{1}{2\pi} \int_{-\pi}^{\pi} \bar{q}(\beta)\, \mathrm{d}\beta$.

The undulating pattern in the $\bar{q}$-factor plots is due to the interacted waves going in and out of phase with the surrounding wave field at the device locations, as we have seen in Chapter 6. Supposing that there is a peak reasonably near but not at the tuning frequency and heading, we may try and recreate the associated relative wave phases at the desired parameters by rotating or scaling the size of the array. If the effect of the resulting changes in wave amplitudes is small compared to that of the phase changes (as it usually is), the peak will be realigned with the tuning frequency, relatively unaltered in shape and size. This will enhance the $\bar{q}$-factor at the tuning parameters, meaning that the original array cannot have been truly optimal. Hence in most cases, we expect that properly optimised arrays should display a stationary point in the $\bar{q}$-factor at the tuning parameters.

The limitation to the argument described above is the case where the peak is already very close to the tuning parameters. Then the benefit of realigning it at the desired parameter value may be outweighed by its change in magnitude, due to the associated differences in wave amplitudes. Hence no such simple improvement to the performance of the array may be made. This allows optimal arrangements to have stationary points in the $\bar{q}$-factor very near but not necessarily at the tuning parameters, as is observed here.

A similar argument may be applied in order to estimate the sensitivity of the arrays to small changes in configuration. If a layout is scaled or rotated slightly, the $\bar{q}$-factor is likely to change to a value that is comparable with those associated with the original array under incidence of waves with slightly different wave number or heading. Hence the arrays that exhibit large variation around the tuning parameters in these plots are likely to be more sensitive to perturbations in their arrangement than others.

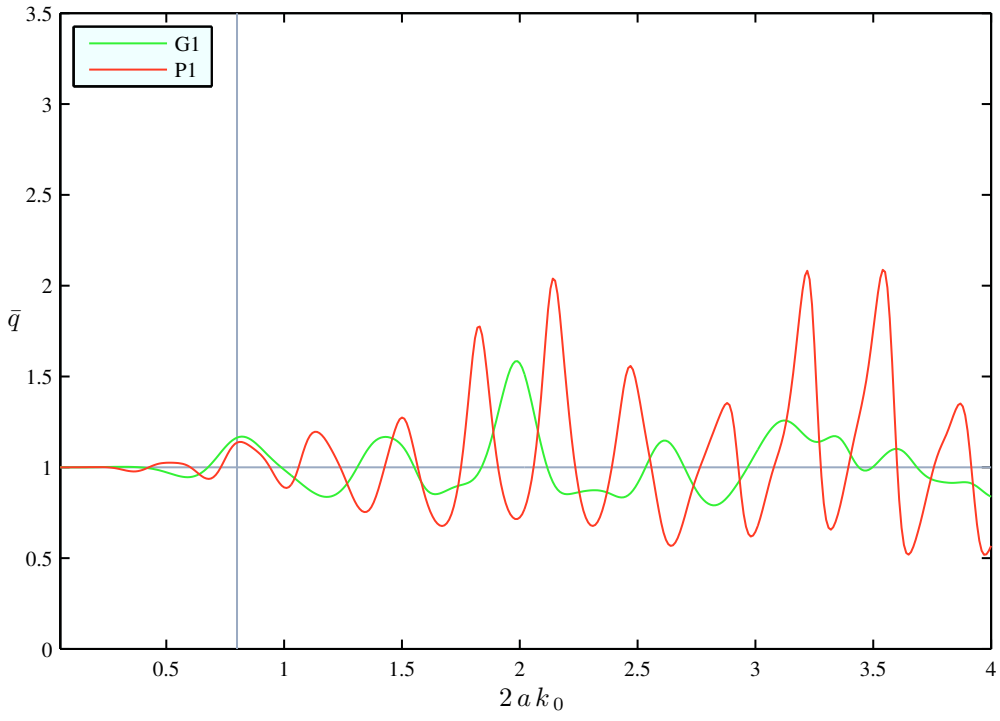

(a)

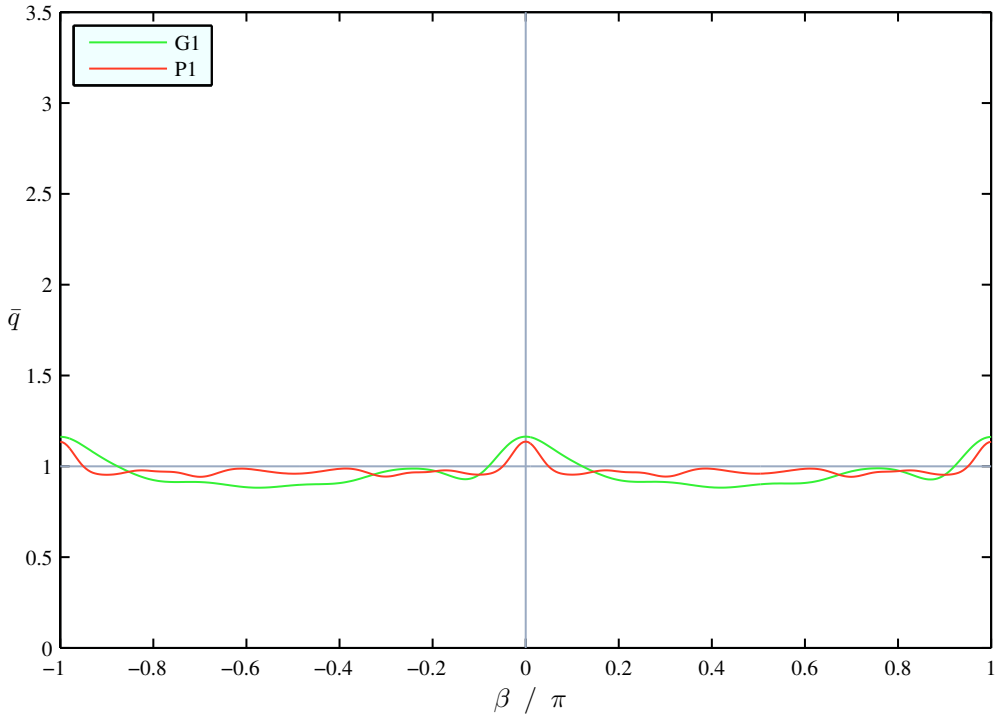

(b)

Figure 8.3: Interaction factor $\bar{q}$. Variation with (a) non-dimensional wave number $2ak_0$ for $\beta = 0$ and (b) angle of attack β for $2ak_0 = 0.8$. Arrays solving Problem 1.

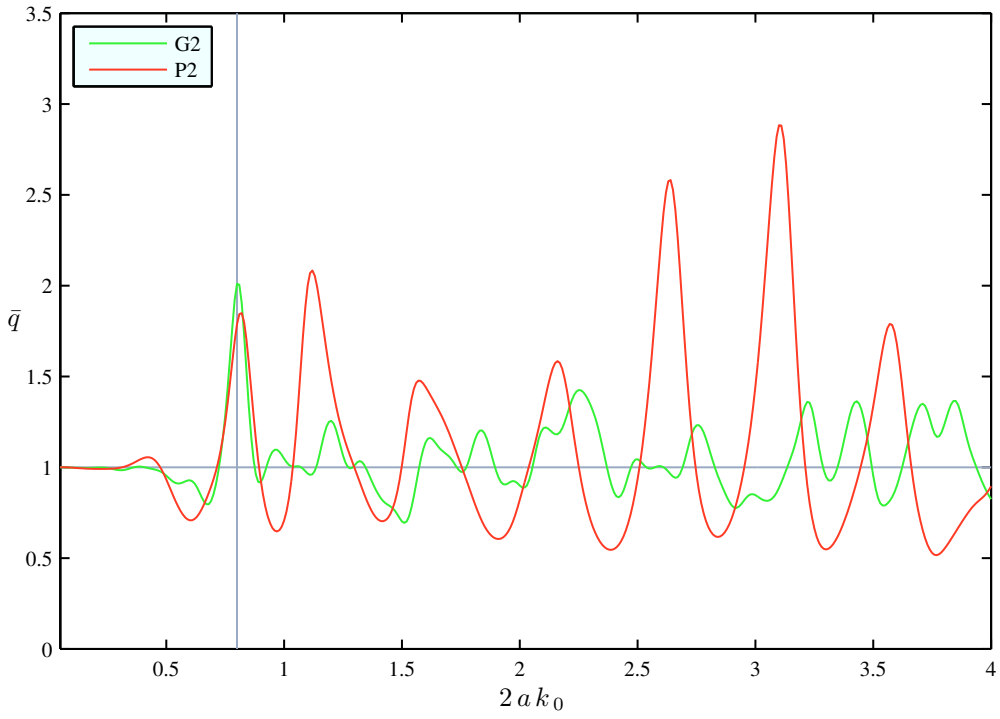

(a)

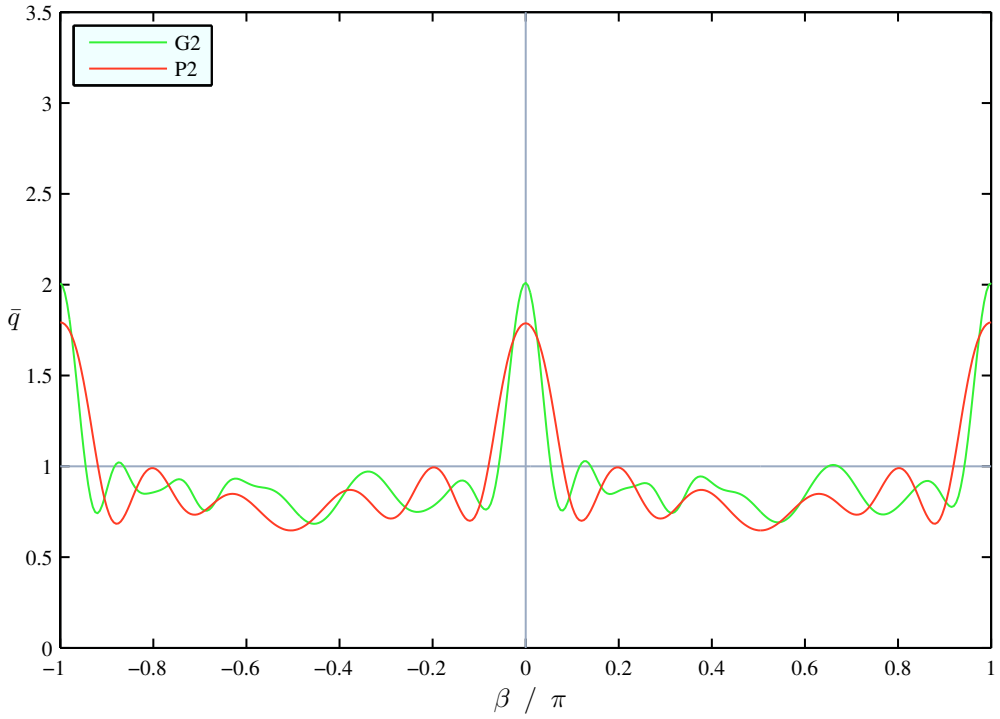

(b)

Figure 8.4: Interaction factor $\bar{q}$. Variation with (a) non-dimensional wave number $2ak_0$ for $\beta = 0$ and (b) angle of attack β for $2ak_0 = 0.8$. Arrays solving Problem 2.

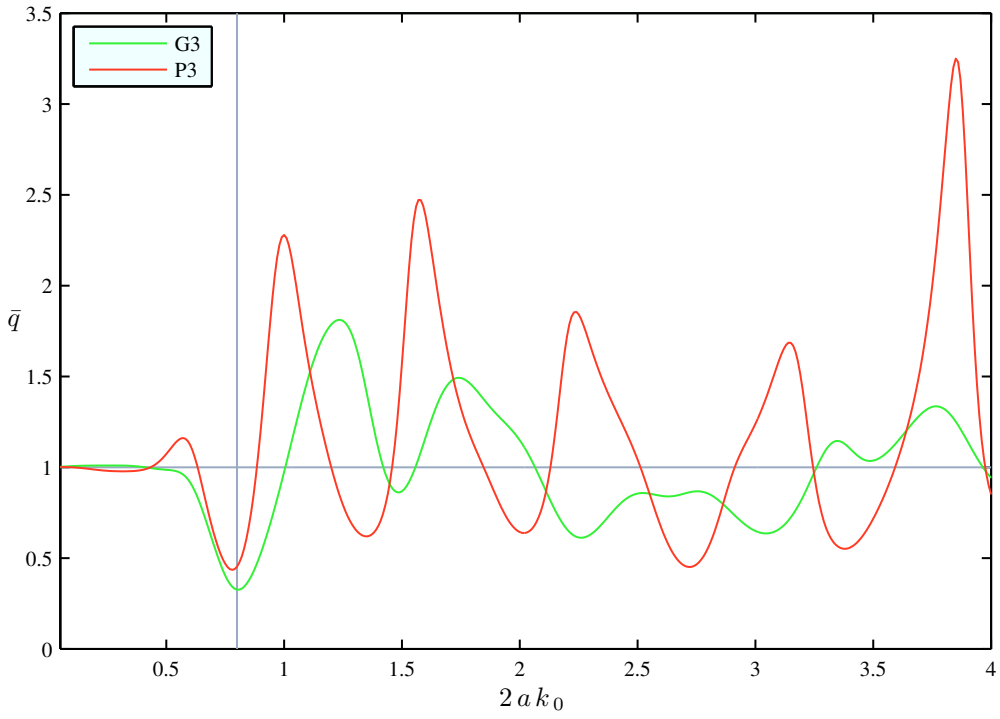

(a)

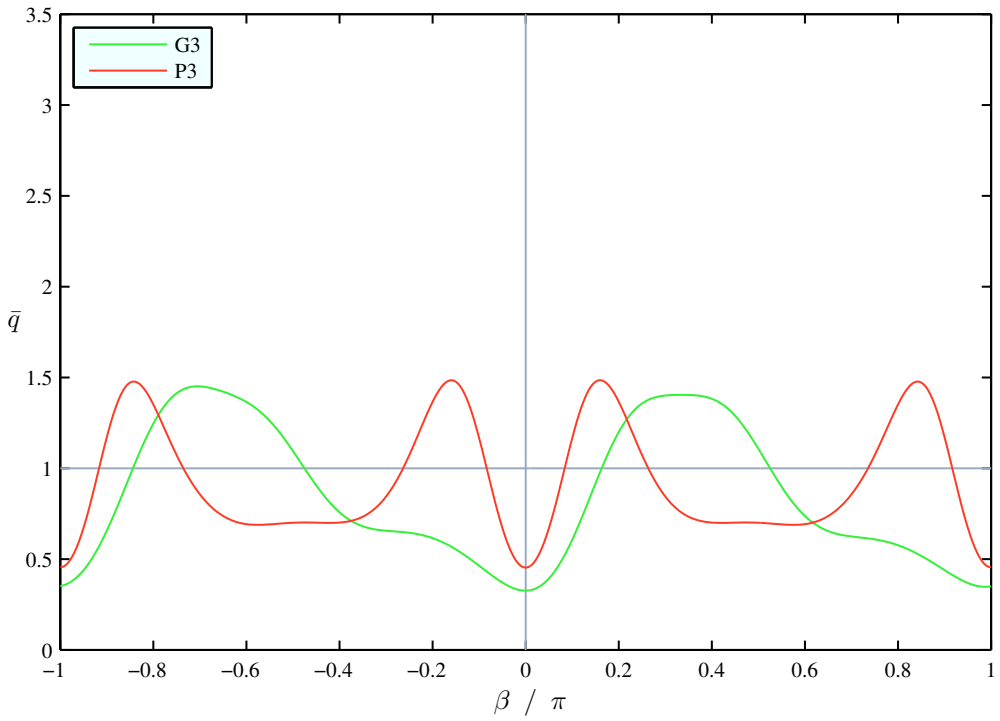

(b)

Figure 8.5: Interaction factor $\bar{q}$. Variation with (a) non-dimensional wave number $2ak_0$ for $\beta = 0$ and (b) angle of attack β for $2ak_0 = 0.8$. Arrays solving Problem 3.

8.4.1 Variation with wave number

Reactive tuning forces resonance at the device tuning frequency ($2ak_0 = 0.8$) and so the increased radiated wave field leads to stronger interactions here than for arrays of real-tuned devices. This results in a larger range of values in $\bar{q}$-factor for P2, G2, P3 and G3 than for P1 and G1 around this wave number.

A better understanding of the variation of the $\bar{q}$-factor with wave number may be gained using the concepts of the interaction distance D and wave number repeat value k_{R}, introduced in Section 6.2. Recall that for a given interaction, the former is the additional distance that interacted waves arriving at the receiving body have travelled in total from some reference line compared to ambient waves finishing there. The latter is the smallest increment in wave number needed to qualitatively replicate the nature of interference (that is, phase difference) between ambient and interacted wave fields experienced by the receiving device.

We have seen in Section 6.3 that large inter-body spacings mean the interaction distances are large and hence the wave number repeat values are small. This leads to rapid fluctuations in the $\bar{q}$-factor plots with respect to $2ak_0$, as can be seen for the more widely spaced arrays (such as P1) in Figures 8.3(a), 8.4(a) and 8.5(a).

For the group of the strongest interactions in the array, the less variation there is amongst the associated wave number repeat values, the more likely that the fluctuations in the $\bar{q}$-factor are pronounced and simple in appearance. Where these values are close to each other, positive interference from interactions that coincides at one wave number will also coincide at other wave numbers in the range. This accentuates the peaks and troughs of the interaction factor plots. On the other hand, if undulations associated with many different wave number repeat values are superimposed on top of each other in the $\bar{q}$-factor plot, the peaks are more numerous and less pronounced. The number of distinct repeat values associated with an array is reduced by several factors, two of which are described in the following paragraph.

If some relative coordinates between body pairs occur more than once (that is to say the array has some regularity) they will share a single repeat value, eliminating some of the variation in the set of values. This is certainly the case for the arrays produced by the PI method. Those produced by the GA show some regularity, although since the coordinate repetition is not exact, the associated repeat values correspond closely rather than precisely. If wave number repeat values are replicated

for several types of interaction, there is also a reduction in the total number of distinct values. Because arrays produced by the PI method all have adjacent intra-row and up-wave adjacent inter-row interactions occurring on the same parabola of constructive interference (Figure 8.2), the corresponding repeat values are equal. Arrays P1, P2 and P3, which have the same wave number repeat value for all of the major interactions have $\bar{q}$-factor plots that are particularly simple in form. Arrays from the GA, with several wave number repeat values that are close but not equal, may exhibit coordinated interaction for low wave numbers. However, discrepancies between repeat values become more significant at higher wave numbers where differences in the associated interaction distances are large compared to the wavelength of interacted waves.

Adjacent intra-row and up-wave adjacent inter-row interactions in Arrays P1, P2 and P3 give rise to repeat values of $2ak_{\mathrm{R}} = 0.33, 0.48, 0.68$ respectively. These lead to the most rapid oscillations of the $\bar{q}$-factor in each case. Down-wave adjacent inter-row interactions, with repeat values of $2ak_{\mathrm{R}} = 1.33, 1.92, 2.74$ respectively, produce the gradually varying trend of oscillations with respect to wave number. Other interactions deform the shape of these undulations slightly.

In Array G1, up-wave adjacent interactions have $0.54 < 2ak_{\mathrm{R}} < 0.64$, leading to reasonably well coordinated interactions at lower wave numbers with apparent undulations in k_0 of repeat value $2ak_{\mathrm{R}} \simeq 0.58$. Again, the other interactions alter the form of the plot further.

Interactions 4-3 and 1-2 are the closest of the up-wave body pairs in Array G2. In the higher frequency range where scattering dominates, these up-wave interactions are likely to produce the strongest interference, with $2ak_{\mathrm{R}} = 0.51, 0.50$ respectively. However, in this case it is difficult to discern a component of $\bar{q}$-factor corresponding to these repeat periods as there are so many other significant interactions.

In Array G3, the closest interactions (for example 2-3, 4-5, 3-2, 5-4) are likely to be the strongest. These have repeat values in the range $2.70 < 2ak_{\mathrm{R}} < 3.70$ and so give rise to a long envelope around the fluctuations in the plot. The next strongest set of up-wave interactions are from inter-row body pairs 3-4 and 1-2 (giving mean repeat value $2ak_{\mathrm{R}} = 0.81$) and intra-row pairs 3-5, 2-4, 1-3 (giving mean $2ak_{\mathrm{R}} = 0.75$) whose contributions to the $\bar{q}$-factor approximately coincide for lower wave numbers. Other notable interactions include 1-4 ($2ak_{\mathrm{R}} = 0.39$) and 1-5 ($2ak_{\mathrm{R}} = 0.38$), whilst the remainder have much longer wave number repeat values, so their influence on the

$\bar{q}$-factor cannot be observed in this frequency range.

8.4.2 Variation with wave heading angle

Certain patterns in the plot of $\bar{q}$-factor with respect to wave heading angle may be observed as a result of geometric features of the array. The symmetry of the arrays produced using the Parabolic Intersection method gives rise to the symmetry in the plot of $\bar{q}$-factor with respect to wave heading about $\beta = 0, \pi$. The arrays produced using this technique also lead to an approximate symmetry in the plot with respect to $\beta = \pm\pi/2$. The most common type of interaction in these arrays is between bodies within the same row and this process is symmetric with respect to the aforementioned angles. Moreover, intra-row interactions along whose path the y-coordinate increases with x (for example, 2-3, 1-5) under some angle of attack $\beta = \pm\pi/2 - \beta_0$ can be approximated by interactions along which y decreases with x (for example, 3-1, 5-4) for $\beta = \pm\pi/2 + \beta_0$. The effects of multiple interactions are responsible for the slight deviation from this symmetry.

All of the arrays display an approximate repetition in $\bar{q}$-factor values as the wave heading is increased by π, that is to say for all wave headings $\beta = \beta_0$, $\bar{q}(\beta_0) \approx \bar{q}(\beta_0 + \pi)$. Fitzgerald and Thomas (2007, Equation (3.8)) proved that this relationship holds precisely where the point absorber approximation is made. In the present scheme, every interaction from a device i to j for $\beta = \beta_0 + \pi$ can be crudely approximated by interactions from j to i for $\beta = \beta_0$ since every ij pair of bodies has rotational symmetry of order two. This provides a partial justification for the result seen here.

In Section 6.4, we showed that the nature of interference for an interaction can be qualitatively reproduced by varying the wave heading angle instead of the wave number. In particular, the remarks following equation (6.9) mean that the resulting fluctuation in performance with respect to angle of attack is more rapid for widely spaced arrays.

If the array performance is to be robust to changes in incident wave direction, it is important that the 'width' of the peak or trough surrounding the tuning angle be taken into consideration. Here, the *width* w given in Table 8.2 is defined as the continuous angular range surrounding the tuning angle ($\beta = 0$) for which $\bar{q}(\beta) - 1$ has the same sign (that is to say, β for which the net interaction is constructive in Problems 1, 2 and destructive in Problem 3). Array G3 has a particularly wide trough because most bodies sit in the broad tail of destructive interference from other devices and this changes slowly

with angle of attack. For Array P3, however, varying wave heading angle in either sense from $\beta = 0$ rapidly finds a parabola of constructive interference, meaning that $\bar{q}$ recovers sharply away from the trough at the tuning angle.

Even though point absorber theory has not been used here, the values of c in Table 8.2 show that the consistency condition $c = 1$ does hold loosely for all the cases studied. Looked at more closely, the average performance of each converter in the arrays over the whole angular range is slightly worse than for an isolated body. In the case of reactively-tuned devices, the main difference to the circumstances for which $c = 1$ was derived is that here, array performance has not been maximised with respect to power take-off coefficients at each device. This may explain some of the deficit in overall performance.

8.5 Heave motion

In this section, we consider the motion responses of devices in the optimised arrays. Heave amplitude, non-dimensionalised by that of the ambient incident waves, is shown in Figures 8.6, 8.7 and 8.8 for Problems 1, 2 and 3 as a function of non-dimensional wave number. The grey vertical line in each plot denotes the tuning frequency $2ak_0 = 0.8$. Because of the symmetry in Arrays P1, P2 and P3 with respect to the x-axis, the curves for Devices 2 and 3 are obscured by those for 4 and 5 respectively.

For all of the examples presented here, maximising (*resp.* minimising) the performance of the array leads to each of its constituent devices having a greater (*resp.* lesser) heave amplitude than an isolated device at the tuning frequency. In fact many of the devices exhibit a peak in the associated curve near this frequency. In Chapter 6, we argued that an increase in heave amplitudes usually leads to an increase in performance, whereas here we have evidence of the converse assertion: that increased performance usually involves an increase in heave amplitudes.

At this point in the analysis, it is appropriate to consider the implications of one of the assumptions of linear wave theory used throughout this thesis. From the remark following equation (3.5), we know that linearising the boundary condition on the under surface of the device requires any motion to be of small amplitude. Thus, large motion amplitudes violate the theory used in their derivation and thus the results may cease to adequately represent physical behaviour. In practice, nonlinear effects which have been neglected in the present formulation, would restrain such excessive movement. Large

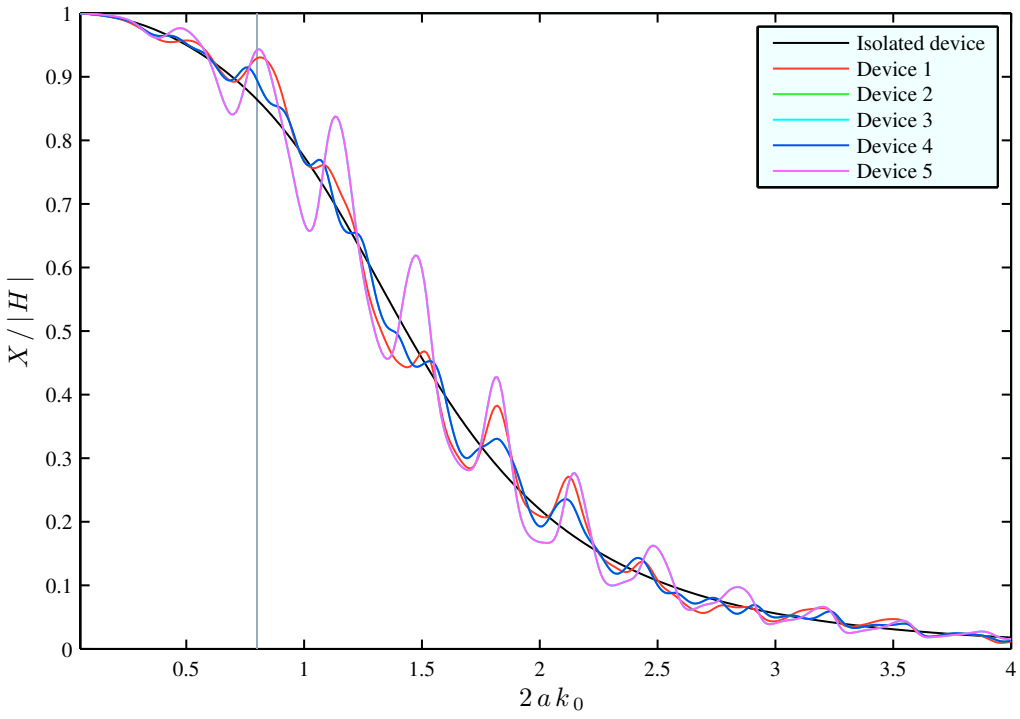

(a) P1

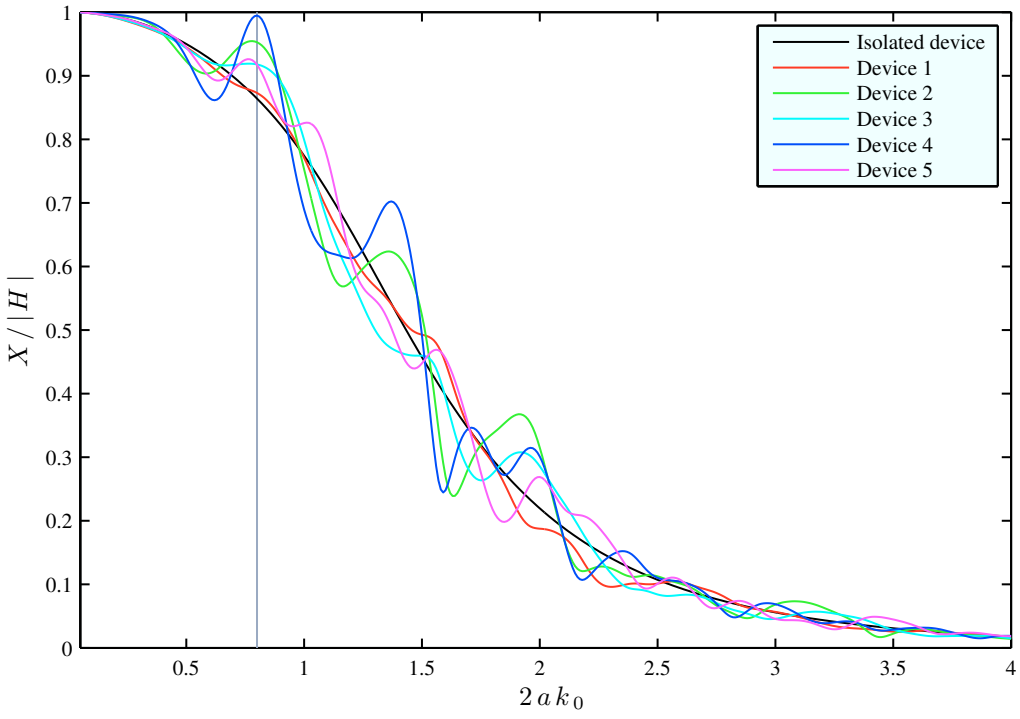

(b) G1

Figure 8.6: Heave response. Variation of non-dimensional heave amplitude $X/|H|$ with non-dimensional wave number $2ak_0$ for $\beta = 0$. Arrays solving Problem 1.

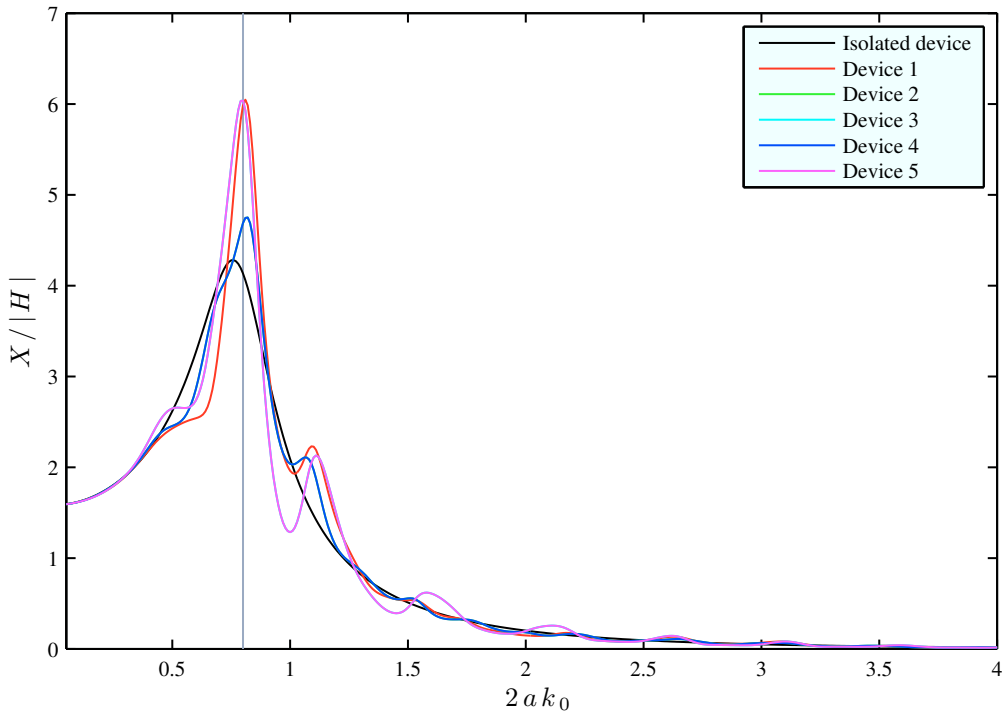

(a) P2

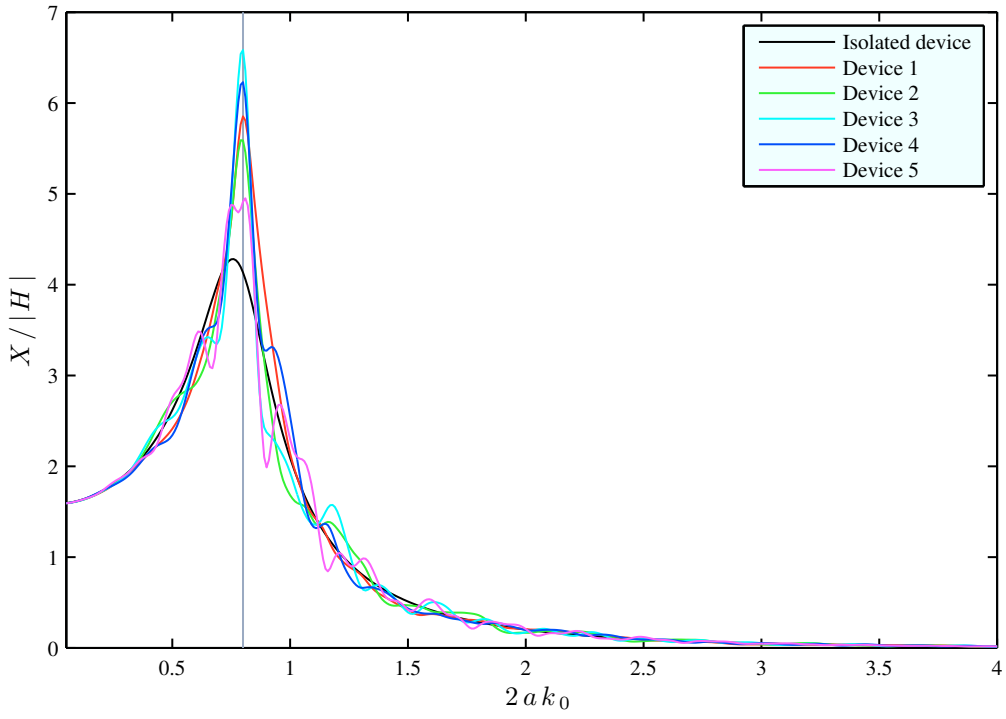

(b) G2

Figure 8.7: Heave response. Variation of non-dimensional heave amplitude $X/|H|$ with non-dimensional wave number $2ak_0$ for $\beta = 0$. Arrays solving Problem 2.

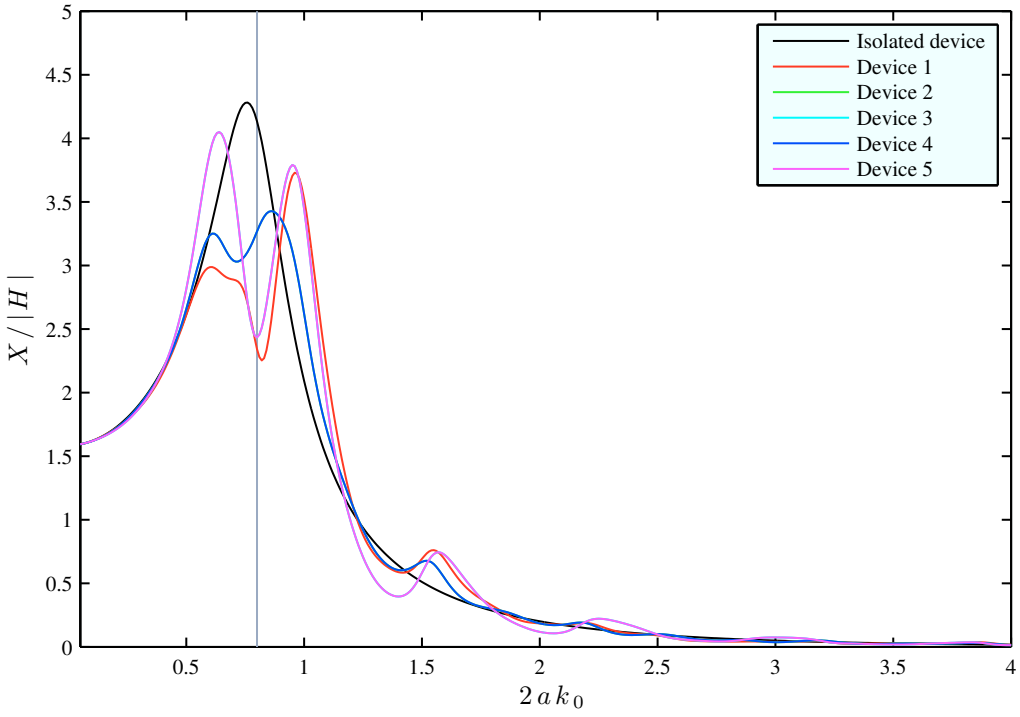

(a) P3

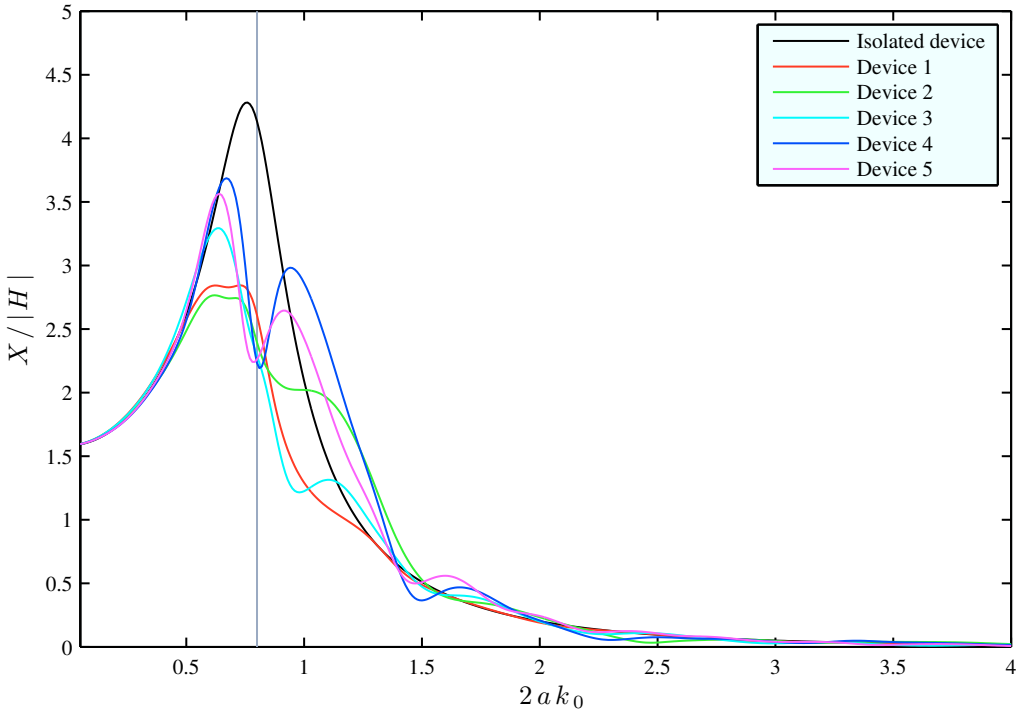

(b) G3

Figure 8.8: Heave response. Variation of non-dimensional heave amplitude $X/|H|$ with non-dimensional wave number $2ak_0$ for $\beta = 0$. Arrays solving Problem 3.

motion amplitudes are not desirable from an engineering perspective either, since this would involve the costly manufacture of correspondingly larger components.

The heave amplitude for an isolated, reactively-tuned device (shown by the black curves in Figure 8.7) peaks at over four times the ambient incident wave amplitude. Furthermore, when power is maximised in an array of these devices (that is, in Problem 2), we have amplitudes increasing to over six times the incident wave amplitude. These values are clearly not feasible and so results for the associated wave numbers should be treated with caution. Even in Problem 3, where the amplitudes are reduced at the tuning frequency, the maximum values attained by these reactively-tuned devices are still only slightly less than in the isolated case. In the arrays of real-tuned devices (Problem 1), there are no such problems with large amplitudes, although the associated power produced by this type of device is significantly less (see Figure 5.10(c)).

If nonlinear hydrodynamic effects (such as viscous drag) were to be taken into account, the device motion amplitudes and hence the interactions due to radiation would be diminished. This would be especially acute in the case of reactively-tuned devices operating at their tuning frequency, due to the large predicted displacement amplitudes. Fitzgerald (2006) investigated the effects of limiting device motion in arrays whose performance had been optimised at one frequency in the absence of such constraints. It was found that even under quite stringent conditions on the displacement amplitudes, the nature of interference at that frequency was the same as in the unconstrained case, albeit with reduced strength. This indicates that unconstrained optimisation using linear theory is of relevance to the design of arrays for nonlinear conditions as well. A fuller treatment of this issue would compare the performance of arrays produced without motion constraints with that of configurations generated by an optimisation process able to incorporate them. For more information regarding the effects of motion constraints on wave energy devices, see Evans (1981b), Thomas and Evans (1981) and Pizer (1993).

8.6 Alternative array layouts

In this section, arrays that are produced by the optimisation methods of Chapter 7, other than those considered in detail thus far, are discussed. The aim is to gain a sense of the variety of possible outputs from each method and therefore learn more about the way that the procedures operate. The array configurations under discussion are

contained in the appendix.

Arrays constructed using the PI method with the three formation types detailed in Section 7.3.2 are shown Figures A.3, A.4 and A.5 for Problems 1, 2 and 3 respectively. The four most highly optimised arrays of each type (linear, pentagonal and staggered) in each problem are given here, along with their label and $\bar{q}$-factor. Note that the final Arrays P1, P2 and P3 considered in the rest of this chapter were selected from a set that includes all of these arrangements, so none given here is more highly optimised.

We also present here arrays from other executions of the GA. Since this is a semi-random process, the same algorithm produces different results upon initialisation with different random seeds. Twelve such arrangements are are shown in Figures A.6, A.7 and A.8 for Problems 1, 2 and 3 respectively. Note that to demonstrate the optimisation procedure and generate Arrays G1, G2 and G3 analysed in this chapter, only a single execution of the algorithm was used. Therefore, some of the alternative arrays (given along with their $\bar{q}$-factors) are more highly optimised than these.

It is interesting to note that Array $\mathrm{PP1}_{2232}$ in Figure A.3(e), along with some of the other pentagonal arrays in the figures, resembles optimal formations S5A and S5C given by Fitzgerald and Thomas (2007). Array $\mathrm{PP1}_{2232}$ was analysed in Child and Venugopal (2009) under the label 'P1,' and was shown to result in constructive interference between the principal wave fields at the up-wave devices as was desired. Array $\mathrm{PL2}_{11}$ of Figure A.4(a) was also considered in the that paper with the label 'P2,' as was $\mathrm{PL3}_{22}$ of Figure A.5(c) under the name 'P3.'

As noted for the main arrays studied in this chapter, the alternative arrays that are produced by the GA here often exhibit a significant degree of regularity. In particular, many of the arrays relating to Problem 1 are approximately staggered in formation, with two rows of devices offset from each other. Some of the remaining arrays solving this problem have four bodies in a regular parallelogram formation with the fifth elsewhere. Furthermore, certain arrangements are almost exactly replicated by other executions of the algorithm. In particular, those in Figures A.6(d) and A.6(h) closely resemble each other and correspond well with 'Array G1' of Child and Venugopal (2009), produced using a GA with a completely different set of options. The similarity between these arrays suggests that the choice of parameters and operators has not biased the formation process. The value of selecting parameters carefully in Chapter 7.4.2 is so that, on average the GA, reaches a better solution in a shorter time period.

We may see from Figures A.6(a) and A.6(b) that the arrangements they depict are in fact approximately the same as each other, after a rotation of π radians. Such repetition is to be expected, since if a particular arrangement is highly rated in terms of its $\bar{q}$-factor, then from the analysis of Section 8.4.2 its performance will be almost unchanged when the wave heading angle is incremented by π. This is equivalent to the aforementioned array rotation and so the transformed configuration will also be highly rated. Indeed, the two arrays considered here do give rise to approximately the same $\bar{q}$-factor.

The configuration shown in Figure A.6(i), when reflected in the x-axis, is almost exactly the same as Array G1 (previously considered in this chapter) and shares the same $\bar{q}$-factor. In general such a transformation on an array will always leave the performance unchanged. This is because the entire set of interaction processes may also be reflected in that line, giving the complete hydrodynamic solution for the transformed array. Hence, as for the rotation of an array by π, highly rated arrays remain highly rated after reflection in the x-axis.

Half of the alternative arrays produced by the GA for Problem 2 are approximately linear in formation, with almost exactly the same average separation between adjacent bodies. These arrangements, whilst not performing quite as well as those with a staggered type of formation, are nonetheless competitive in terms of their performance. Several of the other arrangements in Figure A.7 show similarities with Array G2, having four devices in a regular staggered formation and the fifth almost conforming to the same pattern. The array in Figure A.7(d) resembles a combination of linear and staggered array formations and the arrangement in Figure A.7(a) has all five devices in a staggered formation like G1.

All of the arrays produced by the GA for Problem 3 look approximately the same after the transformations described above. Hence, in this case the GA has settled on only one truly distinct arrangement. This indicates that the performance of the optimisation is especially consistent here. Correspondingly all $\bar{q}$-factors are also approximately the same.

8.7 Evaluation

In this chapter, we have seen that the PI and GA methods are effective in producing optimised arrays with the desired performance at the tuning parameters in a range of

situations. Both methods typically give rise to arrays with some degree of regularity in their formation. Modifications to the behaviour can be significant, especially in the case that the devices are reactively-tuned to the array tuning frequency. In the latter situation, the $\bar{q}$-factor is unlikely to be practically attainable due to nonlinear effects. Notwithstanding limits on the applicability of linear wave theory, Problem 3 demonstrated that hydrodynamic interactions can also be detrimental to overall array performance.

In all of the problems, the GA achieved a more highly optimised array by a relatively small margin compared with the total interaction factor in each case. This demonstrates that although the PI method is capable of producing adequate competitors, there are some phenomena that cannot be understood by these simple means alone. Additionally, it is much less adaptable for use in other relevant optimisation problems (such as maximising the performance in irregular waves – see Chapter 9) than the GA. Despite these limitations, forming arrays by the PI method does promote an understanding of the processes involved. The GA on the other hand only provides the final solution. The clear advantage of the PI method, however, is in terms of efficiency where the most complex arrangement was constructed in less than five minutes in contrast to an execution time of more than 24 hours for the GA.

Chapter 9

Array optimisation and analysis in irregular waves

9.1 Introduction

Up to this point, we have considered only waves of a single amplitude, frequency, direction and phase acting upon an array at any one time. Such regular waves on their own, however, are not representative of typical ocean conditions. However, the free surface of an irregular sea may be described by a linear superposition of sinusoidal wave components. In this chapter, we take advantage of the assumed linearity in the problem and form a solution from a superposition of those relating to the regular wave components. Therefore for the most part, the methods of computation and analysis presented thus far may be adapted for the present purpose without too much difficulty.

Theory relevant to the calculation of array performance in an irregular sea-state is presented in Section 9.2 of this chapter, with details regarding the specific spectra to be employed contained in Section 9.3. The arrays produced by the optimisation procedures described in Chapters 7 and 8 for regular waves are then analysed in irregular waves with the same peak frequency and mean direction. Further array configurations are subsequently created, taking the objective to be power output in irregular waves. This is performed using a Genetic Algorithm (GA) optimisation procedure, as described in Section 9.5. The resulting set of arrays are analysed in detail in Section 9.6, before some concluding remarks regarding the methodology and results given in Section 9.7.

9.2 Theory

Assuming that an irregular wave energy spectrum is linear (that is to say, waves are of small steepness and the water is deep), the principle of linear superposition may be applied to the free surface elevations associated with its regular wave components. Furthermore, by linearity of the governing equations and boundary conditions (3.14-3.19, 3.146), and assuming that externally applied forces are linear functions of the motion (as they are here), the response due to the combination of two or more waves may be calculated as the sum of the responses to those waves individually (see Price et al. (2009) for details of the conditions under which this applies).

First, we must express the ambient sea-state experienced by the device as a linear combination of regular waves. Momentarily assuming that the waves are long-crested and propagating in the positive x-direction, this is then a summation of progressive waves of the type given in equation (3.57). Each component (indexed by p) has a corresponding wave amplitude $H^{[p]}$, progressive wave number $k_0^{[p]}$, corresponding angular frequency $\omega^{[p]}$ given by (3.27) and phase shift $\xi^{[p]}$ taken from a uniform random distribution over the full angular range $[0, 2\pi)$:

$$\zeta^{(t)}(x, y, t) = \sum_p H^{[p]} \cos\left(k_0^{[p]} x - \omega^{[p]} t + \xi^{[p]}\right). \tag{9.1}$$

At any point in the x, y-plane, the variance of the free surface elevation is given by

$$v = \overline{(\zeta^{(t)})^2} \tag{9.2}$$

$$= \sum_p \frac{1}{2}(H^{[p]})^2, \tag{9.3}$$

where the overbar denotes the long-term, time-averaged quantity (Tucker and Pitt, 2001). Note that v is proportional to the average energy per unit of sea area. We may now define a certain function S for each wave number and any length of interval Δk_0. Let Δv be the variance, as given by equation (9.3), of the free surface elevation resulting from only the components $k_0^{[p]}$ that satisfy $k_0 - \frac{\Delta k_0}{2} \leq k_0^{[p]} \leq k_0 + \frac{\Delta k_0}{2}$. Then let

$$S(k_0) = \frac{\Delta v}{\Delta k_0}. \tag{9.4}$$

The function S is known as the *wave energy spectrum* (or simply *wave spectrum*) and

represents the concentration of wave energy in different parts of the wave number range. Note that the definition (9.4) remains adequately defined as $\Delta k_0 \to 0$, giving rise to the following expression for the variance in the limit:

$$v = \int_0^\infty S(k_0)\,\mathrm{d}k_0. \tag{9.5}$$

Relaxing the condition on the direction of propagating waves and allowing each regular wave component p to travel at an angle of $\beta^{[p]}$ to the positive x-axis, (9.1) becomes

$$\zeta^{(t)}(x,y,t) = \sum_p H^{[p]} \cos\left[k_0^{[p]}(x\cos\beta^{[p]} + y\sin\beta^{[p]}) - \omega^{[p]}t + \xi^{[p]}\right]. \tag{9.6}$$

Now for fixed Δk_0 and $\Delta\beta$, let Δv be the free surface variance resulting from wave components satisfying $\beta - \frac{\Delta\beta}{2} \leq \beta^{[p]} \leq \beta + \frac{\Delta\beta}{2}$ and $k_0 - \frac{\Delta k_0}{2} \leq k_0^{[p]} \leq k_0 + \frac{\Delta k_0}{2}$. The directional wave spectrum is then defined as

$$S(k_0,\beta) = \frac{\Delta v}{\Delta k_0 \Delta\beta}, \tag{9.7}$$

whence, letting $\Delta k_0, \Delta\beta \to 0$,

$$v = \int_0^\infty \int_0^{2\pi} S(k_0,\beta)\,\mathrm{d}\beta\,\mathrm{d}k_0. \tag{9.8}$$

The directional spectrum is commonly decomposed into an omni-directional spectrum S_{k_0} of the type defined in (9.4) and a normalised directional distribution S_β such that $\int_0^{2\pi} S_\beta(\beta)\,\mathrm{d}\beta = 1$:

$$S(k_0,\beta) = S_{k_0}(k_0)S_\beta(\beta). \tag{9.9}$$

This version of the spectrum will be used from here onwards. The uni-directional case may then be recovered by setting S_β to be a Dirac delta function whilst the single frequency case involves setting S_{k_0} in a similar way.

Returning to consideration of regular waves, the mean energy density (including kinetic and potential forms) with respect to ocean area is given by (Tucker and Pitt, 2001, (2.2-15))

$$E = \frac{1}{2}\rho g H^2, \tag{9.10}$$

where H is the wave amplitude. We now define the *group velocity* to be the rate of

change of angular frequency with progressive wave number:

$$c_{\mathrm{g}}(k_0) = \frac{\mathrm{d}\omega}{\mathrm{d}k_0} \tag{9.11}$$

$$= \frac{\sqrt{k_0 g \tanh k_0 d}}{2k_0}\left(1 + \frac{2k_0 d}{\sinh 2k_0 d}\right), \tag{9.12}$$

where equation (3.27) has been used. This quantity is the velocity at which energy propagates (Acheson, 2001) and so the power passing through a line of unit length parallel to the wave crests is equal to the product of (9.10) and (9.11):

$$J(k_0) = \frac{1}{2}\rho g H^2 c_{\mathrm{g}}(k_0). \tag{9.13}$$

Now consider the average power produced by Device j over one wave period $P_j(k_0, \beta)$, which may be calculated in accordance with the method of Chapter 3. Under the assumptions of linear wave theory, for each wave number k_0 and heading β, we may normalise this quantity by the wave power per unit width (9.13) to form the *capture width* ℓ_j:

$$\ell_j(k_0, \beta) = \frac{P_j(k_0, \beta)}{J(k_0)}. \tag{9.14}$$

Note that since both P_j of equation (3.162) and J of (9.13) are proportional to the square of the wave amplitude H, the capture width is independent of the value used for calculation purposes. In an irregular sea, the wave amplitude $H^{[p]}$ of the p^{th} component gives rise to the following power per unit width:

$$J^{[p]} = \frac{1}{2}\rho g (H^{[p]})^2 c_{\mathrm{g}}(k_0^{[p]}), \tag{9.15}$$

where equation (9.13) has been used. Hence, the power actually delivered by the device due to the p^{th} wave component of the sea will be the product of the preceding two expressions:

$$P_j^{[p]} = \ell_j(k_0^{[p]}, \beta^{[p]}) J^{[p]}. \tag{9.16}$$

Using linearity again, the instantaneous velocity of each device is equal to the sum of velocities caused by all the wave components. From equation (3.159), the instantaneous power is proportional to the square of the instantaneous velocity. However, when this is averaged over time, the cross terms between different components disappear. Hence the time-averaged *net* power is simply equal to the sum of the time-averaged power

contributions from all the components:

$$P_j^{\mathrm{T}} = \sum_p P_j^{[p]} \tag{9.17}$$

$$= \sum_p \ell_j(k_0^{[p]}, \beta^{[p]}) \, \frac{1}{2} \rho g (H^{[p]})^2 c_{\mathrm{g}}(k_0^{[p]}), \tag{9.18}$$

where (9.15) and (9.16) have been used. Suppose that the components of the irregular sea are separated at regular intervals in wave number and wave heading angle by Δk_0 and $\Delta\beta$ respectively. Then the sum defining Δv (9.3) reduces to just one term and so using equation (9.7), we can express each wave amplitude in terms of the spectrum S:

$$\frac{1}{2}(H^{[p]})^2 = S(k_0^{[p]}, \beta^{[p]}) \, \Delta\beta \Delta k_0. \tag{9.19}$$

Substituting this expression into (9.18), we get

$$P_j^{\mathrm{T}} = \sum_p \ell_j(k_0^{[p]}, \beta^{[p]}) \, \rho g c_{\mathrm{g}}(k_0^{[p]}) S(k_0^{[p]}, \beta^{[p]}) \, \Delta\beta \Delta k_0. \tag{9.20}$$

Letting $\Delta k_0, \Delta\beta \to 0$, equation (9.20) becomes

$$P_j^{\mathrm{T}} = \int_0^{\infty} \int_0^{2\pi} \ell_j(k_0, \beta) \, \rho g c_{\mathrm{g}}(k_0) S(k_0, \beta) \, \mathrm{d}\beta \, \mathrm{d}k_0. \tag{9.21}$$

Now, defining the *power spectrum* S^{P} to be

$$S^{\mathrm{P}}(k_0, \beta) = \rho g c_{\mathrm{g}}(k_0) S(k_0, \beta), \tag{9.22}$$

we obtain

$$P_j^{\mathrm{T}} = \int_0^{\infty} \int_0^{2\pi} \ell_j(k_0, \beta) \, S^{\mathrm{P}}(k_0, \beta) \, \mathrm{d}\beta \, \mathrm{d}k_0. \tag{9.23}$$

Note that for the purposes of calculation, the independent variables may be truncated such that $k_0^{\min} \leq k_0 \leq k_0^{\max}$ and $\beta^{\min} \leq \beta \leq \beta^{\max}$, so long as all the important behaviour is accounted for.

The net power captured from an irregular sea may thus be calculated for each device j in the array as well as for an isolated device P_0^{T}. Then with analogy to (3.163), we may form the *net interaction factor* $\overline{Q}$ as the ratio of total power from the array to that arising from the same number of devices in isolation in the same sea-state. If all devices

are identical, we have

$$\overline{Q} = \frac{\sum_{j=1}^{N} P_j^{\mathrm{T}}}{N \times P_0^{\mathrm{T}}}. \tag{9.24}$$

It must be stressed that this value is heavily dependent on the sea-state, and notation will be defined in due course in order to make this distinction. Conversely, for simplicity, the $\overline{Q}$-factor along with with the $\bar{q}$-factor for regular waves, may be referred to as the *interaction factor*.

9.3 Implementation

In order to obtain useful estimates of array performance in irregular seas, we must employ a realistic wave spectrum. One commonly used omni-directional spectrum was obtained during the Joint North Sea Wave Project (*JONSWAP*), after which it is named (Hasselmann et al., 1973). This is given in Holthuijsen (2007, (6.3.15)) as

$$S_f(f) = \alpha_{\mathrm{p}} g^2 (2\pi)^{-4} f^{-5} \mathrm{e}^{-\frac{5}{4}\left(\frac{f}{f_{\mathrm{peak}}}\right)^{-4}} \gamma_{\mathrm{p}}^{Y}, \tag{9.25}$$

$$Y = \mathrm{e}^{-\frac{1}{2}\left(\frac{f/f_{\mathrm{peak}}-1}{\sigma_{\mathrm{p}}}\right)^2}. \tag{9.26}$$

Here, the independent variable is the wave frequency f, with its value at the peak of the spectrum given by f_{peak}. Also, α_{p} is known as the *Phillips constant*, γ_{p} the *peak enhancement parameter* and σ_{p} a *peak width parameter*. Typical values for these constants that will be used to define the main sea-states here are (Sanil Kumar and Ashok Kumar, 2008):

$$\alpha_{\mathrm{p}} = 0.0081, \tag{9.27}$$

$$\sigma_{\mathrm{p}} = \begin{cases} 0.07 & \text{for} \quad f \leq f_{\mathrm{peak}}, \\ 0.09 & \text{for} \quad f > f_{\mathrm{peak}}, \end{cases} \tag{9.28}$$

$$\gamma_{\mathrm{p}} = 3.3. \tag{9.29}$$

The value of the peak enhancement parameter given here represents the *mean* JONSWAP spectrum, whilst more generally it lies in the range $1 \leq \gamma_{\mathrm{p}} \leq 10$.

The spectrum given by (9.25-9.26) may be re-expressed in terms of the angular frequency ω using the substitution $f(\omega) = \omega/2\pi$. The new spectrum S_ω, along with the

original S_f, satisfies a similar relationship to (9.5), with the integration performed with respect to the appropriate variable. Since the energy of the sea per unit area should not change between the two representations, the variance v must stay the same. This requires multiplication of the spectrum $S_f(f(\omega))$ by $\frac{\mathrm{d}f}{\mathrm{d}\omega} = \frac{1}{2\pi}$ in order to obtain $S_\omega(\omega)$:

$$S_\omega(\omega) = \alpha_\mathrm{p} g^2 \omega^{-5} \mathrm{e}^{-\frac{5}{4}\left(\frac{\omega}{\omega_\mathrm{peak}}\right)^{-4}} \gamma_\mathrm{p}^Y, \tag{9.30}$$

$$Y = \mathrm{e}^{-\frac{1}{2}\left(\frac{\omega/\omega_\mathrm{peak}-1}{\sigma_\mathrm{p}}\right)^2}, \tag{9.31}$$

where $\omega = \omega_\mathrm{peak}$ at $f = f_\mathrm{peak}$. Finally, to obtain the spectrum as a function of wave number, we must substitute $\omega(k_0)$ into (9.30) and multiply by $\frac{\mathrm{d}\omega}{\mathrm{d}k_0} = c_\mathrm{g}(k_0)$:

$$S_{k_0}(k_0) = S_\omega(\omega(k_0)) c_\mathrm{g}(k_0), \tag{9.32}$$

$$\omega(k_0) = \sqrt{g k_0 \tanh k_0 d}. \tag{9.33}$$

One commonly used form of the directional part $S_\beta(\beta)$ of the spectrum $S(k_0, \beta)$ in (9.9) is (Tucker and Pitt, 2001, (2.2-10))

$$S_\beta(\beta) = F_\mathrm{p}(s_\mathrm{p}) \cos^{2s_\mathrm{p}} \frac{1}{2}(\beta - \beta_\mathrm{peak}), \tag{9.34}$$

$$F_\mathrm{p}(s_\mathrm{p}) = \frac{2^{2s_\mathrm{p}-1}}{\pi} \frac{\Gamma^2(s_\mathrm{p}+1)}{\Gamma(2s_\mathrm{p}+1)}, \tag{9.35}$$

where s_p is the *spreading parameter* when taken to be a constant, Γ is the *Gamma function* due to Legendre and β_peak is the predominant direction. Folley and Whittaker (2009) use the values $s_\mathrm{p} = 5, 15$ for wind and swell waves respectively, whilst the main calculations here will be performed with an intermediate value of

$$s_\mathrm{p} = 10. \tag{9.36}$$

The device tuning frequency was chosen in Chapter 5 on the basis that maximum efficiency should roughly coincide with the peak of a wave spectrum, where a large amount of power is delivered to the device. Thus for consistency, we consider here irregular waves for which the parameter ω_peak corresponds to the tuning wave number $2ak_0 = 0.8$. On the same basis, we choose the predominant direction to be the same as the array tuning direction: $\beta_\mathrm{peak} = 0$.

The spectra associated with the aforementioned choices of parameters are shown in Figure 9.1. The omni-directional spectrum of equation (9.30) in the angular frequency variable is given in Figure 9.1(a) for $\gamma_{\mathrm{p}} = 1, 3.3, 10$. Here the tuning frequency is marked on the graph with a vertical grey line, at which all three curves attain their maxima. Note that a higher value of the peak enhancement parameter leads to a more pointed peak, corresponding to swell waves. The curve associated with a value of $\gamma_{\mathrm{p}} = 1$ corresponds to the Pierson-Moskowitz spectrum (Holthuijsen, 2007).

Given the importance of the power spectrum (9.22) in the computation of net power over all wave components, the remaining graphs of Figure 9.1 focus on this function. Here it is calculated using wave spectra (9.32) and (9.34). Figures 9.1(b) and 9.1(c) show the power spectrum as a function of wave number and heading angle respectively. From Figure 9.1(c), it can be seen that higher values of the spreading parameter from the set $s_{\mathrm{p}} = 5, 10, 15$ lead to a narrower peak.

Four sea-states are now defined for use in the creation and analysis of array configurations. These involve either a single component or a spectral distribution in the wave number and angular variables. The former consists of only waves which match the tuning parameter in that variable. The latter consist of wave spectra of the types (9.32) and (9.34) with predominant wave number and direction determined by the same tuning parameters and the remaining constants given by (9.27-9.29) and (9.36). The following summarises these cases:

(R) Regular waves. Wave number: single component $2ak_0 = 0.8$. Wave heading: single component $\beta = 0$.

(K) Multi-frequency, uni-directional irregular waves. Wave number: JONSWAP spectrum with $\gamma_{\mathrm{p}} = 3.3$. Wave heading: $\beta = 0$.

(B) Single frequency, multi-directional irregular waves. Wave number: single component $2ak_0 = 0.8$. Wave heading: Cos-2s spectrum with $s_{\mathrm{p}} = 10$.

(KB) Multi-frequency, multi-directional irregular waves. Wave number: JONSWAP spectrum with $\gamma_{\mathrm{p}} = 3.3$. Wave heading: Cos-2s spectrum with $s_{\mathrm{p}} = 10$.

Note that Sea-states K and KB correspond to long and short crested waves respectively. Although Sea-state B is probably only a pathological case, its application here will prove

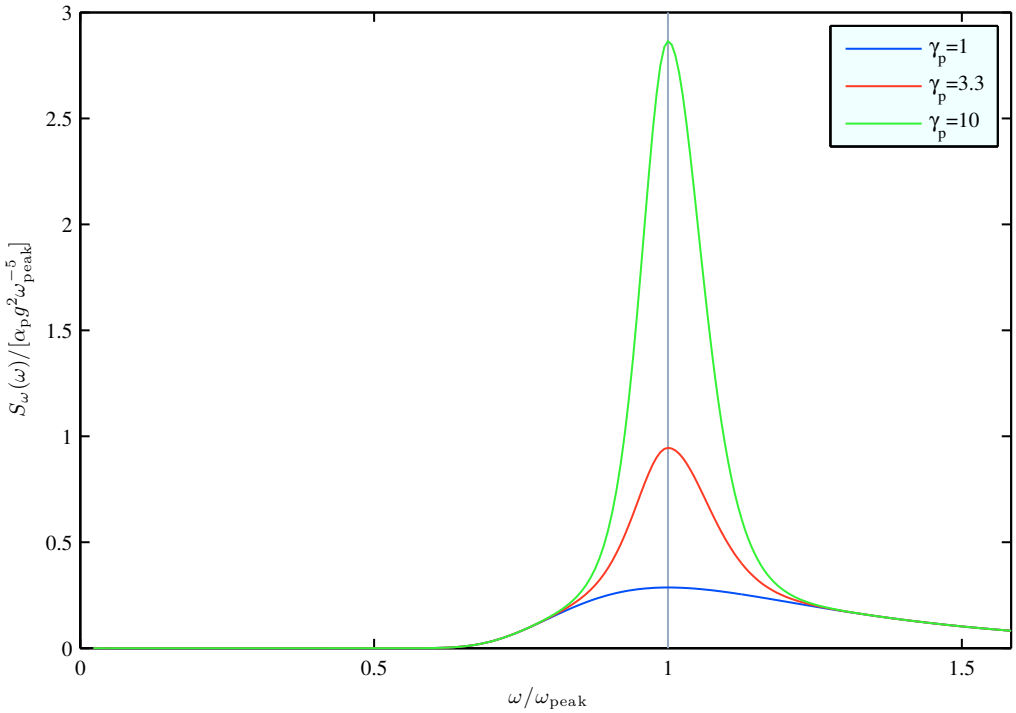

(a) Wave energy spectrum as a function of non-dimensional angular frequency

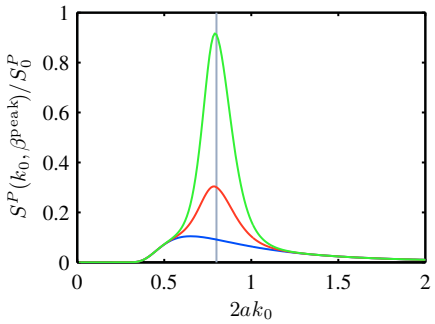

(b) Power spectrum as a function of non-dimensional wave number

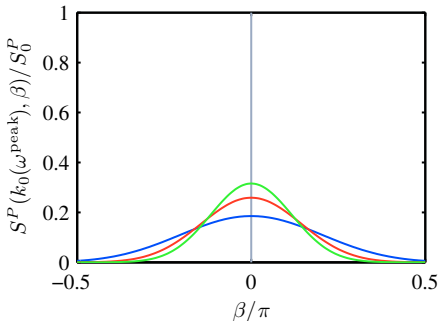

(c) Power spectrum as a function of wave heading angle

Figure 9.1: Sea-state spectra for different parameter values. Power spectra are non-dimensionalised by $S_0^{\mathrm{P}} = [\rho g c_{\mathrm{g}}(k_0(\omega_{\mathrm{peak}}))^2][\alpha_{\mathrm{p}} g^2 \omega_{\mathrm{peak}}^{-5}]$.

enlightening. Other values of the parameters γ_{p} and s_{p} are considered in Section 9.6.4, whilst the remaining results are computed using the default values given above.

The integrations derived from equation (9.23) were performed using trapezoidal summation with twenty-one points each of the wave number and angular ranges. These were also limited to $0.01 \leq 2ak_0 \leq 2$ and $-\pi/2 \leq \beta \leq \pi/2$ in order to allow better accuracy for the largest contributions to overall performance. Such a methodology for estimating the integrals may lead to errors in the value of objective functions, although it is anticipated that it will capture the main features of the solutions without leading to unmanageable computation times.

The regular wave interaction factor $\bar{q}$ will, from here on, be taken to denote its value at the tuning parameters $2ak_0 = 0.8$, $\beta = 0$. Its irregular wave counterpart $\overline{Q}$ will be denoted $\overline{Q}_{\mathrm{K}}$, $\overline{Q}_{\mathrm{B}}$ and $\overline{Q}_{\mathrm{KB}}$ where necessary in order to indicate which sea-state has been used in the calculations.

9.4 Analysis of arrays optimised in regular waves

In Chapter 8, we analysed array configurations that were optimised at the tuning parameters. It was found that significant modifications to the performance of the array occurred around these values, giving rise to a peak or trough in the appropriate $\bar{q}$-factor plots. Furthermore, in the nearby parameter space, the spectra under consideration here enable most power to be delivered to the devices. In this section, we wish to test the hypothesis that matching the modifications in regular wave performance with the peaks in the wave spectra is a reliable way of ensuring advantageous overall performance in irregular seas.

The measure of performance will be provided by the interaction factor, which has been defined for each of the sea-states described in the previous section. These values are given in Table 9.1 for the arrays produced by the Parabolic Intersection method and the Genetic Algorithm in Problems 1, 2 and 3 of Chapter 7.

Most of the arrays give rise to the same qualitative performance in all sea-states, that is to say the interaction factor remains greater or less than unity. This indicates that there is some correlation between array performance under these different conditions. Arrays P1 and G1, however, perform less well in Sea-states B and KB respectively than an equivalent number of devices in isolation, despite their power output having been maximised in regular waves. This is probably due to the fact that the more modest power

Array	$\bar{q}$	$\overline{Q}_{\mathrm{K}}$	$\overline{Q}_{\mathrm{B}}$	$\overline{Q}_{\mathrm{KB}}$
P1	1.136	1.037	0.997	1.000
G1	1.163	1.050	1.029	0.995
P2	1.787	1.286	1.128	1.039
G2	2.010	1.367	1.093	1.041
P3	0.453	0.812	0.982	0.984
G3	0.326	0.547	0.586	0.700

Table 9.1: Interaction factors $\bar{q}$, $\overline{Q}_{\mathrm{K}}$, $\overline{Q}_{\mathrm{B}}$ & $\overline{Q}_{\mathrm{KB}}$, for the Sea-states R, K, B & KB respectively. Array configurations created in Chapter 7 for regular waves. Truncation constants $M_{\mathrm{T}} = 33$, $N_{\mathrm{T}} = 4$.

enhancements from real-tuned devices at the tuning frequency do not make enough of a contribution to overall performance in order that all undesired interferences at other frequencies are offset.

For all the six arrays considered here, introduction of wave components in either the wave number or heading variables forces the interaction factor closer to unity. This is because there is generally an oscillation between constructive and destructive interference with respect to these variables (see Chapter 6 for explanation). Furthermore, only the performance at one component has been optimised so undesirable interference is permitted in influential components close to the tuning parameters. Hence integration over the variables may lead to an averaging effect of the performance modifications.

Although the magnitude of enhancements is generally significantly reduced when more wave components are considered for these layouts, Array G3 still exhibits a large modification in performance for Sea-state KB. In a multi-frequency, multi-directional sea-state, this configuration performs 30% worse than an equivalent number of devices in isolation. The reason is that the $\bar{q}$-factor for this array exhibits a wide trough with respect to wave number and direction (see Figure 8.5). Consequently, the majority of the contributions to net array performance is of the same destructive nature.

9.5 Optimisation of arrays in irregular waves

The definition of the interaction factor in irregular waves not only allows assessment of existing array configurations, but in combination with an optimisation routine, also enables creation of the layouts themselves. The Genetic Algorithm is the most appropriate method to use here since, unlike the Parabolic Intersection method, the

way that is operates is not specific to regular waves. Only a few small modifications are necessary in order to apply the same version of the algorithm here that was presented in Chapter 7 and create arrays of five devices.

First of all, we must redefine the problems detailed in Section 7.2 in order to account for sea-states other than regular waves. Given that devices are tuned to a particular frequency, array layout is therefore optimised in waves from a given sea-state that has a peak at the same frequency, with the following objectives:

Problem 1 Maximise net power in an array of real-tuned devices

Problem 2 Maximise net power in an array of reactively-tuned devices

Problem 3 Minimise net power in an array of reactively-tuned devices

The change of fitness function is the only major difference here to the manner in which the GA was implemented for regular waves (see Section 7.4.2 for details). The value of $-\overline{Q}$ using the appropriate sea-state was employed for this purpose in Problems 1 and 2, whilst $\overline{Q}$ was employed in Problem 3.

Since the calculation of the net interaction factor in irregular waves involves consideration of several wave components, the computation time for the optimisation is correspondingly increased over that for array generation in regular waves. Hence in order to mitigate this effect, the truncation constants used in the solution of the hydrodynamic problem were decreased from $M_{\mathrm{T}} = 33$ and $N_{\mathrm{T}} = 4$ to $M_{\mathrm{T}} = 8$ and $N_{\mathrm{T}} = 2$. This is justified as a result of the favourable convergence characteristics of this method (see Section 4.5). Furthermore, it was not found to significantly affect the ability of the routine to find adequate solutions. Nonetheless, all values of $\bar{q}$ and $\overline{Q}$ in the graphs and tables presented here are calculated with the full values $M_{\mathrm{T}} = 33$ and $N_{\mathrm{T}} = 4$.

Arrays were created for Sea-states R, K, B and KB of Section 9.3 and labelled GR, GK, GB and GKB respectively followed by the number (1, 2 or 3) of the problem to which they relate. Although the case of array creation in regular waves has already been treated in previous chapters, it is repeated here with the fitness function ($-\bar{q}$ or $\bar{q}$) calculated using the reduced truncation constants. Alternative configurations were also created by re-running the same optimisations with different random seeds. Further array layouts were formed using different sea parameters, which are contained in Section 9.6.4.

9.6 Analysis of arrays optimised in different sea-states

9.6.1 Array layouts

The arrays produced by the optimisation process are shown in Figures 9.2 and 9.3. In common with those presented in Chapter 8, all of the arrays displayed here are approximately regular in their formation. That is to say, many of the relative positions between body pairs are approximately replicated within the layout. Table 9.2 contains the coordinates of four of the five devices in each case (the first being located at the origin).

Array	$(x_2/a, y_2/a)$	$(x_3/a, y_3/a)$	$(x_4/a, y_4/a)$	$(x_5/a, y_5/a)$
GR1	(5.08,14.26)	(11.45,0.32)	(-5.08,-15.42)	(6.06,-14.07)
GK1	(-0.10,-5.33)	(-0.10,-10.06)	(-0.10,-14.78)	(-0.03,-20.12)
GB1	(-0.01,5.79)	(-11.18,-3.15)	(-11.47,3.20)	(-10.81,9.72)
GKB1	(-0.02,-4.67)	(-0.04,-9.16)	(-0.01,-13.66)	(0.01,-18.31)
GR2	(-8.62,-14.41)	(-16.50,18.54)	(-7.96,32.53)	(-23.78,52.72)
GK2	(-0.35,10.13)	(-0.44,21.46)	(-0.29,32.84)	(0.11,42.84)
GB2	(-0.14,-8.78)	(-0.14,-17.54)	(-0.14,-26.30)	(0.00,-35.11)
GKB2	(-0.13,8.52)	(-0.18,16.96)	(-0.17,25.41)	(-0.05,33.92)
GR3	(-0.64,3.95)	(7.09,5.07)	(7.01,9.07)	(14.55,11.54)
GK3	(6.88,-4.26)	(-0.39,-3.98)	(7.21,-8.24)	(14.94,-11.82)
GB3	(-8.24,-1.95)	(0.03,-4.02)	(8.10,-0.08)	(8.22,-4.10)
GKB3	(8.22,2.02)	(8.33,-1.98)	(16.41,1.19)	(16.91,-2.78)

Table 9.2: Global Cartesian coordinates of devices belonging to arrays optimised in different sea-states.

Alternative arrays that have been generated using exactly the same process but initiated with a different random seed are shown in Figures A.9, A.10 and A.11 of the appendix for Sea-states R, K and B respectively. Included alongside each is the interaction factor relating to the sea-state in which the array was optimised. In several cases, the array formation process produces more consistent formations in irregular waves than regular waves. This is certainly true for Problem 1 in multi-frequency uni-directional irregular waves and for Problem 2.

9.6.2 Interaction factors

Interaction factors for the arrays produced by the GA in different sea-states are shown in Table 9.3. The entry corresponding to the sea-state in which each array has been optimised is shown in bold.

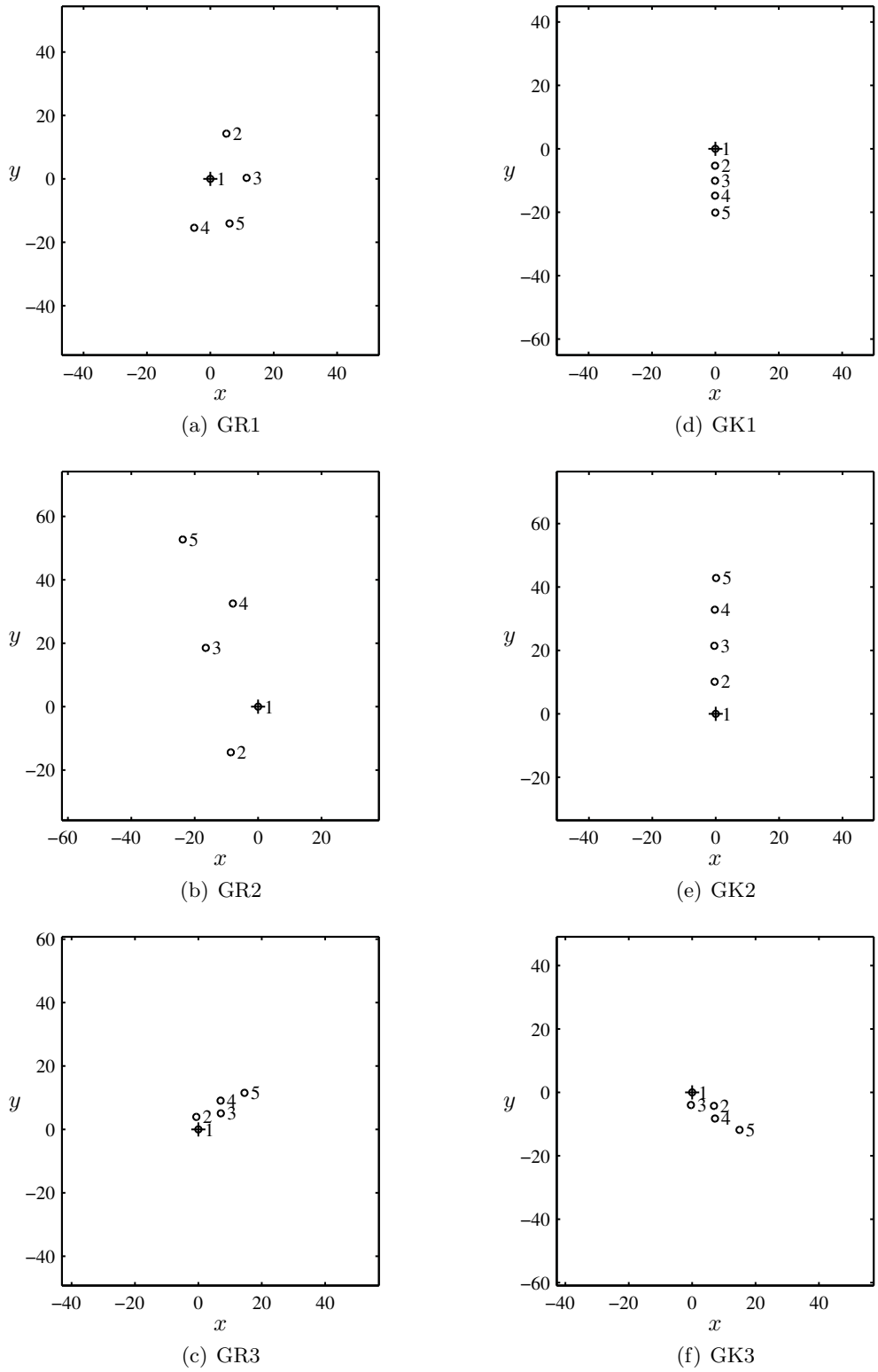

Figure 9.2: Array configurations optimised in different sea-states. Labels: Genetic Algorithm (G), Sea-states (R) and (K), Problem (1,2,3).

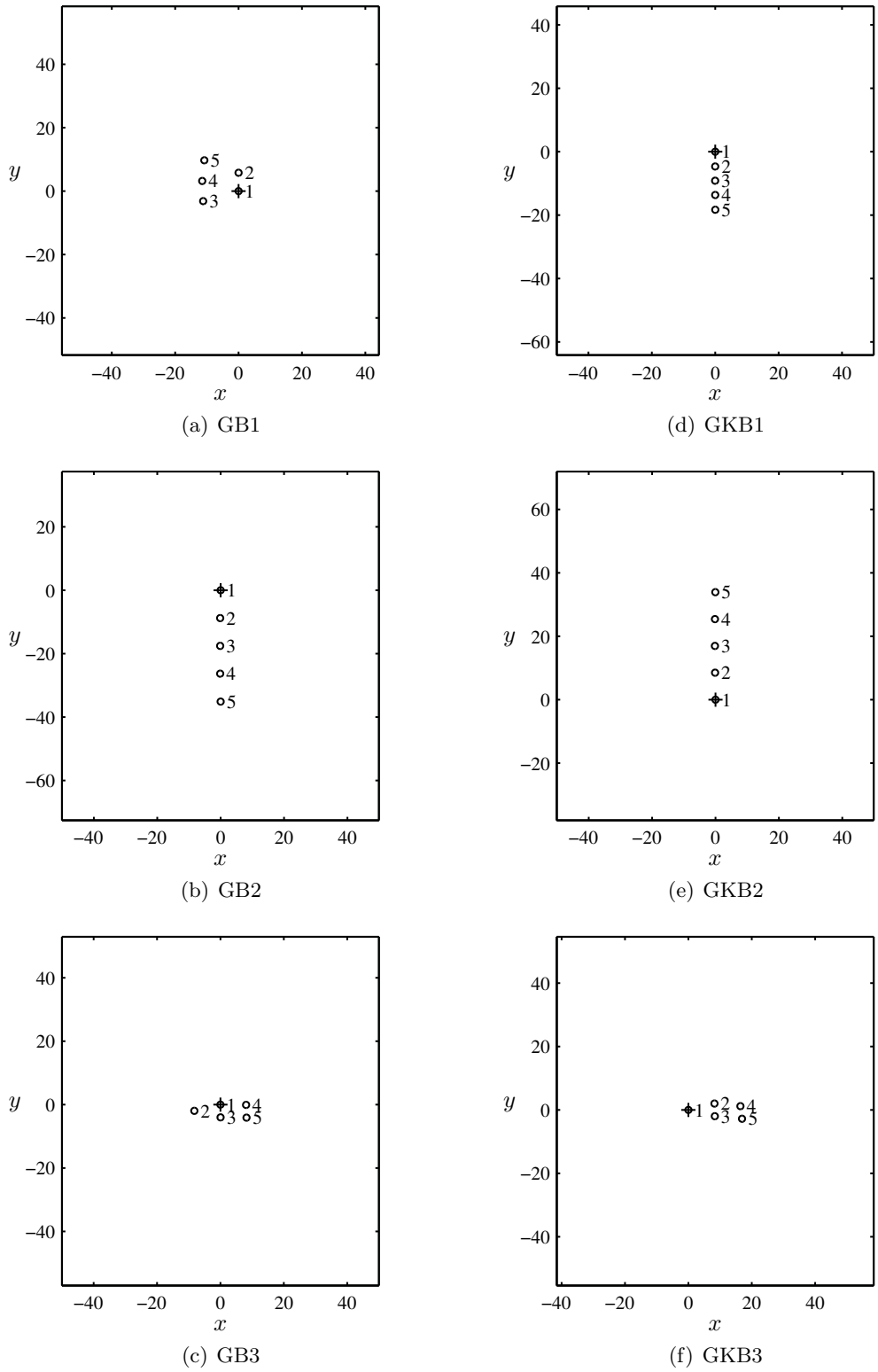

Figure 9.3: Array configurations optimised in different sea-states. Labels: Genetic Algorithm (G), Sea-states (B) and (KB), Problem (1,2,3).

Array	$\bar{q}$	$\overline{Q}_{\mathrm{K}}$	$\overline{Q}_{\mathrm{B}}$	$\overline{Q}_{\mathrm{KB}}$
GR1	**1.162**	1.051	1.029	0.995
GK1	1.061	**1.109**	1.028	1.044
GB1	1.121	1.043	**1.066**	1.003
GKB1	1.044	1.106	1.018	**1.046**
GR2	**1.950**	1.349	1.106	1.043
GK2	1.768	**1.411**	1.245	1.129
GB2	1.528	1.356	**1.338**	1.175
GKB2	1.475	1.339	1.330	**1.176**
GR3	**0.326**	0.543	0.579	0.693
GK3	0.337	**0.538**	0.580	0.690
GB3	0.376	0.593	**0.487**	0.640
GKB3	0.391	0.597	0.489	**0.640**

Table 9.3: Interaction factors ($\bar{q}$, $\overline{Q}_{\mathrm{K}}$, $\overline{Q}_{\mathrm{B}}$ & $\overline{Q}_{\mathrm{KB}}$) for arrays optimised in different sea-states (R, K, B & KB). Truncation constants $M_{\mathrm{T}} = 33$, $N_{\mathrm{T}} = 4$.

For a given sea-state, the arrays that perform best in terms of the relevant objective in each problem are those which have been optimised using the same sea description. This is a direct result of the effectiveness of the optimisation process.

In common with the arrays analysed in Section 9.4, the most significant interactions in multi-frequency multi-directional waves occur in Problem 3 where power is minimised. This is because the associated layouts involve closely spaced devices up-wave of one another. Hence shadowing effects produce a significant modification in performance over a large range of wave components, as described for Array G3 in Section 8.4.

It is important to note that arrays that have been optimised in irregular waves do not necessarily lead to more modest modifications in performance as more wave components are introduced. For example, Array GK1 has a higher net interaction factor in Sea-state K than R. Hence, frequencies and wave headings other than those at the peak of the spectra can enhance the desired effects if exploited correctly. However, it may still be the case that the strongest possible modification in performance over all array configurations weakens as more wave components are added. The results presented here are certainly consistent with this hypothesis.

The arrays that have been optimised in Sea-states K and B perform better in Sea-state KB with respect to the relevant objective of each problem than the array optimised in Sea-state R. This is because Sea-state KB shares a greater number of wave components with Sea-states K and B than with R. Hence a larger contribution to the overall performance is also common to those cases.

As noted in relation to the arrays studied in Section 9.4, those considered here generally exhibit the same qualitative performance in all sea-states. Some exceptions occur in Problem 1, however, for the reasons previously outlined.

Table 9.3 clearly shows that even in fully irregular seas (Sea-state KB), interactions may still be significant. The strongest positive interference occurs for Array GKB2, where $\overline{Q} = 1.176$ and the most destructive effects take place for Arrays GB3 and GKB3 where $\overline{Q} = 0.640$. This implies a discrepancy of 53.6% in the possible performance of arrays as a result configuration changes (calculated as a proportion of the power attainable from an equivalent number of devices in isolation). Although in practice this is likely to be reduced as a result of the limitations of linear theory, it is still a significant figure.

9.6.3 Power

Array performance in this section is analysed using the total power generated by constituent devices, normalised by that contained in a wave of equal breadth to one converter $P/(2Ja) = \sum_{j=1}^{N} \ell_j/(2a)$. The variation of this quantity with respect to wave number and heading is shown in Figures 9.4, 9.5 and 9.6 for each array. Plotted alongside these curves is the power from an isolated device, multiplied by the number of elements in the array (five). Thus when the array power curve is greater than this, the performance of the devices is enhanced and vice-versa. The range of wave headings and angles reflects those used in the calculation of the net interaction factors and the vertical grey line represents the tuning parameter value. For reference, the heave amplitudes corresponding to the aforementioned plots of array power are given in Figures A.12, A.13 and A.14 of the appendix.

Sea-state R

The only difference between the creation of arrays for Sea-state R (GR1-3) and those first presented in Chapter 8 (G1-3) is the reduction in truncation constants used to calculate the fitness function here. As can be seen from Figure 9.2(a)-(c) and Figure 8.1(d)-(f), there is no significant difference in the formation between these cases, once certain equivalences (reflections in the x-axis and rotations of π radians) have been taken into account. Consequently, the interaction factors achieved (Tables 9.1 and 9.3) are also similar. Hence the reduction in truncation constants was justified,

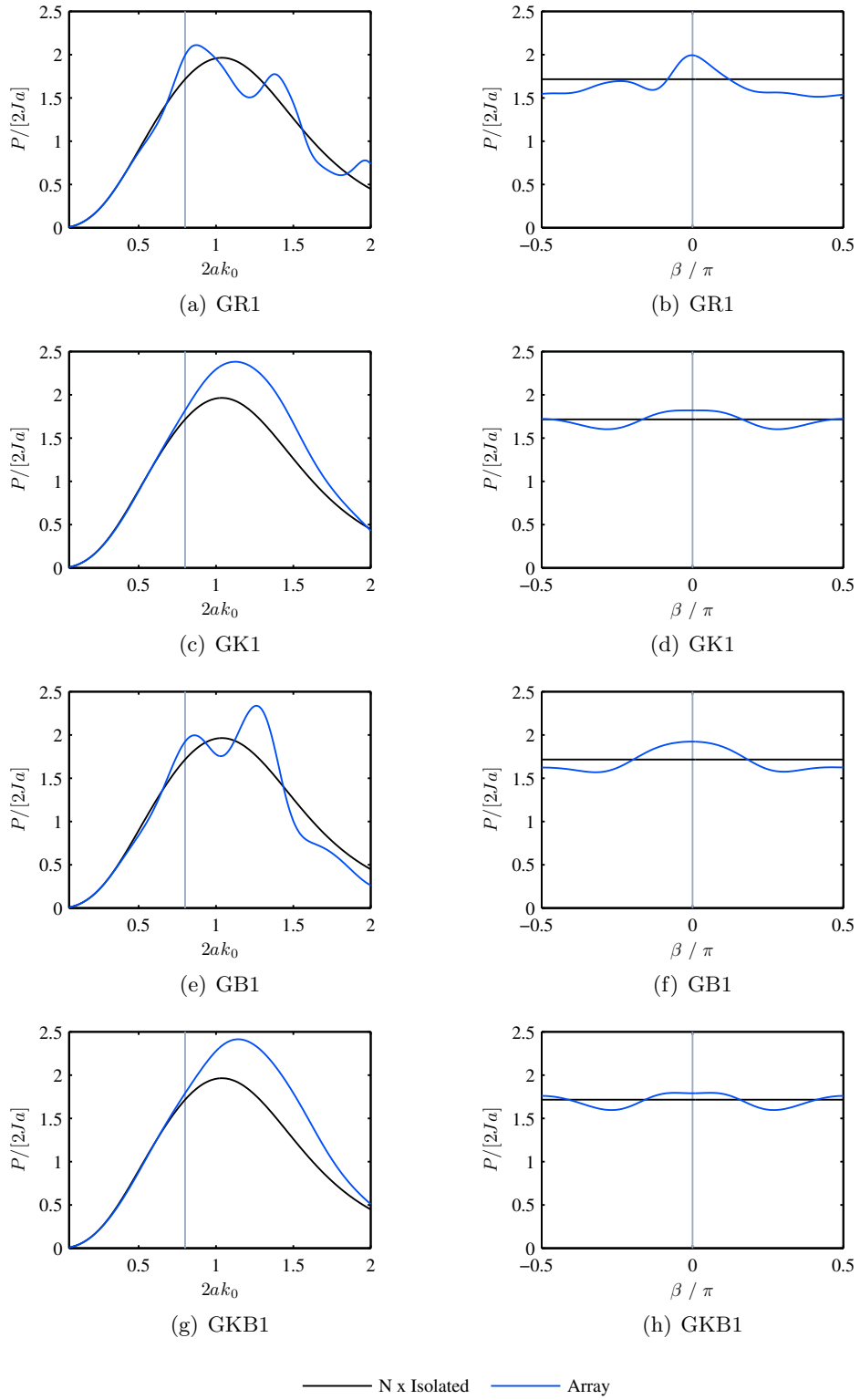

(a) GR1 (b) GR1

(c) GK1 (d) GK1

(e) GB1 (f) GB1

(g) GKB1 (h) GKB1

Figure 9.4: Power absorbed by arrays solving Problem 1. Variation of non-dimensional power $P/[2Ja]$ with non-dimensional wave number $2ak_0$ for $\beta = 0$ and wave heading β for $2ak_0 = 0.8$.

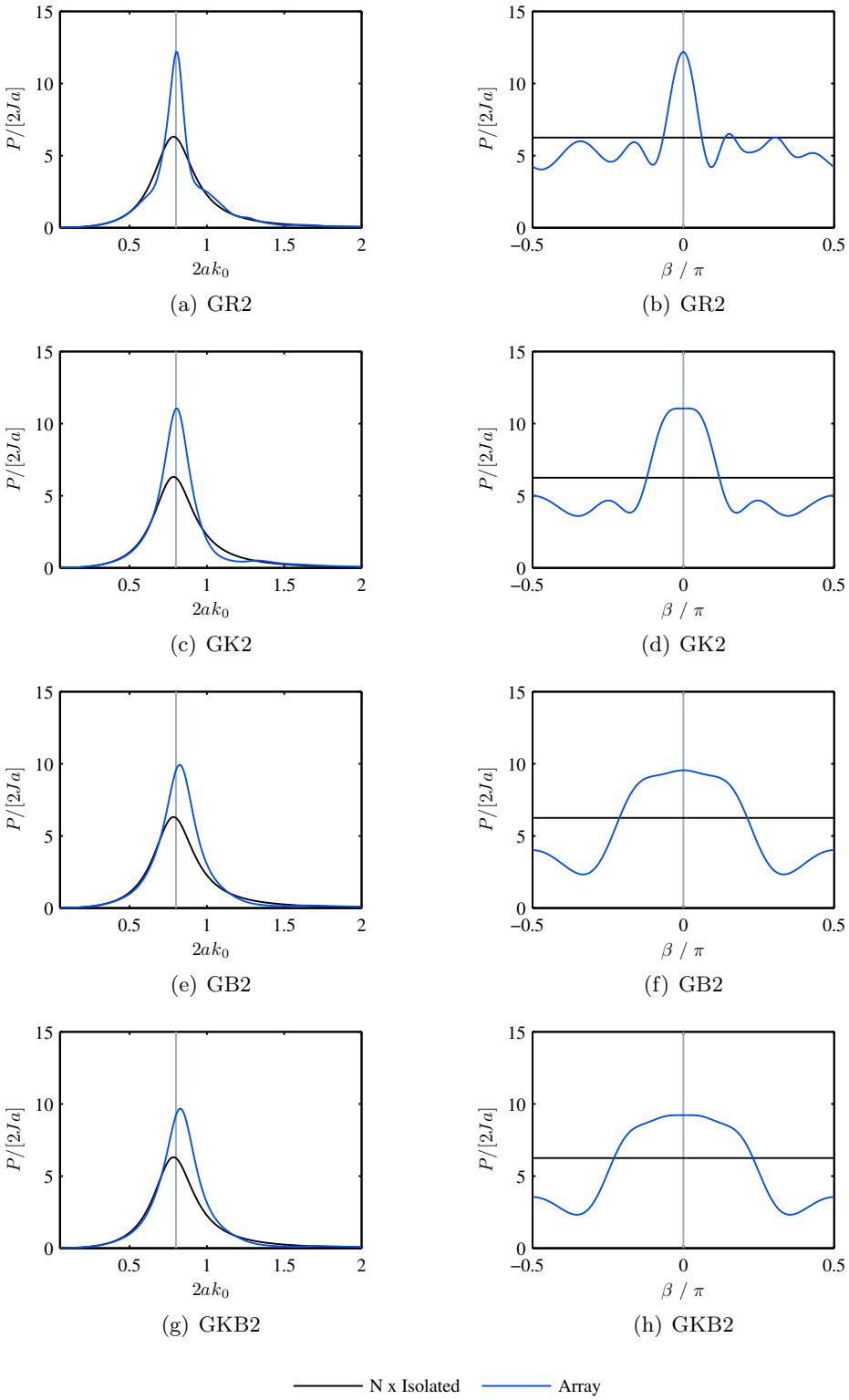

(a) GR2 (b) GR2

(c) GK2 (d) GK2

(e) GB2 (f) GB2

(g) GKB2 (h) GKB2

Figure 9.5: Power absorbed by arrays solving Problem 2. Variation of non-dimensional power $P/[2Ja]$ with non-dimensional wave number $2ak_0$ for $\beta = 0$ and wave heading β for $2ak_0 = 0.8$.

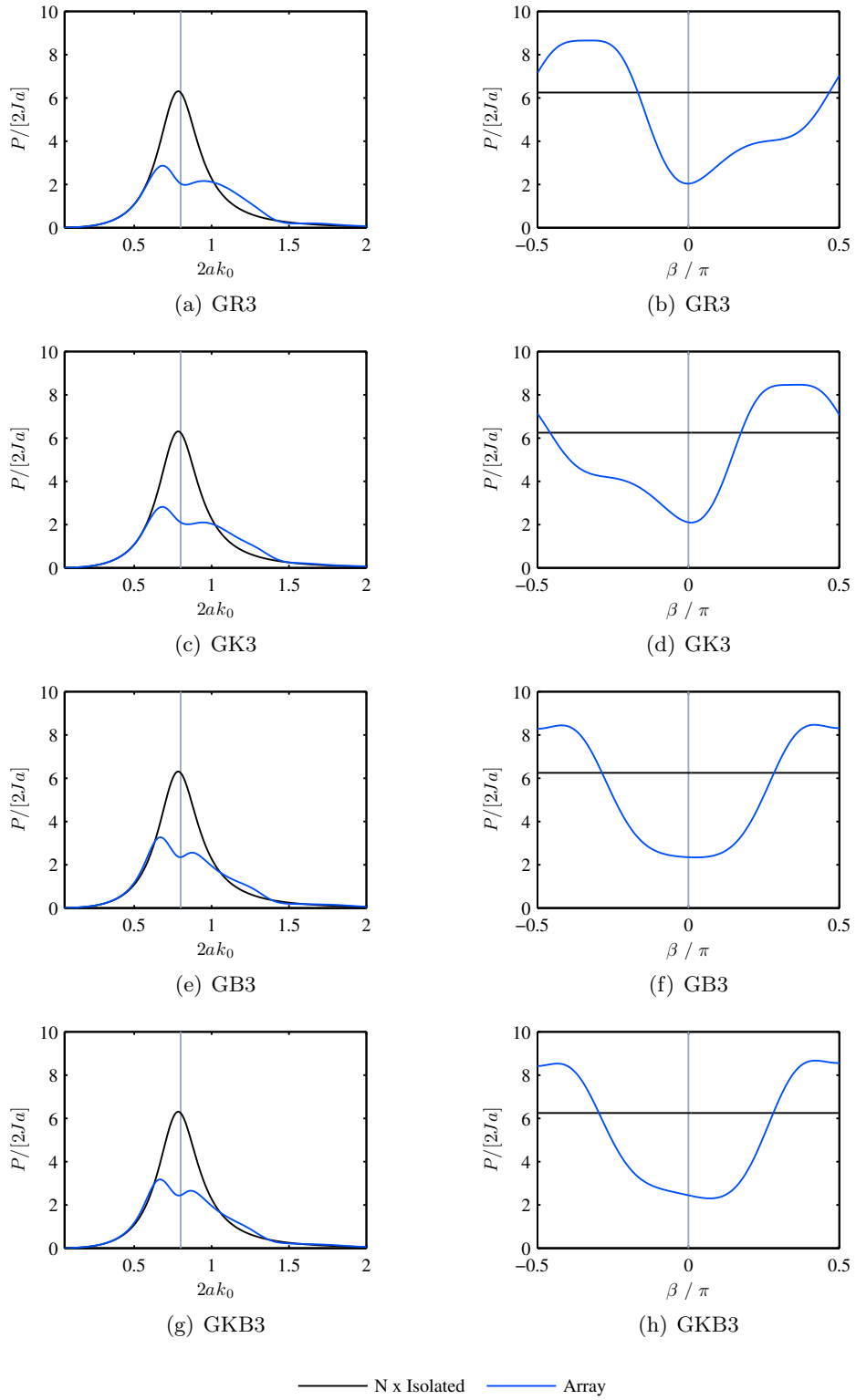

(a) GR3 (b) GR3

(c) GK3 (d) GK3

(e) GB3 (f) GB3

(g) GKB3 (h) GKB3

Figure 9.6: Power absorbed by arrays solving Problem 3. Variation of non-dimensional power $P/[2Ja]$ with non-dimensional wave number $2ak_0$ for $\beta = 0$ and wave heading β for $2ak_0 = 0.8$.

in that the optimisation process has remained effective. The plots of power output for Arrays GR1, GR2 and GR3 (considered in relation to the isolated device curves) are therefore qualitatively similar to the $\bar{q}$-factor plots for Arrays G1, G2 and G3 analysed in Section 8.4.

Note that there is more fluctuation in the plots of power as a function of wave number and heading for arrays created in Sea-state R than other seas, especially in Problems 1 and 2. This is because in this sea-state, only the performance of the array at one wave component makes a contribution to the fitness value, whilst the values at other wave numbers and headings are not required by the optimisation. Hence, the procedure has allowed widely spaced arrays to be created involving long interaction distances and thus rapid oscillations with respect to both β and k_0.

Sea-state K

For Problems 1 and 2, the arrays created by the GA in Sea-state K all have a linear formation, with the line joining the devices perpendicular to the incident wave direction (see Figures 9.2(d) and 9.2(e)). This type of arrangement has been exhibited in the collection of alternative arrays for Problem 2 of Chapter 7 in the regular wave case (Figure A.7). However, linear arrays have not been produced for Problem 1 in regular waves. One possible reason for the suitability of this formation to a multi-frequency sea-state is that for other configurations, there is at least one pair of devices where one device is up-wave of another. In this situation, one short and one long interaction distance result, the longer of which leads to more rapid fluctuation in the type of interference with respect to wave number. For a given separation between devices, a pair which are normal to the wave direction offers the shortest maximum interaction distance. Hence we have the largest minimum repeat value and the power output is the most stable with respect to wave number.

Array GK1 has less variation in power output with respect to wave number than GR1. This means that it is more suited to capturing energy that is not at the peak of the power spectrum, since enhancements are then sustained over a large range of wave components. Even though the peak power output is is not well aligned with the tuning frequency, the power spectrum (Figure 9.1(b)) still contains a significant amount of energy at higher frequencies and hence the power enhancement there is able to make a reasonable contribution to the overall performance. Thus Array GK1 provides an

example of where wave components other than those at the tuning parameters are exploited in the optimisation process rather than simply relying on the peak power output.

The layout GK2 gives rise to a power curve that has marginally less variation with respect to wave number in relation to the isolated device power than GR2. Therefore GK2 captures slightly more energy on average ($\overline{Q}_{\mathrm{K}} = 1.411$) than the latter configuration ($\overline{Q}_{\mathrm{K}} = 1.349$) in Sea-state K. The two arrays both give rise to a tall, narrow peak in the power plots. It is therefore clear that the largest contribution to net interaction factor for both arrangements is at the tuning frequency.

Array GK3 has almost exactly the same configuration as GR3 after the permitted reflections and rotations. As can be seen in Figure 9.6(a) and 9.6(c), the associated shadowing properties are effective in a large range of frequencies as well as at the tuning frequency. Hence the degradation in the power output is maintained when this formation type is placed in multi-frequency irregular waves. Another important feature of the arrangement is its capacity to create significant modifications to the power output at the tuning frequency. Because the reactively-tuned isolated device power peaks here along with the power spectrum, any modifications are certain to impact heavily on the net interaction factor. Hence to some extent, the objectives of the optimisation in Sea-states R and K converge, providing a further reason why Arrays GK3 and GR3 should have similar geometries. Correspondingly, the plots of power output from these arrangements are almost the same.

Sea-state B

Arrays created with Sea-state B (that is GB1, GB2 and GB3) are all symmetric with respect to the x-axis. Since the power spectrum is symmetric about its peak, it is more advantageous to form arrangements that exhibit moderately desirable characteristics for positive and negative angles than ones for which the desirable performance in one portion of the range is achieved to the detriment of performance for angles the other side of the mean direction. This naturally leads to symmetric formations being favoured where processes are equivalent either side of the mean wave heading angle. However, the symmetry is not always exact; slight deviations from this type of formation may be observed in the set of alternative arrays in Figure A.11.

One particular example of the benefits of symmetry in this sea-state is Array GB3.

This is similar in formation to GR3 and GK3, after a shear map is applied to the latter two such that they are symmetric with respect to mean oncoming wave direction. From the plot of the radiated velocity potential surrounding a single device (Figure 5.6(d)), it can be seen that the strongest destructive interference will occur where the receiving device is offset from the originating device with respect to the oncoming wave direction. However, changing the angle of attack slightly in one of the directions then finds a curve of constructive interference. Therefore, it is more advantageous for the receiving device to be in the centre of an area of partially destructive interference that remains as such over a representative angular range. This leads to a symmetric formation. As can be seen from the variation of power with wave heading angle, the trough is not as wide for Array GB3 as for GR3 under positive angles of attack. However, because it is symmetric, the trough is about the same width for negative angles too and so is better aligned with the mean wave direction. Hence the net interaction factor in this sea-state is lower than for GK3 and GR3.

The separation and orientation of the devices within the up- and down-wave rows of Array GB1 is very similar to those of GK1. This allows the configuration to exploit up-wave interactions that are strong for this tuning regime. Consequently, Array GB1 achieves a higher power output at the tuning parameters than GK1. Note that this sort of interference leads to a larger interaction distance than the cross-wave type, given a certain separation distance between devices (see equation (6.1)). Hence, there is a rapid variation in the plot of power as a function of wave number here. However, there is also an increased chance of an up-wave device shadowing a down-wave converter, where a proportion of the incident wave energy at the latter is lost, usually over a large frequency range. This means that such a configuration is not well suited to a multi-frequency irregular sea.

Because of its similarity in form to Array GK2, GB2 gives rise to a similar plot of power output with respect to wave number and heading. However, these configurations have average separations of $8.18a$ and $6.58a$ respectively meaning that the latter is associated with smaller interaction distances and thus less rapid fluctuations in performance with respect to both variables.

Despite the modification in performance with respect to wave heading angle compared to Arrays GR3 and GK3, Array GB3 has almost exactly the same relationship of performance to wave number.

Sea-state KB

The arrays created in Sea-state KB have very similar formations and power output curves to Arrays GK1, GB2 and GB3 in Problems 1, 2 and 3 respectively. Hence detailed analysis of these results may be obtained by referring to the relevant sections above. Significantly, on the basis of this evidence, the optimisation process in Sea-state KB simply reverts to finding the best solution in a sea-state with components in either wave number or heading angle. If this were to be the case in general, it would be sufficient to optimise arrays in irregular seas with components in each parameter separately and choose the best from the resulting array pair. This would represent a considerable saving in computation time, and thus merits further investigation.

9.6.4 Variation of spectral shape parameters

Figure 9.7 shows arrangements that have been optimised for each problem in a sea-state identical to K except for the peak enhancement parameter which has been changed from its mean value of $\gamma_p = 3.3$. As can be seen from Fig 9.1, the two values $\gamma_p = 1$ and $\gamma_p = 10$ used here correspond to broad and narrow distributions of incident power over the frequency range respectively.

When considered along with their counterparts for $\gamma_p = 3.3$ (that is, GK1, GK2 and GK3), the arrangements shown here do not appear to be significantly altered in nature by the changes in peak enhancement parameter. That is to say the configurations for Problems 1 and 2 are regular and linear in formation, perpendicular to the oncoming wave direction. Problem 3 gives rise to closely spaced staggered formations, which correspond almost exactly with GR3 and GK3 after permitted rotations and reflections have been taken into account.

The slight difference between arrays for the two extreme parameter values is that the lower value of γ_p produces a more closely spaced array in Problems 1 and 2. This is because a broader spectrum encourages formations which produce power enhancement over a wide frequency range. Closer separations mean that typical interaction distances are small, wave number repeat values are large and thus performance enhancements persist over a large interval of wave numbers.

The depth and width of the degradation in power production at the tuning frequency for arrays of the type GR3 are clearly sufficient to modify net performance with both narrow and broad power spectra. Hence there is no significant deviation from that

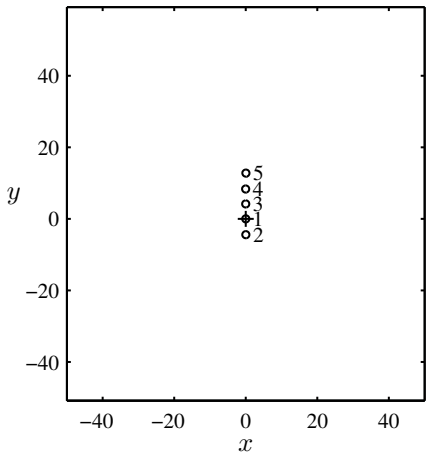

(a) Problem 1: $\gamma_{\mathrm{p}} = 1$

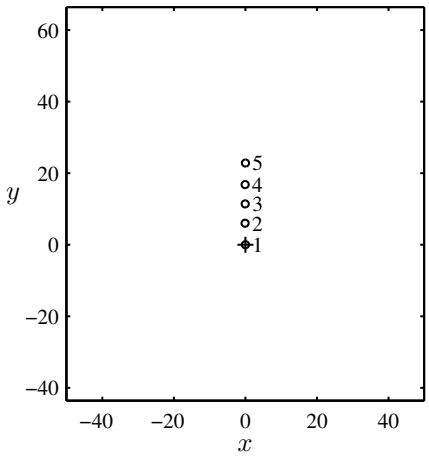

(d) Problem 1: $\gamma_{\mathrm{p}} = 10$

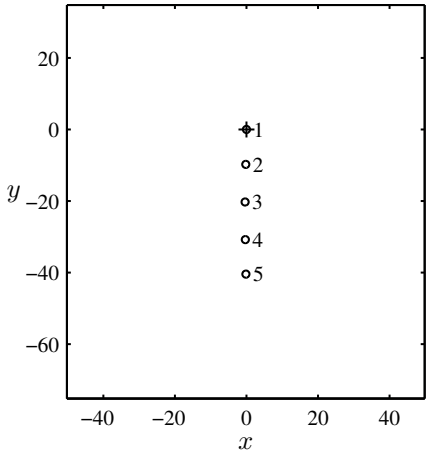

(b) Problem 2: $\gamma_{\mathrm{p}} = 1$

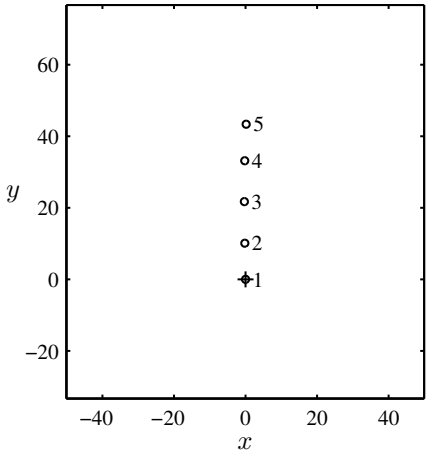

(e) Problem 2: $\gamma_{\mathrm{p}} = 10$

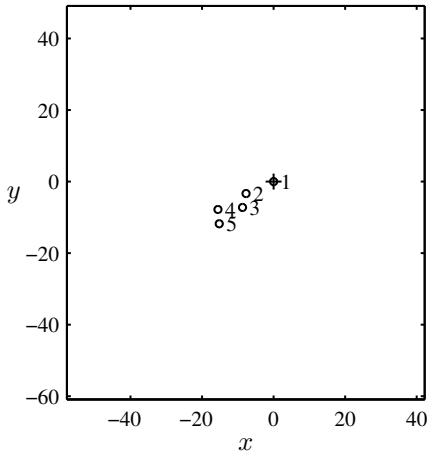

(c) Problem 3: $\gamma_{\mathrm{p}} = 1$

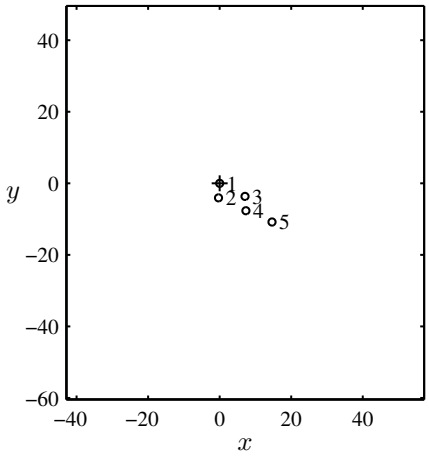

(f) Problem 3: $\gamma_{\mathrm{p}} = 10$

Figure 9.7: Array configurations optimised in Sea-state K with different values of the peak enhancement parameter γ_{p}.

formation in the arrays solving Problem 3 presented here.

Figure 9.8 shows arrangements that have been optimised for each problem in a sea-state identical to B except for the spreading parameter, which has been altered from $s_\mathrm{p} = 10$. As can be seen from Figure 9.1, the two values $s_\mathrm{p} = 5$ and $s_\mathrm{p} = 15$ correspond to broad and narrow distributions of power over the angular range respectively. Note that both of these spectral shapes do not differ greatly from the spectrum used to create the main arrays GB1, GB2 and GB3.

It was remarked in Section 9.6.3 that the arrays created for multi-directional irregular waves appeared to be symmetric with respect to the mean wave direction. In cases where the power spectrum has either a very narrow or broad peak, this does not necessarily hold. In the former situation, the regular wave case is approached and thus only the power value at one wave heading is important. In the limit of the latter case where all incident wave directions contain an equal amount of power, the shape of the power curve is irrelevant so long as the total area beneath it is as large or small as desired. In both these cases symmetry in array formation which leads to symmetry in the power plots near the tuning heading is not required.

Array symmetry is certainly broken in Problem 1 for $s_\mathrm{p} = 5$ (Figure 9.8(a)). The equivalent array for $s_\mathrm{p} = 15$ (Figure 9.8(d)) is similar in formation to one of the alternative arrays for $s_\mathrm{p} = 10$ (Figure A.11(b)). That is to say, there are two rows of devices perpendicular to the mean wave direction, offset from each other. However, here the arrangement is slightly perturbed from a symmetric configuration.

The arrays solving Problem 2 are linear in formation for each value of the spreading parameter here, as well as for the original value $s_\mathrm{p} = 10$. As with multi-frequency irregular waves, the broader the power spectrum is (that is to say, the lower the value of s_p), the more closely spaced the converters need to be to take advantage of all the significant wave components.

For Problem 3 with $s_\mathrm{p} = 15$, the arrangement closely resembles Array GB3. However when $s_\mathrm{p} = 5$, a configuration which is wider in the y-direction results. This allows shadowing of the back row by the front row over a larger range of angles than arrays of the type GB3. Hence the configuration is better suited to the broad angular power spectrum in which it was optimised.

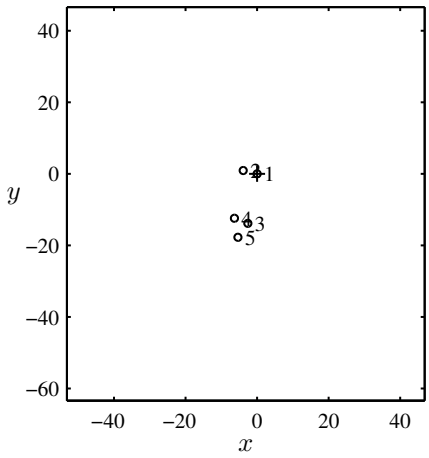

(a) Problem 1: $s_{\mathrm{p}} = 5$

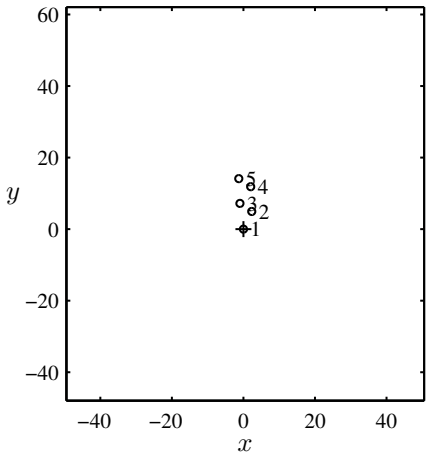

(d) Problem 1: $s_{\mathrm{p}} = 15$

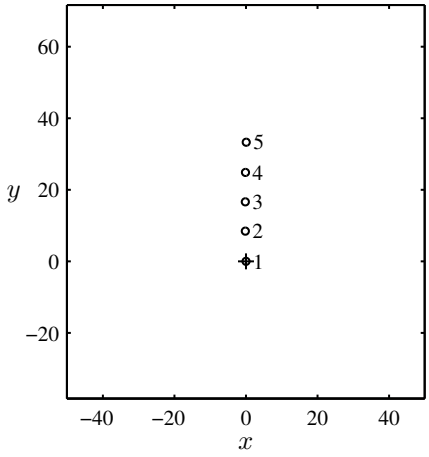

(b) Problem 2: $s_{\mathrm{p}} = 5$

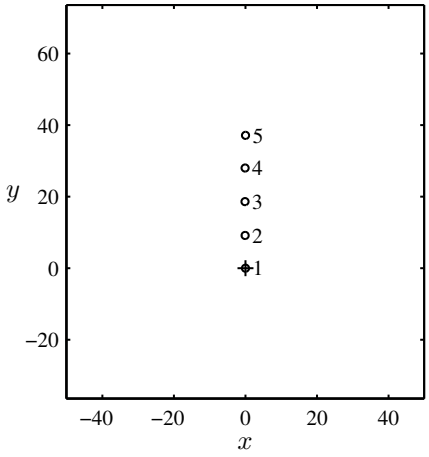

(e) Problem 2: $s_{\mathrm{p}} = 15$

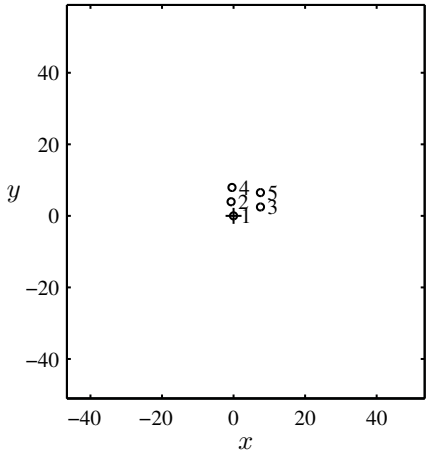

(c) Problem 3: $s_{\mathrm{p}} = 5$

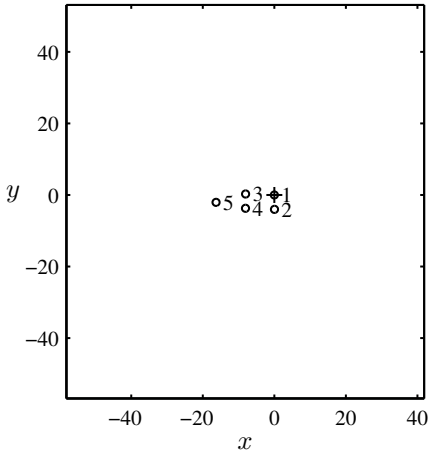

(f) Problem 3: $s_{\mathrm{p}} = 15$

Figure 9.8: Array configurations optimised in Sea-state B with different values of the spreading parameter s_{p}.

9.7 Evaluation

Because the GA optimisation is a semi-random procedure and there are so many different processes occurring simultaneously in arrays surrounded by irregular seas, it is difficult to draw firm conclusions on the basis of the examples studied here. Furthermore, it should not be forgotten that these results are subject to the limitations of the hydrodynamic theory used, including those relating to the principle of superposition and to large motion amplitudes. However, some general patterns in the present set of results may be highlighted.

Matching a regular sea-state to the peak of a wave spectrum and optimising performance under these conditions has been applied here with generally successful results. That is to say, the desired modification to the power output occurs still for irregular waves in most but not all cases. This is a commonly used principle in the design of isolated converters and it is important to note its applicability to arrays.

Arrays optimised in the aforementioned regular waves have net interaction factors which are closer to unity in irregular waves. This means that there is a lesser overall modification in performance in the latter case. However, configurations specifically optimised in an irregular sea-state can exhibit larger modifications than the same array in a corresponding regular wave climate. Furthermore, there is a significant difference in interference effects between the best- and worst-case arrangements in irregular waves with components in frequency and direction.

A general trend in the formation of arrays is that broader spectra lead to more closely spaced devices in the optimal arrangements. However, this effect was not found to be considerable compared to that resulting from other factors such as the power take-off tuning regime.

Finally, the arrays created in multi-directional, multi-frequency waves resemble those formed with components in either the wave number or heading variables. If replicated more generally, this could be used to improve the efficiency of the optimisation process.

Chapter 10

Conclusions

10.1 Summary

The discourse contained herein began in Chapter 1 with a description of the context and scope of this research. In Chapter 2 the relevant published literature was reviewed, including topics concerning isolated structures, arrays and the optimisation of their layout. Particular areas that seem to be under-represented in this body of work are 'exact' hydrodynamic solutions with respect to linear wave theory, free optimisations of array configuration and irregular wave analysis.

Chapter 3 described a simplified model of an array of generic 'point absorber' devices or a single 'multiple-float' device. The combination of 'exact' hydrodynamic theories described here, has been applied in the field of wave energy for the first time by the author. Unlike existing solutions, the effects of scattered waves, independent movement of the bodies, and sub-optimal power take-off characteristics have been taken into account. Incorrect equations contained in a related work (Yilmaz, 1998) have also been amended in this process.

The interaction theory was subsequently implemented as computer code, as described in Chapter 4. Convergence analysis has been performed and the results verified against the commercial boundary element code WAMIT, with excellent agreement. Furthermore, the present method was found to be considerably more efficient.

The behaviour of an isolated converter was reviewed in Chapter 5 using the analogy of a second-order linear oscillator. Motions, forces, power values and disturbances to the flow surrounding the device were analysed as power take-off coefficients, tuning regime,

water depth and device dimensions were altered. Real tuning at the chosen frequency ($2ak_0 = 0.8$) was found to result in more moderate motion amplitudes than the other regimes and so may be desirable from an engineering perspective, despite the diminished performance.

The effects of array-related parameters (that is, device separation, wave heading angle, array size and configuration) on collective performance were systematically analysed in in Chapter 6 for elementary arrays of real- and reactively-tuned devices. Real tuning at the chosen frequency was found to result in scattering effects mostly dominating over those from radiation, with the converse holding for reactive tuning. Scattered waves were seen to be strongest directly up-wave of the originating device, whilst both scattering and radiation led to a down-wave 'shadow' where total wave amplitudes are reduced. The concepts of *interaction distance* and *wave number repeat value* were introduced in order to explain the fluctuating variation of performance modifications (measured by the *interaction factor*) with respect to wave number and heading. These quantities, derived from information regarding the geometrical configuration of the array, proved to be effective predictors of observed behaviour. In particular, it was shown that the performance of closely spaced arrays is more stable with respect to the aforementioned incident wave variables than for ones with wider separations.

In Chapter 7, the methodology for optimising the performance of an array with respect to its configuration was presented for regular waves. Power output was maximised at a single frequency and direction for real- and reactively-tuned devices whilst the same quantity was minimised in a third case. Two procedures were used for this purpose; The Parabolic Intersection (PI) method, especially devised for this study, and a Genetic Algorithm (GA) with a novel 'crossover operator.' The first of these, was found to perform well, providing fast solutions along with an insight into the physical processes concerned. The GA on the other hand produced the most highly optimised arrays in each case, aided by the purpose-built crossover function.

Results from the optimisation of array configuration in regular waves were analysed in Chapter 8. In most cases, formations with some degree of regularity were generated. The flow patterns around the devices and the motion amplitudes were calculated, as well as the interaction factor in regular waves of various frequencies and directions. Significant modifications to array performance were brought about for the desired

regular wave component (subject to the limitations of linear wave theory). In particular, shadowing was found to have a particularly detrimental effect on overall performance under these conditions. Moreover, this phenomenon persists over a large wave number and angular range and so should be strenuously avoided in the design of arrays. The results also showed a strong link between constructive interference of the principal wave fields at certain devices and favourable overall performance. Finally, some array-related results derived from 'point absorber theory' (Fitzgerald, 2006) were seen to hold approximately in the cases considered.

In Chapter 9, the configurations generated by regular wave optimisation were analysed in irregular sea-states of corresponding peak frequency and mean direction. Four sea-states were defined, with either a single or multiple components in the frequency and angular variables. Optimisations of array layout were then performed with respect to net performance in each sea-state using the GA. This is the first time such an optimisation in irregular waves has been carried out with the full linear wave theory solution and without the constraints of a formation type. The resulting arrays were then analysed and the influence of certain spectral parameters on the optimal formation examined.

The arrays produced for regular waves performed reasonably in the irregular sea-states, although not as well as those specifically optimised for the latter conditions. However, it was shown that changing from a regular to an irregular sea-state does not necessarily lead to more moderate overall interaction effects in a given array. Additionally, the potential for strong modifications to the total power output is not limited to the regular wave case. In fact for irregular directionally spread seas, differences in array performance of over half the power from an equivalent number of isolated devices were found as a result of altering the layout alone. Finally the peak enhancement and spreading parameters were not seen to have a significant effect on the optimal formations, although broader spectra did give rise to slightly more closely spaced arrays.

10.2 Further work

A natural extension of the theory presented in this thesis would be to model arrays of devices with other geometries, moving in different modes of motion. It may also be desirable to perform a fuller convergence analysis on the solution, since fewer terms may

be needed in the summation than are given here. This and other efficiencies may be important in extending the analysis to a larger number of devices.

In order to make the results more realistic and to account for likely practical restrictions, it would be highly desirable to constrain the motion amplitudes of the devices in an optimisation. An even more physically accurate solution might operate in the time domain, so nonlinear power take-off forces that are not time-harmonic may be taken into account. Site-specific sea-states could be considered, although the spatial and temporal variability in these would ideally also be accounted for. With any of these approaches, validation with experimental results would be valuable, especially in the case where power is extracted from the devices. However there are formidable practical obstacles involved with performing experiments on arrays, not least concerning the conflicting demands of using scales large enough to adequately model the devices but small enough so that existing test facilities may be used.

Despite its limitation to regular wave optimisation, it may prove worthwhile to develop the Parabolic Intersection method further. Other functions could be used to generate the interference map around a single device, such as the total wave field or the interaction factor from a two-device array. Improvements in the performance of the Genetic Algorithm may be observed if the parameters it employs could be refined. More generally, alternative global optimisation routines or local algorithms using a number of different initial points could also prove valuable in the search for a more effective procedure. Naturally, the use of more computation time (or equivalently processing power) would improve both the optimisation and indeed interaction calculations.

Other than layout, the main variables that may be optimised over in the context of arrays relate to the control of the devices. Further considerations could also be taken into account to make the optimisation process more realistic. Constraints may be placed on the solution and penalties or different objective functions applied. Ultimately, these would incorporate all of the important economical and practical considerations so that the cost of energy may be reduced directly. It is expected that this would significantly enhance the financial viability of wave farm projects and thus accelerate their wide scale deployment.

Appendix A

Supplementary results

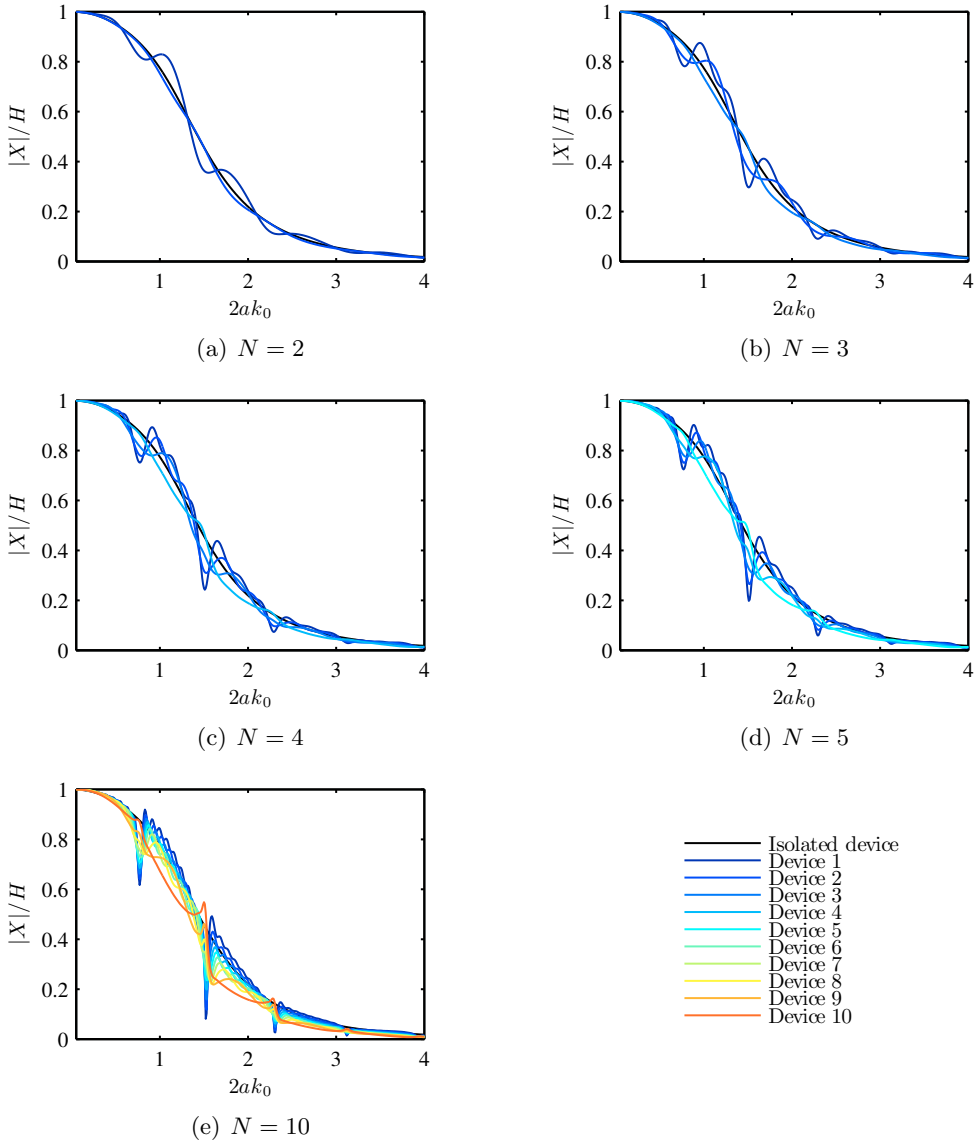

(a) $N = 2$ (b) $N = 3$

(c) $N = 4$ (d) $N = 5$

(e) $N = 10$

Figure A.1: Heave amplitude. Linear array configuration of real-tuned devices with separation $L = 8a$, wave heading angle $\beta = 0$ and different array sizes N.

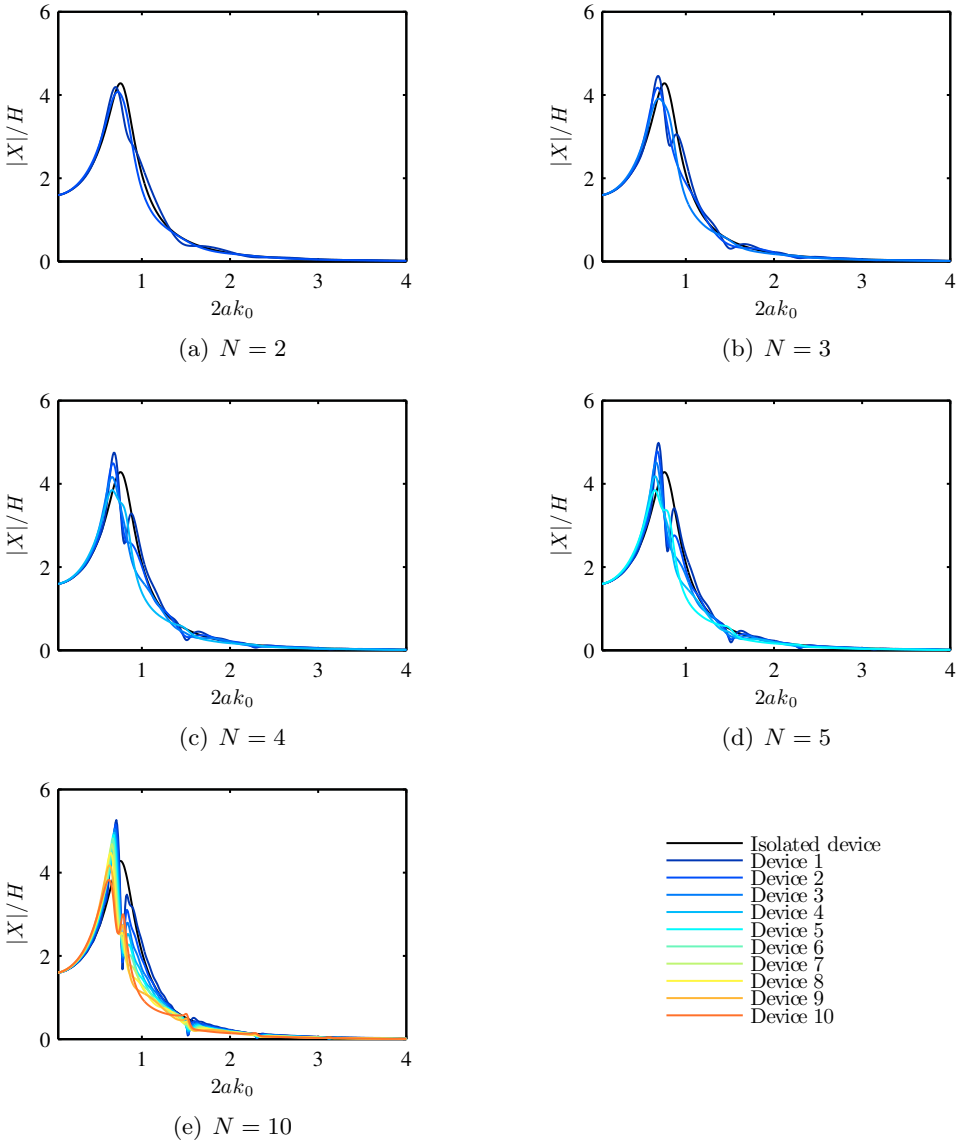

(a) $N = 2$ (b) $N = 3$

(c) $N = 4$ (d) $N = 5$

(e) $N = 10$

Figure A.2: Heave amplitude. Linear array configuration of reactively-tuned devices with separation $L = 8a$, wave heading angle $\beta = 0$ and different array sizes N.

(a) Linear

Array	$\bar{q}$-factor
$PL1_{11}$	1.085
$PL1_{21}$	1.062
$PL1_{31}$	1.051
$PL1_{22}$	1.047
$PL1_{41}$	1.044
$PL1_{32}$	1.041
$PL1_{51}$	1.040
$PL1_{42}$	1.037
$PL1_{61}$	1.037
$PL1_{33}$	1.036
$PL1_{52}$	1.034

(b) Pentagonal

Array	$\bar{q}$-factor
$PP1_{2232}$	1.115
$PP1_{3452}$	1.098
$PP1_{3563}$	1.091
$PP1_{3342}$	1.079
$PP1_{2233}$	1.075
$PP1_{2344}$	1.072
$PP1_{2345}$	1.069
$PP1_{2346}$	1.064
$PP1_{3564}$	1.061
$PP1_{2234}$	1.059
$PP1_{2343}$	1.056
$PP1_{2235}$	1.055
$PP1_{2453}$	1.051
$PP1_{2454}$	1.050
$PP1_{3453}$	1.050
$PP1_{2455}$	1.046
$PP1_{3565}$	1.045
$PP1_{2456}$	1.041
$PP1_{3343}$	1.035
$PP1_{3345}$	1.033
$PP1_{3344}$	1.031
$PP1_{3232}$	1.031
$PP1_{3454}$	1.028
$PP1_{2342}$	1.027
$PP1_{3562}$	1.026
$PP1_{3455}$	1.023
$PP1_{3234}$	1.022
$PP1_{3233}$	1.022

(c) Staggered

Array	$\bar{q}$-factor
$\mathbf{PS1_{33}}$	**1.136**
$PS1_{13}$	1.131
$PS1_{14}$	1.129
$PS1_{12}$	1.128
$PS1_{15}$	1.127
$PS1_{22}$	1.118
$PS1_{34}$	1.100
$PS1_{23}$	1.068
$PS1_{25}$	1.055
$PS1_{24}$	1.052
$PS1_{35}$	1.037
$PS1_{32}$	1.031

Table A.1: Array candidates for Problem 1 generated by the PI method, ranked by descending $\bar{q}$-factor.

(a) Linear

Array	$\bar{q}$-factor
$PL2_{11}$	1.707
$PL2_{21}$	1.476
$PL2_{31}$	1.377
$PL2_{22}$	1.376
$PL2_{41}$	1.319
$PL2_{32}$	1.319
$PL2_{51}$	1.281
$PL2_{42}$	1.281

(b) Pentagonal

Array	$\bar{q}$-factor
$PP2_{2565}$	1.259
$PP2_{2232}$	1.246
$PP2_{2121}$	1.244
$PP2_{2453}$	1.213
$PP2_{2564}$	1.199
$PP2_{2454}$	1.190
$PP2_{2341}$	1.166
$PP2_{2235}$	1.114
$PP2_{2233}$	1.098
$PP2_{2234}$	1.096
$PP2_{2455}$	1.083
$PP2_{2342}$	1.022
$PP2_{2343}$	1.022
$PP2_{2344}$	0.935
$PP2_{2563}$	0.927
$PP2_{2345}$	0.915
$PP2_{2452}$	0.898
$PP2_{2122}$	0.802
$PP2_{2125}$	0.779
$PP2_{2124}$	0.770
$PP2_{2123}$	0.767

(c) Staggered

Array	$\bar{q}$-factor
$\mathbf{PS2_{22}}$	**1.787**
$PS2_{23}$	1.537
$PS2_{15}$	1.448
$PS2_{12}$	1.442
$PS2_{13}$	1.432
$PS2_{14}$	1.431
$PS2_{24}$	1.341
$PS2_{11}$	1.311
$PS2_{25}$	1.229

Table A.2: Array candidates for Problem 2 generated by the PI method, ranked by descending $\bar{q}$-factor.

(a) Linear

Array	$\bar{q}$-factor
$PL3_{21}$	0.680
$PL3_{31}$	0.733
$PL3_{22}$	0.735
$PL3_{41}$	0.765
$PL3_{32}$	0.767
$PL3_{51}$	0.787
$PL3_{42}$	0.788
$PL3_{33}$	0.789
$PL3_{52}$	0.796
$PL3_{61}$	0.804
$PL3_{62}$	0.818
$PL3_{12}$	0.680
$PL3_{13}$	0.733
$PL3_{22}$	0.735
$PL3_{14}$	0.765
$PL3_{23}$	0.767
$PL3_{15}$	0.787
$PL3_{24}$	0.788
$PL3_{33}$	0.789
$PL3_{25}$	0.796
$PL3_{16}$	0.804
$PL3_{26}$	0.818

(b) Pentagonal

Array	$\bar{q}$-factor
$PP3_{2235}$	0.470
$PP3_{3234}$	0.471
$PP3_{2234}$	0.472
$PP3_{3233}$	0.474
$PP3_{3236}$	0.474
$PP3_{3235}$	0.476
$PP3_{2236}$	0.479
$PP3_{3232}$	0.497
$PP3_{2233}$	0.514
$PP3_{2343}$	0.544
$PP3_{2232}$	0.582
$PP3_{3343}$	0.589
$PP3_{3454}$	0.593
$PP3_{3344}$	0.601
$PP3_{3455}$	0.602
$PP3_{3453}$	0.608
$PP3_{3456}$	0.615
$PP3_{3345}$	0.622
$PP3_{3452}$	0.644
$PP3_{3346}$	0.651
$PP3_{3566}$	0.652
$PP3_{3342}$	0.652
$PP3_{3565}$	0.654
$PP3_{2344}$	0.672
$PP3_{3564}$	0.678
$PP3_{2453}$	0.694
$PP3_{2346}$	0.695
$PP3_{2345}$	0.705
$PP3_{3563}$	0.721
$PP3_{2455}$	0.743
$PP3_{2454}$	0.750
$PP3_{2456}$	0.770

(c) Staggered

Array	$\bar{q}$-factor
$PS3_{22}$	**0.453**
$PS3_{23}$	0.463
$PS3_{32}$	0.556
$PS3_{24}$	0.581
$PS3_{34}$	0.597
$PS3_{25}$	0.651
$PS3_{35}$	0.658
$PS3_{36}$	0.686
$PS3_{33}$	0.700

Table A.3: Array candidates for Problem 3 generated by the PI method, ranked by ascending $\bar{q}$-factor.

Array	$\bar{q}$-factor	Array	$\bar{q}$-factor	Array	$\bar{q}$-factor
$G1_1$	**1.163**	$G1_{34}$	1.154	$G1_{67}$	1.113
$G1_2$	1.163	$G1_{35}$	1.147	$G1_{68}$	1.113
$G1_3$	1.163	$G1_{36}$	1.147	$G1_{69}$	1.109
$G1_4$	1.163	$G1_{37}$	1.145	$G1_{70}$	1.107
$G1_5$	1.163	$G1_{38}$	1.142	$G1_{71}$	1.107
$G1_6$	1.163	$G1_{39}$	1.142	$G1_{72}$	1.107
$G1_7$	1.163	$G1_{40}$	1.142	$G1_{73}$	1.106
$G1_8$	1.163	$G1_{41}$	1.141	$G1_{74}$	1.106
$G1_9$	1.163	$G1_{42}$	1.141	$G1_{75}$	1.106
$G1_{10}$	1.163	$G1_{43}$	1.141	$G1_{76}$	1.105
$G1_{11}$	1.163	$G1_{44}$	1.140	$G1_{77}$	1.105
$G1_{12}$	1.163	$G1_{45}$	1.140	$G1_{78}$	1.105
$G1_{13}$	1.163	$G1_{46}$	1.140	$G1_{79}$	1.104
$G1_{14}$	1.163	$G1_{47}$	1.139	$G1_{80}$	1.103
$G1_{15}$	1.162	$G1_{48}$	1.139	$G1_{81}$	1.103
$G1_{16}$	1.162	$G1_{49}$	1.138	$G1_{82}$	1.103
$G1_{17}$	1.162	$G1_{50}$	1.138	$G1_{83}$	1.101
$G1_{18}$	1.162	$G1_{51}$	1.136	$G1_{84}$	1.101
$G1_{19}$	1.162	$G1_{52}$	1.136	$G1_{85}$	1.100
$G1_{20}$	1.162	$G1_{53}$	1.136	$G1_{86}$	1.099
$G1_{21}$	1.162	$G1_{54}$	1.135	$G1_{87}$	1.099
$G1_{22}$	1.161	$G1_{55}$	1.133	$G1_{88}$	1.097
$G1_{23}$	1.161	$G1_{56}$	1.133	$G1_{89}$	1.092
$G1_{24}$	1.160	$G1_{57}$	1.132	$G1_{90}$	1.092
$G1_{25}$	1.160	$G1_{58}$	1.132	$G1_{91}$	1.089
$G1_{26}$	1.159	$G1_{59}$	1.132	$G1_{92}$	1.087
$G1_{27}$	1.159	$G1_{60}$	1.129	$G1_{93}$	1.078
$G1_{28}$	1.159	$G1_{61}$	1.128	$G1_{94}$	1.077
$G1_{29}$	1.159	$G1_{62}$	1.127	$G1_{95}$	1.077
$G1_{30}$	1.157	$G1_{63}$	1.125	$G1_{96}$	1.076
$G1_{31}$	1.156	$G1_{64}$	1.124	$G1_{97}$	1.067
$G1_{32}$	1.155	$G1_{65}$	1.121	$G1_{98}$	1.066
$G1_{33}$	1.155	$G1_{66}$	1.117	$G1_{99}$	1.058
				$G1_{100}$	1.042

Table A.4: Array candidates for Problem 1 generated by the GA method, ranked by descending $\bar{q}$-factor.

Array	$\bar{q}$-factor	Array	$\bar{q}$-factor	Array	$\bar{q}$-factor
$G2_1$	**2.010**	$G2_{34}$	2.010	$G2_{67}$	2.007
$G2_2$	2.010	$G2_{35}$	2.010	$G2_{68}$	2.007
$G2_3$	2.010	$G2_{36}$	2.010	$G2_{69}$	2.007
$G2_4$	2.010	$G2_{37}$	2.010	$G2_{70}$	2.006
$G2_5$	2.010	$G2_{38}$	2.010	$G2_{71}$	2.006
$G2_6$	2.010	$G2_{39}$	2.010	$G2_{72}$	2.005
$G2_7$	2.010	$G2_{40}$	2.010	$G2_{73}$	2.002
$G2_8$	2.010	$G2_{41}$	2.010	$G2_{74}$	2.002
$G2_9$	2.010	$G2_{42}$	2.010	$G2_{75}$	1.999
$G2_{10}$	2.010	$G2_{43}$	2.010	$G2_{76}$	1.997
$G2_{11}$	2.010	$G2_{44}$	2.010	$G2_{77}$	1.801
$G2_{12}$	2.010	$G2_{45}$	2.010	$G2_{78}$	1.781
$G2_{13}$	2.010	$G2_{46}$	2.010	$G2_{79}$	1.780
$G2_{14}$	2.010	$G2_{47}$	2.010	$G2_{80}$	1.779
$G2_{15}$	2.010	$G2_{48}$	2.009	$G2_{81}$	1.767
$G2_{16}$	2.010	$G2_{49}$	2.009	$G2_{82}$	1.767
$G2_{17}$	2.010	$G2_{50}$	2.009	$G2_{83}$	1.751
$G2_{18}$	2.010	$G2_{51}$	2.009	$G2_{84}$	1.747
$G2_{19}$	2.010	$G2_{52}$	2.009	$G2_{85}$	1.747
$G2_{20}$	2.010	$G2_{53}$	2.009	$G2_{86}$	1.720
$G2_{21}$	2.010	$G2_{54}$	2.009	$G2_{87}$	1.719
$G2_{22}$	2.010	$G2_{55}$	2.009	$G2_{88}$	1.712
$G2_{23}$	2.010	$G2_{56}$	2.009	$G2_{89}$	1.712
$G2_{24}$	2.010	$G2_{57}$	2.009	$G2_{90}$	1.712
$G2_{25}$	2.010	$G2_{58}$	2.009	$G2_{91}$	1.712
$G2_{26}$	2.010	$G2_{59}$	2.009	$G2_{92}$	1.623
$G2_{27}$	2.010	$G2_{60}$	2.008	$G2_{93}$	1.619
$G2_{28}$	2.010	$G2_{61}$	2.008	$G2_{94}$	1.549
$G2_{29}$	2.010	$G2_{62}$	2.008	$G2_{95}$	1.534
$G2_{30}$	2.010	$G2_{63}$	2.008	$G2_{96}$	1.508
$G2_{31}$	2.010	$G2_{64}$	2.008	$G2_{97}$	1.472
$G2_{32}$	2.010	$G2_{65}$	2.008	$G2_{98}$	1.423
$G2_{33}$	2.010	$G2_{66}$	2.008	$G2_{99}$	1.401
				$G2_{100}$	1.250

Table A.5: Array candidates for Problem 2 generated by the GA method, ranked by descending $\bar{q}$-factor.

Array	$\bar{q}$-factor	Array	$\bar{q}$-factor	Array	$\bar{q}$-factor
$G3_1$	**0.326**	$G3_{34}$	0.347	$G3_{67}$	0.384
$G3_2$	0.327	$G3_{35}$	0.348	$G3_{68}$	0.385
$G3_3$	0.327	$G3_{36}$	0.349	$G3_{69}$	0.387
$G3_4$	0.327	$G3_{37}$	0.349	$G3_{70}$	0.390
$G3_5$	0.327	$G3_{38}$	0.350	$G3_{71}$	0.393
$G3_6$	0.327	$G3_{39}$	0.351	$G3_{72}$	0.397
$G3_7$	0.327	$G3_{40}$	0.351	$G3_{73}$	0.397
$G3_8$	0.327	$G3_{41}$	0.352	$G3_{74}$	0.398
$G3_9$	0.327	$G3_{42}$	0.353	$G3_{75}$	0.398
$G3_{10}$	0.327	$G3_{43}$	0.354	$G3_{76}$	0.399
$G3_{11}$	0.328	$G3_{44}$	0.355	$G3_{77}$	0.408
$G3_{12}$	0.328	$G3_{45}$	0.355	$G3_{78}$	0.409
$G3_{13}$	0.329	$G3_{46}$	0.355	$G3_{79}$	0.411
$G3_{14}$	0.329	$G3_{47}$	0.356	$G3_{80}$	0.412
$G3_{15}$	0.329	$G3_{48}$	0.356	$G3_{81}$	0.412
$G3_{16}$	0.329	$G3_{49}$	0.357	$G3_{82}$	0.416
$G3_{17}$	0.330	$G3_{50}$	0.357	$G3_{83}$	0.419
$G3_{18}$	0.330	$G3_{51}$	0.359	$G3_{84}$	0.423
$G3_{19}$	0.331	$G3_{52}$	0.359	$G3_{85}$	0.423
$G3_{20}$	0.331	$G3_{53}$	0.360	$G3_{86}$	0.423
$G3_{21}$	0.333	$G3_{54}$	0.363	$G3_{87}$	0.426
$G3_{22}$	0.335	$G3_{55}$	0.365	$G3_{88}$	0.429
$G3_{23}$	0.336	$G3_{56}$	0.367	$G3_{89}$	0.430
$G3_{24}$	0.336	$G3_{57}$	0.368	$G3_{90}$	0.438
$G3_{25}$	0.337	$G3_{58}$	0.374	$G3_{91}$	0.445
$G3_{26}$	0.338	$G3_{59}$	0.374	$G3_{92}$	0.466
$G3_{27}$	0.339	$G3_{60}$	0.377	$G3_{93}$	0.472
$G3_{28}$	0.345	$G3_{61}$	0.378	$G3_{94}$	0.479
$G3_{29}$	0.345	$G3_{62}$	0.379	$G3_{95}$	0.485
$G3_{30}$	0.346	$G3_{63}$	0.380	$G3_{96}$	0.506
$G3_{31}$	0.346	$G3_{64}$	0.381	$G3_{97}$	0.516
$G3_{32}$	0.346	$G3_{65}$	0.381	$G3_{98}$	0.522
$G3_{33}$	0.347	$G3_{66}$	0.384	$G3_{99}$	0.538
				$G3_{100}$	0.582

Table A.6: Array candidates for Problem 3 generated by the GA method, ranked by ascending $\bar{q}$-factor.

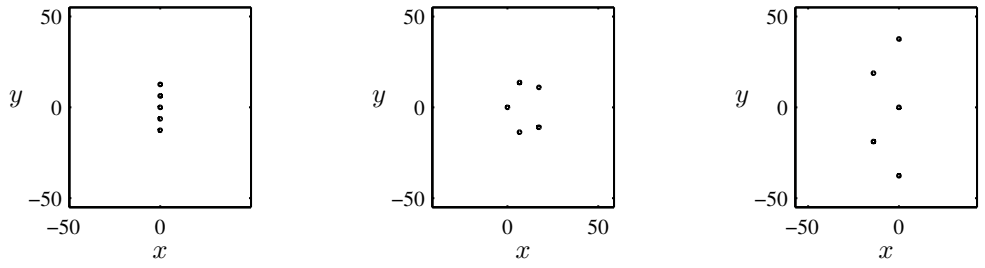

(a) PL1$_{11}$: $\bar{q} = 1.085$ (e) PP1$_{2232}$: $\bar{q} = 1.115$ (i) PS1$_{33}$: $\bar{q} = 1.136$

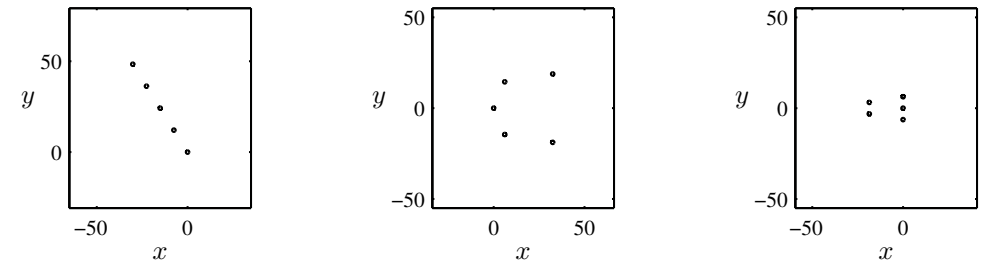

(b) PL1$_{21}$: $\bar{q} = 1.062$ (f) PP1$_{3452}$: $\bar{q} = 1.098$ (j) PS1$_{13}$: $\bar{q} = 1.131$

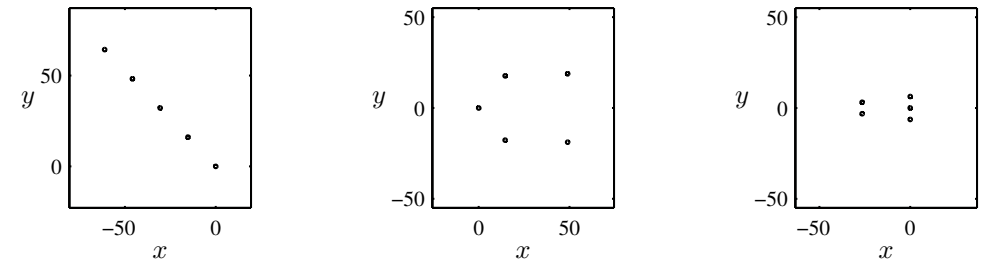

(c) PL1$_{31}$: $\bar{q} = 1.051$ (g) PP1$_{3563}$: $\bar{q} = 1.091$ (k) PS1$_{14}$: $\bar{q} = 1.129$

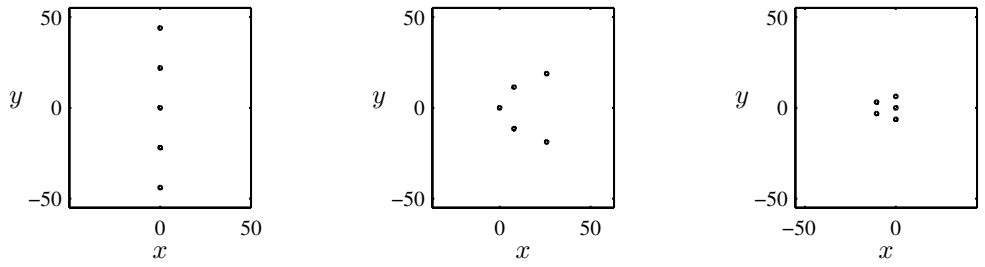

(d) PL1$_{22}$: $\bar{q} = 1.047$ (h) PP1$_{3342}$: $\bar{q} = 1.079$ (l) PS1$_{12}$: $\bar{q} = 1.128$

Figure A.3: Alternative arrays generated by the PI method for Problem 1 in regular waves. Four most highly optimised configurations for each formation type.

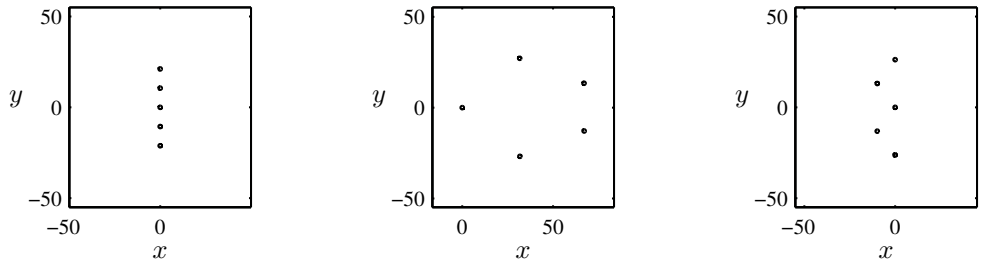

(a) PL2$_{11}$: $\bar{q} = 1.707$ (e) PP2$_{2565}$: $\bar{q} = 1.259$ (i) PS2$_{22}$: $\bar{q} = 1.787$

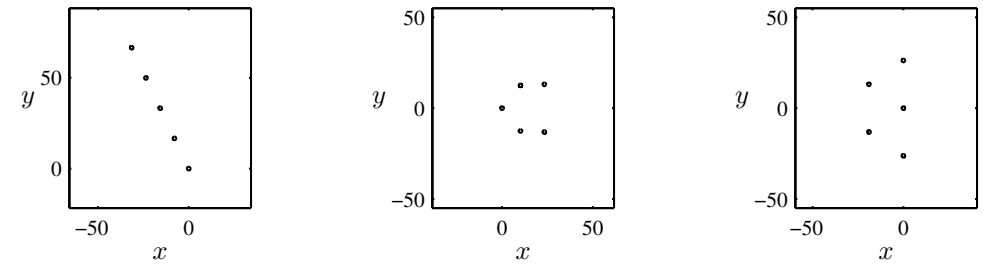

(b) PL2$_{21}$: $\bar{q} = 1.476$ (f) PP2$_{2232}$: $\bar{q} = 1.246$ (j) PS2$_{23}$: $\bar{q} = 1.537$

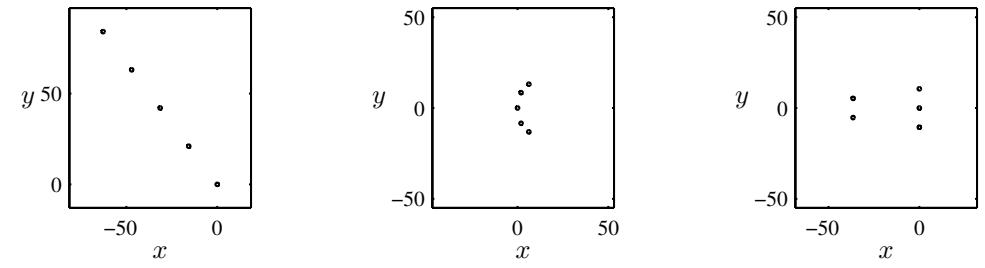

(c) PL2$_{31}$: $\bar{q} = 1.377$ (g) PP2$_{2121}$: $\bar{q} = 1.244$ (k) PS2$_{15}$: $\bar{q} = 1.448$

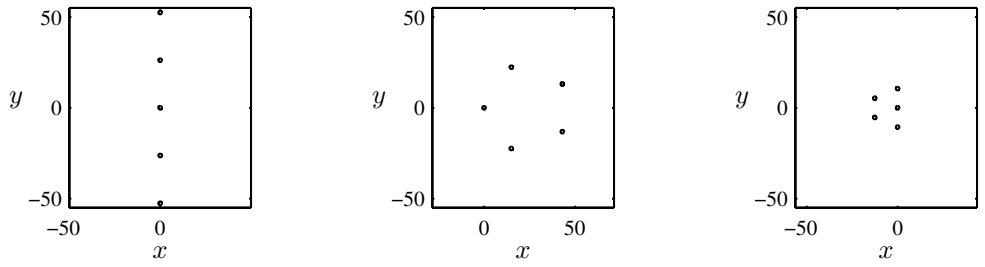

(d) PL2$_{22}$: $\bar{q} = 1.376$ (h) PP2$_{2453}$: $\bar{q} = 1.213$ (l) PS2$_{12}$: $\bar{q} = 1.442$

Figure A.4: Alternative arrays generated by the PI method for Problem 2 in regular waves. Four most highly optimised configurations for each formation type.

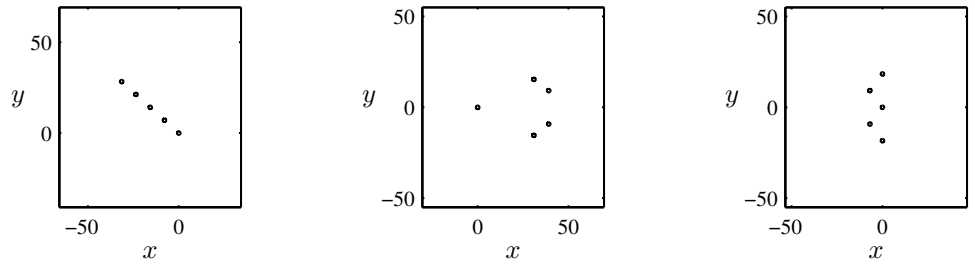

(a) PL3$_{21}$: $\bar{q} = 0.680$ (e) PP3$_{2235}$: $\bar{q} = 0.470$ (i) PS3$_{22}$: $\bar{q} = 0.453$

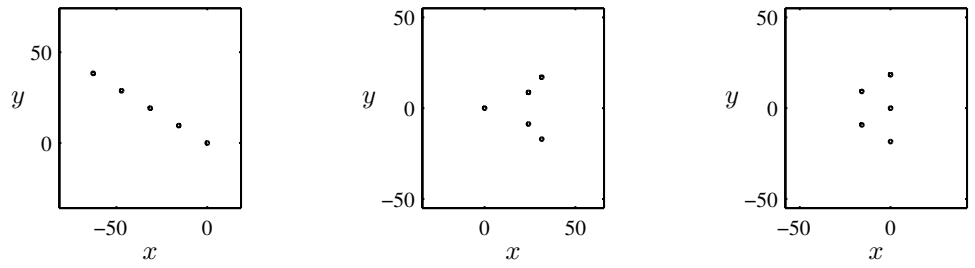

(b) PL3$_{31}$: $\bar{q} = 0.733$ (f) PP3$_{3234}$: $\bar{q} = 0.471$ (j) PS3$_{23}$: $\bar{q} = 0.463$

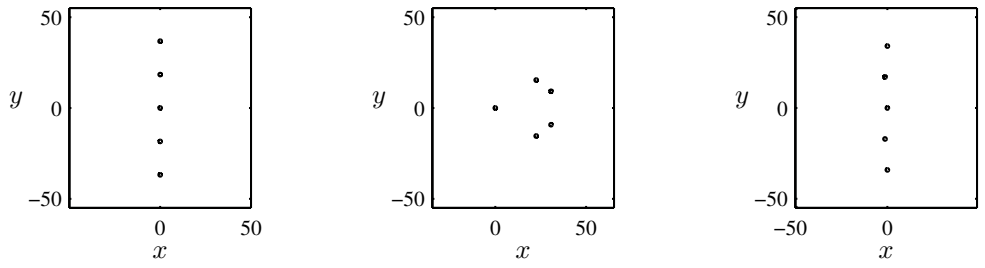

(c) PL3$_{22}$: $\bar{q} = 0.735$ (g) PP3$_{2234}$: $\bar{q} = 0.472$ (k) PS3$_{32}$: $\bar{q} = 0.556$

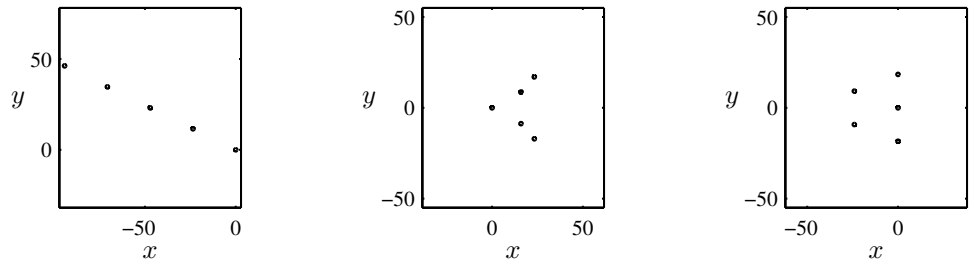

(d) PL3$_{41}$: $\bar{q} = 0.765$ (h) PP3$_{3233}$: $\bar{q} = 0.474$ (l) PS3$_{24}$: $\bar{q} = 0.581$

Figure A.5: Alternative arrays generated by the PI method for Problem 3 in regular waves. Four most highly optimised configurations for each formation type.

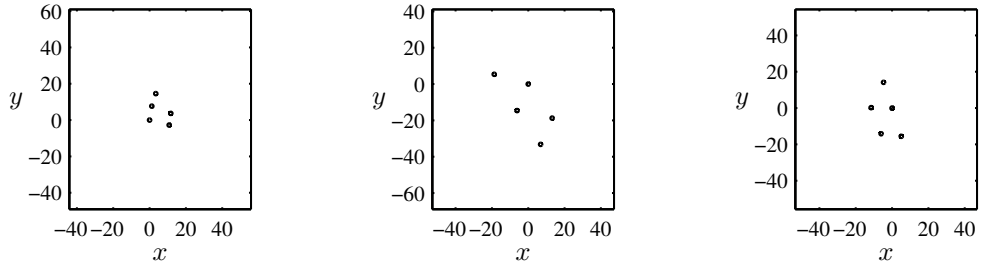

(a) $\bar{q} = 1.143$ (e) $\bar{q} = 1.155$ (i) $\bar{q} = 1.163$

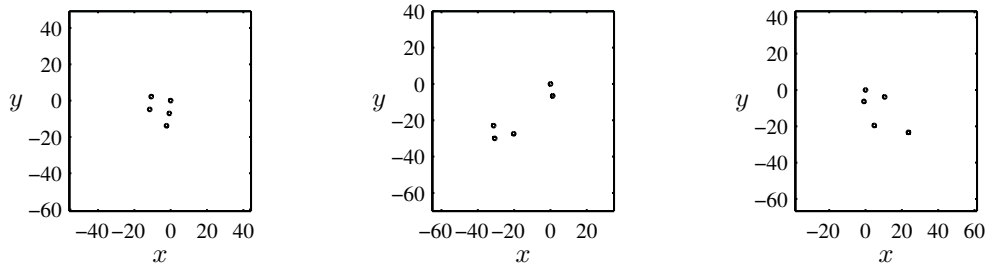

(b) $\bar{q} = 1.142$ (f) $\bar{q} = 1.150$ (j) $\bar{q} = 1.155$

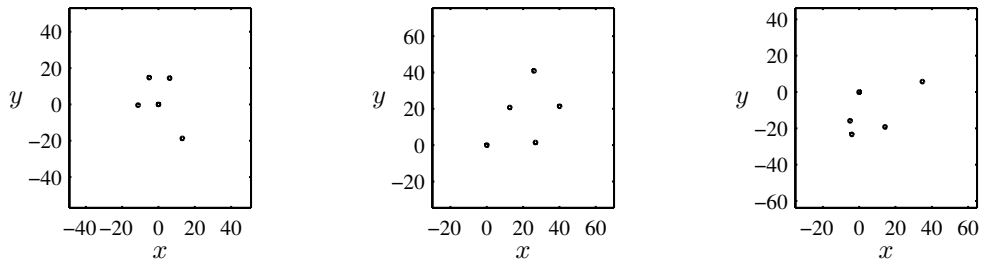

(c) $\bar{q} = 1.165$ (g) $\bar{q} = 1.158$ (k) $\bar{q} = 1.145$

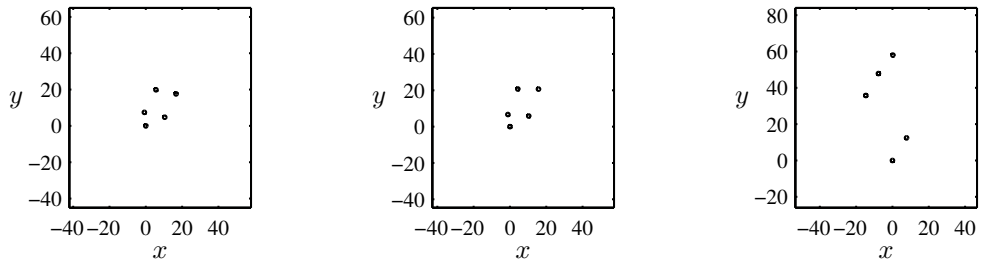

(d) $\bar{q} = 1.146$ (h) $\bar{q} = 1.164$ (l) $\bar{q} = 1.143$

Figure A.6: Alternative arrays generated by the GA method for Problem 1 in regular waves. Twelve configurations, each for a different random seed.

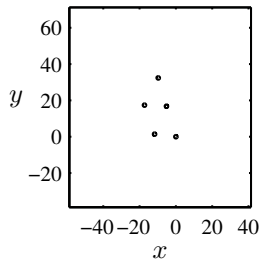

(a) $\bar{q} = 1.883$

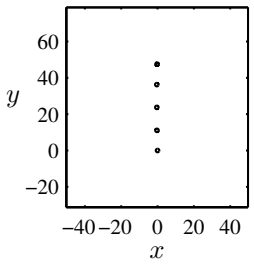

(e) $\bar{q} = 1.840$

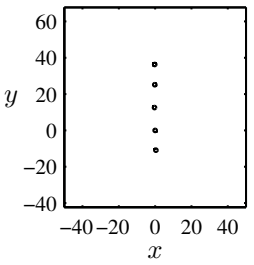

(i) $\bar{q} = 1.837$

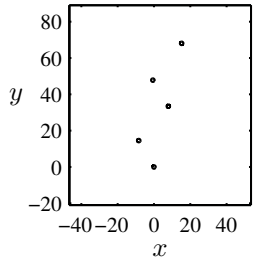

(b) $\bar{q} = 1.947$

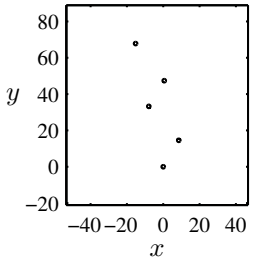

(f) $\bar{q} = 1.954$

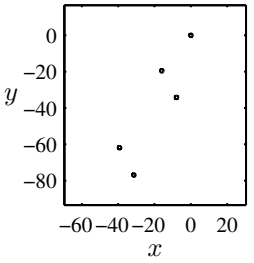

(j) $\bar{q} = 2.021$

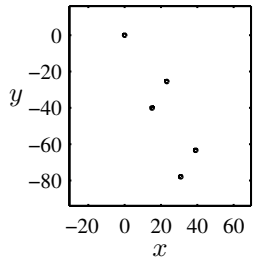

(c) $\bar{q} = 1.982$

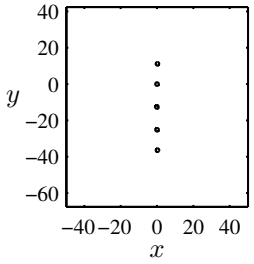

(g) $\bar{q} = 1.841$

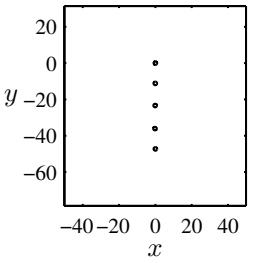

(k) $\bar{q} = 1.837$

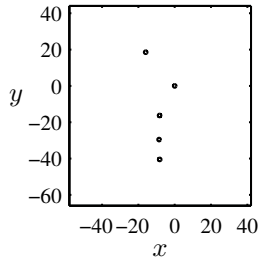

(d) $\bar{q} = 1.802$

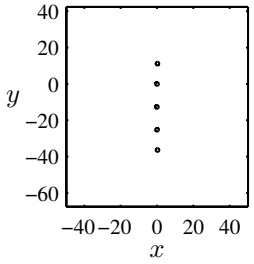

(h) $\bar{q} = 1.841$

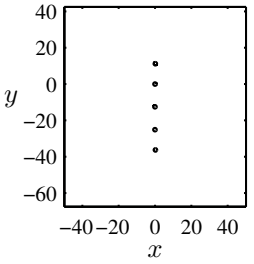

(l) $\bar{q} = 1.841$

Figure A.7: Alternative arrays generated by the GA method for Problem 2 in regular waves. Twelve configurations, each for a different random seed.

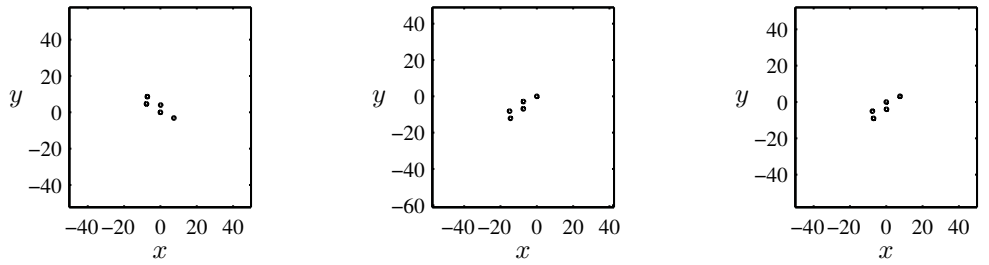

(a) $\bar{q} = 0.326$

(e) $\bar{q} = 0.325$

(i) $\bar{q} = 0.326$

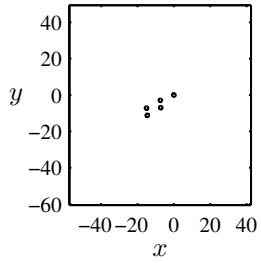

(b) $\bar{q} = 0.327$

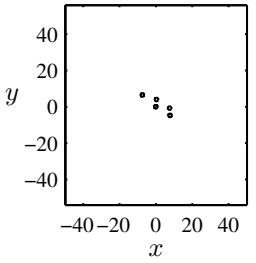

(f) $\bar{q} = 0.331$

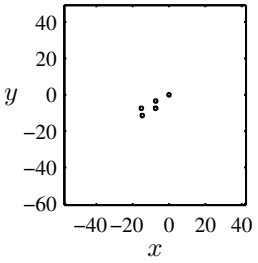

(j) $\bar{q} = 0.330$

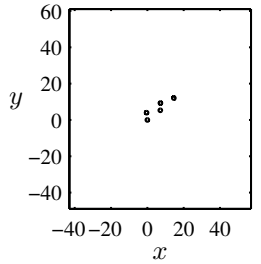

(c) $\bar{q} = 0.326$

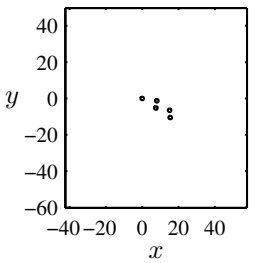

(g) $\bar{q} = 0.333$

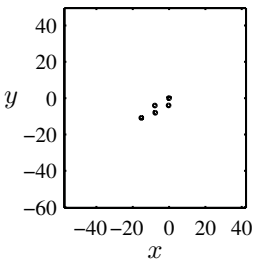

(k) $\bar{q} = 0.332$

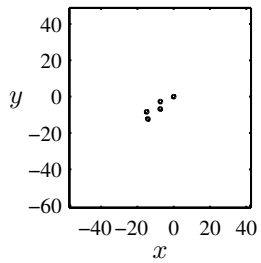

(d) $\bar{q} = 0.329$

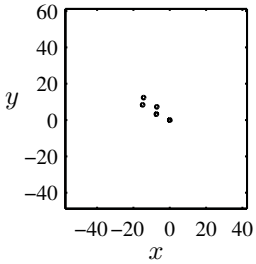

(h) $\bar{q} = 0.327$

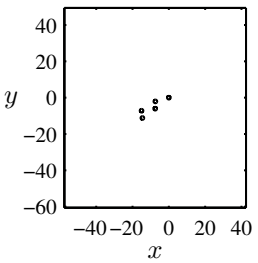

(l) $\bar{q} = 0.328$

Figure A.8: Alternative arrays generated by the GA method for Problem 3 in regular waves. Twelve configurations, each for a different random seed.

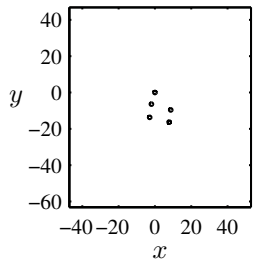

(a) Problem 1: $\bar{q} = 1.143$

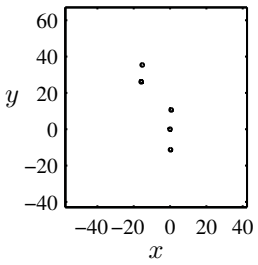

(e) Problem 2: $\bar{q} = 1.758$

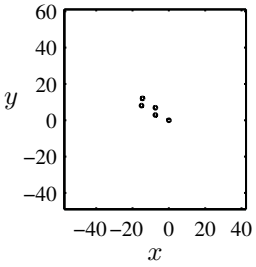

(i) Problem 3: $\bar{q} = 0.324$

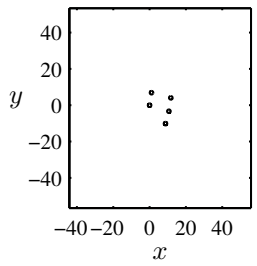

(b) Problem 1: $\bar{q} = 1.144$

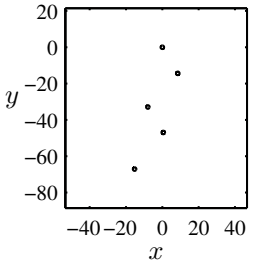

(f) Problem 2: $\bar{q} = 1.976$

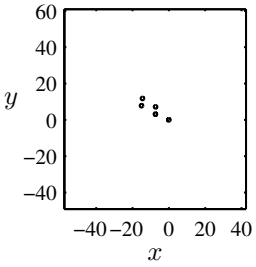

(j) Problem 3: $\bar{q} = 0.324$

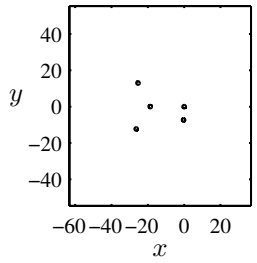

(c) Problem 1: $\bar{q} = 1.140$

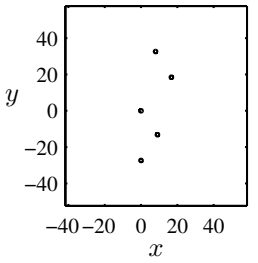

(g) Problem 2: $\bar{q} = 1.972$

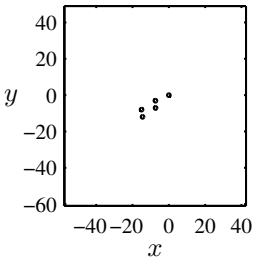

(k) Problem 3: $\bar{q} = 0.324$

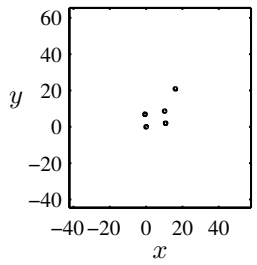

(d) Problem 1: $\bar{q} = 1.145$

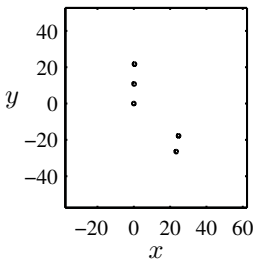

(h) Problem 2: $\bar{q} = 1.762$

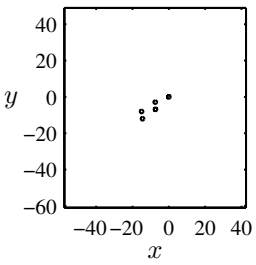

(l) Problem 3: $\bar{q} = 0.324$

Figure A.9: Alternative arrays generated by the GA method in Sea-state R. Four configurations for every problem, each for a different random seed.

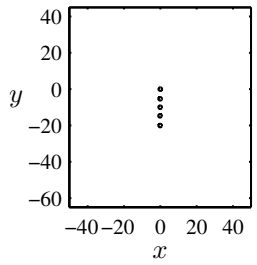

(a) Problem 1: $\overline{Q} = 1.109$

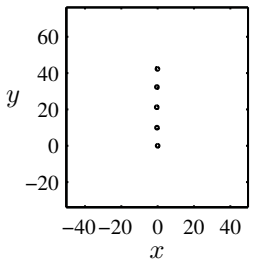

(e) Problem 2: $\overline{Q} = 1.409$

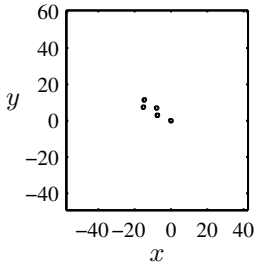

(i) Problem 3: $\overline{Q} = 0.536$

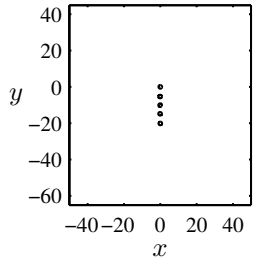

(b) Problem 1: $\overline{Q} = 1.109$

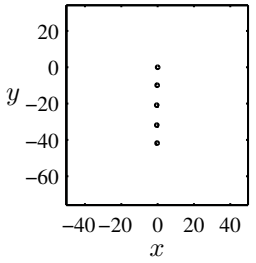

(f) Problem 2: $\overline{Q} = 1.408$

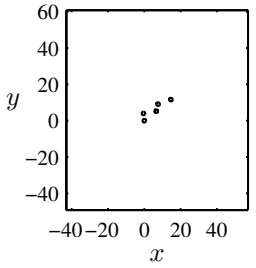

(j) Problem 3: $\overline{Q} = 0.541$

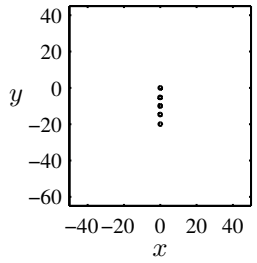

(c) Problem 1: $\overline{Q} = 1.109$

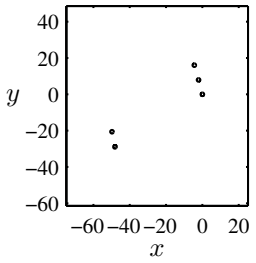

(g) Problem 2: $\overline{Q} = 1.500$

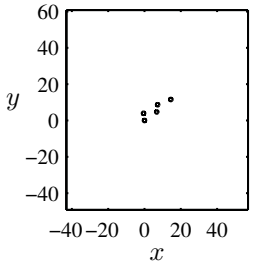

(k) Problem 3: $\overline{Q} = 0.536$

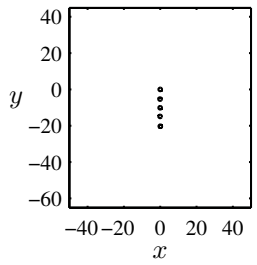

(d) Problem 1: $\overline{Q} = 1.109$

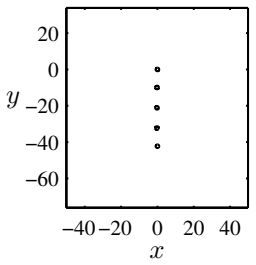

(h) Problem 2: $\overline{Q} = 1.409$

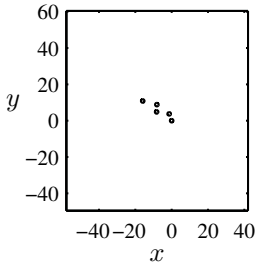

(l) Problem 3: $\overline{Q} = 0.545$

Figure A.10: Alternative arrays generated by the GA method in Sea-state K. Four configurations for every problem, each for a different random seed.

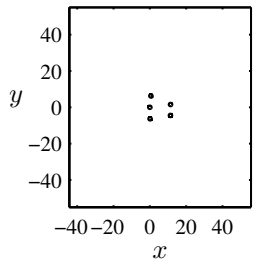

(a) Problem 1: $\overline{Q} = 1.067$

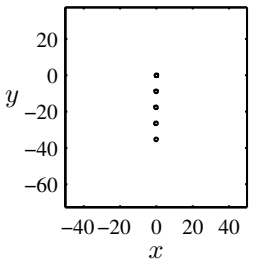

(e) Problem 2: $\overline{Q} = 1.358$

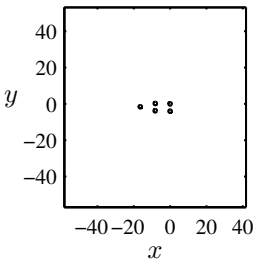

(i) Problem 3: $\overline{Q} = 0.479$

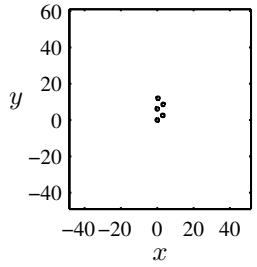

(b) Problem 1: $\overline{Q} = 1.066$

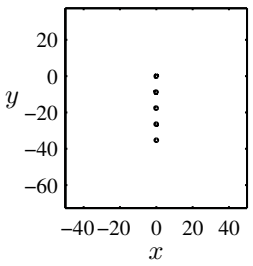

(f) Problem 2: $\overline{Q} = 1.358$

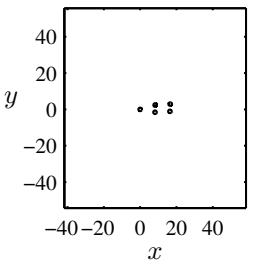

(j) Problem 3: $\overline{Q} = 0.480$

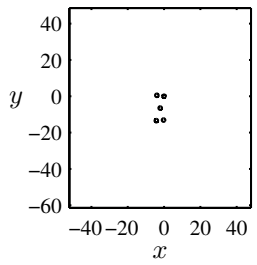

(c) Problem 1: $\overline{Q} = 1.069$

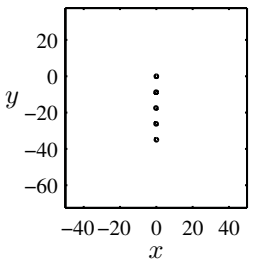

(g) Problem 2: $\overline{Q} = 1.358$

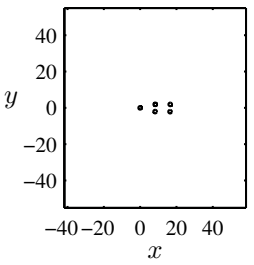

(k) Problem 3: $\overline{Q} = 0.479$

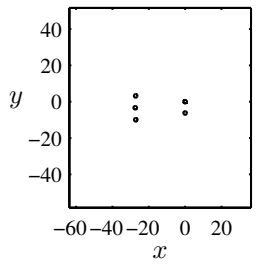

(d) Problem 1: $\overline{Q} = 1.059$

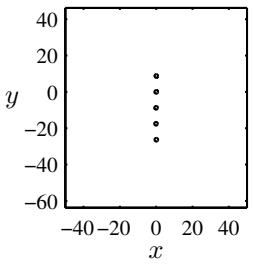

(h) Problem 2: $\overline{Q} = 1.358$

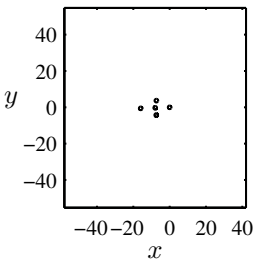

(l) Problem 3: $\overline{Q} = 0.480$

Figure A.11: Alternative arrays generated by the GA method in Sea-state B. Four configurations for every problem, each for a different random seed.

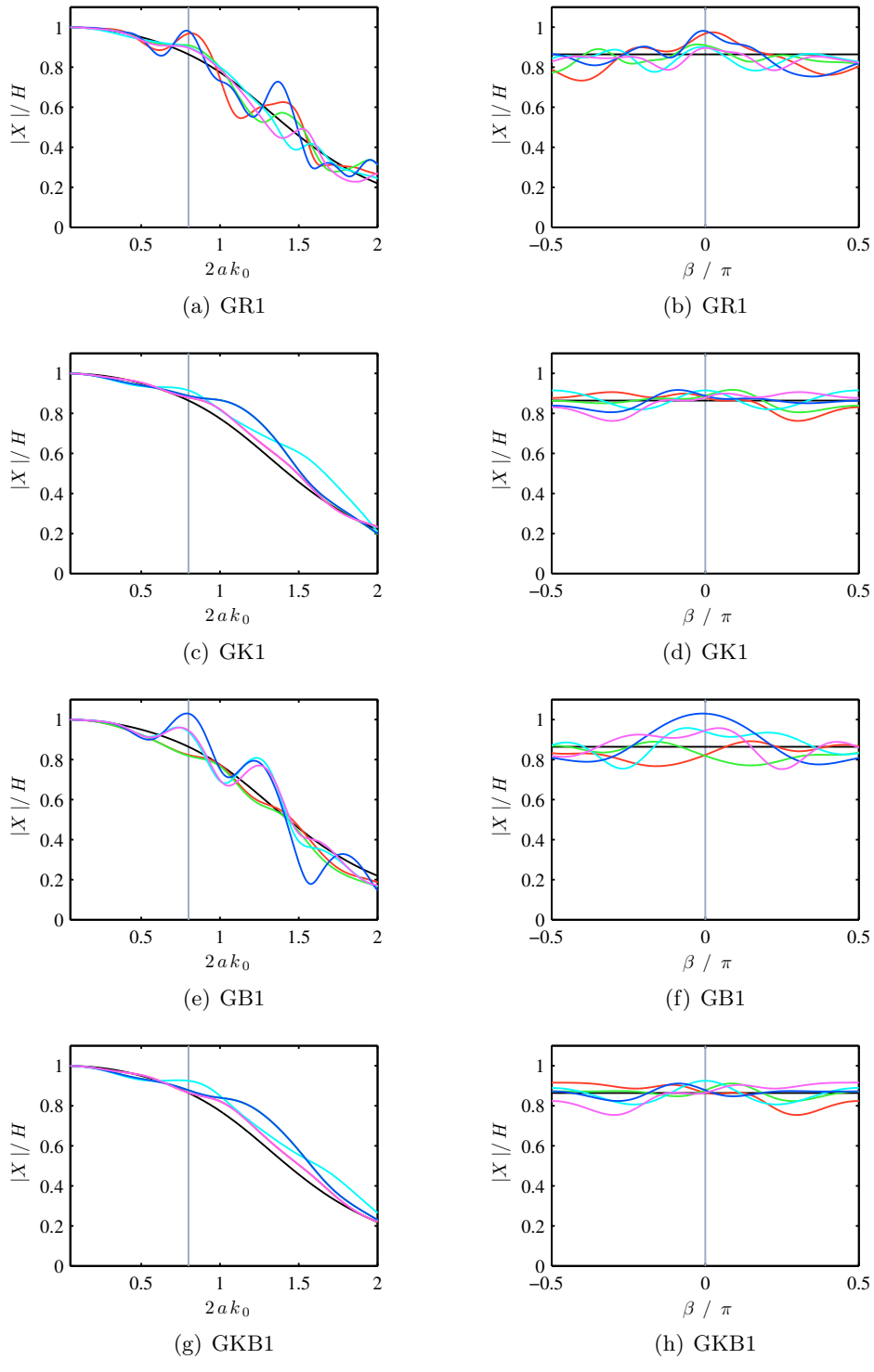

Figure A.12: Heave amplitude of devices in arrays solving Problem 1 of Chapter 9.

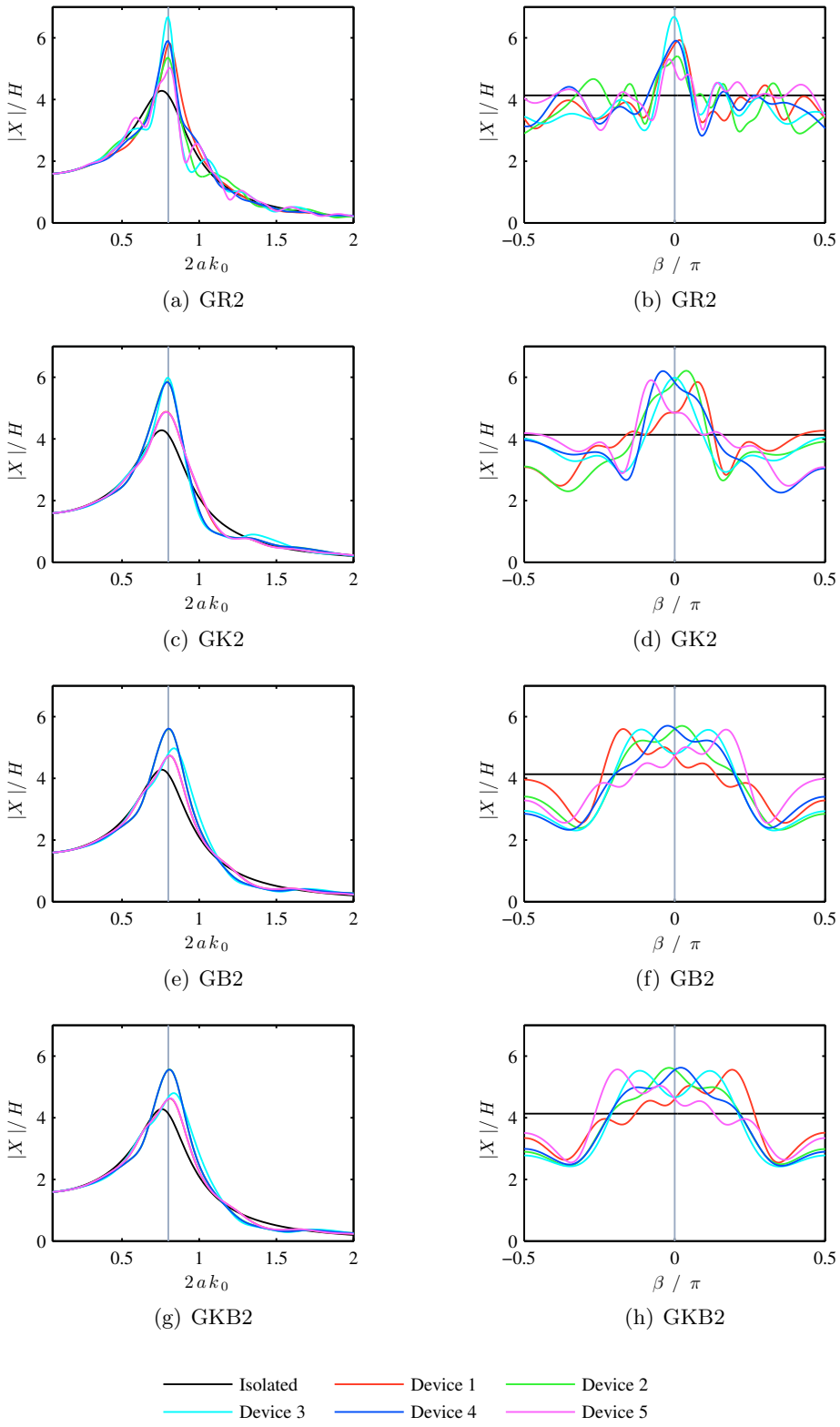

Figure A.13: Heave amplitude of devices in arrays solving Problem 2 of Chapter 9.

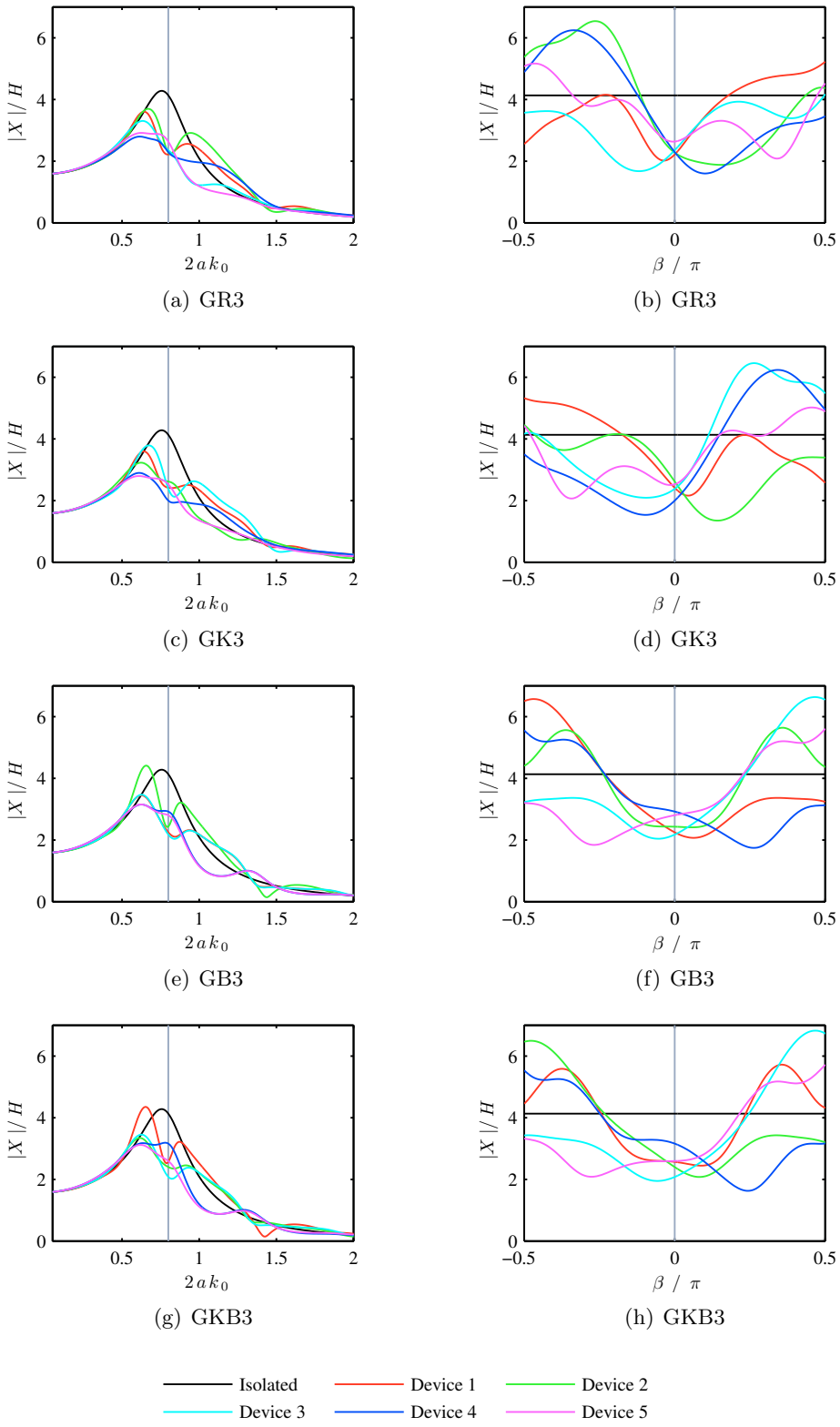

Figure A.14: Heave amplitude of devices in arrays solving Problem 3 of Chapter 9.

References

Abramowitz, M. and Stegun, I. A., editors. *Handbook of mathematical functions*. Government Printing Office, Washington DC, USA, 1964.

Acheson, D. J. *Elementary fluid dynamics*. Oxford University Press, 2001.

Alexandre, A., Stallard, T., and Stansby, P. K. Transformation of wave spectra across a line of wave devices. In Leijon, M., editor, *Proceedings of the 8th European Wave and Tidal Energy Conference (EWTEC2009)*, 1–9, 2009.

Aquamarine Power. `http://www.aquamarinepower.com/`, 30th Spetember 2010.

Ashton, I. G. C., Johanning, L., and Linfoot, B. Measurement of the effect of power absorption in the lee of a wave energy converter. In Ertekin, R. C. and Riggs, R., editors, *Proceedings of the ASME 28th International Conference on Ocean, Offshore and Arctic Engineering (OMAE2009)*, 2009.

Babarit, A. Impact of long separating distances on the energy production of two interacting wave energy converters. *Ocean Engineering*, 37(8-9):718–729, 2010.

Beels, C. *Optimization of the lay-out of a farm of wave energy converters in the North Sea: analysis of wave power resources, wake effects, production and cost*. PhD thesis, Ghent University, 2009.

Beels, C., Troch, P., De Backer, G., Vantorre, M., and De Rouck, J. Numerical implementation and sensitivity analysis of a wave energy converter in a time-dependent mild-slope equation model. *Coastal Engineering*, 57(5):471–492, May 2010a.

Beels, C., Troch, P., De Visch, K., Kofoed, J. P., and De Backer, G. Application of the time-dependent mild-slope equations for the simulation of wake effects in the lee of

a farm of Wave Dragon wave energy converters. *Renewable Energy*, 35(8):1644–1661, Aug. 2010b.

Bellew, S. and Stallard, T. Linear modelling of wave device arrays and comparison to experimental and second order models. In Duan, W. Y., editor, *Proceedings of the 25th International Workshop on Water Waves and Floating Bodies (IWWWFB25)*, 2010.

Bellew, S., Stallard, T., and Stansby, P. Optimisation of a heterogeneous array of heaving bodies. In Leijon, M., editor, *Proceedings of the 8th European Wave and Tidal Energy Conference (EWTEC2009)*, 1–9, 2009.

Bhatta, D. D. and Rahman, M. Wave loadings on a vertical cylinder due to heave motion. *International Journal of Mathematics and Mathematical Sciences*, 18(1): 151–170, 1995.

Bhatta, D. D. and Rahman, M. On scattering and radiation problem for a cylinder in water of finite depth. *International Journal of Engineering Science*, 41:931–967, 2003.

Borgarino, B., Babarit, A., and Ferrant, P. Extension of the free-surface Green's function multipole expansion for the infinite water depth case. In Chung, J. S., Ayer, R., Prinsenberg, S., Hong, S. W., and Langen, I., editors, *Proceedings of the 20th International Offshore and Polar Engineering Conference (ISOPE2010)*, volume 7, 802–809, 2010.

Bryden, I. and Linfoot, B. Wave and current testing of an array of wave energy converters. Proceedings of the HYDRALAB III joint user meeting, Hannover, February 2010, SuperGen Marine, 2010.

Budal, K. Theory for absorption of wave power by a system of interacting bodies. *Journal of Ship Research*, 21(4):248–253, 1977.

Budal, K. and Falnes, J. A resonant point absorber of ocean-wave power. *Nature*, 256: 478–9, 1975. Corrigendum 257:626.

Budal, K., Falnes, J., Kyllingstad, A., and Oltedal, G. Experiments with point absorbers. In Jansson, K.-G., Lunde, J. K., and Rindby, T., editors, *Proceedings of the 1st Symposium on Wave Energy Utilization*, 253–282, 1980.

Carbon Trust. Future Marine Energy. Results of the Marine Energy Challenge: Cost competitiveness and growth of wave and tidal stream energy. `http://www.carbontrust.co.uk/Publications/pages/PublicationDetail.aspx?id=CTC601`, January 2006.

Carbon Trust. Marine Renewables Proving Fund. `http://www.carbontrust.co.uk/emerging-technologies/current-focus-areas/marine-renewables-proving-fund/pages/default.aspx`, 30th September 2010.

Chakrabarti, S. Hydrodynamic interaction forces on multi-moduled structures. *Ocean Engineering*, 27:1037–1063, 2000.

Chatjigeorgiou, I. K. and Mavrakos, S. A. An analytical approach for the solution of the hydrodynamic diffraction by arrays of elliptical cylinders. *Applied Ocean Research*, 32(2):1–10, 2010.

Child, B. F. M. Hydrodynamic analysis of the wave energy device 'SPERBOY'. Master's thesis, The University of Bristol, 2006.

Child, B. F. M. and Venugopal, V. Interaction of waves with an array of floating wave energy devices. In Falcão, A., editor, *Proceedings of the 7th European Wave and Tidal Energy Conference (EWTEC2007)*, 2007.

Child, B. F. M. and Venugopal, V. Non-optimal tuning of wave energy device arrays. In Bamberger, Y. and Perrot, J.-Y., editors, *Proceedings of the 2nd International Conference on Ocean Energy (ICOE2008)*, 2008.

Child, B. F. M. and Venugopal, V. Modification of power characteristics in an array of floating wave energy devices. In Leijon, M., editor, *Proceedings of the 8th European Wave and Tidal Energy Conference (EWTEC2009)*, 2009.

Child, B. F. M. and Venugopal, V. Optimal configurations of wave energy device arrays. *Ocean Engineering*, 37(16):1402–1417, 2010.

Chopard, B., Baggi, Y., Luthi, P., and Wagen, J. Wave propagation and optimal antenna layout using a genetic algorithm. *SPEEDUP Journal*, 11(2):42–47, 1997.

Count, B. M. and Jeffereys, E. R. Wave power: the primary interface. In Inui, T., editor, *Proceedings of the 13th Symposium on Naval Hydrodynamics*, 817–826, 1980.

Courant, R. and John, F. *Introduction to calculus and analysis, Volume 1.* Springer-Verlag New York, Inc., 1989.

Cruz, J., editor. *Ocean wave energy: current status and future prepectives.* Springer-Verlag, 2008.

Cruz, J., Sykes, R., Siddorn, P., and Eatock Taylor, R. Wave farm design: preliminary studies on the influences of wave climate, array layout and farm control. In Leijon, M., editor, *Proceedings of the 8th European Wave and Tidal Energy Conference (EWTEC2009)*, 736–745, 2009.

Czech, B., Bauer, P., Polinder, H., Zhou, Y., and Korondi, P. Comparing the electrical transmission systems for Archimedes Wave Swing parks. In Leijon, M., editor, *Proceedings of the 8th European Wave and Tidal Energy Conference (EWTEC2009)*, 36–43, 2009.

De Backer, G., Vantorre, M., Beels, C., De Rouck, J., and Frigaard, P. Performance of closely spaced point absorbers with constrained floater motion. In Leijon, M., editor, *Proceedings of the 8th European Wave and Tidal Energy Conference (EWTEC2009)*, 806–817, 2009.

Department of Energy & Climate Change. The Renewable Energy Strategy (RES). `http://www.decc.gov.uk/en/content/cms/what_we_do/uk_supply/energy_mix/renewable/res/res.aspx`, 30th September 2010a.

Department of Energy & Climate Change. Marine Renewables Deployment Fund. `http://www.decc.gov.uk/en/content/cms/what_we_do/lc_uk/lc_business/lc_economy/env_trans_fund/marine_fund/marine_fund.aspx`, 30th September 2010b.

Department of Trade and Industry. Meeting the Energy Challenge: A White Paper on Energy. `http://www.berr.gov.uk/files/file39387.pdf`, May 2007.

Embley Energy Ltd. `http://www.sperboy.com/`, 30th September 2010.

Energy Technologies Institute. Marine Programme. `http://www.energytechnologies.co.uk/Home/Technology-Programmes/marine.aspx`, 30th September 2010a.

Energy Technologies Institute. £8m Marine Project announced. `http://www.energytechnologies.co.uk/Home/news/09-10-30/%C2%A38m_marine_project_announced.aspx`, 30th September 2010b.

Eriksson, M., Isberg, J., and Leijon, M. Hydrodynamic modelling of a direct drive wave energy converter. *International Journal of Engineering Science*, 43:1377–1387, 2005.

Evans, D. V. A theory for wave-power absorption by oscillating bodies. *Journal of Fluid Mechanics*, 77(1):1–25, 1976.

Evans, D. V. Some theoretical aspects of three dimensional wave-energy absorbers. In Jansson, K.-G., Lunde, J. K., and Rindby, T., editors, *Proceedings of the 1st Symposium on Ocean Wave Energy Utilization*, 1979.

Evans, D. V. Some analytic results for two and three dimensional wave-energy absorbers. In Count, B. M., editor, *Power from sea waves*, 213–249. Academic Press Inc., London, UK, 1980.

Evans, D. V. Power from water waves. *Annual Review of Fluid Mechanics*, 13:157–187, 1981a.

Evans, D. V. Maximum wave-power absorption under motion constraints. *Applied Ocean Research*, 3(4):200–203, 1981b.

Evans, D. V. and Porter, R. Near-trapping of waves by circular arrays of vertical cylinders. *Applied Ocean Research*, 19:83–99, 1997.

Falcão, A. Wave-power absorption by a periodic linear array of oscillating water columns. *Ocean Engineering*, 29:1163–1186, 2002.

Falcão, A. Wave energy utilization: a review of the technologies. *Renewable and Sustainable Energy Reviews*, 14:899–918, 2010.

Falnes, J. Radiation impedance matrix and optimum power absorption for interacting oscillators in surface waves. *Applied Ocean Research*, 2(2):75–80, 1980.

Falnes, J. Wave-power absorption by an array of attenuators oscillating with unconstrained amplitudes. *Applied Ocean Research*, 6(1):16–22, 1984.

Falnes, J. *Ocean waves and oscillating systems: Linear interactions including wave-energy extraction*. Cambridge University Press, 2002.

Falnes, J. A review of wave-energy extraction. *Marine Structures*, 20(4):185–201, 2007.

Falnes, J. and Budal, K. Wave-power conversion by point absorbers. *Norwegian Maritime Research*, 6:2–11, 1978.

Falnes, J. and Budal, K. Wave-power absorption by parallel rows of interacting oscillating bodies. *Applied Ocean Research*, 4(4):194–207, 1982.

Fitzgerald, C. Optimal configurations of arrays of wave-power devices. Master's thesis, National University of Ireland, Cork, November 2006.

Fitzgerald, C. and Thomas, G. A preliminary study on the optimal formation of an array of wave power devices. In Falcão, A., editor, *Proceedings of the 7th European Wave and Tidal Energy Conference (EWTEC2007)*, 2007.

Folley, M. and Whittaker, T. J. T. The effect of sub-optimal control and the spectral wave climate on the performance of wave energy converter arrays. *Applied Ocean Research*, 31(4):260–266, 2009.

Fridman, P. Optimal array configuration search using genetic algorithms. In Tescher, AG, editor, *Applications Of Digital Image Processing XXIV*, volume 4472 of *Proceedings of the Society of Photo-Optical Instrumentation Engineers (SPIE)*, 518–527, 2001.

Gao, Z. and Moan, T. Mooring system analysis of multiple wave energy converters in a farm configuration. In Leijon, M., editor, *Proceedings of the 8th European Wave and Tidal Energy Conference (EWTEC2009)*, 509–518, 2009.

Garnaud, X. and Mei, C. C. Bragg scattering and wave-power extraction by an array of small buoys. *Proceedings of the Royal Society A*, 466(2113):79–106, 2010.

Garrett, C. J. R. Wave forces on a circular dock. *Journal of Fluid Mechanics*, 46(1): 129–139, 1971.

Golub, G. H. and Van Loan, C. F. *Matrix computations*. Oxford: North Oxford Academic, 1983.

Goo, J.-S. and Yoshida, K. A numerical method for huge semisubmersible responses in waves. *Transactions - Society of Naval Architects and Marine Engineers*, 98:365–387, 1990.

Håkansson, A., Sánchez-Dehesa, J., and Sanchis, L. Acoustic lens design by genetic algorithms. *Physical Review B*, 70(21):214302, 2004.

Hasselmann, K., Barnett, T., Bouws, E., Carlson, H., Cartwright, D., Enke, K., Ewing, J., Gienapp, H., Hasselmann, D., Kruseman, P., Meerburg, A., P. Mller, D. O., Richter, K., Sell, W., and Walden, H. Measurements of wind-wave growth and swell decay during the Joint North Sea Wave Project (JONSWAP). *Ergnzungsheft zur Deutschen Hydrographischen Zeitschrift Reihe*, 8(12):95, 1973.

Haupt, R. L. An introduction to genetic algorithms for electromagnetics. *IEEE Antennas and Propagation Magazine*, 37(2):7–15, Apr 1995.

Holland, J. H. *Adaptation in Natural and Artificial Systems.* University of Michigan Press (Second edition: MIT Press, 1992), 1975.

Holthuijsen, L. H. *Waves in oceanic and coastal waters.* Cambridge University Press, 2007.

Isaacson, E. and Keller, H. B. *Analysis of numerical methods.* Dover Publications, Inc., New York, 1994.

Justino, P. A. P. and Clément, A. H. Hydrodynamic performance for small arrays of submerged spheres. In Lewis, A., editor, *Proceedings of the Fifth European Wave Energy Conference*, 266–273, 2003.

Justino, P. A. P. and Falcão, A. Hydrodynamic interactions for small arrays of wave energy devices. In Naess, A., editor, *Proceedings of the 21st International Conference on Offshore Mechanics and Arctic Engineering.* ASME, 2002.

Kagemoto, H. Minimization of wave forces on an array of floating bodies – The inverse hydrodynamic interaction theory. *Applied Ocean Research*, 14:83–92, 1992.

Kagemoto, H. and Yue, D. K. P. Interactions among multiple three-dimensional bodies in water waves: an exact algebraic method. *Journal of Fluid Mechanics*, 166:189–209, 1986.

Kagemoto, H. and Yue, D. K. P. Hydrodynamic interaction analyses of very large floating structures. *Marine Structures*, 6:295–322, 1993.

Kashiwagi, M. Hydrodynamic interactions among a great number of columns supporting a very large flexible structure. *Journal of Fluids and Structures*, 14:1013–1034, 2000.

Kiprakis, A., Nambiar, A., Forehand, D., and Wallace, A. Modelling arrays of wave energy converters connected to weak rural electricity networks. In Brandon, N. and Lu, Q., editors, *Proceedings of the International Conference on Sustainable Power Generation and Supply (SUPERGEN09)*, 2009.

Kyllingstad, A. A low-scattering approximation for the hydrodynamic interactions of small wave-power devices. *Applied Ocean Research*, 6(3):132–139, 1984.

Langhamer, O. *Wave energy conversion and the marine environment: Colonization patterns and habitat dynamics*. PhD thesis, Uppsala University, 2009.

Lee, C. *WAMIT Theory Manual*. Cambridge, MASS. 02139, October 1995.

Li, D. and Gong, Z. Design of hexagonal planar arrays using genetic algorithms for performance improvement. In Liu, S., editor, *2nd International Conference on Microwave and Millimeter Wave Technology (ICMMT)*, 455–460, 2000.

Li, Y. and Mei, C. C. Bragg scattering by a line array of small cylinders in a waveguide. Part 1. Linear aspects. *Journal of Fluid Mechanics*, 583:161–187, 2007.

Lin, P. *Numerical modeling of water waves*. Routledge, 2008.

Linton, C. M. and Evans, D. V. The interaction of waves with arrays of vertical cylinders. *Journal of Fluid Mechanics*, 215:549–569, 1990.

Linton, C. M. and Evans, D. V. The radiation and scattering of surface waves by a vertical circular cylinder in a channel. *Philosophical Transactions: Physical Sciences and Engineering*, 338(1650):325–357, 1992.

Linton, C. M. and Evans, D. V. The interaction of waves with a row of circular cylinders. *Journal of Fluid Mechanics*, 251:687–708, 1993.

Linton, C. M. and McIver, P. *Handbook of mathematical techniques for wave/structure interactions*. Chapman & Hall/CRC, 2001.

MacCamy, R. C. and Fuchs, R. A. Wave forces on piles: a diffraction theory. Technical Report AD 699 406, Beach Erosion Board, Corps of Engineers, Washington, D.C., December 1954.

Mak, K. L., Wong, Y. S., and Chan, F. T. S. A genetic algorithm for facility layout problems. *Computer Integrated Manufacturing Systems*, 11(1-2):113 – 127, 1998.

Malenica, S., Eatock Taylor, R., and Huang, J. B. Second-order water wave diffraction by an array of vertical cylinders. *Journal of Fluid Mechanics*, 390:349–373, 1999.

Manchester Bobber. `http://www.manchesterbobber.com`, 30th September 2010.

Maniar, H. D. and Newman, J. N. Wave diffraction by a long array of cylinders. *Journal of Fluid Mechanics*, 339:309–330, 1997.

Martin, P. A. *Multiple scattering: interaction of time-harmonic waves with N obstacles*. Cambridge University Press, 2006.

Matsui, T. and Tamaki, T. Hydrodynamic interaction between groups of vertical axisymmetric bodies floating in waves. In *Proceedings of the lnternational Symposium on Hydrodynamics in Ocean Engineering*, volume 2, 817–836, 1981.

Mavrakos, S. A. Hydrodynamic coefficients for groups of interacting vertical axisymmetric bodies. *Ocean Engineering*, 18:485–515, 1991.

Mavrakos, S. A. and Kalofonos, A. Power absorption by arrays of interacting vertical axisymmetric wave-energy devices. *Journal of Offshore Mechanics and Artic Engineering*, 119(4):244–250, 1997.

Mavrakos, S. A. and Koumoutsakos, P. Hydrodynamic interaction among vertical axisymmetric bodies restrained in waves. *Applied Ocean Research*, 9(3):128–140, 1987.

Mavrakos, S. A. and McIver, P. Comparison of methods for computing hydrodynamic characteristics of arrays of wave power devices. *Applied Ocean Research*, 19:283–291, 1997.

Mavrakos, S. A., Katsaounis, G. M., Nielsen, K., and Lemonis, G. Numerical Performance Investigation of an Array of Heaving Wave Power Converters in front of a Vertical Breakwater. In Chung, J. S., Izumiyama, K., Sayed, M., and Hong, S. W., editors, *Proceedings of the Fourteenth International Offshore and Polar Engineering Conference (ISOPE-2004)*, 238–245, 2004.

McIver, P. Wave forces on arrays of floating bodies. *Journal of Engineering Mathematics*, 18:273–285, 1984.

McIver, P. Wave interaction with arrays of structures. *Applied Ocean Research*, 24: 121–126, 2002.

McIver, P. and Evans, D. V. Approximation of wave forces on cylinder arrays. *Applied Ocean Research*, 6(2):101–107, 1984.

McIver, P. and Evans, D. V. An approximate theory for the performance of a number of wave-energy devices set into a reflecting wall. *Applied Ocean Research*, 10(2):58–65, 1988.

McIver, P. and McIver, M. Wave-power absorption by a line of submerged horizontal cylinders. *Applied Ocean Research*, 17:117–126, 1995.

McIver, P., Mavrakos, S., and Singh, G. Wave-power absorption by arrays of devices. In Elliot, G. and Diamantaras, K., editors, *Proceedings of the Second European Wave Power Conference*, 126–133, 1996a.

McIver, P., Mavrakos, S., and Singh, G. Wave-power absorption by arrays of devices. Technical report, Commission of the European Communities, Danish Wave Power aps, 1996b.

Mei, C. C. Power extraction from water waves. *Journal of Ship Research*, 20:63–66, 1976.

Mei, C. C. *The applied dynamics of ocean surface waves.* World Scientific, 2nd print with corrections edition, 1989.

Miles, J. and Gilbert, F. Scattering of gravity waves by a circular dock. *Journal of Fluid Mechanics*, 34(4):783–793, 1968.

Mitchell, M. *An introduction to genetic algorithms.* MIT Press, Cambridge, MA, 1996.

Molinas, M., Skjervheim, O., Sorby, B., Andreasen, P., Lundberg, S., and Undeland, T. Power smoothing by aggregation of wave energy converters for minimizing electrical energy storage requirements. In Falcão, A., editor, *Proceedings of the 7th European Wave and Tidal Energy Conference (EWTEC2007)*, 2007.

Newman, J. N. The interaction of stationary vessels with regular waves. In Bishop, R., Parkinson, A., and Price, W., editors, *Proceedings of the 11th Symposium on Naval Hydrodynamics*, 491–501, 1976.

Newman, J. N. *Marine hydrodynamics*. The MIT Press, 1977.

Newman, J. N. Wave effects on multiple bodies. In Kashiwagi, M., editor, *Hydrodynamics in ship and ocean engineering*, 3–26. RIAM, Kyushu University, 2001.

Ocean Power Technologies. `http://www.oceanpowertechnologies.com/`, 30th September 2010.

Ohkusu, M. Wave action on groups of vertical circular cylinders. *Journal of the Society of Naval Architects in Japan*, 131, 1972.

Ohkusu, M. Hydrodynamic forces on multiple cylinders in waves. In *Proceedings of the International Symposium on Dynamics of Marine Vehicles and Structures in Waves*, 107–112, 1974.

Patel, M. H. *Dynamics of offshore structures*. Butterworths, 1989.

Payne, G. S. *Numerical modelling of a sloped wave energy device*. PhD thesis, The University of Edinburgh, 2006.

Pelamis Wave Power. `http://www.pelamiswave.com/`, 30th September 2010.

Peter, M. A. and Meylan, M. H. Infinite-depth interaction theory for arbitrary floating bodies applied to wave forcing of ice floes. *Journal of Fluid Mechanics*, 500:145–167, 2004.

Pizer, D. J. Maximum wave-power absorption of point absorbers under motion constraints. *Applied Ocean Research*, 15:227–234, 1993.

Price, A. A. E. *New perspectives on wave energy converter control*. PhD thesis, The University of Edinburgh, 2009.

Price, A. A. E., Forehand, D., and Wallace, R. Time-span of future information necessary for theoretical acausal optimal control of wave energy converters. In Keviczky, L., editor, *Proceedings of the European Control Conference*, 2009.

Priestley, H. *Introduction to integration*. Oxford University Press, 1997.

Ricci, P., Saulnier, J.-B., and de O. Falcão, A. F. Point-absorber arrays: a configuration study off the Portuguese West-Coast. In Falcão, A., editor, *Proceedings of the 7th European Wave and Tidal Energy Conference (EWTEC2007)*, 2007.

Ricci, P., Mendia, J. L., Macias, J. P., and Scuotto, M. Equitable testing and evaluation of marine energy extraction devices in terms of performance, cost and environmental impact. Technical report, Equimar, 2009.

Rouck, J. D. and Meirschaert, V. SEEWEC Publishable final activity report. `http://www.seewec.org/results/Publishable%20final%20activity%20report.pdf`, May 2009.

Salter, S. Looking back. In Cruz, J., editor, *Ocean wave energy: current status and future prepectives*, 7–39. Springer-Verlag, 2008.

Salter, S. H. Wave power. *Nature*, 249:720–724, 1974.

Sanchis, L., Håkansson, A., López-Zanon, D., Bravo-Abad, J., and Sánchez-Dehesab, J. Integrated optical devices design by genetic algorithm. *Applied Physics Letters*, 84 (22):4460–4462, 2004.

Sanil Kumar, V. and Ashok Kumar, K. Spectral characteristics of high shallow water waves. *Ocean Engineering*, 35(8-9):900–911, 2008.

Seabased. `http://www.seabased.com/`, 30th September 2010.

SEEWEC. `http://www.seewec.org/`, 30th September 2010.

Siddorn, P. and Eatock Taylor, R. Diffraction and independent radiation by an array of floating cylinders. *Ocean Engineering*, 35:1289–1303, 2008.

Simon, M. J. Multiple scattering in arrays of axisymmetric wave-energy devices. Part 1. A matrix method using a plane-wave approximation. *Journal of Fluid Mechanics*, 120:1–25, 1982.

Söylemez, M. and Yilmaz, O. Hydrodynamic design of a TLP type offloading platform. *Ocean Engineering*, 30:1269–1282, 2003.

Spring, B. H. and Monkmeyer, P. L. Interaction of plane waves with vertical cylinders. In *Proceedings of 14th International Conference on Coastal Engineering*, 1828–1845, 1974.

Srokosz, M. A. Some relations for bodies in a canal, with an application to wave-power absorption. *Journal of Fluid Mechanics*, 99(1):145–162, 1980.

Stallard, T., Rothschild, R., and Aggidis, G. A comparative approach to the economic modelling of a large-scale wave power scheme. *European Journal of Operational Research*, 185:884–898, 2008a.

Stallard, T., Stansby, P. K., and Williamson, A. J. An experimental study of closely spaced point absorber arrays. In *Proceedings of the Eighteenth (2008) International Offshore and Polar Engineering Conference*, 2008b.

Stewart, G. W. *Matrix algorithms*. Society for Industrial and Applied Mathematics, Philadelphia, Pa., 1998.

SuperGen Marine Consortium. `http://www.supergen-marine.org.uk/`, 30th September 2010.

Taghipour, R. and Moan, T. Efficient frequency-domain analysis of dynamic response for the multi-body wave energy converter in multi-directional waves. In *Proceedings of the Eighteenth (2008) International Offshore and Polar Engineering Conference*, 2008.

Taghipour, R., Arswendy, A., Devergez, M., and Moan, T. Structural analysis of a multi-body wave energy converter in the frequency domain by interfacing wamit and abaqus. In Soares, C. G., editor, *Proceedings of the ASME 27th International Conference on Offshore Mechanics and Arctic Engineering (OMAE2008)*, 2008.

The Crown Estate. `http://www.thecrownestate.co.uk`, 30th September 2010.

The European Marine Energy Centre Ltd. Wave Developers. `http://www.emec.org.uk/wave_energy_developers.asp`, 30th September 2010.

The MathWorks, Inc. Genetic Algorithm options: options reference (Global Optimization Toolbox). `http://www.mathworks.com/help/toolbox/gads/f6174dfi10.html`, 30th September 2010a.

The MathWorks, Inc. Bug reports - 450787 - Compiled application terminates with a segment violation on 64-bit Linux in `mkl.so` when doing left division. `http://www.mathworks.com/support/bugreports/450787`, 30th September 2010b.

The MathWorks, Inc. MATLAB documentation. `http://www.mathworks.com/access/helpdesk/help/techdoc/`, 30th September 2010c.

The Scottish Government. The Saltire Prize. `http://www.scotland.gov.uk/Topics/Business-Industry/Energy/Action/leading/saltire-prize`, 30th September 2010.

The Universtiy of Edinburgh. `http://www.mech.ed.ac.uk/research/wavepower/`, 30th September 2010.

Thomas, G. The theory behind the conversion of ocean wave energy: a review. In Cruz, J., editor, *Ocean wave energy: current status and future prepectives*, 41–91. Springer-Verlag, 2008.

Thomas, G. P. and Evans, D. V. Arrays of three-dimensional wave-energy absorbers. *Journal of Fluid Mechanics*, 108:67–88, 1981.

Thomas, S., Weller, S., and Stallard, T. Float response within an array: numerical and experimental comparison. In Bamberger, Y. and Perrot, J.-Y., editors, *Proceedings of the 2nd International Conference on Ocean Energy (ICOE2008)*, 2008.

Thorburn, K. and Leijon, M. Farm size comparison with analytical model of linear generator wave energy converters. *Ocean Engineering*, 34(5-6):908–916, 2007.

Tissandier, J., Babarit, A., and Clément, A. H. Smoothing of the instantaneous power production by grouping effect in an array of SEAREV wave energy converters. In Bamberger, Y. and Perrot, J.-Y., editors, *Proceedings of the 2nd International Conference on Ocean Energy (ICOE2008)*, 1–8, 2008.

Trident Energy. `http://www.tridentenergy.co.uk/`, 30th September 2010.

Tucker, M. J. and Pitt, E. G. *Waves in ocean engineering.* Elsevier, 2001.

Twersky, V. Multiple scattering and radiation by an arbitrary configuration of parallel cylinders. *Journal of the Acoustical Society of America*, 24:42–46, 1952.

Uppsala University. Wave Power Project - Lysekil. `http://www.el.angstrom.uu.se/forskningsprojekt/WavePower/Lysekilsprojektet_E.html`, 30th September 2010.

Venugopal, V. and Smith, G. H. Wave climate investigation for an array of wave power devices. In Falcão, A., editor, *Proceedings of the 7th European Wave and Tidal Energy Conference (EWTEC2007)*, 2007a.

Venugopal, V. and Smith, G. H. The effect of wave period filtering on wave power extraction and device tuning. *Ocean Engineering*, 34(8-9):1120 – 1137, 2007b.

Venugopal, V., Bryden, I. G., and Wallace, A. R. On the interaction of waves with an array of open chambered structures: application to wave energy converters. In Gang, C. and Jianmin, Y., editors, *Proceedings of the ASME 29th International Conference on Ocean, Offshore and Arctic Engineering (OMAE2010)*, 1–9, 2010.

Vicente, P. C., de O. Falcão, A. F., Gato, L. M. C., and Justino, P. A. P. Dynamics of arrays of floating point-absorber wave energy converters with inter-body and bottom slack-mooring connections. *Applied Ocean Research*, 31(4):1–15, 2009.

Vickers, A. W. and Johanning, L. Comparison of damping properties for three different mooring arrangements. In Leijon, M., editor, *Proceedings of the 8th European Wave and Tidal Energy Conference (EWTEC2009)*, 637–645, 2009.

Voith Hydro Wavegen Ltd. `http://www.wavegen.co.uk/`, 30th September 2010.

WAMIT, Inc. *WAMIT User Manual*. 822 Boylston St. – Suite 202, Chestnut Hill, MA 02467–2504, USA, 6.0 edition, 2000.

Wang, C. and Wu, G. Interactions between fully nonlinear water waves and cylinder arrays in a wave tank. *Ocean Engineering*, 37(4):400 – 417, 2010.

Wave Hub. `http://www.southwestrda.org.uk/working_for_the_region/areas/cornwall__the_isles_of_scilly/wave_hub.aspx`, 30th September 2010.

Wave Star A/S. `http://www.wavestarenergy.com/`, 30th September 2010.

Weller, S., Stallard, T., and Stansby, P. Experimental measurements of irregular wave interaction factors in closely spaced arrays. In Leijon, M., editor, *Proceedings of the 8th European Wave and Tidal Energy Conference (EWTEC2009)*, 2009.

Weller, S. D., Stallard, T., and Stansby, P. K. Response of a small array due to irregular waves: comparison to predictions based on measured regular wave response. In Chung, J. S., Ayer, R., Prinsenberg, S., Hong, S. W., and Langen, I., editors, *Proceedings of the 20th International Offshore and Polar Engineering Conference (ISOPE2010)*, volume 7, 900–906, 2010.

Winstone, R., Bolton, P., and Gore, D. Energy security. House of Commons Library. Research Paper 07/42. `http://www.parliament.uk/documents/commons/lib/research/rp2007/rp07-042.pdf`, May 2007.

Yang, C., Löhner, R., and Yim, S. Development of a CFD simulation method for extreme wave and structure interactions. In Mavrakos, S. A. and Bernitsas, M. M., editors, *Proceedings of the ASME 24th International Conference on Offshore Mechanics and Arctic Engineering (OMAE2005)*, 2005.

Yang, L., Jones, B., and Yang, S. A fuzzy multi-objective programming for optimization of fire station locations through genetic algorithms. *European Journal of Operational Research*, 181(2):903–915, 2007.

Yeung, R. W. Added mass and damping of a vertical cylinder in finite-depth waters. *Applied Ocean Research*, 3(3):119–133, 1981.

Yilmaz, O. Hydrodynamic interactions of waves with group of truncated vertical cylinders. *Journal of Waterway, Port, Coastal and Ocean Engineering*, 124(5): 272–279, 1998.

Yilmaz, O. Second order diffraction of water waves by a bottom mounted vertical circular cylinder and some related numerical problems. *Journal of Offshore Mechanics and Arctic Engineering*, 129(1):68–70, 2007.

Zaviska, F. Uber die Beugung elektromagnetischer Wellen an parallelen, unendlich langen Kreiszylindern. *Annalen der Physik, Folge*, 1913.